Numerical Investigation of Stationary Crossflow Instability Evolution in a Rapidly Deformed Base Flow

Srijit Sen

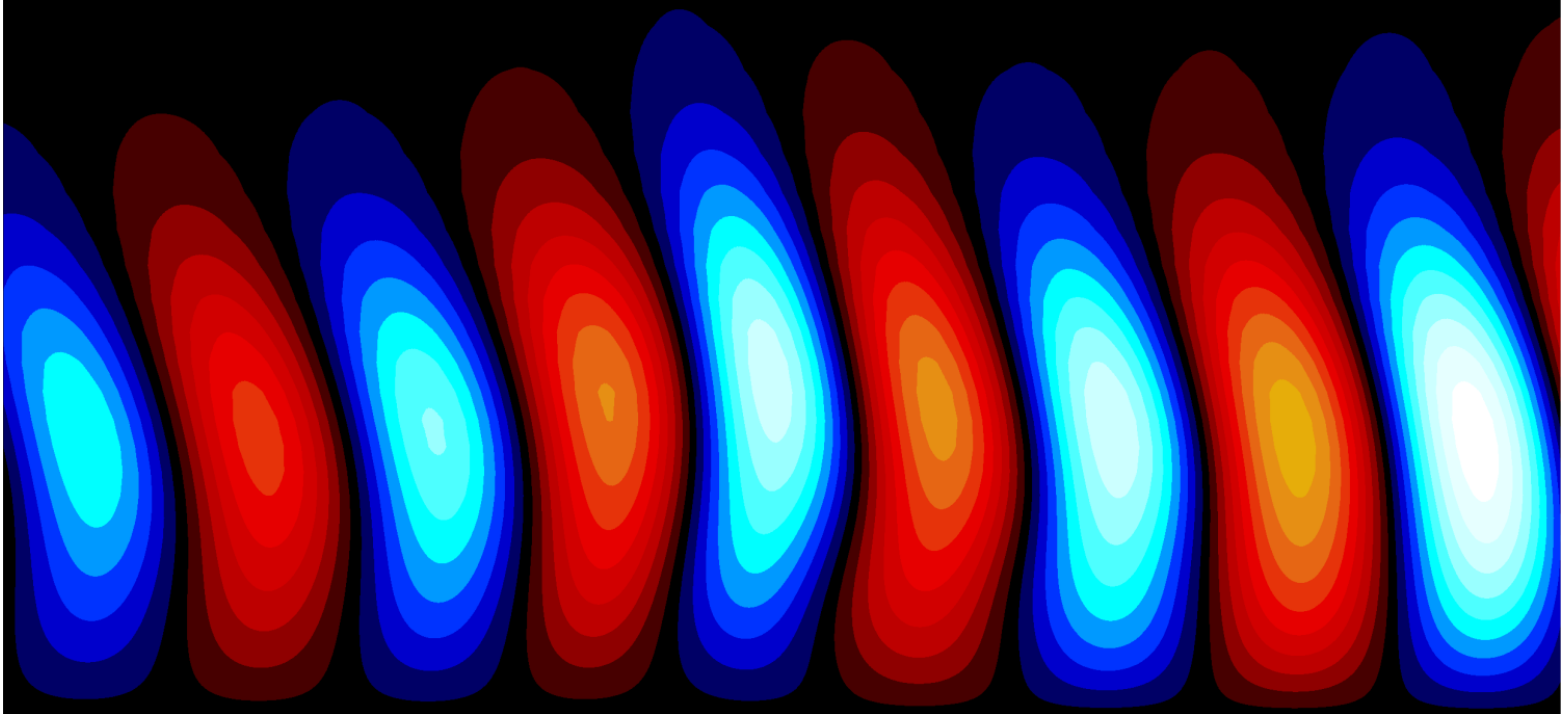

TU Delft

Numerical Investigation of Stationary Crossflow Instability Evolution in a Rapidly Deformed Base Flow

by

Srijit Sen

to obtain the degree of Master of Science
at the Delft University of Technology,
to be defended publicly on Monday Dec 19, 2022 at 10:30 AM.

Student number:	5220823	
Project Duration:	Nov 1,2021 - Dec 19,2022	
Thesis Committee:	Dr. Marios Kotsonis,	Aerodynamics
	Dr. -Ing habil. Stefan Hickel,	Aerodynamics
	Dr. Frits de Prenter,	Wind Energy
	Ir. Jordi Casacuberta Puig,	Aerodynamics

TU Delft

Acknowledgement

,

This thesis marks the end of my journey of immense learning and personal growth at TU Delft. Looking back, I believe that I owe a thank you to multiple people who helped me through this challenging yet wonderful journey. Even though the pandemic imposed multiple challenges in the way knowledge was disseminated in the first year of MSc, I thoroughly enjoyed the courses I took. Thus, I extend a big thank you to all my professors, whose lectures and rigorous assignments deepened my love for flow physics and prepared me for the challenges I would face in my thesis. I also extend my gratitude to my seniors Uttam, Abhyuday, Ravi, and Sophie, whose advice I could always count on when I faced road blocks during my first MSc year.

The journey of my thesis started with a presentation shown by my daily supervisor Jordi, who appeared to be searching for an MSc student to support his brave effort to understand mechanisms of the very complex phenomena of step induced turbulent transition on aircraft wings. I pounced on the opportunity, and even though it took me four months to fully appreciate the depth of his work and my own research topic, I loved every bit of the process, thanks to Jordi's patience answering every question I asked. I would thereby convey my deepest gratitude to my favourite scientist and mathematician, for inspiring my curiosity, patiently answering my silliest questions, encouraging me to explore different avenues, and teaching me to be critical of my own results. Huge swathes of this thesis would be incomplete without the continued support of my second supervisor, Professor Marios. Thank you for bearing with my seemingly random one on one meeting requests. I went to each meeting unsure of where my thesis was headed, and came out with fresh perspective to tackle the problems in my thesis head on. To my third supervisor, Professor Stefan, I have dreamed of working with you ever since I took the courses you delivered, and I am grateful that you could closely follow the progress of my thesis, even with the plethora of tasks on your plate. I would also like to thank Sven for fruitful discussions on the tools used in this thesis, Aaron for being approachable to discuss doubts, and other members of the Low Speed Lab whose depth of knowledge of transition phenomena appears to be formidable. I am rooting for the members of this lab to make a big breakthrough on delaying aircraft wing transition, and I will keenly follow its progress after departing from TU Delft.

Apart from my rich learning experience in Delft, my friends made my MSc journey extra special, being the reason for many of my ups, and standing firmly by my side during my downs. Rahul, thank you for being an empathetic listener, and for guiding me to seek professional help when I hit rock-bottom at the end of my first MSc year. I shall forever cherish the amazing cycling trips and Formula 1 races watched together. Raghav, I am grateful for the role you played in helping me realize the value of socializing. I shall always treasure our dinner conversations, parties, and amazing food you cooked for me. Siddharth, thanks for getting me glued to the gym, cracking the funniest jokes, and cooking exceptional food for me. Pratik and Revanth, thanks for inspiring me with your unparalleled work ethic. Maitreyee, thanks for the ever-refreshing "chai" and constant gym motivation. Thanks to my "Camelot" squad composed of Ivana, Rohan Katkam, Kanhai, and Vivian, with whom I shall treasure the memorable dinners, Christmas celebrations, and our visit to the tulip fields. To my "Leegh" squad composed of Prateek, Divvay, Rohan Kaushik, and Prithvish, a big thank you for all the amazing tennis memories, and the vlogs which still make me laugh till date. Members of the "Extra" squad: Shriram, Kartik, Dhruv, Anirvin, and Avi, I sometimes wish you pulled my leg a little lesser, but I shall forever cherish our trips to Italy and Belgium. Special thanks to all other classmates and friends who I could not fit in this list, for making my journey here memorable.

My final thank you is reserved for my family. I shall always be indebted to my dad, Saikat Sen, for teaching me a broad range of complicated physics and mathematical concepts at a very young age, which enables me to simplify challenging physics and math problems today. To my mom, Sarmistha Sen, thanks for setting an example of balancing work and life, and diligently writing down food recipes which helped me develop my hobby of cooking during my time at Delft. To my grandmoms, Anjali Mukherjee and Chaya Sen, and my cousin and aunt, Srijata Roy and Srirupa Roy, thanks for remaining supportive throughout my journey, and for always checking on how I am doing. I truly realized the value of a loving family during my never-ending thesis writing phase, when their encouragement kept me motivated to reach the finishing line.

Srijit Sen
Delft, December 2022

Summary

Flow of air over a swept wing initially starts in a smooth laminar state before transitioning to a chaotic turbulent state. Flow in a turbulent state results in larger drag than flow in a laminar state, resulting in more fuel consumption and larger carbon footprint, motivating research into causes of transition and efforts to delay its location. The destabilization of stationary crossflow modes is the dominant cause of transition in swept wings. They start off as small disturbances coexisting with the laminar flow on the swept wing (base flow) until they grow to such an extent that they distort the base flow, causing it to transition to a turbulent state. Multiple attempts have focused on finding ways to inhibit crossflow instability growth and delay transition location. However, excrescences on swept wings like a sharp geometric discontinuity in the form of a forward-facing step (FFS) of the thickness of a few millimetres, has the potential of nullifying any control efforts, and causing transition at the location of the FFS, exposing a large region of the wing to increased drag. Although it is known that the FFS deforms the base flow by imposing a rapid pressure change, separation and upwash due to geometrical blockage, the mechanisms by which it impacts stationary crossflow instability evolution are yet to be fully understood. Surprisingly, some swept wings with an FFS of appropriate height have been found to postpone the transition location beyond the clean wing location. This provides further motivation to understand the mechanisms by which a rapid base flow deformation affects stationary crossflow instability evolution since surface excrescences themselves have the potential to act as transition control methods if designed appropriately.

The current thesis considers a spanwise invariant, synthetic, and idealized base flow deformation on a swept flat plate with infinite span (an idealization of a swept wing without curvature effects). The synthetic deformation is obtained by superposing a Gaussian-like pressure variation, approximately spanning width scales close to the order of boundary layer thickness, on the favourable external pressure distribution of a clean swept flat plate (without any roughness elements such as an FFS). The change in external pressure distribution is propagated down to the wall by means of boundary layer equation assumptions, resulting in local pressure changes in the boundary layer like the FFS. The linear evolution of stationary crossflow instability through the region of deformed base flow, initialized as a single wavelength spanwise periodic mode, is modelled using a Harmonic Linearized Navier Stokes Equations solver. An energy balance framework is developed that identifies the production term's behaviour as the differentiator between regions of perturbation growth and decay. The behaviour of the production term is described by two competing mechanisms, the first controlled by wall-tangential base flow shear and the second controlled by wall-tangential base flow acceleration or deceleration. The balance of these mechanisms shows that the perturbation grows faster than the clean case in regions of wall-tangential base flow deceleration and slower than the clean case in regions of wall-tangential base flow acceleration. Perturbations are even found to attenuate in some cases when a region of wall-tangential base flow acceleration follows a region of wall-tangential base flow deceleration. The modification of energy transfer mechanisms brings into question whether the initial modal perturbation deviates from modal character on interacting with the base flow deformation. The Orr mechanism is shown to identify differences in perturbation behaviour from local modal character. However, criteria from the literature hint towards an absence of any non-modal effects. Finally, the extent to which a synthetic idealized base flow deformation mimics the effects of an FFS on deforming the base flow and stationary crossflow instability evolution is tested to show the applicability of methods developed in the thesis to instances of natural base flow deformation. The progress made in this thesis on understanding mechanisms governing the linear phase of perturbation growth on interacting with a base flow deformation leads to suggestions on devices that can be tested to delay the linear primary stage and subsequent stages of stationary crossflow instability growth, with the hope that these devices would lead to the development of new transition delay techniques, making aviation more sustainable than its current state.

Nomenclature

Some of the most commonly used abbreviations, symbols, acronyms and subscripts used in the thesis are listed here.

Abbreviations

BLS	Boundary layer solver
DNS	Direct Numerical Simulation
FFS	Forward-facing step
HLNS	Harmonic Linear Navier Stokes Equation
ILST	Incompressible Linear Stability Theory
LPSE	Linear Parabolized Stabilized Equation
PSE	Parabolized Stability Equation

Symbols

α	Complex streamwise wavenumber
β	Complex spanwise wavenumber (real for stationary crossflow modes)
η'	Wall-normal perturbation vorticity
ζ	Angle between base flow tangential perturbation vector and total perturbation vector
ρ	Density
ϕ	Perturbation phase
ω	Complex circular frequency
ω'	Perturbation vorticity
μ	Mean
ν	Kinematic viscosity
A	Amplitude
$\mathcal{D}$	Work of viscous forces
E	Perturbation energy
i	Iota
p'	Perturbation pressure
P	Pressure
$\mathcal{P}$	Pressure term
Re	Reynolds Number
$\mathcal{T}$	Transport term
u'	Chordwise perturbation velocity
U	Chordwise flow velocity
v'	Wall-normal perturbation velocity
V	Wall-normal flow velocity
w	Width of Gaussian styled pressure variation
w'	Spanwise perturbation velocity
W	Spanwise flow velocity
x	Chordwise direction coordinate
y	Wall-normal direction coordinate
z	Spanwise direction coordinate

Subscripts

0	Initial
∞	Freestream
B	Base flow
i	Imaginary
n	Normal
r	Real
S	Direction of inviscid streamline
st	Step station
t	Tangential
x	x partial derivative
x_c	x contribution
x_d	x derivative terms
y	y partial derivative
y_c	y contribution
y_d	y derivative terms

Special Symbols

ϕ_d	Angular difference between direction of perturbation xz lines of constant phase and inviscid streamline
ΔP	Pressure variation
p_f	Pressure factor

Acronyms

2D	Two-dimensional
3D	Three-dimensional

Contents

List of Figures

List of Tables

1 Introduction

1.1. Motivation

Air travel has become a ubiquitous part of human life. It is widely used for activities such as business, tourism, and migration. It contributes 4.1 % to the global GDP and supports 87.7 million livelihoods (Gill, 2016). Given the benefits of aviation, there is no surprise that air transport has experienced significant growth in the recent past (Sgouridis, Bonnefoy, & Hansman, 2011). However, like any other mode of transport, air travel also contributes to the increase of greenhouse gases like carbon dioxide and other undesirable gases such as nitrogen oxides, sulphur dioxide, soot, and water vapour in the atmosphere. These are products of combustion that takes place in aircraft engines (Anger, 2010). Given these adverse effects, there is an active strive to make aviation more sustainable. Improving jet engine efficiencies might seem like the first choice to achieve this objective. But this approach has reached its physical and technical plateaus (Beck et al., 2018). Thus, efforts to make aviation sustainable can broadly be classified into reducing aircraft drag and switching to alternative forms of aircraft power. While considering the latter, promising advances have been made in the field of electric and hydrogen powered aircraft, that would replace polluting fuel powered engines. However, challenges still remain in fully scaling up these technologies for commercial use (Sahoo, Zhao, & Kyprianidis, 2020; Haglind, Hasselrot, & Singh, 2006). This leaves drag reduction as one of the best possible ways to make aviation more eco-friendly in the immediate future. An aircraft that experiences lesser drag spends lesser fuel while flying, leaving a lower carbon footprint.

Friction drag constitutes the biggest contributor of aircraft drag, with skin friction drag of wings contributing 18% and horizontal tail planes contributing 4% of the total drag (Schrauf, 2005). When air flows over a wing, viscous shear in a thin region near the wing surface (known as the boundary layer) creates friction drag. This viscous shear increases when the air flowing over the wing transitions from a smooth laminar state to a chaotic turbulent state. Turbulent drag is almost 5 to 10 times more than laminar drag (Beck et al., 2018). If the flow were to be laminar on 20%, 30% or 40% of the above stated surfaces by finding methods to delay transition, the total aircraft drag could reduce as much as 8%, 12% or 16% (Schrauf, 2005). The subject of flow transition on swept wings (most common in aviation) is not fully understood. One commonly accepted view of transition in low disturbance environments common for flight is the entrainment and subsequent growth of unstable wave-like modal perturbations. Their growth distorts the undisturbed laminar boundary layer flow (base flow), leading to turbulent transition. Multiple modal mechanisms have been proposed to be active in swept wings (Saric, Reed, & White, 2003). Among these mechanisms, experiments of Gray (1952) and Anscombe and Illingworth (1956) showed that the growth of crossflow instability prepones transition in swept wings to a location much closer to the leading edge compared to unswept wings, proving its dominance in swept wings. The instability manifests as stationary and travelling waves, out of which stationary waves generated by surface roughness dominate transition scenarios in low turbulence environments characteristic of flight (Bippes, 1999). Laminar flow control has thus been proposed to control the development of crossflow modes (Saric, West, Tufts, & Reed, 2019; Wassermann & Kloker, 2002; Serpieri & Kotsonis, 2016).

Unfortunately, laminar flow control has its own set of challenges. Achieving laminar flow throughout the life cycle of an aircraft wing is difficult given the high standards of surface quality that need to be ensured (Hansen, 2010). An increase in surface roughness by wear, for instance, could disturb the airflow over the wing, contributing to preponement of transition location. Similarly, spanwise distributed steps or gaps between wing panels, insect remnants, excrescences, or surface protuberances could also trip the laminar flow earlier than expected (Eppink, 2020). Hence, efforts are being dedicated to understanding how tolerances for these negatively affecting factors can be defined. This is done with the hope that these design or manufacturing tolerances eventually motivate aircraft designs compatible with laminar flow control.

One element that can potentially prepone transition location in a swept wing (or swept flat plate) boundary layer, on interacting with stationary crossflow instabilities, is a spanwise distributed forward-facing step (FFS) of appropriate height (Tufts, Reed, Crawford, Duncan, & Saric, 2017; Rius-Vidales & Kotsonis, 2021; Eppink, 2020). When an FFS is placed in the favourable pressure gradient region of a swept wing (or swept flat plate) boundary layer, local pressure changes are induced in the base flow, upstream and downstream of the step location (Tufts et al., 2017; Casacuberta, Hickel, Westerbeek, & Kotsonis, 2022). This is complemented by regions of separation upstream and downstream of the step and a strong upward flow deflection upstream of the step (Casacuberta, Hickel, Westerbeek, & Kotsonis, 2022). Constructive/destructive interference of crossflow vortices with secondary separation bubble (Tufts et al., 2017), double inflection point theory (Eppink, 2020), and non-modal growth (Casacuberta, Hickel, Westerbeek, & Kotsonis, 2022) are some of the mechanisms proposed to explain the modification of an incoming stationary crossflow mode. However, these theories often do not yield similar conclusions, meaning that the topic is still a matter of debate. The topic is further complicated as the initial perturbation amplitude (Eppink, 2020), spanwise wavelength (Rius-Vidales & Kotsonis, 2020), and unsteady effects (Rius-Vidales & Kotsonis, 2022) also seem to influence behaviour of transition location in addition to step height. Remarkably, Rius-Vidales and Kotsonis (2021) also found that an appropriately designed FFS can lead to a delay of transition front in comparison with an undisturbed flow. Thus, understanding the mechanisms of interaction of stationary crossflow instability with FFS remains an active area of research so that the upstream movement of transition front can be prevented to pave the way for passive or active control of stationary crossflow instability, and to potentially exploit the transition delay results of Rius-Vidales and Kotsonis (2021) to develop new flow control techniques.

The coexistence of base flow phenomena such as the vertical deflection of flow due to geometric blockage, separation bubble formation, and non-monotonic pressure variation in the step vicinity are one of the primary reasons for the difficulty in analyzing stationary crossflow instability response. Although the three phenomena stated above are inevitably coupled, there remains scope to break the problem to its bear parts, and first explain the mechanisms of the interaction of an incoming stationary crossflow mode and a boundary layer with a base flow deformation induced by a rapid pressure change. The analysis can be restricted to the linear regime of stationary crossflow instability growth with a single wavelength to ensure that the first stage of instability growth is fully understood. The tools used for this investigation would be lower-fidelity than those used to capture step effects given the absence of geometric discontinuity, which would allow for a wider sweep of parameters. Answers on physical mechanisms to explain the effect of base flow deformation can be obtained by developing appropriate analysis procedures. Moreover, it is hoped that appropriate pressure variations can be designed to dampen stationary crossflow instability in its linear development stage, thus potentially delaying the forthcoming stages of development. The procedures developed in due course of the thesis can be extrapolated in the future to develop a general framework to describe the interaction of stationary crossflow instability in the linear regime with instances of deformed base flow such as steps, humps and troughs. Considering the larger picture, this project would be a tiny step in the journey of achieving laminar flow airfoils, in the process making aviation a lot more sustainable than what it currently is.

1.2. Organization and Conventions

The motivation for the project (Section 1.1) provides inspiration to introduce specific topics in this chapter, organized in a logical sequence to define the questions and objectives of this thesis clearly. The fundamentals of boundary layers and transition are first discussed. An introduction to the traditional view of modelling transition via modal instability amplification is then provided. Modal instabilities found in swept wing boundary layers are then introduced and special emphasis is placed on the features and control of the dominant instability in such boundary layers i.e. the crossflow instability. The interaction of stationary crossflow instability (the predominant form of crossflow instability in low turbulence environments) with an FFS is then considered due to the ability of the FFS to nullify crossflow instability control techniques. Key deficiencies in understanding interaction mechanisms are clearly highlighted. One theory hints at the instability being governed by non-modal mechanisms on interaction with the FFS (Casacuberta, Hickel, Westerbeek, & Kotsonis, 2022), which subsequently motivates an investigation of criteria and mechanisms to identify non-modal growth. This concludes the survey of state of art, leading to a discussion on the gaps in literature and the scope of the current thesis. This is followed by the development of research questions, the objective, and sub-objectives. The outline of the full report is then presented, and the unique contributions of the thesis are highlighted.

The swept flat plate coordinate system is continually used in this thesis wherein the leading edge orthogonal or chordwise or streamwise direction corresponds to the x direction, the leading edge parallel or spanwise direction corresponds to the z direction and the wall-normal direction corresponds to the y direction. The undisturbed flow called the ”base flow” (also denoted by a subscript B), has velocity U_B in the x direction, V_B in the y direction, and W_B in the z direction. The base flow is also exposed to a varying base flow pressure (P_B). Perturbations seeded on the base flow give rise to the total flow. The perturbation has velocity u' in the x direction, v' in the y direction, w' in the z direction, and pressure p'.

Partial derivatives in x, y, and z direction are denoted by subscripts x, y, and z respectively (for example U_{B_y} represents $\partial U_B/\partial y$).

1.3. Boundary Layer and Transition

Fluids experience friction while moving over a stationary solid surface by virtue of viscous effects in a thin region of flow near the surface known as the boundary layer, where velocity increases from zero at the wall (by virtue of the no-slip condition) to the external velocity (U_e) outside the boundary layer. The friction experienced depends on the velocity difference between adjacent layers in the wall-normal direction, and is appropriately quantified by the shear stress, expressed as $\tau = \nu\rho\, dU_B/dy$, where ν is the kinematic viscosity and ρ is the density. The wall-normal gradient of U_B is highest in the near-wall viscous region and decreases to zero outside the boundary layer in the inviscid region. There is no hard boundary between the viscous and inviscid regions, and boundary layer thickness can thus be defined in multiple ways. One measure is δ_{99}, which considers the height of the boundary layer as the height at which the streamwise flow velocity reaches 99% of freestream velocity ($U = 0.99U_\infty$). Some other physical representations of boundary layer thickness are displacement thickness, momentum thickness, and shape factor, whose physical implications and derivations are explained in Anderson (2011).

When a uniform fluid flow with constant external velocity $U_e = U_\infty$ tangentially comes into contact with a surface such as a flat plate, the boundary layer thickens as it evolves in space. The thickening can be explained using a vorticity analogue (Abernathy, 1968; Vos & Farokhi, 2015), where the variation of velocity in wall-normal direction on fluid contact with the flat plate induces vorticity in the flow field. The circulation or total vorticity contained remains constant, but viscosity acts to diffuse vorticity away from the wall, thickening the boundary layer in the process. Often, boundary layers do not have a constant external velocity but have a varying external velocity by virtue of pressure gradients. A negative pressure gradient is favourable in nature since it increases the external velocity. It also corresponds to an increase of near-wall momentum owing to the lesser time available to viscosity to diffuse the newly introduced vorticity with an increase of external velocity (Abernathy, 1968; Vos & Farokhi, 2015). A positive pressure gradient is adverse since it decreases the external velocity, giving viscosity more time to diffuse vorticity. Continual exposure to adverse pressure gradient leads to flow separation wherein the shears of flow tend to zero leading to flow reversal.

The properties of boundary layers considered so far have been for smooth and laminar boundary layers. A laminar boundary layer under certain conditions has the tendency to transition to a turbulent and chaotic state. The mean profile of a turbulent boundary layer has a higher velocity gradient compared to the mean profile of a laminar boundary layer, which leads to higher shear stress and skin-friction drag in the former compared with the latter. The higher shear is due to unsteady fluctuations in turbulent boundary layers transferring low momentum from far-wall to near-wall regions and vice versa. The transfer of momentum to near-wall regions makes a turbulent boundary layer resistant to separation. However, in cases where flow separation isn't encountered, turbulent transition acts as a drag enhancer.

The mechanisms for turbulent transition are not fully understood, but they vary for two-dimensional (2D) and three-dimensional (3D) boundary layers. Boundary layers in unswept wings are 2D, wherein no fluid flow occurs along the spanwise direction. Whereas boundary layers are 3D in swept wings, wherein a component of flow exists in the spanwise direction. The unswept wing is the most weight-efficient way to extend an airfoil to form a wing that can generate lift. However, its structural and weight advantages are up against the onset of wave drag effects in transonic flight regimes, wherein the presence of shocks drastically increases drag. It was found that the leading edge orthogonal or chordwise component governs the onset of wave drag effects (Anderson, 2011; Vos & Farokhi, 2015). Hence, wing sweep was suggested as the chordwise component of a swept wing was smaller than that of an unswept wing, resulting in lower top speeds in the suction side of the wing, leading to a later onset of wave drag. Two prominent features of swept boundary layers absent in unswept wing boundary layers are the presence of an attachment line and crossflow component. The attachment line is a line of fluid flow replacing the stagnation point, usually present on airfoils or unswept wings owing to the non-zero spanwise component along the leading edge. Crossflow, on the other hand, is attributed to the near-wall base flow not following the direction of the inviscid base flow. The influence of sweep and pressure gradient results in curved inviscid streamlines (Saric et al., 2003). Compared to the inviscid region, the chordwise velocity is lesser, but the pressure gradient remains the same in the near-wall region. Thus, centripetal acceleration in the near-wall region is not sufficient to balance the pressure gradient, resulting in a flow with a component in the direction perpendicular to the inviscid streamline, known as crossflow. Since crossflow tends to zero in the inviscid region and the wall, its profile is inflectional in nature. In the favourable pressure gradient region of backward swept wings, the attachment line flow moves from root to tip, and the near-wall streamlines are tilted less outboard compared to inviscid streamlines resulting in positive crossflow as per the conventions considered here.

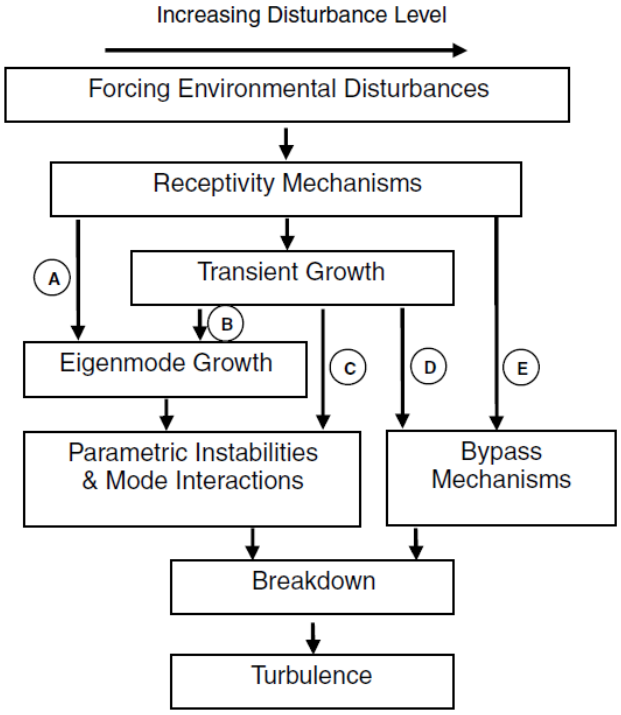

Figure 1.1: Various paths to transition in wall boundary layers; reproduced from Reshotko (2008).

Turbulent transition in both 2D and 3D boundary layers starts with receptivity, a process by which disturbances in the freestream enter a boundary layer as steady or unsteady fluctuations of basic state (Morkovin, 1969). Following receptivity, five paths to transition have been proposed, as shown in Figure 1.1. Of these, path A to path C correspond to low disturbance environments characteristic of flight (Reshotko, 2008), and are hence elaborated upon. In path A, external disturbances are low, and transition scenarios are dominated by the amplification of modal instabilities. In 2D boundary layers, for the dominant instability mechanism of Tollmien-Schlicting wave growth, receptivity is followed by a stage of linear growth, referred to as the primary growth phase. The growth of amplitude leads to the development of secondary instabilities (Reshotko, 2008), which induce non-linearities and three-dimensional effects (Herbert, 1988), leading to the onset of transition. In 3D boundary layers, for the dominant modal mechanism of crossflow instability growth, although the initial growth after receptivity follows a linear trend, the primary stage of growth also contains a non-linear phase, wherein the amplitude of the disturbance saturates (Reed, Saric, & Arnal, 1996). Following the primary phase, the flow becomes susceptible to high frequency secondary instabilities. This leads to the breakdown of laminar flow and subsequent transition to turbulence. The details of unstable waves or modes and their evolution in the linear regime are captured by Linear Stability Equations. The e^N method (Smith & Gamberoni, 1956; Van Ingen, 1956) predicts transition based on the primary linear growth phase and works well for 2D boundary layers but falters in predicting 3D boundary layer transition due to the extended non-linear regime before the action of secondary instabilities (Reed et al., 1996).

Path B corresponds to slightly higher levels of external disturbance. In flow regimes where unstable modes can't be identified, a superposition of stable modes can cause short-term transient or non-modal growth (Schmid & Henningson, 2001). Path B represents scenarios where these non-modal conditions initialized upstream, lead to the development of modal disturbances downstream, when modal theory predicts that an unstable mode only exists in the downstream region. Numerical studies have shown that such scenarios can be prominent in 3D boundary layers, where an initially non-modal instability can precondition the growth of a modal crossflow instability (Corbett & Bottaro, 2001; Tempelmann, Hanifi, & Henningson, 2010; Lucas, 2014). In 2D boundary layers, dominant modal perturbations are 2D in nature, whereas dominant non-modal initial conditions are 3D in nature (2D instabilities do not have any periodic variation in the spanwise direction unlike 3D instabilities). Thus, the evolution of a non-modal disturbance to a modal disturbance is difficult to perceive in 2D boundary layer flows (Reshotko, 2008). In path C, the external disturbance levels are further higher than scenarios of path B, and non-modal growth totally overrides modal amplification. The Orr mechanism (Orr, 1907) and lift-up effect (Ellingsen & Palm, 1975) in parallel 2D flows, and their extension to non-parallel 2D flows (Andersson, Berggren, & Henningson, 1999) come under the umbrella of theories that were proposed to explain the possibility of bypassing modal growth. Path A is the traditional theory to predict the onset of turbulence, and transition fronts in flight

conditions have shown evidence of modal instability dominated transition (Gray, 1952; Anscombe & Illingworth, 1956), motivating an investigation of modal growth is presented in the upcoming section.

1.4. Analysis of Modal Growth

The stages of modal perturbation growth were defined for two-dimensional and three-dimensional flows in Section 1.3. However, it is important to understand how the existence of unstable modes is predicted. Skipping the phase of receptivity, linear stability theory (LST) can be used to identify unstable modes assuming a parallel base flow ($V_B = 0$,$U_{B_x} = 0$, and $W_{B_x} = 0$). The Navier Stokes equation of the base flow subtracted from the total flow yields the perturbation equation. The linearized equation (derived in Section 4.2) written in terms of Einstein convention reads

$$\frac{\partial u_j'}{\partial x_j} = 0, \tag{1.1}$$

$$\frac{\partial u_k'}{\partial t} + U_B\frac{\partial u_k'}{\partial x} + W_B\frac{\partial u_k'}{\partial z} + v'\frac{dU_B}{dy} + v'\frac{dW_B}{dy} = -\frac{1}{\rho}\frac{\partial p'}{\partial x_k} + \nu\frac{\partial^2 u_k'}{\partial x_j^2}. \tag{1.2}$$

The subscript k considers quantities one at a time wherein $k = 1$ denotes quantities along x, $k = 2$ denotes quantities along y, and $k = 3$ denotes quantities along z. x, y, and z can be equivalently represented as x_1, x_2, and x_3. u', v', and w' are represented by u_1', u_2', and u_3' respectively. The quantities represented by the index j are the same as those represented by k, but it considers the summation of quantities along x, y, and z instead of considering them one at a time. In Equation 1.2, the coefficients of perturbation terms are functions of y, owing to which a solution of velocity and pressure perturbation can be obtained by the separation of variables using normal modes (Reed et al., 1996). The Fourier ansatz typically used for such problems is of the form

$$u_k' = \hat{u}_k(y)e^{\mathrm{i}(\alpha x+\beta z-\omega t)} + \text{c.c.}, \tag{1.3}$$

$$p' = \hat{p}(y)e^{\mathrm{i}(\alpha x+\beta z-\omega t)} + \text{c.c.}, \tag{1.4}$$

where $\hat{u}_k(y)$ and $\hat{p}(y)$ are complex in nature and encapsulate the y dependency of the ansatz. α, β and ω are complex in nature with their real parts (α_r, β_r and ω_r) determining periodicity, and imaginary parts (α_i, β_i and ω_i) determining whether there is growth or decay in x, z, and t, respectively. When the ansatz presented in Equation 1.3 and Equation 1.4 is substituted into the linearized perturbation equations after dropping the complex conjugate and recast in terms of wall-normal velocity (v') and wall-normal vorticity (η') perturbations by eliminating perturbation pressure terms (as shown in (Schmid & Henningson, 2001)), the result is the Orr-Sommerfeld and Squire Equation which read

$$\left[\Big(-\mathrm{i}\omega + \mathrm{i}(\alpha U_B + \beta W_B)\Big)\Big(D^2 - k^2\Big) - \mathrm{i}\left(\alpha\frac{d^2U_B}{\partial y^2} + \beta\frac{d^2W_B}{\partial y^2}\right) - \nu\Big(D^2 - k^2\Big)^2\right]\hat{v} = 0, \tag{1.5}$$

$$\Big[(-\mathrm{i}\omega + \mathrm{i}\alpha U_B + \mathrm{i}\beta W_B - \nu(D^2 - k^2)\Big]\hat{\eta} = -\mathrm{i}\beta\frac{dU_B}{dy}\hat{v}, \tag{1.6}$$

where

$$D^2 = \frac{\partial^2}{\partial y^2}, \tag{1.7}$$

$$k^2 = \alpha^2 + \beta^2, \tag{1.8}$$

$$\hat{\eta} = \mathrm{i}(\beta\hat{u} - \alpha\hat{w}). \tag{1.9}$$

The non-dimensionalized version of Equation 1.5 and Equation 1.6 are more popularly used, wherein the velocities and length scales are scaled by reference scales U_{ref} and l_{ref}, respectively, resulting in a Reynolds Number $Re = U_{ref}l_{ref}/\nu$. To solve the non-dimensional form of the above equations, the direction in which perturbation grows or decays needs to be specified. In spatial analysis with growth in chordwise direction, α is assumed to be the complex output of the analysis, and β and ω are assumed to be real inputs to the equation along with a specification of Re. With appropriate boundary conditions, the Orr-Sommerfeld equation simplifies to an eigenvalue problem of fourth-order with eigenvector $\hat{v}$ and eigenvalue α, determined as a function of inputs β, ω, and Re. The non-homogenous Squire equation can be solved using the forced value of $\hat{v}$ to obtain a particular solution, namely $\hat{\eta}_P$, such that $[\hat{v},\ \hat{\eta}_P]$ is called the Orr-Sommerfeld mode (Schmid & Henningson, 2001). The homogenous solution of Squire equation ($\hat{\eta}_H$) reveals another set of modes $[0,\ \hat{\eta}_H]$, which are stable (Schmid & Henningson, 2001), and hence not considered while determining the least stable mode. In temporal analysis, ω is the complex eigenvalue, determined as a function of real inputs α, β and Re. Temporal equations are usually easier to solve since the determination of α in spatial analysis makes the eigenvalue problem non-linear (Boiko et al., 2011). Since all coefficients of the eigenvalue problem are real, the solutions occur in complex conjugate pairs (Reed et al., 1996).

Initial attempts to solve the eigenvalue problem a century ago faced hurdles due to the lack of computing technology to solve fourth-order eigenvalue problems. Hence, simplifications were made to the Orr-Sommerfield equation by assuming a larger Reynolds number limit, which simplified Equation 1.5 to the Rayleigh equation, whose solution yielded an "inviscid" instability. For a temporal problem with 2D base flow ($W_B = 0$) considering 2D instability ($\beta = 0$), Rayleigh (1879) stated that the presence of an inflection point in the base flow profile is a necessary condition for the existence of an inviscid instability. Pioneering contributions were also made by Fjørtoft (1950) and Howard (1961) to define theorems for the existence of such an instability. When the temporal problem assuming viscous terms was solved for a flow with piecewise linear velocity distribution (Prandtl, 1921), it was proven that unstable modes could exist without an inflection point. It is known today that a lot of flows destabilize without the existence of an inflection point via the action of instabilities called "viscous instability" (Boiko et al., 2011).

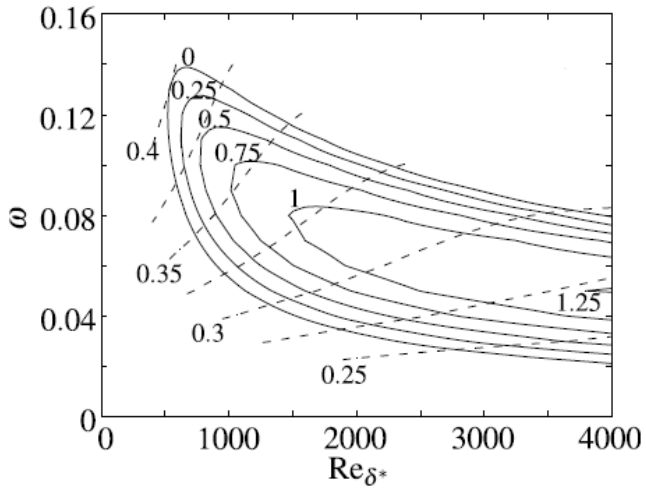

Figure 1.2: Stability characteristics curve of Blasius Boundary Layer with inputs ω on y axis and Reynolds number based on displacement thickness ($Re_{\delta*}$) on the x axis. Constant $-\alpha_i$ (solid lines), Phase velocity ω/α_r (dashed lines), Neutral Curve (solid line α_i = 0); reproduced from Boiko et al. (2011).

The usual aim of a stability analysis is to determine regimes of flow where an instability can grow, and thus eventually transition the laminar flow to a turbulent state. An example of the result of a spatial analysis for a 2D Blasius Boundary layer susceptible to 2D instability ($\beta = 0$) growth is shown in Figure 1.2 (Boiko et al., 2011). A sweep across ω and spatial locations (obtained by varying $Re_{\delta*}$, the Reynolds number based on displacement thickness, δ^*, in Figure 1.2) is conducted for a given base flow, and the lines of constant α_i are plotted. The neutral curve corresponds to $\alpha_i = 0$. Within the neutral curve envelope, values of α_i are negative, meaning the instability can grow. Whereas, outside the neutral curve, values of α_i are positive, meaning the instability decays. The minimum x coordinate of the neutral curve projected onto the x axis denotes the value of $Re_{\delta*}$ beyond which unstable eigenmodes can exist. The value of the streamwise coordinate at this Reynolds number can be denoted "critical" streamwise position (x_{cr}). $x < x_{cr}$ denotes subcritical regimes, where all eigenmodes are stable. The knowledge of transition location comes from the e^N method, where N at a certain position is the maximum logarithm of amplitude gain for a particular frequency. Iterating over a range of frequencies generates an N envelope, and it is estimated that flow transitions to turbulence when N takes values between 7 and 9 (Smith & Gamberoni, 1956; Van Ingen, 1956).

While LST provides insight into determining regions of instability growth, it has several limitations such as the assumption of parallel flow, ignoring upstream effects, ignoring non-linear effects, and ignoring receptivity details, and hence can't be accurately used to model instability evolution. Techniques such as Parabolized Stability Equation (PSE) and Direct Numerical Simulations (DNS) take into account these limitations. If receptivity details are not considered, these methods can be initialized by an Orr-Sommerfeld mode, and the evolution of instability through a predetermined base flow can be predicted. PSE is a parabolic marching technique and solves perturbation evolution at a fraction of the computational cost of DNS which solves an elliptic system (Bertolotti, Herbert, & Spalart, 1992). However, the full modelling of all stages of the transition process is more accurately described by DNS (Bertolotti et al., 1992). PSE also faces difficulty negotiating strong streamwise changes in base flow as its formulation assumes that the laminar base flow and perturbation properties encounter small changes over scales of the order of the characteristic wavelength of the mode (Franco, Hein, & Valero, 1821). The DNS again is a legitimate alternative in such cases. However, to avoid excessive computational cost,

linear evolution can be captured using the fully elliptic Harmonic Linearized Navier Stokes Solver (HLNS).

Although the above introduced tools are capable of identifying unstable modes (i.e. LST) and modelling their evolution (i.e. PSE, HLNS, and DNS), they do not provide information on the mechanisms by which modal instabilities grow. For 2D parallel flows, Lin (1944) provided separate vorticity based mechanisms for identifying the existence of inviscid and viscous instabilities. However, the theory doesn't explain behaviour in non-parallel base flows. The Reynolds-Orr energy balance framework is a method to understand mechanisms by which a perturbation grows or decays in non-parallel base flow. The linear perturbation energy equation integrated over a control volume V reads

$$\int_V \frac{\partial E}{\partial t} = \underbrace{-\int_V U_{B,j}\frac{\partial E}{\partial x_j}dV}_{\text{Transport}} \underbrace{-\sum_{k=1}^{3}\int_V u'_k u'_j \frac{\partial U_{B,k}}{\partial x_j}dV}_{\text{Production}} \underbrace{-\sum_{k=1}^{3}\int_V u'_k \frac{\partial p'}{\partial x_k}dV}_{\text{Pressure Work}} + \underbrace{\frac{1}{Re}\sum_{k=1}^{3}\int_V \frac{\partial^2 u'_k}{\partial x_j^2}dV}_{\text{Work of Viscous Forces}}. \tag{1.10}$$

where u'_k is the real-valued representation of perturbation field and perturbation energy E is defined as

$$E = \frac{1}{2}\sum_{k=1}^{3} u'^2_k. \tag{1.11}$$

In case of a temporal framework, $\partial E/\partial t$ represents energy growth in time. Due to the periodicity of perturbation in x and z directions, the transport terms yield a very small result in a periodic domain. The pressure perturbation is also usually small compared to the magnitude of perturbation energy and yields negligible contributions. The main terms contributing to the energy budget are production and work of viscous forces. The term representing work of viscous forces simplifies to dissipation under the assumption of periodicity in x, representing the energy dissipated by perturbation by viscous effects (Schmid & Henningson, 2001). Production represents the kinetic energy exchange of perturbation with base flow (Albensoeder, Kuhlmann, & Rath, 2001). Analyzing the behaviour of production term can lend insight into the mechanisms by which a perturbation grows or decays, with a positive sign indicating energy transfer from base flow to perturbation and a negative sign indicating energy transfer from perturbation to base flow (Albensoeder et al., 2001). In the spatial framework with growth in the chordwise direction, the analysis becomes more convoluted as the energy growth ($\partial E/\partial x$) in space is part of the advection term. Nevertheless, the Reynolds-Orr framework has been used to elaborate mechanisms of modal evolution for spatially evolving instabilities by dividing the entire energy balance equation (Equation 1.10) by U_B to isolate $\partial E/\partial x$ (Karp & Hack, 2018).

1.5. Crossflow Instability

Multiple modal growth mechanisms are active in 3D boundary layers (Saric et al., 2003). The instabilities not considered in this thesis are streamwise instability, attachment line instability, and centrifugal instability. Streamwise instabilities destabilize by the growth of TS waves, which are unstable only in regions of the wing exposed to an adverse pressure gradient. They are thus less critical than instabilities that grow near the leading edge or the favourable pressure gradient region of swept wings. The attachment line flow can destabilize when the leading edge flow is contaminated or when an instability develops which eventually transitions an initially smooth attachment line flow. The action of these instabilities can be prevented by considering an appropriate leading edge radius (Reed & Saric, 2014). The centrifugal instability on the other hand occurs in regions of concave curvature and results in the development and destabilization of Görtler vortices. A relatively large number of wings use predominantly convex airfoil profiles, which shields such wings from centrifugal instability driven transition. This leads to a discussion on the instability considered in this thesis which could arguably be considered the dominant instability in 3D boundary layers. Directional profiles i.e. the component of 3D boundary layer in a direction along the wavenumber vector govern instability evolution (Mack, 1984), and the directional profiles close to crossflow direction are inflectional, leading to the development of an inviscid instability called crossflow instability (Bippes, 1999). The crossflow instability amplifies in a favourable pressure gradient regime since crossflow profiles are inflectional in this regime, and thus have a potential to reduce the laminar flow regime on swept wings compared to unswept wings (Gray, 1952; Anscombe & Illingworth, 1956), prompting studies on understanding its behaviour. The study of crossflow instability is usually conducted on swept wings or swept flat plates, wherein the latter focuses only on the effect of pressure gradient without taking into account the effects of curvature.

The crossflow instability manifests as oblique waves that take both the form of travelling and stationary waves (Bippes, 1999; Saric et al., 2003). In low turbulence environments characteristic of flight, stationary disturbances generated by surface roughness elements dominate (Bippes, 1999). The instability is experimentally visualized in wind tunnels with low turbulence intensity by placing discrete roughness elements (DREs) in a spanwise repeated pattern on a swept wing or

a swept flat plate with swept wing-like pressure gradient, separated by a gap of the disturbance wavelength estimated from linear stability theory. Experimental techniques have been complemented by numerical analysis through PSE and DNS on swept flat plates with pressure gradients mimicking experimental conditions. These allow easy separation of the total flow into base flow and perturbation, which is considerably harder in experimental studies where the base flow can only be estimated to some degree by a spanwise averaged temporal mean flow, and perturbation behaviour is subsequently obtained by subtracting mean flow from total flow (Bippes, 1999). Numerical investigations can be initialized via various methods. A spanwise periodic Orr-Sommerfeld mode can be used to initialize perturbations in case receptivity details are neglected. Whereas the modelling of cylindrical disturbance elements (Tempelmann, Schrader, Hanifi, Brandt, & Henningson, 2012) or localized disturbance strips (Wassermann & Kloker, 2002) are methods to initialize stationary crossflow instabilities accounting for receptivity. Details of receptivity play an important role in determining unsteady interactions. Although numerical simulations provide insightful data, experimental uncertainties make matching numerical and experimental data very difficult (Tempelmann et al., 2012).

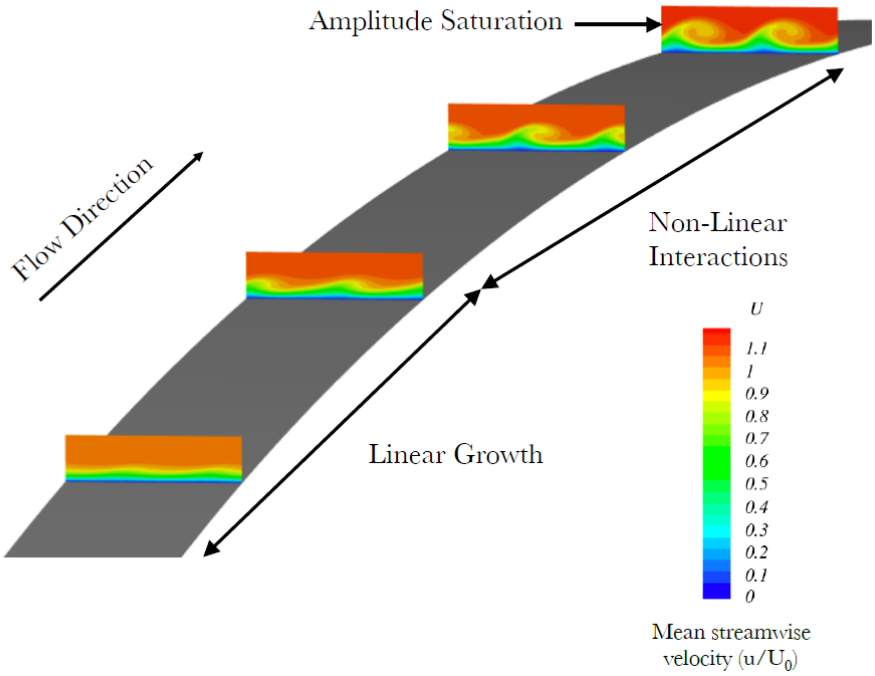

Figure 1.3: Stages of stationary crossflow mode evolution explained with contours of streamwise velocity (U_B/U_∞, denoted u/U_0 in author's convention); reproduced from Mistry (2014)

Experimental investigations reveal that the perturbation takes the form of counter-rotating vortices with lines of constant phase (axes) very close to the direction of inviscid streamlines (Bippes, 1999). When the perturbation is superposed onto the mean flow, the total flow has traces of co-rotating vortices. The growth of instability following receptivity can be classified into primary and secondary phases. In the primary phase, perturbation growth initially occurs linearly. Small vertical and spanwise perturbations convect high-momentum fluid away from the wall and high-momentum towards the wall (Saric et al., 2003). The high gradient region near the wall favours this momentum exchange. These small momentum displacements lead to large streamwise disturbances. The effect of these perturbations on mean flow can be seen as spanwise modulations of the streamwise velocity profile as depicted in Figure 1.3. These streamwise disturbances soon get large ($> 10\%U_\infty$) to the extent that computations of results from linear theory depart from experimentally observed features (Reibert, Saric, Carrillo, & Chapman, 1996). This marks the onset of non-linear growth where evidence of harmonics of the wavelength forced by the DREs are found (Reibert et al., 1996) (for a forcing of 12mm, harmonics are 6mm, 4mm, and so on). The non-linear regime leads to the saturation of perturbation amplitude (Bippes, 1999). Figure 1.3 depicts the transformation from linear to non-linear regime, characterized by rollover (Mistry, 2014). The initial amplitude of stationary crossflow mode can also play a role in determining the extent of linear and non-linear primary regimes, thereby affecting transition location (Radeztsky Jr, Reibert, & Saric, 1999). The primary stage of growth distorts the base flow which now has strong shear layers and inflectional velocity profiles (Saric et al., 2003; Casacuberta, Groot, Hickel, & Kotsonis, 2022). The distorted base flow is susceptible to unsteady secondary instabilities of three types (Malik, Li, &

Chang, 1994), which rapidly amplify leading to breakdown and transition to turbulence. This breakdown is characterized by a saw-tooth pattern since transition develops locally leading to uneven distribution in span (Saric et al., 2003).

Since this instability substantially reduces the laminar flow on a swept wing compared to an unswept wing (Anscombe & Illingworth, 1956; Gray, 1952), its control has received considerable attention. Saric et al. (2019) note the results of Reibert et al. (1996), wherein only the harmonics of wavelength lesser than the forced wavelengths appear in the non-linear regime. The authors use this as inspiration to force a subcritical stationary crossflow mode with wavelength lower than the naturally dominant critical mode. This ends up forcing the harmonics of the subcritical mode in the non-linear growth regime but does not force the critical wavelength itself, which results in a transition delay. Wassermann and Kloker (2002) explained that the subcritical modes induce a deformation of the mean flow, which postpones the amplification of the critical mode and its harmonics. This process is called upstream flow deformation (UFD), referring to a set of techniques that can be used to force subcritical modes to cause transition delay. Another class of techniques proposed to alter the base flow itself to reduce the crossflow component and stabilize crossflow vortices to induce transition delay (Dörr & Kloker, 2015). This method falls under the category of Base Flow Deformation methods. The above described flow control techniques, however, face significant challenges for incorporation into the mainstream as some degree of roughness ubiquitous in swept wings can prepone the location of turbulent transition.

1.6. Interaction of FFS with Stationary Crossflow Instability

An FFS of appropriate height, placed in the favourable pressure gradient region of a swept flat plate or wing, interacts with an incoming stationary crossflow instability to prepone transition location significantly compared with a no-step or clean case (Tufts et al., 2017; Eppink, 2020; Rius-Vidales & Kotsonis, 2021). This has been reported to occur across different values of spanwise wavelength of crossflow instability, wherein appropriate step heights have preponed transition location to the approximate location of the FFS (Rius-Vidales & Kotsonis, 2020). The presence of an FFS can thereby invalidate control efforts such as forcing of subcritical crossflow modes proposed by Saric et al. (2019), which can trip at the FFS location. Initial attempts to investigate the phenomena of transition preponement were directed at designing empirical one-factor criteria to develop tolerances for this threshold, namely the critical step height, beneath which transition location wouldn't move significantly upstream compared to the clean case (Tufts et al., 2017). Recent studies of Eppink (2020) and Rius-Vidales and Kotsonis (2020) revealed that one-factor criteria might not be adequate to explain transition preponement. Moreover, Rius-Vidales and Kotsonis (2021) also found a particular step height that postponed transition location compared to a clean case (without the presence of FFS). Thus, the focus shifted to observing physical features of the FFS base flow and finding mechanisms by which the modified base flow influences perturbation behaviour.

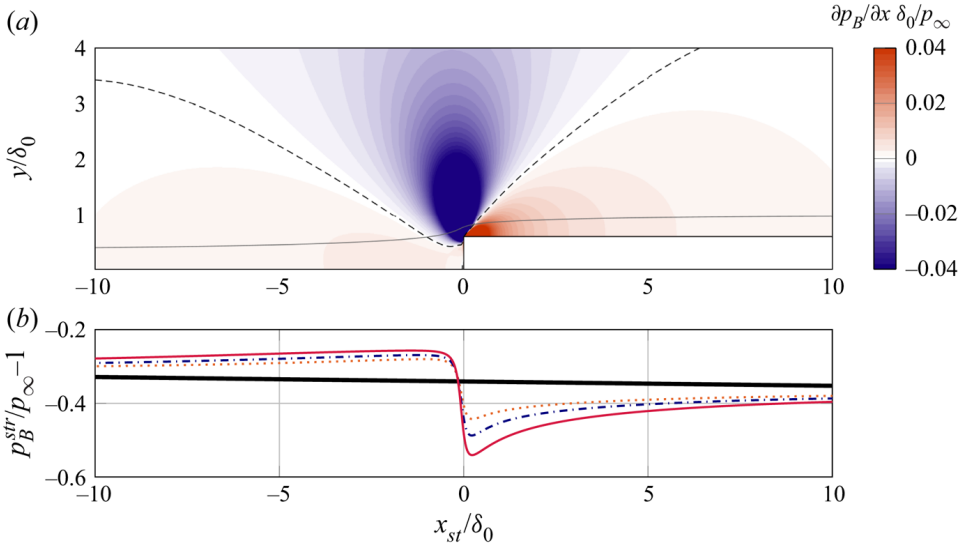

Figure 1.4: (a) Pressure gradient in chordwise direction (colour map), line of zero pressure chordwise gradient (dashed black), streamline seeded at inlet (grey) (b) Variation of static pressure along streamline seeded at $y/\delta_0 = 0.2$ in clean case (thick solid black), step case I (dotted orange), step case II (dash-dotted blue), step case III (thin solid red); reproduced from Casacuberta, Hickel, Westerbeek, and Kotsonis (2022).

1.6.1. Effects of FFS on Base Flow

The presence of an FFS alters the local pressure distribution of the boundary layer compared with the clean case (Casacuberta, Hickel, Westerbeek, & Kotsonis, 2022; Tufts et al., 2017). Casacuberta, Hickel, Westerbeek, and Kotsonis (2022) test three different steps and observe consistent base flow pressure modification trends for all steps as shown in Figure 1.4. In this figure, x_{st}/δ_0 corresponds to a transformed non-dimensionalized coordinate in chordwise direction wherein $\delta_0 = \delta_{99}$ at domain inlet, such that $x_{st}/\delta_0 = 0$ denotes step location (whose negative values denote step upstream regions, and positive values denote step downstream regions). Contours of base flow pressure in Figure 1.4(a) and a plot of pressure along a characteristic boundary layer streamline in Figure 1.4(b) show a region of adverse pressure gradient upstream of the step, a strong favourable pressure gradient region in the vicinity of the step and another adverse pressure gradient region downstream, as opposed to the smooth favourable pressure gradient in the clean case. Exposure to regions of strong adverse pressure gradient can lead to flow separation. The works of Casacuberta, Hickel, Westerbeek, and Kotsonis (2022) and Tufts et al. (2017) reveal two regions of flow reversal within the adverse pressure regions just upstream and downstream of the step. Tufts et al. (2017) note that these recirculation regions are areas of open helical flow and also note that the size of these recirculation bubbles increases with the step size. Casacuberta, Hickel, Westerbeek, and Kotsonis (2022) comment that the size of the first bubble is larger than the second bubble. Another manifestation of the change in local pressure gradient is the change of crossflow velocity direction. Mack (1984) shows that Falkner Skan Cooke profiles with adverse and favourable pressure gradient have crossflow components in opposite direction. In the presence of a favourable pressure gradient in the clean case, the crossflow velocity is positive as per conventions considered here. With the presence of step, Eppink (2020) observes that upstream of the step, there exists a local region of negative crossflow, which changes to positive crossflow at the step which then changes back to negative crossflow further downstream of the step, before relaxing back to the clean case conditions. Eppink (2020) attributes the presence of adverse pressure gradient regions as the likely cause for crossflow profile reversal upstream and downstream of the step.

The change in direction of crossflow velocity is a direct consequence of the change in behaviour of the base flow velocity vector near the step. Casacuberta, Hickel, Westerbeek, and Kotsonis (2022) note that this can be attributed to the behavioural difference of base flow in the near-step and inviscid regions. The inviscid region mildly feels the effect of local step pressure gradient, evidenced by the inviscid streamline angle of step cases being similar to the clean case. However, in regions of local adverse pressure gradient upstream and downstream of the step, the chordwise velocity decelerates. Such effects are not as pronounced in the spanwise velocity. This causes a strong outboard turn of streamlines in adverse pressure gradient region thus reversing crossflow. In the local favourable pressure gradient region near the step in between these local regions of adverse pressure gradient, the rapid acceleration of chordwise velocity causes an inboard flow resulting in a crossflow velocity profile directed in the positive direction. The difference between spanwise and chordwise velocity behaviour in the near-wall region is attributed to the presence of pressure gradient only in the chordwise direction, with no spanwise pressure gradient to directly influence spanwise velocity evolution. Additionally, an upwash is also noted upstream of the step, which gets enhanced at the step, especially in the near wall region, which then decays further downstream.

1.6.2. Effects of FFS on Perturbation Evolution

Casacuberta, Hickel, Westerbeek, and Kotsonis (2022) propose the study of amplitude function of fundamental chordwise perturbation velocity field to contrast behaviour in clean and FFS regimes (fundamental mode corresponds to the monochromatic wavelength that is forced upstream of the step). The evolution of amplitude function over the step is shown in Figure 1.5. Upstream of the step, two peaks appear, wherein the primary peak deflects away from the wall, and the secondary peak remains close to the wall. These secondary peaks appear as near wall streaks, phase shifted with respect to the streaks caused by primary peaks. Downstream of the step, a secondary peak is again present in all step heights considered. This peak intensifies with step height. For the highest step considered, this secondary peak passes the main peak of the perturbation. These secondary peaks start decaying further downstream, merging into a single peaked profile. Secondary peaks also appear in the investigations of Eppink (2020) and Tufts et al. (2017). However, since these do not appear in the clean case, Casacuberta, Hickel, Westerbeek, and Kotsonis (2022) claim that these are secondary structures, and the primary peak is more representative of the behaviour of the crossflow instability. Upstream of the step, this theory agrees well with the observations of Rius-Vidales and Kotsonis (2021) and Eppink (2020) who observe that the instability does not directly interact with the step, but rather sees an upward deflection.

Since the structural modifications of the instability are now clear, the focus shifts to understanding the amplitude evolution of the instability. Upstream of the step, Casacuberta, Hickel, Westerbeek, and Kotsonis (2022) observe the evolution of the value of amplitude function of fundamental chordwise perturbation velocity at its primary peak. With respect to the clean case, the step cases show higher amplification in the step upstream region. The author points out that this evolution is linear as the results of LPSE closely match DNS results in the step upstream region before the appearance of secondary

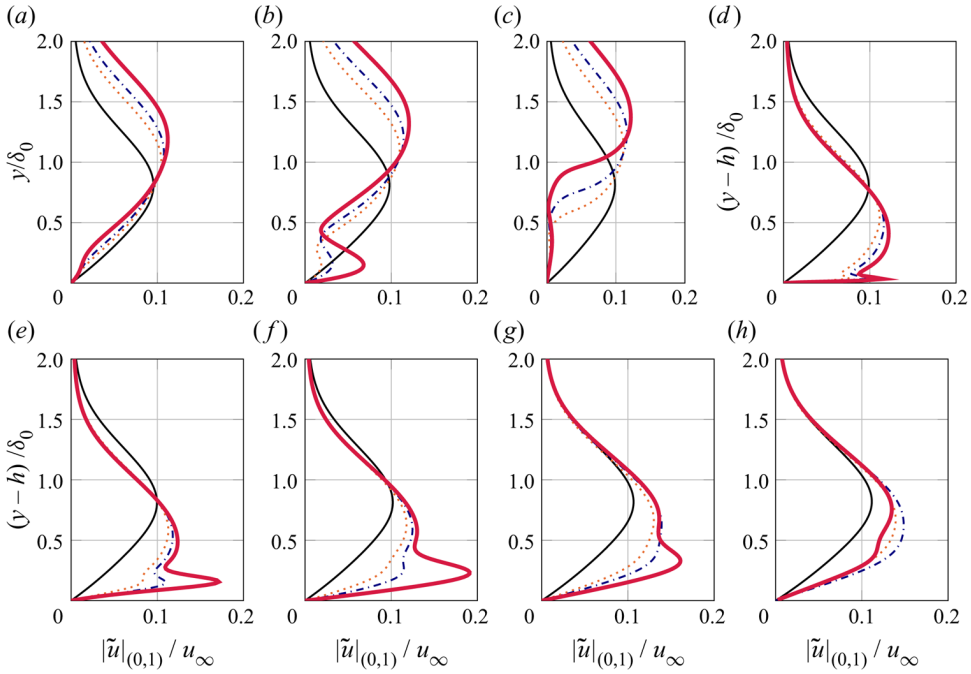

Figure 1.5: Variation of Amplitude function with wall-normal coordinate at various near step locations, given by non-dimensionalized coordinate x_{st}/δ_0 = (a) -2.04, (b) -0.45, (c) -0.07, (d) 0.01, (e) 0.61, (f) 2, (g) 5, (h) 8; reproduced from Casacuberta, Hickel, Westerbeek, and Kotsonis (2022)

structures. At the step vicinity, Casacuberta, Hickel, and Kotsonis (2021) claim that observing the evolution of a quantity representative of perturbation energy is better suited as the growth rate of u' and v' show different behavioural trends. Casacuberta, Hickel, Westerbeek, and Kotsonis (2022) thus observe the evolution of amplitude of total perturbation velocity vector norm at its primary peak. They observe a relatively constant trend of amplitude growth in two of the smaller steps. However, a strong decay is observed in the largest step in the region downstream of the step. The authors explain these effects by observing the behaviour of the production term of the spanwise integrated Reynolds-Orr equation (elaborated in section 5.1), which is representative of the exchange of kinetic energy between the base flow and fundamental perturbation (Albensoeder et al., 2001; Lanzerstorfer & Kuhlmann, 2012; Picella et al., 2018). For the largest step, the production term shows a decay in the step downstream region, consistent with the trends seen in amplitude evolution. Casacuberta, Hickel, Westerbeek, and Kotsonis (2022) also find that the tangential and total perturbation vectors misalign from each other and do not have same growth rates in the FFS vicinity across all cases, prompting them to suspect that non-modal mechanisms drive instability growth in conjunction with modal mechanisms in this region. In a region further downstream, significant growth of higher order harmonics is reported. The authors find that the fundamental perturbation component preserves its own behaviour for the largest step, pointing towards a linear mechanism of growth. However, for the smaller steps, they find that instability growth is non-linear, indicating that the step height plays a role in determining the type of evolution in terms of linearity. Previous studies have proposed a different picture of instability amplitude evolution and mechanisms governing the same.

Eppink (2020) experimentally observes a non-monotonic amplitude evolution trend in the step vicinity based on the observations of chordwise perturbation. The author considers the global peak of the chordwise instability for representing amplitude evolution, instead of the primary peak chosen by Casacuberta, Hickel, Westerbeek, and Kotsonis (2022). Starting from the step, to a region slightly downstream, in the second flow reversal region, enhanced growth of perturbation amplitude is noted. This is followed by a short region of decay. Further downstream the trend changes, with an enhanced region of growth followed by saturation. To elaborate mechanisms responsible for amplification, the author tests two different initial stationary crossflow amplitudes. The author finds that the first region of growth is similar for different initial amplitudes, providing evidence that this region is governed by linear mechanisms. Since this region of growth is in a region of reversed flow, Eppink (2020) draws parallels with the studies on interaction of crossflow instability with a separation bubble on a swept wing (Hosseinverdi & Fasel, 2016). They explain that the coexistence of separation and crossflow components lead to two separate inflection points, one each in the chordwise and crossflow profile. Thus, this region of flow can be considered 'double inflectional', and the inflection points in these regions provide impetus for the growth of crossflow instability. The second region of growth shows different trends for different initial amplitudes, hinting at the presence of non-linear effects. These are linked to the presence of higher harmonics in the reattachment

region, which are triggered by a shear layer strongly deformed in the spanwise direction by strong crossflow vortices near the step. Rius-Vidales and Kotsonis (2021) observe a non-monotonic growth trend similar to Eppink (2020). However, the regions of growth and decay are different, and spanwise perturbation profiles are used for the study amplitude evolution. Instability amplification starts upstream of the step, and continues until a region of favourable pressure gradient is encountered. Decay of instability occurs in a region of adverse pressure gradient, and further growth is observed when the pressure gradient relaxes back to that of the clean case. The appearance of harmonics in a region downstream of the FFS is also another similarity observed with Eppink (2020). However, Rius-Vidales and Kotsonis (2021) suggest that the harmonic components amplify by the nonlinear forcing of the fundamental component, which is different from the mechanism proposed by Eppink (2020).

Thus, it appears that the mechanisms explaining amplitude evolution of a stationary primary crossflow instability are still unclear. Although mechanisms of primary growth are unclear, some factors that might eventually affect transition location are the secondary recirculation region size (Tufts et al., 2017), initial amplitude (Eppink, 2020), wavelength of initial stationary crossflow mode (Rius-Vidales & Kotsonis, 2020), and the different action of secondary instabilities for different step heights (Rius-Vidales & Kotsonis, 2022). This provides insights into how complicated the mechanisms governing transition are, and highlights the need to simplify the FFS problem. A first step could be to understand mechanisms governing linear amplitude evolution in the primary phase of instability growth, before attempting to understand nonlinear trends and transition location behaviour.

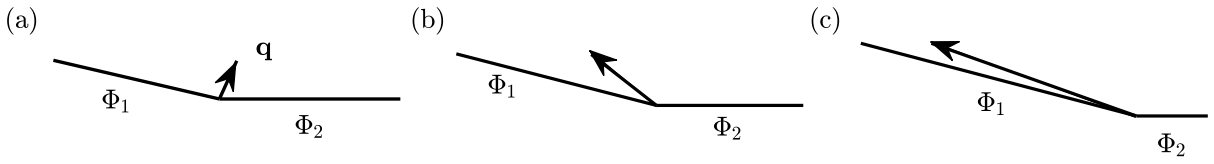

Figure 1.6: Depiction of temporal growth of the superposition of decaying eigenmodes Φ_1 and Φ_2, when initialized by **q**; (a) t = 0, (b) and (c) t>0, adapted from Schmid and Henningson (2001)

1.7. Analysis of Non-modal Growth

1.7.1. 2D Flows

The shortcomings of modal analysis can be explained considering parallel flows. LST only considers the behaviour of the least stable eigenmode, which thereby determines the long term behaviour of the perturbation. However, this approach neglects the behaviour in the short term, wherein a superposition of non-orthogonal stable Orr-Somerfield and Squire modes can lead to transient growth (Schmid & Henningson, 2001). This is demonstrated with an example from Schmid and Henningson (2001) in Figure 1.6, wherein two decaying non-orthogonal eigenvectors sum up to yield a resultant vector that grows in the short term. The growth or decay of perturbations in such scenarios is heavily dependent on the initial condition, whose determination can be physically explained for different flow scenarios using the Orr mechanism and the lift-up effect.

Orr Mechanism

The Orr mechanism stemmed from efforts to explain an inviscid mechanism for Couette flow transition, wherein Rayleigh (1879) stated that the flow could not destabilize considering just inviscid effects. Orr (1907) however looked at the inviscid problem from the initial value problem perspective and suggested that there was potential for growth in the short-term for a perturbation initially tilted against shear (Lindzen, 1988; Butler & Farrell, 1992). First, the issue of perturbation tilt is considered. A physical description of perturbation tilt can be provided by visualizing perturbations as a line of ink droplets initially aligned in a direction opposite to shear, wherein the droplets farthest from the wall would travel faster than the ones close to the wall. After a period of time, the line of droplets will first align neutrally (i.e. parallel to the y axis), and then align in the direction of shear (Roy & Govindarajan, 2010). Lindzen (1988) states that z perturbation vorticity (ω_3') remains constant for a 2D perturbation growing through the Orr mechanism. Using this fact, a mathematical demonstration of perturbation tilt is developed here. An appropriate artificial value of $\omega_3' = |\hat{\omega}_3(y)|\, e^{\mathrm{i}\phi(x,y,t)}$ can be selected with the assumption of $D\omega_3'/Dt = 0$ to conserve z perturbation vorticity. Assuming that ϕ is real, and a y dependent shape function of the form $\hat{\omega}_3(y) = ye^{-y^2}/max(ye^{-y^2})$ ensures that the perturbation vorticity does not grow in space or time. Initially, the phase ϕ would be such that the lines of constant phase would be aligned in a direction away from shear. This can be obtained by assuming initial conditions to be

$$\phi_0 = \gamma y + \alpha x, \tag{1.12}$$

with lines of constant phase given by $\gamma y + \alpha x = C$, where $\gamma = 2$, $\alpha = 2$, and C is a constant. The misalignment with shear is shown in Figure 1.7 (a). To satisfy $D\omega_3'/Dt = 0$, ϕ must evolve such that

$$\frac{\partial \phi}{\partial t} + U_B \frac{\partial \phi}{\partial x} = 0, \tag{1.13}$$

which presents an initial value problem for ϕ. The solution of this initial value problem for Couette flow ($U_B = y$) is given by

$$\phi(x, y, t) = \phi_0(x - U_B t, y) = \gamma y + \alpha(x - U_B t) = (\gamma - \alpha t)y + \alpha x, \tag{1.14}$$

where lines of constant phase are given by $(\gamma - \alpha t)y + \alpha x = C$. At $t = 1$ the lines of constant phase are given by $x = c$, so the perturbations are neutrally aligned, shown in Figure 1.7 (b). Whereas at $t = 1$ the perturbation tilts in such a way that the lines of constant phase align with shear as shown in Figure 1.7 (c).

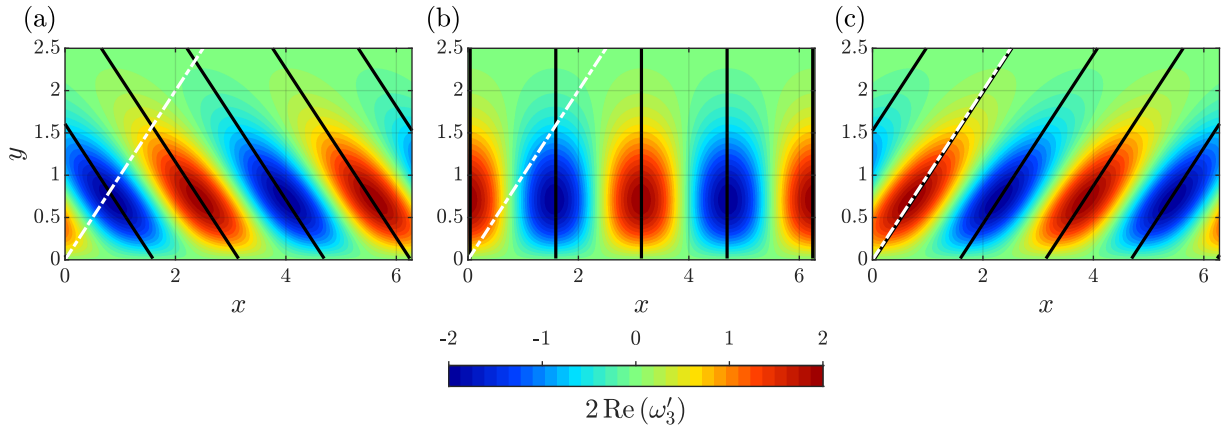

Figure 1.7: Contours of temporal evolution of manufactured field of ω_3' at (a) $t = 0$, (b) $t = 1$, (c) $t = 2$; black solid lines depict the lines of constant phase in xy plane, white dash-dotted lines depict the base flow shear.

Two explanations have been proposed to relate titlting with perturbation energy growth. Lindzen (1988) proposes a theory based on distance between centres of perturbation vorticity. They claim that the perpendicular distance between perturbation vorticity lines of constant phase would change when the perturbation tilts with base flow shear. This can be inferred from the manufactured perturbation field in Figure 1.7, where the perpendicular distance between these adjacent lines of constant phase is maximum during neutral alignment (Figure 1.7 b), and lesser in shear aligned (Figure 1.7 c) and misaligned states (Figure 1.7 a). Lindzen (1988) suggests that the perturbation velocities need to increase in the first phase of rotation from shear misaligned to neutral state, to account for perturbation centres being stretched apart in order to keep the perturbation velocity derivatives (or vorticity) constant. The growth of perturbation velocities leads to perturbation energy growth. In the second phase of rotation from neutral to shear aligned state, the perturbation lines of constant phase grow closer, thus leading to perturbation velocity and energy decay in a manner opposite to behaviour described for first half of tilt.

The second approach to quantify the growth of energy associated with tilting was proposed by Butler and Farrell (1992). They consider the inviscid perturbation energy equation given by

$$\frac{dE}{dt} = -\frac{1}{2} \int \frac{dU_B}{dy} \overline{u'\, v'}. \tag{1.15}$$

where the overbar denotes an averaging in chordwise direction. The term on the right-hand side of Equation 1.15 is the Reynolds Stress term which represents a mechanism by which perturbations grow by extracting energy from the mean flow shear. The stream function of perturbation (ψ') can now be considered, wherein for 2D flows, $u' = \partial\psi'/\partial y$ and $v' = -\partial\psi'/\partial x$. The expression $-u'\, v'$ determines the sign of Reynolds Stress, which can be expressed in terms of perturbation streamfunction as

$$-u'\, v' = \frac{\partial \psi'}{\partial x} \frac{\partial \psi'}{\partial y} \frac{dU_B}{dy} = -\left(\frac{\partial y}{\partial x}\right)_{\psi} \left(\frac{\partial \psi'}{\partial y}\right)^2 \frac{dU_B}{dy}, \tag{1.16}$$

where $\partial y/\partial x_\psi$ determines the tilt of the perturbation streamfunction, with a negative value indicating misalignment with shear and a positive value indicating alignment with shear. When perturbation streamlines are oppositely aligned with mean shear, $\partial y/\partial x_\psi < 0$, the integral in Equation 1.15 is negative, meaning that the perturbation gains energy. When the shear advects the perturbation such that the streamfunction changes its orientation with respect to base flow shear, the integral becomes positive, driving the perturbation to lose energy. This subsection thus provides an idea of how a 2D perturbation initial condition can transiently grow in a 2D parallel flow. However, 3D perturbations can also exist in 2D flows, and their consideration is shown in the upcoming subsection.

Lift-up Effect

The first mention of the lift-up effect was made by Ellingsen and Palm (1975). They considered the base flow as an incompressible, two-dimensional, steady, and parallel flow between two horizontal plates. They chose to model the linear behaviour of inviscid infinitesimal perturbations invariant in streamwise direction, and found that the streamwise perturbation had potential to grow in time as per

$$u' = u'_0 - v' \frac{dU_B}{dy} t, \tag{1.17}$$

where the subscript 0 denotes initial condition at $t = 0$. The growth of u' in Equation 1.17 is not exponential, and instead called "algebraic". Hultgren and Gustavsson (1981) suggested the viscous counterpart of this effect by finding potential for u' to grow in scales of $t/Re << 1$. Schmid and Henningson (2001) later expressed this algebraic growth in terms of solutions of linear stability equations solved as an initial value problem in time instead of the approach taken by traditional modal analysis to find the least stable mode. They find that an initial condition $[v_0\ \eta_0]$ grows by the superposition of Squire modes and the least-stable Orr-Somerfeld mode, which results in the tendency of short-term growth in η' (undetected by analysis of modal growth), as per

$$\hat{\eta} = \hat{\eta}_0 - i\beta \frac{dU_B}{dy} \hat{v}_0 t + O(t/Re). \tag{1.18}$$

The relation between growth in η' and u' can be explained using a physical vortex tilting mechanism shown in Figure 1.8 (Roy & Subramanian, 2014). They explain that the vorticity of total flow, originally present only in the z direction (dU_B/dy) gets tilted to give rise to a new component of y vorticity, by virtue of spanwise variation of wall-normal velocity. They claim that the developed y vorticity is a representation of the vorticity field of "streaks" i.e. spanwise variations in streamwise velocity (Butler & Farrell, 1992), thus providing the link between growth of η' and u'.

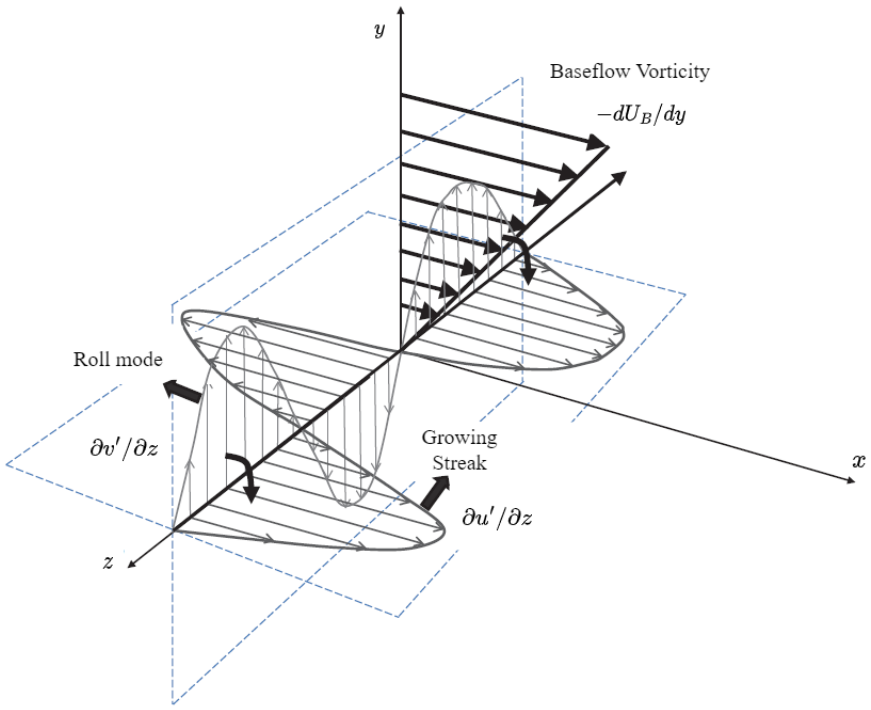

Figure 1.8: Mechanism of roll mode ($\partial v'/\partial z$) tilting base flow vorticity giving rise to streaks ($\partial u'/\partial z$), adapted from Roy and Subramanian (2014)

The question then arises as to which flow features can be responsible for spanwise variation of v'. Streamwise vorticity can potentially lead to the rise to such behaviour of wall-normal perturbation velocity, and this can be shown by evaluating the expression of streamwise vorticity which reads

$$\xi' = \frac{\partial v'}{\partial z} - \frac{\partial w'}{\partial y}. \tag{1.19}$$

Thus, infinitely long streamwise vortices form a very dangerous initial condition in shear flows (Brandt, 2014). Physically, an explanation for the effect of streamwise vortices, comes from the work of (Landahl, 1980). Assuming inviscid flow, fluid particles retain their horizontal momentum when displaced from one layer to another by these streamwise vortices. From high momentum regions, large velocity fluid is displaced to a low momentum region and vice versa, leading to the development of streaks. The lift-up effect has potential to bypass traditional TS transition in 2D flows (Tempelmann et al., 2010).

Adjoint Analysis

Both the physical mechanisms stated above have their own typical initial condition. Their initial conditions that gain most energy in a specific time period or spatial domain are referred to as optimal initial conditions (Butler & Farrell, 1992). Perturbation energy growth is possibly a more relevant metric than individual component growth, as different components have different growth rates in non-modal flow problems. In a temporal framework, perturbation energy is maximized a period of time, whereas in the spatial framework, perturbation energy is maximized over a given chordwise length to determine optimal initial conditions. The first attempts to maximize disturbance energy were made for parallel flows using a temporal framework, where the optimal initial conditions were obtained by ”optimizing over eigenmodes of the Orr-Somerfield operator” (Andersson et al., 1999). Considering perturbations to be two-dimensional Butler and Farrell (1992) were able to recreate the characteristic perturbation tilting seen in the Orr mechanism. However, when 3D disturbances were accounted for, Butler and Farrell (1992) and Reddy and Henningson (1993) were able to identify streamwise vortices as an initial condition, which led to the development of streamwise streaks, providing evidence of the lift-up effect. A spatial framework accounting for non-parallel effects, however suits boundary layer flows better since these flows are convectively unstable. Thus, Andersson et al. (1999) and Luchini (2000) developed spatial frameworks to determine optimal initial conditions using adjoint based optimization techniques. They also concluded that streamwise vortices were the optimal initial condition that later developed into streaks, providing evidence of the lift-up effect. Levin and Henningson (2003) compared the behaviour of modal (exponential) and non-modal (algebraic) instabilities in a flat plate boundary layer. They found that the algebraic instability in the form of streaks dominates in favourable pressure gradient regimes. In contrast, the exponential instability in the form of TS waves dominates in adverse pressure gradient regimes. For zero pressure gradient, it was found that exponential and algebraic instabilities co-exist.

1.7.2. 3D flows

The more relevant scenario of non-modal growth in 3D boundary layers is now considered. As already stated in Section 1.3, non-modal growth can precondition modal growth in 3D bounday layers in Path B of the various transtion paths shown in Figure 1.1. This subsection explores the results of spatial adjoint analysis that have shed light on this phenomena. Byström (2007), Tempelmann et al. (2010) and Lucas (2014) used different modifications of Parabolized Stability Equations and its corresponding adjoint equations to obtain optimal initial conditions for maximum perturbation growth in Falkner Skan Cooke Boundary layers. They all find that the initial disturbances are streamwise-oriented vortices tilted against mean crossflow shear. These vortices evolve in an external streamline aligned direction into streaks that are slightly aligned in the direction of mean crossflow shear. Tempelmann et al. (2010) and Lucas (2014) point that the tilting with respect to mean crossflow shear points towards the presence of Orr mechanism, whereas the streamwise vortex to streak conversion points towards to the lift-up effect. Furthermore, Byström (2007), Tempelmann et al. (2010) and Lucas (2014) initialized an optimal initial condition in subcritical regime where no unstable modes could be found, and allowed it to develop downstream into a supercritical regime where unstable modes could be identified. They find that the shape function of the evolved non-modal perturbation is similar to the modal perturbation shape function in the supercritical regime. Furthermore, the slope of perturbation energy amplitude evolution curves remains the same in the supercritical regime for both modal and non-modal instabilities. These features point towards the potential of a non-modal perturbation initialized in a subcritical regime providing an initial amplitude to the crossflow mode in the supercritical regime.

1.7.3. Step Flows

The discussion above corresponds to non-modal growth in smooth base flows wherein perturbations initially non-modal with respect to a given base flow can bypass modal growth in 2D flows or precondition modal growth in 3D flows. These situations are referred to as initial condition driven non-modality in this thesis. Step flows provide an alternative representation of the problem, wherein a region of rapid base flow change can potentially induce differences relative to behaviour

predicted by modal mechanisms. These effects are referred to as base flow deformation driven non-modality. Some criteria can be observed in literature that attempt to differentiate modal from non-modal growth in step flows which are first presented. Physical features of the lift-up effect observed in initial condition driven non-modality also feature in step flows, and are thus presented later.

Criteria

Marxen, Lang, Rist, Levin, and Henningson (2009) propose to observe the growth rates of base flow tangential and normal perturbation components, such that a difference in growth rates indicate non-modal behaviour and similarity in growth rates indicate modal growth. The authors also claim that non-modal growth corresponds to perturbation being misaligned with respect to direction of non-modal cases. These criteria were proposed for a non-step 2D flow subjected to favourable pressure gradient followed by adverse pressure gradient, leading up to separation. Inspired by these criteria, Casacuberta, Hickel, Westerbeek, and Kotsonis (2022) propose to observe the growth rates of base flow tangential and total perturbation vector, and the alignment/misalignment of the primary total perturbation vector with the base flow to distinguish non-modal and modal mechanisms in cases involving interaction of stationary crossflow instability with an FFS (as elaborated upon in Section 5.2.2). They note that far upstream and downstream of the step, these growth rates match each other, while in the vicinity of the step, they do not match each other. The authors then find the cosine of the angle between the primary perturbation vector and the base flow. They find that corresponding to the regions of growth rate discrepancy, there are regions where the cosine does not take a value near one, indicating that the perturbation vector is misaligned with the base flow. Shortly downstream of the step, tangential and total perturbation growth rates match each other again. Therefore, they claim that at the vicinity of the step, modal and non-modal effects might be present together.

Lift-up Effect

To observe the lift-up effect in step cases, Lanzerstorfer and Kuhlmann (2012) propose to decompose the perturbation ($\boldsymbol{v}'$) into components paralllel ($\boldsymbol{v}'_{\parallel}$) and perpendicular ($\boldsymbol{v}'_{\perp}$) to the base flow (possessing velocity $\mathbf{V_B}$) as per

$$\boldsymbol{v}' = \boldsymbol{v}'_{\parallel} + \boldsymbol{v}'_{\perp}. \tag{1.20}$$

Physically $\boldsymbol{v}'_{\parallel}$ corresponds to the field of streaky structures and $\boldsymbol{v}'_{\parallel}$ corresponds to the field of counter-rotating rollers (Picella et al., 2018). The production term ($P = -(\boldsymbol{v}' \cdot (\nabla \mathbf{V_B} \cdot \boldsymbol{v}'))$) in the Reynolds-Orr energy balance is then decomposed into four different contributions as per

$$P = \sum_{i=1}^{4} I_i = -\boldsymbol{v}'_{\perp} \cdot (\nabla \mathbf{V_B} \cdot \boldsymbol{v}'_{\perp}) - \boldsymbol{v}'_{\parallel} \cdot (\nabla \mathbf{V_B} \cdot \boldsymbol{v}'_{\perp}) - \boldsymbol{v}'_{\perp} \cdot (\nabla \mathbf{V_B} \cdot \boldsymbol{v}'_{\parallel}) - \boldsymbol{v}'_{\parallel} \cdot (\nabla \mathbf{V_B} \cdot \boldsymbol{v}'_{\parallel}). \tag{1.21}$$

The second component I_2 is considered indicative of the lift-up effect by Lanzerstorfer and Kuhlmann (2012). I_2 has been used to identify lift-up effect in many non-step base flows as well (Albensoeder et al., 2001; Loiseau, Robinet, & Leriche, 2016; Picella et al., 2018). Physically, the effect corresponds to energy transfer from the base flow to the perturbation component parallel to base flow (or streaks) via the perturbation component perpendicular to base flow (or rollers) (Picella et al., 2018). Although, there appears to be a contrasting observation compared to conventional lift-up effect which destabilizes perturbations. Lanzerstorfer and Kuhlmann (2012) observe the lift-up effect to be stabilizing in the region near existence of separation bubbles, where perturbations are found to grow. In these regions I_4 is dominant, and the authors claim that the sustenance of streaks is due to feedback from the recirculating bubble. It is to be noted that Lanzerstorfer and Kuhlmann (2012) do not draw any connection to transient growth.

Casacuberta, Hickel, and Kotsonis (2022) also find evidence of lift-up driven perturbation stabilization. For interactions of the stationary crossflow instability with an FFS, Casacuberta, Hickel, and Kotsonis (2022) perform a similar decomposition of production term to monitor I_2 for the cases simulated in Casacuberta, Hickel, Westerbeek, and Kotsonis (2022), whose results were elaborated upon in Section 1.6.2. The authors claim that the lift-up effect drives crossflow instability growth in the clean case, evidenced by a consistent positive value of I_2 dominating the production term budget (Equation 1.21). In the largest step case, they show that the production term decomposition of the largest step case yields stabilized values of I_2, in a step-downstream region where the production term showed stabilization. The authors call this effect the ”reverse lift-up effect”, a stabilizing effect in opposition to the ”classic lift-up effect” which consistently destabilizes perturbations in the clean case. The reversal of I_2 sign is attributed to the cosine of phase difference between base flow normal and tangential perturbation components reversing sign.

1.8. Gaps in Literature and Scope of Thesis

As discussed in Section 1.6.2, there is a lack of consensus on the mechanisms describing stationary crossflow instability amplitude evolution on interacting with an FFS. The first step towards understanding this complex interaction would be to

consider the response of primary stationary crossflow instability to an artificial base flow deformation via the imposition of a pressure change that does not cause separation. Flow separation and the upwash associated with it complicate the base flow further and might contribute towards making perturbation behaviour difficult to interpret. Since the initial amplitude and wavelength of the crossflow mode seeded at the inlet can also affect the mechanisms by which the instability interacts with the base flow (as examined in Section 1.6.2), the scope of this study is limited to studying the behaviour of linear evolution with one particular wavelength. Appropriate frameworks need to be developed to understand mechanisms of amplitude evolution when an incoming stationary crossflow mode faces an artificially developed rapid base flow variation. The spanwise integrated production term proposed by Casacuberta, Hickel, Westerbeek, and Kotsonis (2022) is a good starting point to interpret perturbation behaviour, but it is important to understand what factors determines the behavioural trends of production term. There is also a need to formulate the entire energy balance equation, to isolate the growth of energy in x (as shown by Karp and Hack (2018)) and relate it to production term behaviour, rather than relying on directly correlating production term and perturbation amplitude behaviour. Counting the number of inflection points (Eppink, 2020) and the nature of directional profile (Mack, 1984) might also prove to be relevant theories to explain perturbation behaviour, and the universality of these theories need to be tested.

If the mechanisms of amplitude evolution are clear, there remains a need to investigate whether the initially modal perturbation undergoes transformation in character. Mechanisms such as the lift-up effect serve as a starting point to compare the behaviour of perturbation in base flow deformed cases and the clean case. The lift-up effect appears to be destabilizing in the clean case. If there is a possibility of stabilization via reverse lift-up in base flow deformed cases as observed by Casacuberta, Hickel, and Kotsonis (2022) in the largest step, it could be considered as a hint of deviation from modal behaviour. Although the Orr mechanism does not find mention in step studies, a change in shear in a rapid base flow could possibly affect perturbation tilt, and thus show differences with respect to clean case behaviour. Whether the perturbation tilt connects to energy exchange mechanisms or other relevant features of modal evolution needs to be explored via frameworks to understand factors affecting perturbation tilt and its influence on perturbation behaviour. Furthermore, the action of lift-up effect and Orr mechanism can be compared with local modal behaviour, which can be approximated by the Orr-Sommerfeld mode. Final decisions regarding deviation from modal character can be taken by observing whether the local mode shows different character from the perspective of the Orr mechanism and lift-up effect, with respect to the actual perturbation behaviour simulated by a method more accurate than LST. If some evidence of these mechanisms showing behavioural differences with respect to local modal behaviour is found, the criteria mentioned in subsection 1.7.3 are examined. If they are satisfied, it could be claimed that the incoming mode undergoes transformation to base flow deformed non-modal character. Else, it can be claimed that the incoming mode is simply a manifestation of a base flow deformed mode. This leads to the definition of the research questions and objective of the project in the upcoming section.

1.9. Research Questions and Objective

The research questions for the thesis are

1. What mechanisms govern the amplitude evolution of a stationary primary crossflow perturbation on its interaction with a rapid base flow deformation?
    - Does a linear energy balance explain the mechanisms governing amplitude evolution?
    - Can the effect of an FFS on amplitude evolution be reproduced by an appropriately designed synthetic base flow deformation?
2. What mechanisms and criteria can be identified to explain if an initially modal perturbation deviates from modal character under the influence of a rapidly deformed base flow?
    - What metrics can identify mechanisms such as the lift-up effect or Orr mechanism when the perturbation evolves in a clean or deformed base flow?
    - Do these mechanisms capture deviation of perturbation from local modal behaviour?
    - Does the perturbation become non-modal based on criteria identified from literature?

Associated with the research questions, the main research objective of this thesis is

> ”To assess the evolution of a stationary primary crossflow perturbation in the region of a rapid base flow deformation by performing numerical simulations, developing frameworks to identify mechanisms governing instability evolution and observing whether the instability deviates from its initial modal character.”

The research objective can be accomplished by achieving the following sub-objectives

1. Designing an appropriate base flow deformation and selecting appropriate methods to simulate base flow and perturbation response to such a base flow.
2. Developing energy balance frameworks to explain mechanisms by which a perturbation gains or loses energy, potentially explaining its amplitude response.
3. Identifying mechanisms and criteria that can compare instability behaviour with modal behaviour in regions of deformed base flow.
4. Comparing mechanisms of perturbation response to an FFS to the perturbation response of an appropriately designed base flow deformation with similar pressure characteristics to validate whether similar mechanisms govern perturbation evolution in both rapidly changing flow regimes.

1.10. Outline

The sub-objectives defined above provide inspiration for the sequence of subsequent chapters in this thesis. Inspired by the base flow deformation imposed by an FFS, details of the method developed to rapidly deform a base flow and the subsequent development of test cases to be simulated in this thesis are presented in Chapter 2. The flow problem to simulate the base flow of test cases is then defined, followed by the selection of the best method to simulate base flow in Chapter 3. The perturbation evolution problem is then considered, and an elaborate selection procedure to select the best method to model perturbation evolution is presented in Chapter 4. The numerical framework to understand mechanisms of perturbation evolution via the spanwise Reynolds-Orr framework, and to evaluate deviation of perturbation from modal behaviour via the perspective of mechanisms and criteria are then presented in Chapter 5. This is followed by analyzing the results of perturbation evolution through the developed base flow deformations in Chapter 6. A validation study comparing the mechanisms influencing perturbation evolution in step cases with some representative test cases is then considered in Chapter 7. This is followed by the conclusions and recommendations for future work in Chapter 8.

1.11. Unique Contributions

It may appear difficult to segregate the unique contributions of this thesis from already implemented techniques in literature, thus motivating this section to highlight these contributions explicitly. The idea of observing terms of the Reynolds-Orr energy balance to understand perturbation propagation has already been implemented multiple times, with prominent examples relevant for this thesis being Albensoeder et al. (2001) (investigation of 3D perturbation in temporal framework in a 2D base flow), Karp and Hack (2018) (investigation of 3D perturbation in spatial framework in a 2D base flow), and Lanzerstorfer and Kuhlmann (2012) (investigation of 3D perturbation in spatio-temporal framework in a 2D base flow). In the above-stated investigations, the authors used spanwise periodic perturbations with no growth in spanwise direction, prompting them to integrate the energy balance equation in the spanwise direction, in order to isolate energy growth either in space or time. Albensoeder et al. (2001), Lanzerstorfer and Kuhlmann (2012), and Karp and Hack (2018) evaluated all terms of the energy balance equation, and explicitly related the growth of energy in space or time to the dominant term in the energy balance i.e. the production term. These studies potentially motivated Casacuberta, Hickel, Westerbeek, and Kotsonis (2022) to use the spanwise integrated Reynolds-Orr approach to understand the spatial growth or decay of spanwise periodic stationary crossflow instability in a 3D base flow. But, the authors chose to observe the production term and correlate its behaviour to the amplitude evolution of a spanwise periodic perturbation, without explicitly showing how the production term relates to spatial energy growth. Also, Casacuberta, Hickel, and Kotsonis (2022) provide a method to interpret production term behaviour in Casacuberta, Hickel, Westerbeek, and Kotsonis (2022) via the I_1 to I_4 decomposition. Although physically relevant (refer Section 1.7.3), this approach does not help identify features of base flow that might cause a perturbation to behave differently in base flow deformed cases compared to the clean case. This motivates the first unique contribution of the current thesis, where an attempt is made to decompose the production term by which the differences in perturbation behaviour between deformed cases and the clean case can be linked to differences in the behaviour of their underlying base flows (Section 5.1.2 and Section 6.3.1), and to subsequently show how the production term's behaviour explicitly relates to spatial energy growth or decay of linearly evolving primary stationary crossflow instability interacting with a rapid base flow deformation (Section 5.1.3, Section 5.1.4, and Section 6.3.2). The second unique contribution is the development of a mathematical framework to understand perturbation phase evolution, which is then related to the Orr mechanism, as presented in Section 5.2.1 and Section 6.4.2.

2

Synthetic Base Flow Deformation Design

In this thesis, a synthetic base flow deformation is obtained by imposing a rapid pressure variation on the external pressure distribution of the clean case (which varies slowly and has a favourable gradient), with the assumption that the changed external pressure distribution propagates down to the boundary layer, thus imposing a locally changed pressure field. In this chapter, the details of the clean case external pressure distribution are first provided. Next, details on the pressure variation imposed by an FFS are presented. This provides inspiration to develop pressure variations that are to be imposed on the clean case pressure distribution. Finally, an overview of the test cases to be simulated in this thesis are provided.

2.1. Clean Case Pressure Distribution

The clean case pressure distribution is obtained from a part of the chordwise pressure distribution of a 45° swept wing tested experimentally at TU Delft by Rius-Vidales and Kotsonis (2021). This part of the swept wing pressure distribution has a favourable pressure gradient, beginning at 5% of wing chord, where the δ_{99} thickness is $\delta_0 = 7.71{\times}10^{-4}\ m$, and the part stretches 517 δ_0. A plot of the clean case pressure distribution is shown in Appendix A.1.

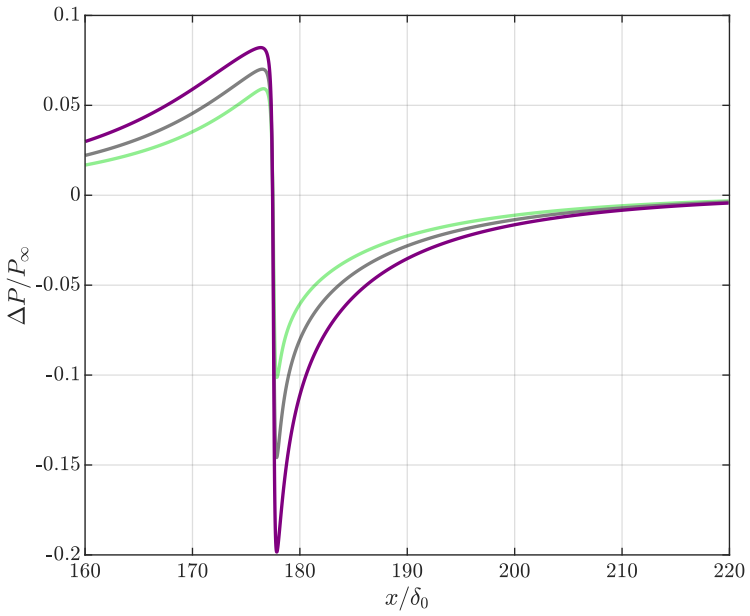

Figure 2.1: Evolution of ΔP in three different step cases (a) Step A (light green) (b) Step B (grey) (c) Step C (purple); plotted using data taken from the work of Casacuberta, Hickel, Westerbeek, and Kotsonis (2022).

2.2. Inspiration from the FFS

In Section 1.6.1, it is observed that the step imposes a non-monotonic pressure field, which subsequently contributes to rapidly deforming the base flow. The behaviour changes from the clean case favourable pressure gradient to an adverse pressure gradient region upstream of the step, followed by a strong favourable pressure gradient region at the step vicinity, followed by an adverse pressure gradient region downstream of the step, before eventually relaxing back to the clean case favourable pressure gradient (Tufts et al., 2017; Casacuberta, Hickel, Westerbeek, & Kotsonis, 2022). This behaviour is captured by comparing the behaviour of a streamline seeded at $y/\delta_0 = 0.2$ and subtracting the clean case pressure distribution from it as shown in Figure 2.1. This parameter is denoted as pressure variation or ΔP and shown in Figure 2.1. Here, the location $x/\delta_0 = 177.62$ corresponds to the location of the step. For ease of interpretation, a coordinate x_{st} can be introduced so that $x_{st}/\delta_0 = x - 177.62 = 0$ corresponds to the step location. The pressure variation in Figure 2.1 can be considered to locally be "three-way", with two local regions of increasing ΔP (adverse) and a sharp local region of decreasing ΔP (favourable) in between. This provides motivation to investigate two different types of ΔP distributions. One would have an adverse ΔP region followed by a favourable ΔP region, whereas the other would have a favourable ΔP region followed by an adverse ΔP region. These constitute "two-way" ΔP distributions. A ΔP distribution combining two two-way distributions can form an adverse, favourable, adverse three-way ΔP distribution, similar to that simulated in the step. These ΔP distributions are superimposed on the pressure distribution of the clean case to give rise to an external pressure distribution P_e, also referred to as "effective pressure distribution". Using a numerical method that allows the propagation of effective pressure distribution down to the boundary layer, the base flow can be deformed locally.

2.3. Development of Gaussian-like Pressure Variation

The developed ΔP distributions should satisfy three criteria. The first criterion is to ensure a smooth ΔP distribution (i.e. the distribution is continuous and differentiable), such that the resulting P_e profile is also smooth, leading to no unphysical jump conditions while simulating base flow. The second criterion is to ensure that the change of P_e is rapid such that the resulting base flow deformation would also be rapid in nature. This implies that the ΔP distribution is localized to a short width scale, closer to the order of boundary layer thickness than numerical domain size, such that P_e relaxes back to clean case pressure distribution beyond the realm of imposed ΔP. The third criterion is that the ΔP distribution should be easily parametrizable, which would allow for an easy development of test cases. The width of ΔP distribution would naturally be the first parameter, as its appropriate selection would ensure a rapid base flow deformation. The second parameter would be the gradient of the ΔP distribution, as its increased magnitude for a fixed width would lead to stronger base flow deformation. The third parameter would be the location of ΔP imposition, where a location close to $x_{st}/\delta_0 = 0$ would help in comparisons against FFS behaviour.

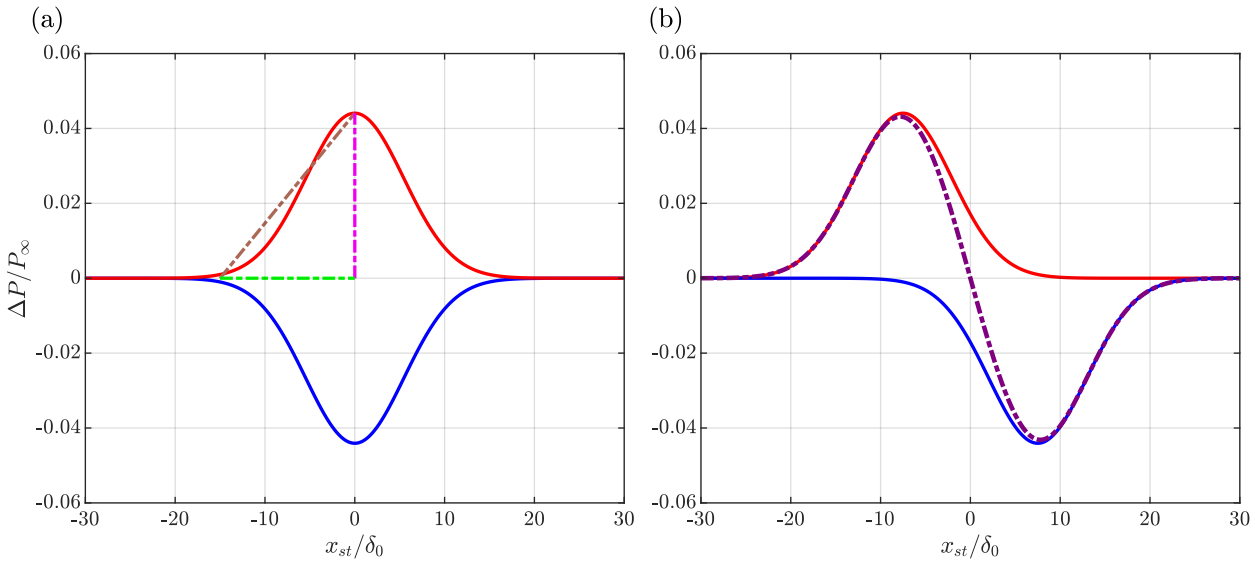

Figure 2.2: (a) ΔP distribution of a positive p_f case (blue) and a negative p_f case (red) case; green dash-dotted line denotes $w/2$, magenta dash-dotted line denotes A, brown dash-dotted line completes the triangle formed by A and $w/2$ with its slope representing -p_f; (b) Formation of a three-way ΔP distribution (purple dash-dotted) combining a positive and a negative p_f ΔP distribution.

Gaussian distributions form an excellent starting point for designing ΔP distributions satisfying majority of the above criteria. A gaussian curve ($g(x)$) is quantified by

$$g = \frac{1}{\sigma\sqrt{2\pi}} e^{-\frac{1}{2}(\frac{x-\mu}{\sigma})^2} \tag{2.1}$$

where μ is the mean and σ is the standard deviation. By design, about 99% of the area of a standardized Gaussian falls under $\mu - 3\sigma$ to $\mu + 3\sigma$. If ΔP is prescribed as a Gaussian curve, its inherent nature would be of the form of a two-way distribution. Since the curve itself is smooth, a superposition onto the clean case freestream pressure curve would give an effective pressure distribution which is also smooth. The normalization of Gaussian ($1/\sigma\sqrt{2\pi}$) in Equation 2.1 can be dropped and replaced by an amplitude (G), such that the change of the amplitude can result in stronger pressure changes ($g = Ge^{-((x-\mu)/\sigma)^2}$). However, the issue with directly choosing the Gaussian is that the width of the ΔP distribution is not easily controllable. Hence, the Gaussian is modified such that it always takes the same arbitrarily low value at $x \pm w/2$, thus resulting in a concrete definition of ΔP width. The function is specified as

$$\Delta P = Ae^{-B(x-\mu)^2}, \tag{2.2}$$

where A and B are coefficients that need to be defined. For ensuring the same arbitrary limit at $x \pm \mu = \pm w/2$, the value of the limit 'L' is substituted into Equation 2.2 yields

$$L = Ae^{\frac{-Bw^2}{4}}. \tag{2.3}$$

This limit is chosen to be an arbitrarily small number 1E-3. Now, an expression of B is obtained as

$$B = -\frac{4}{w^2}\ln\Big(\frac{L}{A}\Big). \tag{2.4}$$

The last coefficient that needs to be specified is A. This is representative of the amplitude of the ΔP curve. The maximum pressure gradient of the ΔP curve would be a naturally suited candidate to derive A. However, this would result in a complicated implicit procedure involving differentiation of the ΔP expression in Equation 2.2. Instead, a simple representation of pressure gradient in terms of the slope of a line joining the peak of the curve on the y axis and $x \pm \mu = \pm w/2$ on the x axis is proposed. This pressure gradient representation is called pressure factor, denoted as p_f, given by

$$p_f = -\frac{2A}{w}. \tag{2.5}$$

A diagrammatic visualization of the definition of p_f, A and w is provided in the Figure 2.2. Specifying p_f, w and μ thus lead to the definition of coefficients A and B, which result in the ΔP curve. A region of negative ΔP gradient is called a favourable ΔP regime, and a region of positive ΔP gradient is called an adverse ΔP regime. A positive p_f distribution has a favourable ΔP regime followed by an adverse ΔP regime. Whereas, a negative p_f distribution has an adverse ΔP regime followed by a favourable ΔP regime. The developed ΔP distribution is superposed onto the external pressure distribution of clean case to generate the effective pressure distribution of two-way cases.

The option of superposing two two-way distributions to create a three-way distribution is now considered. Sample three-way distributions are inspired by the step (Figure 2.1), which has an adverse-favourable-adverse ΔP behaviour, with ΔP taking zero value in the favourable ΔP regime. For this purpose, a negative p_f distribution with mean μ_1 and a positive p_f distribution with mean μ_2 are considered. Both distributions are assumed to have the same width w. The means μ_1 and μ_2 are offset from μ_0, the previous near-step mean for two-way cases, as per

$$\mu_1 = \mu_0 - w/4, \tag{2.6}$$

$$\mu_2 = \mu_0 + w/4. \tag{2.7}$$

A diagrammatic visualization of the formation of a three-way ΔP as a resultant of addition of two two-way ΔP distributions is shown in Figure 2.2. The adverse ΔP regimes of the resultant curve retain the same ΔP gradient as the underlying two-way ΔP distributions. However, the favourable ΔP regime is now a superposition of both cases, with a larger ΔP gradient than the underlying distributions. This mimics the character of step ΔP distributions (Figure 2.1) wherein a favourable ΔP region of higher gradient is surrounded by two adverse ΔP regions with lower gradient. The developed ΔP distribution is superposed onto the external pressure distribution of clean case to generate the effective pressure distribution of three-way cases.

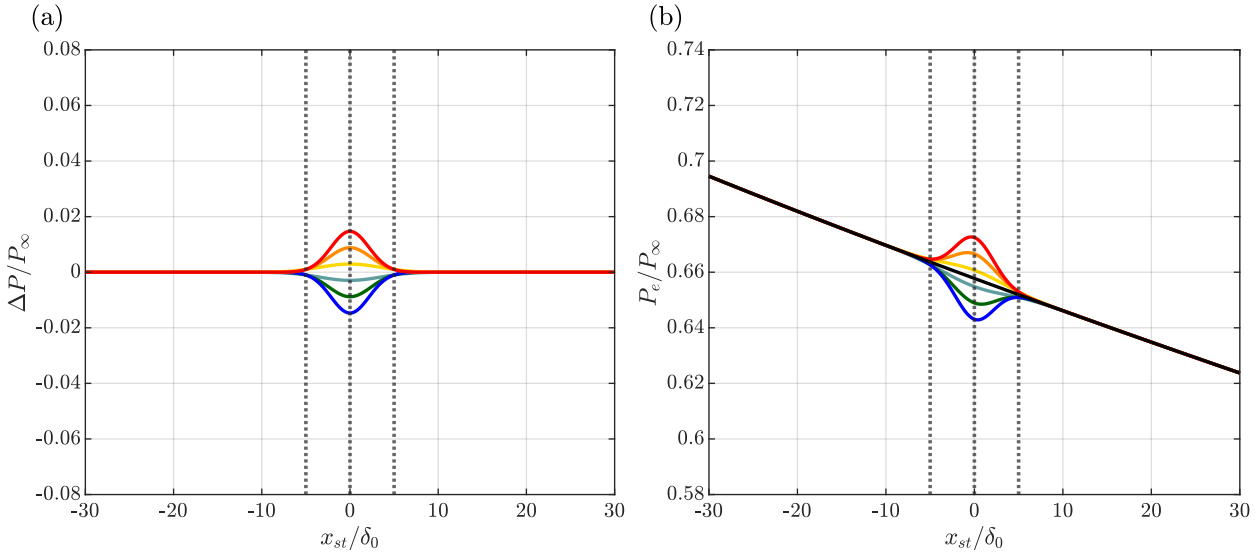

Figure 2.3: (a) ΔP distribution and (b) Effective pressure distribution in $10\delta_0$ cases; $-2.5p_f$ (red), $-1.5p_f$ (orange), $-0.5p_f$ (yellow), $0.5p_f$ (cyan), $1.5p_f$ (dark green), $2.5p_f$ (blue), and clean case (black); black dotted lines at $x_{st}/\delta_0 = -w/2,\ 0,$ and $w/2$ show the region of ΔP imposition in deformed cases.

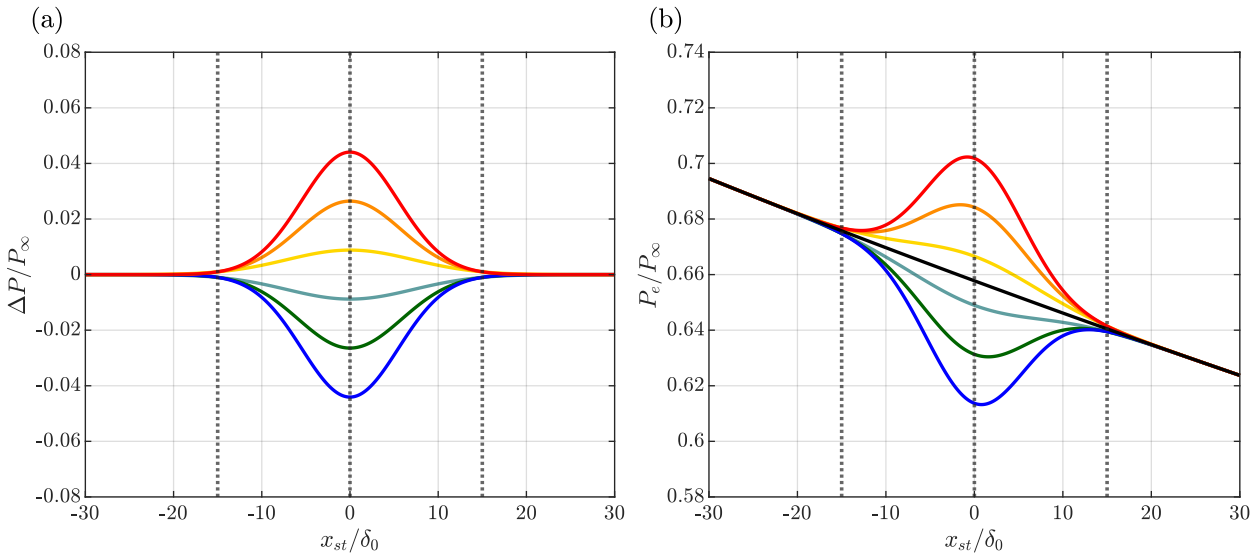

Figure 2.4: (a) ΔP distribution and (b) Effective pressure distribution in $30\delta_0$ cases; $-2.5p_f$ (red), $-1.5p_f$ (orange), $-0.5p_f$ (yellow), $0.5p_f$ (cyan), $1.5p_f$ (dark green), $2.5p_f$ (blue), and clean case (black); black dotted lines at $x_{st}/\delta_0 = -w/2,\ 0,$ and $w/2$ show the region of ΔP imposition in deformed cases.

2.4. Two-way ΔP cases

Three different width scales i.e. $10\delta_0$, $30\delta_0$ and $50\delta_0$ are considered inspired the observation of non-modal effects by Casacuberta, Hickel, Westerbeek, and Kotsonis (2022) at $O(10\delta_0)$. For each of these width scales, six different levels of p_f are considered i.e. $p_f = \pm 0.5, \pm 1.5, \pm 2.5$. The same set of p_f values are selected for different width scales to ensure that the maximum gradient of ΔP distributions are similar for a particular p_f value across width scales considered. The highest width scale would have the tendency to separate the most at a given p_f. This tendency is higher for a negative p_f which faces an adverse pressure gradient first. For the $50\delta_0$ cases, the -2.5 p_f case separates when simulated using a boundary layer solver. Hence, it is replaced by a -2.0 p_f case just for the highest width scale. These ΔP distributions have their centre located at $x/\delta_0 = 177.62$ which is the step location considered by Casacuberta, Hickel, Westerbeek, and Kotsonis (2022). The two-way ΔP distributions and resulting P_e distributions with width $10\delta_0$, $30\delta_0$, and $50\delta_0$ are shown in Figure 2.3, Figure 2.4, and Figure 2.5 respectively. The effective pressure distributions show that the lowest p_f

cases do not change the sign of pressure gradient, whereas the moderate and higher p_f cases result in a change in pressure gradient sign. It should also be noted that the peak of the ΔP distribution does not exactly correspond to the local peak of P_e distribution since the clean case pressure distribution has non-zero gradient. Numerical values of characteristics such as gradient of ΔP distribution and P_e distribution are shown in the Appendix A.2. These two-way distributions are abbreviated for easier referencing in future sections, i.e. a two-way ΔP case with $p_f = 2.5$ and $w = 30\delta_0$ is called $2.5p_f\ 30w$.

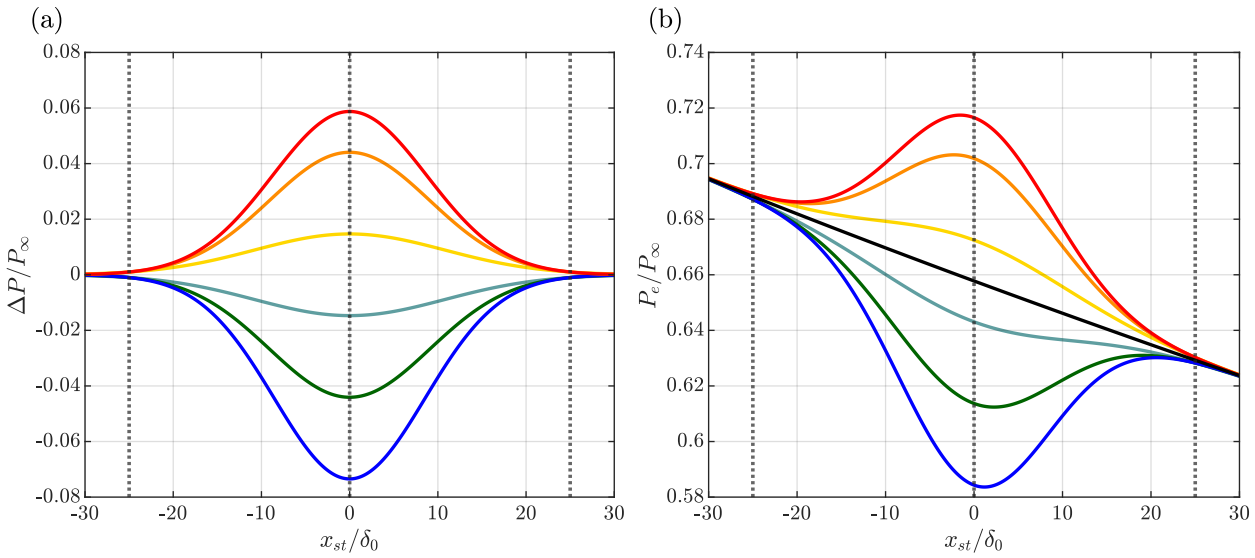

Figure 2.5: (a) ΔP distribution and (b) Effective pressure distribution in $50\delta_0$ cases; $-2.0p_f$ (red), $-1.5p_f$ (orange), $-0.5p_f$ (yellow), $0.5p_f$ (cyan), $1.5p_f$ (dark green), $2.5p_f$ (blue), and clean case (black); black dotted lines at $x_{st}/\delta_0 = -w/2,\ 0,$ and $w/2$ show the region of ΔP imposition in deformed cases.

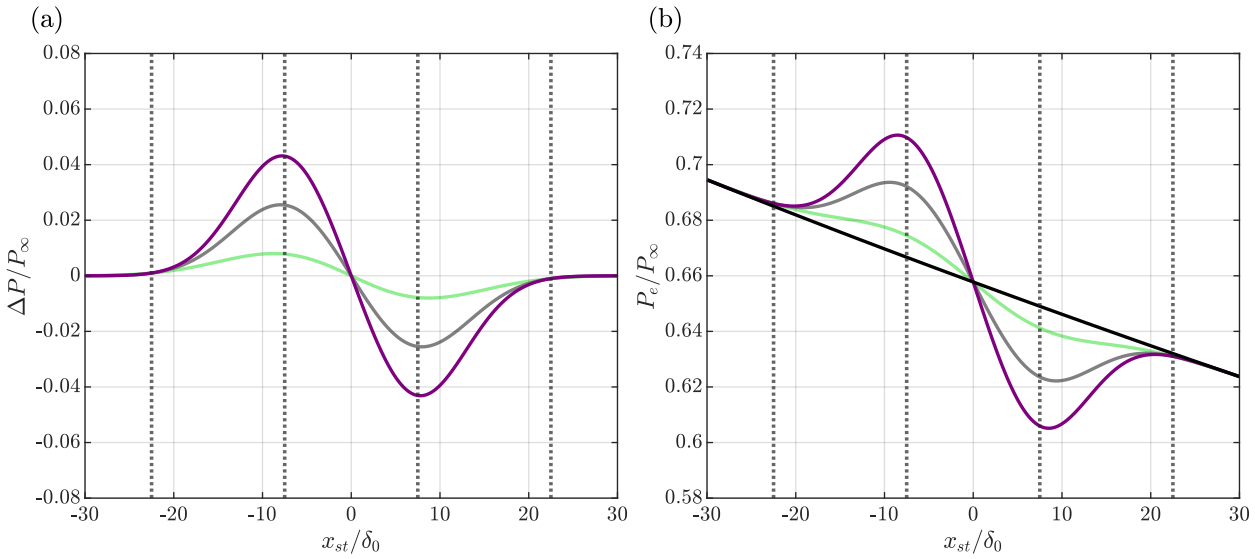

Figure 2.6: (a) ΔP distribution and (b) Effective pressure distribution in three-way cases; $0.5p_f$ (light green), $1.5p_f$ (grey), $2.5p_f$ (purple), and clean case (black); black dotted lines at $x_{st}/\delta_0 = -3w/4,\ -w/4,\ w/4,$ and $3w/4$ show the region of ΔP imposition in deformed cases.

2.5. Three-way ΔP cases

Three-way ΔP distributions considered here are formed by superposing a negative p_f and a positive p_f distribution of width $30\delta_0$ each. Three different pressure factor magnitudes are considered for the two-way pressure gradient distributions i.e. $p_f = 0.5, 1.5, 2.5$, with the resultant three-way ΔP distributions shown in Figure 2.6 (a), and effective pressure

distributions shown in Figure 2.6 (b). The mean of the first and second distributions are calculated in accordance with Equation 2.6 and Equation 2.7, assuming that $\mu_0/\delta_0 = 177.62$. It should be noted that most results in this thesis are generated primarily using the two-way ΔP distributions, with the three-way ΔP cases serving as a good reference to compare results against FFS results. Numerical values of characteristics such as gradient of ΔP distribution and P_e distribution are shown in the Appendix A.2. These three-way distributions are abbreviated for easier referencing in future sections, i.e. a three-way ΔP case with $p_f = 2.5$ and $w = 30\delta_0$ is called $2.5p_f\ 30w \times 2$.

3

Modelling Base Flow Evolution

The previous chapter provides an overview of the method proposed to synthetically deform the base flow, which would only work if the changes imposed on the external pressure distribution of the clean case (possessing a favourable pressure gradient) propagate down to the wall. This chapter entails the selection of the best method to simulate the base flow to ensure the effective pressure gradient propagates down to the wall. It starts with the definition of the flow problem to be solved. An overview of the full Navier Stokes Equation that governs the base flow problem is then presented. The setup of Direct Numerical Simulation (DNS) is then discussed, which solves the governing equations with minimal assumptions. The disadvantages of DNS are then presented, which leads to the exploration of Boundary Layer Equations and the setup of the Boundary Layer Solver (BLS) to solve these equations. A comparison between DNS and BLS base flow for one particular test case is presented, following which a method is finalized for simulation. The grid for the selected method is presented next, and the change of grid is shown not to influence results.

3.1. Base Flow Problem Definition

The base flow problem definition closely corresponds to the work of Casacuberta, Hickel, Westerbeek, and Kotsonis (2022) with the exception of the kind of external pressure distribution imposed. The coordinate system corresponds to the swept flat plate coordinate system defined in Section 1.2. Base flow properties are assumed to be spanwise invariant, reducing the complexity of the problem from 3 to 2.5 dimensions. To compute the base flow, a domain of chordwise length $517\delta_0$ (same as the chordwise extent of pressure distribution in Section 2.1) and wall-normal height $26\delta_0$ is considered. Whether the domain needs any resolution in the spanwise direction or not is controlled by the method selected to represent the base flow. The xy representation of the domain is presented in Appendix B.1. The pressure distribution at the top boundary of the domain corresponds to the effective pressure distributions developed in Chapter 2. The chordwise velocity at the inlet (U_∞) takes a value of 15.10 m/s. The ratio of inviscid spanwise velocity (W_∞) and U_∞ is maintained as -1.24. U_∞ and δ_0 are consistently used as the velocity and length scales for non-dimensionalization, respectively, and the Reynolds number based on these scales $Re = U_\infty \delta_0 / \nu$ is maintained as 791.37.

3.2. Full Navier Stokes Equation

The reference flow referred to as the base flow is a steady laminar three-dimensional boundary layer with spanwise invariance, implying that derivatives in z are zero. The velocities in x, y, and z are U_B, V_B, and W_B, respectively, consistent with conventions specified in Section 1.2. A spanwise invariant pressure field P_B is also present. The steady Navier Stokes Equations governing base flow evolution read

$$\frac{\partial U_B}{\partial x} + \frac{\partial V_B}{\partial y} = 0, \tag{3.1}$$

$$U_B \frac{\partial U_B}{\partial x} + V_B \frac{\partial U_B}{\partial y} = -\frac{1}{\rho}\frac{\partial P_B}{\partial x} + \nu\left(\frac{\partial^2 U_B}{\partial x^2} + \frac{\partial^2 U_B}{\partial y^2}\right), \tag{3.2}$$

$$U_B \frac{\partial V_B}{\partial x} + V_B \frac{\partial V_B}{\partial y} = -\frac{1}{\rho}\frac{\partial P_B}{\partial y} + \nu\left(\frac{\partial^2 V_B}{\partial x^2} + \frac{\partial^2 V_B}{\partial y^2}\right), \tag{3.3}$$

$$U_B \frac{\partial W_B}{\partial x} + V_B \frac{\partial W_B}{\partial y} = \nu\left(\frac{\partial^2 W_B}{\partial x^2} + \frac{\partial^2 W_B}{\partial y^2}\right). \tag{3.4}$$

3.3. Direct Numerical Simulation

Direct Numerical Simulation is a technique used to solve the full elliptic Navier Stokes Equations with no assumptions. In this thesis, the three-dimensional Navier Stokes equations are solved using an in-house conservative finite volume solver, namely, INCA (Hickel & Adams, 2008; Hickel, Egerer, & Larsson, 2014). The setup of steady state DNS used in this thesis closely mimics the setup of Casacuberta, Hickel, Westerbeek, and Kotsonis (2022). The assumption of spanwise invariance of the flow field implies that the discretization is primarily done in x and y directions, with two grid points in z direction. At the inflow, a 3D boundary layer obtained from the solution to the Falkner-Skan-Cooke equations is imposed. At the top boundary, a Dirichlet boundary condition is used for specifying external pressure, which is obtained from the expressions obtained from Chapter 2. For velocities at the top boundary, a homogeneous Neumann boundary condition is prescribed. At the wall, the standard no-slip condition is used. At the outlet, the external pressure is specified, and a second-order Neumann Boundary condition is used for velocity. The initial condition at the first time step is specified by initializing Falkner-Skan-Cooke profiles at each location. The equations are marched in time till the flow reaches a steady state using an explicit third-order Runge Kutta scheme. Each iteration in time involves converging the Poisson equation, where the limit is set to 1E-9 for convergence. The stopping criteria for time is based on a L_2 norm of temporal derivatives reaching an arbitrarily small value of 1E-8. Beyond this, a steady state of base flow can be safely claimed since temporal derivatives become extremely small. During the solution procedure, there is a provision for vertical momentum to flow upwards or downwards in the top boundary so as to ensure that the solutions are physical. DNS is computationally expensive due to the elliptic nature of governing equations, which motivates a simplification of these governing equations to a parabolic state under certain assumptions, subsequently resulting in a significant reduction of computational cost.

3.4. Boundary Layer Equations and Solver

The elliptic Navier Stokes equation can be simplified to parabolic form under three assumptions:

1. The boundary layer thickness (δ) is much smaller than the characteristic length scale of the problem (l) i.e. $\delta << l$.
2. The order of magnitude of second-order derivatives of wall-tangential components of base flow in x are much smaller than the second-order derivatives in y, and can subsequently be neglected.
3. The base flow y momentum equation (Equation 3.3) is assumed to simplify to

$$\frac{\partial P_B}{\partial y} = 0. \tag{3.5}$$

   Schlichting and Gersten (2000) explains that this assumption physically corresponds to a fluid particle having no mass or experiencing no friction while moving in the wall-normal direction in the boundary layer. The invariance of base flow pressure in y implies that the external pressure applied at the top boundary is felt unaltered in the near-wall region.

The simplified parabolic equations, termed Boundary Layer Equations, read

$$\frac{\partial U_B}{\partial x} + \frac{\partial V_B}{\partial y} = 0, \tag{3.6}$$

$$U_B \frac{\partial U_B}{\partial x} + V_B \frac{\partial U_B}{\partial y} = U_e \frac{\partial U_e}{\partial x} + \nu \frac{\partial^2 U_B}{\partial y^2}, \tag{3.7}$$

$$U_B \frac{\partial W_B}{\partial x} + V_B \frac{\partial W_B}{\partial y} = \nu \frac{\partial^2 W_B}{\partial y^2}, \tag{3.8}$$

where U_e represents the external velocity, which can be obtained from the externally imposed pressure (P_e) by means of the differential version of the Bernoulli Equation which reads

$$U_e \frac{\partial U_e}{\partial x} = -\frac{1}{\rho} \frac{\partial P_e}{\partial x}. \tag{3.9}$$

The process of simplifying Navier Stokes Equations to Boundary Layer Equations along with the motivation for the above-stated assumptions is provided in Appendix B.2.

The boundary layer solver (BLS) simultaneously satisfies Equation 3.6, Equation 3.7, and Equation 3.8 to generate the base flow. The system of equations is parabolic, which can be solved using a chordwise marching procedure at a fraction of the cost of solving the fully elliptic Navier Stokes equations. Marching in the x direction is conducted using a second-order implicit finite difference scheme on a uniformly spaced grid. Chebyshev polynomials are used for discretizing the equations in the wall-normal direction using the procedure proposed by Malik (1990). Using Chebyshev polynomials gives dual benefits of spectral convergence in the wall-normal direction and allows placement of half the points within the boundary layer, where derivatives of base flow are of much higher magnitude than the inviscid region. The inflow condition of the marching procedure is specified by a Falkner-Skan-Cooke boundary layer solution. The boundary conditions at the wall are given by the no-slip condition. At the top boundary placed far away from the wall, an external velocity is imposed. It is obtained from the effective pressure distributions specified in Chapter 2 by satisfying the Bernoulli Equation. It is to be noted that effective pressure, base flow pressure and external pressure are synonymous in boundary layer solver base flows.

BLS although fast is limited in usage by its assumptions. BLS can't march past separation since these scenarios involve a backward propagating base flow, where the parabolic marching procedure of BLS fails (Goldstein, 1948). Some assumptions of BLS fail in adverse pressure gradient regions where an inflection point appears. Clearly, in such cases the assumption of $U_{B_{xx}} << U_{B_{yy}}$ is wrong, since $U_{B_{yy}}$ goes to zero near the inflection point. Boundary layer solvers also cannot capture any pressure variation in y, which could be relevant in natural manifestations of deformed base flow, as seen in the case of the FFS in Figure 1.4, where pressure varies with y.

3.5. Comparison of DNS and BLS Base Flow

With regards to the cases considered in this thesis, it is preferred that the pressure field imposed at the top propagates down to the wall, such that the boundary layer experiences a local pressure change. The BLS would be an appropriate fit since it does not impose any wall-normal changes in base flow pressure. The BLS and DNS results for the clean case are similar in terms of pressure distribution imposed at the top boundary propagating down to the wall without any alteration. However, the usage of BLS in cases where the external pressure changes in the order of boundary layer thickness might result in a flow field different from that predicted by DNS due to the violation of assumptions of boundary layer theory. A comparison of BLS results with DNS results is thus conducted in this section to understand if these assumptions are violated. The external pressure distribution of the $-2.5\,p_f30w$ case is imposed directly as the top boundary condition of DNS and via computation of external velocity using the Bernoulli Equation in BLS to evaluate differences between the generated flow fields. The grid used for DNS has $y+$ values less than 1.3, and the details of the boundary layer grid are provided in Section 3.6.

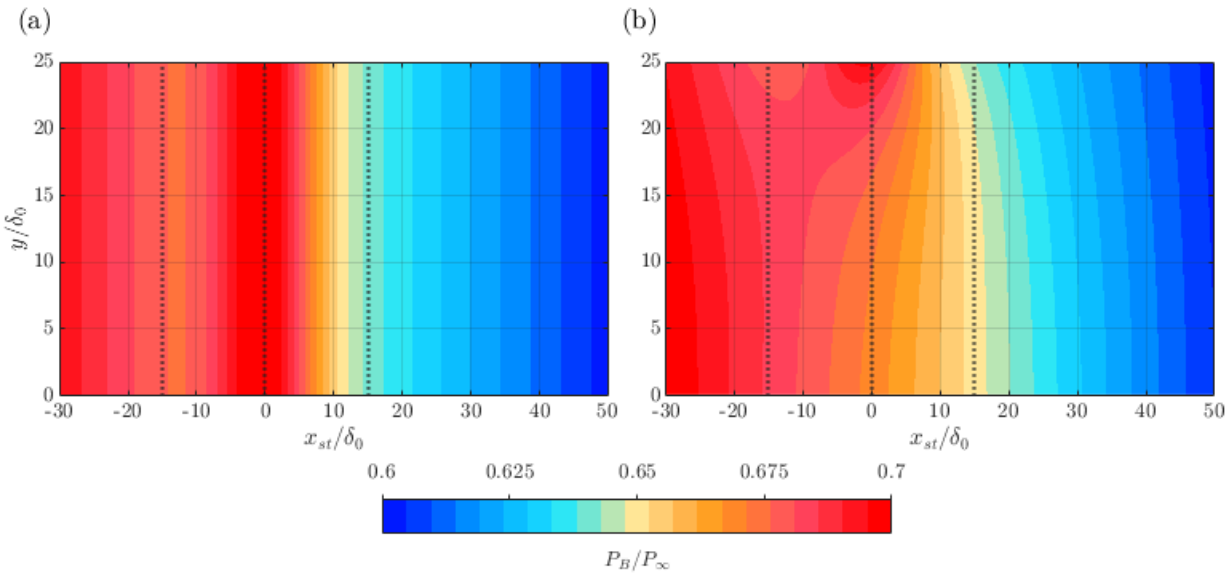

Figure 3.1: Contours of base flow pressure in (a) BLS and (b) DNS solution of $-2.5p_f\ 30w$ case; black dotted lines at $x_{st}/\delta_0 = -w/2,\ 0,$ and $w/2$ show the region of ΔP imposition

The pressure field for the BLS solution is a uniform extension of the pressure in the top boundary in the wall-normal direction since no wall-normal gradients are allowed, as seen in Figure 3.1 (a). However, in the DNS solution, the pressure distribution at the top boundary (featuring a local increase and subsequent decrease) does not resemble the pressure distribution near the wall, which appears close to a monotonically decreasing pressure variation, as seen in Figure 3.1 (b). Plots of base flow pressure at the top and near-wall region further reveal this discrepancy, as shown in Appendix B.3. It is thus evident that the wall-normal variation of pressure is non-zero in the DNS solution. This has consequences for the V_B field, where the V_B field predicted by BLS is orders of magnitude higher than that predicted by DNS as shown in Figure 3.2. The discrepancy in V_B fields of DNS and BLS is also shown using plots at two different wall-normal levels in Appendix B.3. This can potentially be attributed to the inviscid nature of particles moving in the y direction in the BLS solution, compared with viscous effects inhibiting y motion in the DNS solution.

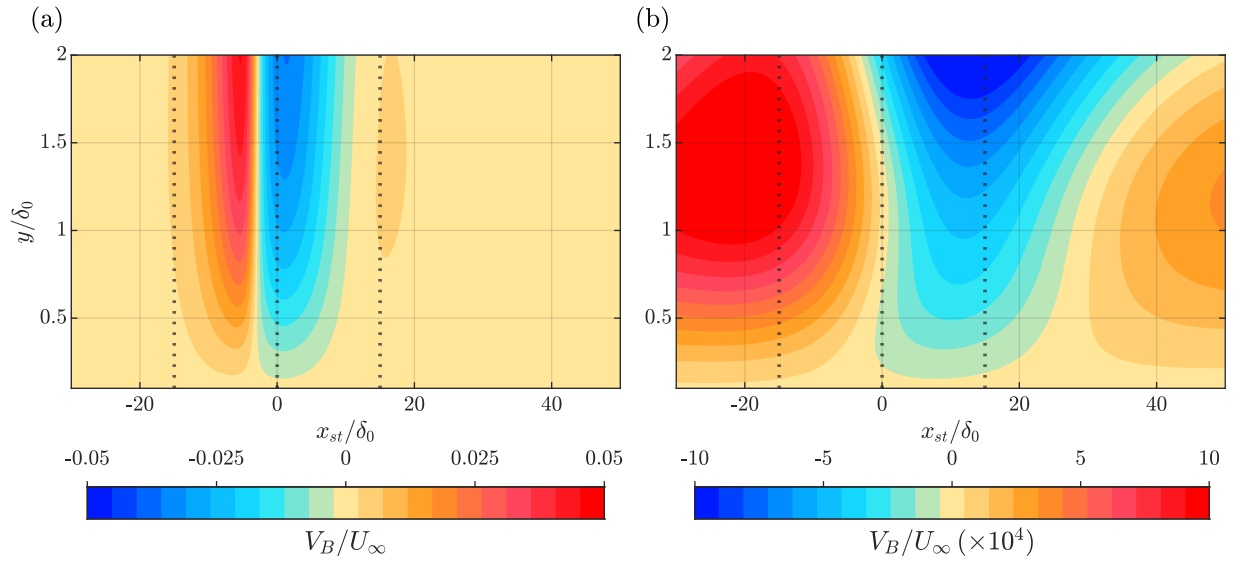

Figure 3.2: Contours of wall-normal velocity in (a) BLS and (b) DNS solution of $-2.5p_f$ $30w$ case; black dotted lines at $x_{st}/\delta_0 = -w/2,\ 0,$ and $w/2$ show the region of ΔP imposition.

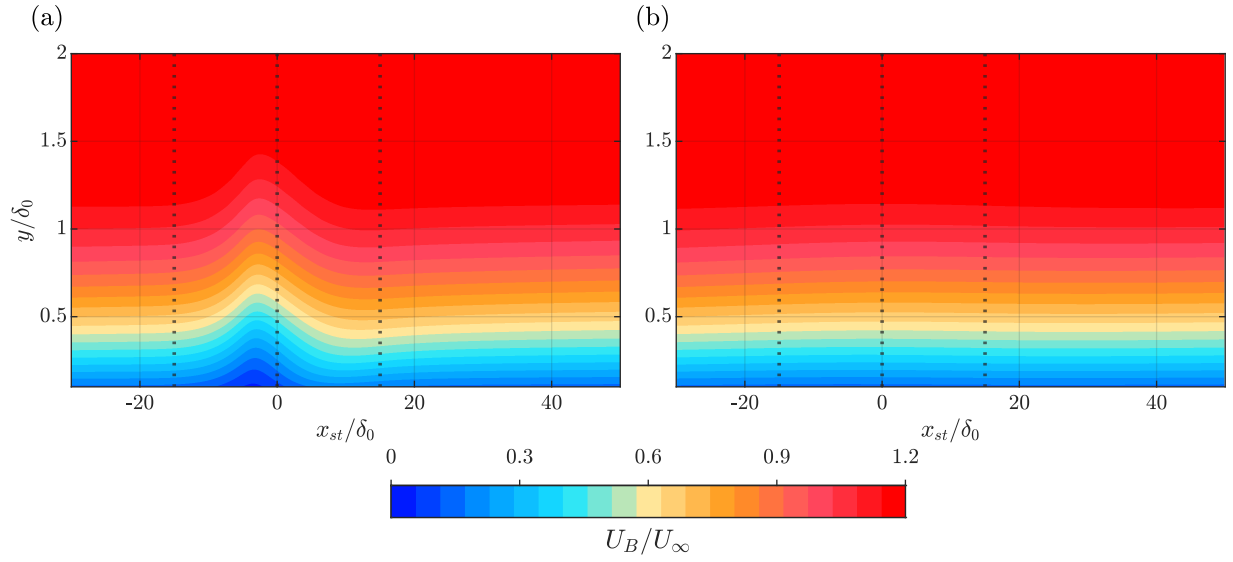

Figure 3.3: Contours of chordwise velocity in (a) BLS and (b) DNS solution of $-2.5p_f$ $30w$ case; black dotted lines at $x_{st}/\delta_0 = -w/2,\ 0,$ and $w/2$ show the region of ΔP imposition.

The pressure not propagating down to the boundary layer would imply that the local acceleration or deceleration experienced in the region of deformation would also be much lesser in the DNS solution compared with the boundary layer solution. This can be seen observing the U_B contours in Figure 3.3. An upward deflection of constant contour levels in boundary layer solver implies that chordwise velocity experiences deceleration along a line drawn at a fixed y level (i.e.

in a region on an xy plane where the y variation of a quantity follows a monotonically increasing trend, an upward deflection of constant contour levels would correspond to decrease of the value of the quantity along the chordwise direction, when monitored at a constant wall-normal height and vice versa). A downward deflection has the opposite consequence. The BLS base flow has much more significant upward and downward deflection of U_B contour levels in the region of deformation when compared with the DNS base flow, indicating a larger value of the chordwise derivative of U_B in the near-wall region of base flow deformation. This is also evidenced in the U_{B_x} plots at different wall-normal levels attached in the Appendix B.3, where U_{B_x} at near-wall levels is very different for the BLS solution compared to the DNS solution.

Thus, the boundary layer approximation of neglecting terms in the y momentum equation is invalid in the full Navier Stokes representation of fluid flow captured by DNS, rendering the BLS solution an idealized base flow. The BLS is used for the rest of the thesis to ensure that the pressure change imposed at the top propagates down to the wall, resulting in a local pressure change in the near-wall boundary layer and subsequent rapid base flow deformation. Since the base flow results are idealized, their usage in calculating perturbation properties could yield idealized results. Hence, the results are accepted with caution, and a validation section is also presented in Chapter 7, wherein the results of a BLS baseflow and subsequent perturbation analysis of base flow deformations imposed by a three-way pressure change are compared with the results of a DNS base flow and perturbation analysis of a natural base flow deformation i.e. the FFS. This checks if the effects of an FFS on deviating base flow and perturbation behaviour from clean case behaviour can be captured by a synthetic base flow deformation.

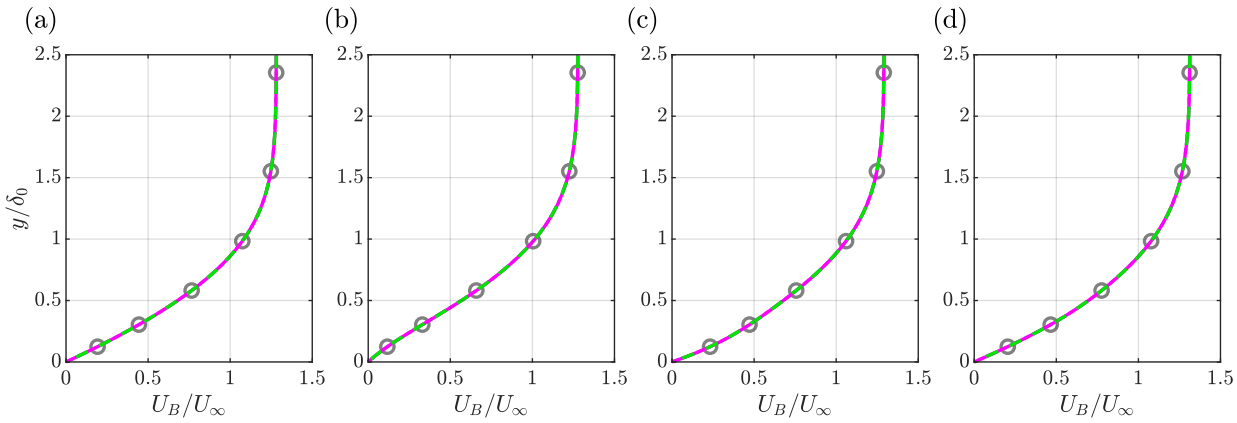

Figure 3.4: Plot of wall-normal variation of chordwise velocity in $-2.5p_f$ $30w$ case at x_{st}/δ_0 = (a) $-0.6w$, (b) $-0.25w$, (c) $0.25w$, and (d) $0.6w$ when N_x = 12000 (grey circles), 15000 (magenta solid), and 18000 (light green dashed).

3.6. Grid for Selected Method

The grid for the boundary layer solver has 15000 uniform divisions in x direction. Since Chebyshev polynomials are used to discretize the equations in y direction, the y grid is non-uniform, with 100 divisions such that half of the points are placed beneath $y/\delta_0 = 0.1$. To ensure that the results of the base flow do not vary with the grid, different grids are tested by varying x and y divisions one at a time. A grid with more resolution and another with lesser resolution are considered compared to the current grid. Values of U_B profiles at four different locations and δ^* values in the vicinity of deformation are compared to show that the grid used does not impact flow physics. The results of x refinement are shown in Figure 3.4 and Figure 3.5. The results of the grid used here superpose those of a grid of higher and lower x resolution verifying that results generated wouldn't be dependent on the number of grid points in x. A similar study is conducted for wall-normal discretization which shows that results are independent of y discretization, and the results are attached in Appendix B.5.

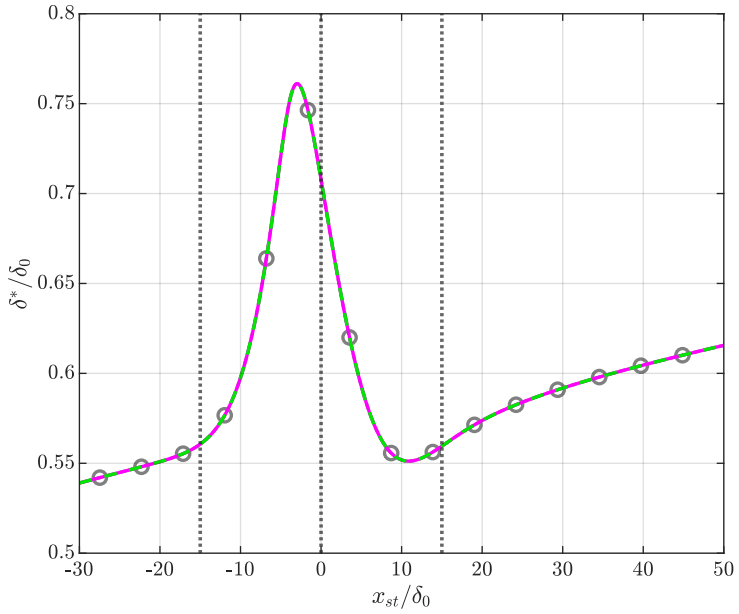

Figure 3.5: Plot of chordwise variation of displacement thickness in $-2.5p_f$ $30w$ case when N_x = 12000 (grey circles), 15000 (magenta solid), and 18000 (light green dashed); black dotted lines at $x_{st}/\delta_0 = -w/2,\ 0,$ and $w/2$ show the region of ΔP imposition.

4

Modelling Perturbation Evolution

This chapter tackles the selection of an appropriate method to model perturbation evolution using the base flow solution generated using BLS. The derivation of linearized perturbation equations is first presented. This is followed by the description of various ansatz used to model perturbation behaviour. A description of various methods used to solve linearized perturbation equations using various ansatz is then provided with a brief of solution techniques and detailed explanations of limitations. A section then follows on selecting the best-suited method to achieve the objectives of the current thesis. This is followed by a description of the domain and grid for the selected method, with a verification procedure to prove that the results do not depend on the grid selected.

4.1. Perturbation Evolution Problem Definition

The perturbation is seeded as a spanwise periodic stationary crossflow mode with spanwise wavelength 7.5 mm obtained as a solution of linear local stability analysis (explained in Section 4.3.2) as specified by Casacuberta, Hickel, Westerbeek, and Kotsonis (2022). The authors ground their choice by the ability of the mode to achieve maximum amplification at the end of the domain considered in Section 3.1. In the current thesis, the same mode is used to ease the comparison process with FFS cases simulated by Casacuberta, Hickel, Westerbeek, and Kotsonis (2022). The size of the domain for perturbation evolution in wall-normal direction remains consistent with specifications in Section 3.1. However, the chordwise extent of the base flow domain is cropped since the analysis of perturbation behaviour only needs to be conducted in regions around the vicinity of the base flow deformation. The inlet is placed at $x/\delta_0 = 140$, sufficiently upstream of the largest imposed pressure variation. The outlet is placed at $x/\delta_0 = 273$ to provide enough domain length to observe perturbation evolution trends downstream of the base flow deformation. The domain (visualized in Appendix B.1) does not have any z extension as the properties of perturbation remain spanwise periodic throughout the domain. The selected mode is allowed to grow or decay in the chordwise direction, and the equations governing its evolution are presented in Section 4.2.

4.2. Linearized Perturbation Equations

Linearized perturbation equations can be derived by subtracting the equation of base flow from the equation of total flow. The base flow components U_B, V_B and W_B are interchangeably denoted $U_{B,1}$, $U_{B,2}$ and $U_{B,3}$ in Einstein convention, and perturbation velocity u', v' and w' are also interchangeably denoted u'_1, u'_2 and u'_3 in Einstein convention. The equation of total flow is first considered. The total flow consists of velocity components superposed on their respective base flow velocity components. A pressure perturbation p' is also superposed on the base flow pressure. The perturbations modelled in this thesis are stationary, subsequently implying that the total flow is steady since the base flow is already steady. The Navier Stokes equation for total flow are

$$\frac{\partial(U_{B,j} + u'_j)}{\partial x_j} = 0, \tag{4.1}$$

$$(U_{B,j} + u'_j)\frac{\partial(U_{B,k} + u'_k)}{\partial x_j} = -\frac{1}{\rho}\frac{\partial(P_B + p')}{\partial x_j} + \nu\frac{\partial^2(U_{B,k} + u'_k)}{\partial x_j^2}, \tag{4.2}$$

where the index k considers quantities one at a time, and the index j considers sum of quantities over $j = 1$, 2, and 3 (similar to Section 1.4). Subtracting the base flow equations (Equation 3.1 to Equation 3.4) from the total flow equations,

the equations describing perturbation behaviour are obtained as

$$\frac{\partial u'_j}{\partial x_j} = 0, \tag{4.3}$$

$$U_{B,j}\frac{\partial u'_k}{\partial x_j} + u'_j\frac{\partial U_{B,k}}{\partial x_j} = -\frac{1}{\rho}\frac{\partial p'}{\partial x_j} + \nu\frac{\partial^2 u'_k}{\partial x_j^2} - u'_j\frac{\partial u'_k}{\partial x_j}. \tag{4.4}$$

To linearize the perturbation equations, the definition of a linear operator is considered as per Haberman (1983). Any operator $\mathcal{L}$ is said to be linear if

$$\mathcal{L}(c_1 v_1 + c_2 v_2) = c_1\mathcal{L}(v_1) + c_2\mathcal{L}(v_2), \tag{4.5}$$

where v_1 and v_2 are two variables whereas c_1 and c_2 are arbitrary constants. The operator $\mathcal{L}$ can be a linear polynomial or a partial derivative for Equation 4.5 to be satisfied. However if $\mathcal{L}$ involves the multiplication of partial derivatives or linear polynomials, the linearity condition doesn't hold anymore. Linearizing Equation 4.5 would thus entail removing products of partial derivatives, and the result of linearization is

$$U_{B,j}\frac{\partial u'_k}{\partial x_j} + u'_j\frac{\partial U_{B,k}}{\partial x_j} = -\frac{1}{\rho}\frac{\partial p'}{\partial x_j} + \nu\frac{\partial^2 u'_k}{\partial x_k^2} \tag{4.6}$$

The eliminated term $-u'_j\partial u'_k/\partial x_j$ is negligible when the amplitude of perturbation is orders of magnitude lower than the base flow velocity and its derivative. The perturbation continuity equation Equation 4.3 does not need linearization as it is already linear in nature.

4.3. Ansatz and Solution Techniques

To solve the perturbation equations in a modal framework, a separation of variables approach can be used (refer Section 1.4), where the solution is composed of a sum of complex Fourier modes. The Fourier modes always exist in complex conjugate pairs, ensuring that the reconstructed perturbation field summing these modes is real. In linear methods, it is sufficient to assume that one such Fourier mode and its corresponding conjugate pair satisfy the linear perturbation equations individually. Their summation yields the total perturbation, which also satisfies the perturbation equation by the linearity property. The Fourier ansatz for linear perturbation equations relevant for modelling stationary crossflow instability evolution is first introduced. This is followed by substituting the ansatz into perturbation equations to generate different solution techniques for perturbation equations.

4.3.1. Ansatz

The most basic ansatz assumed to solve the linearized perturbation equation assumes a periodic dependency in z, and combined growth and periodicity in x, represented as

$$u'_k = \hat{u}_k(y)\, e^{\mathrm{i}(\alpha x + \beta z)}. \tag{4.7}$$

Growth (or decay) in x is captured by the imaginary part of α (α_i), whereas periodicity in x is captured by the real part of α (α_r). β is real since the base flow does not vary in z leaving no scope for perturbation growth in z. $\hat{u}_k(y)$ is a complex field representing the shape and phase variation of the perturbation field in y. This ansatz is called the LST ansatz (owing to similarities with the LST ansatz shown in section 1.4).

The shortcoming of this ansatz lies in its inability to capture history effects. To be able to capture history effects, Equation 4.7 is modified to

$$u'_k = \hat{u}_k(x, y)\, e^{\mathrm{i}(\int_{x_0}^{x} \alpha ds + \beta z)}. \tag{4.8}$$

Equation 4.8 is known as the PSE ansatz. The ability to capture history effects is attributed to the integration of α (Westerbeek, 2020). The difference between the effects of integrated and non-integrated α is visualized in Figure 4.1, where α varies from the beginning of the domain to the end of the domain. Non-parallel boundary layers feature changing values of α, whose effects ILST can only capture in a local sense without accounting for history. The existence of streamwise derivatives in non-parallel flows motivates the need to keep $\hat{u}_k$ a function of x.

However, the PSE ansatz does not completely allow the presence of different growth rates among different components. The common growth rate α_i captures the bulk of growth common across all components, whereas any difference in growth rate among components can only be partially captured by differences in $\hat{u}_k$ evolution across components. In strong non-parallel boundary layers, perturbations tend to have different growth rates across different components as evidenced in the

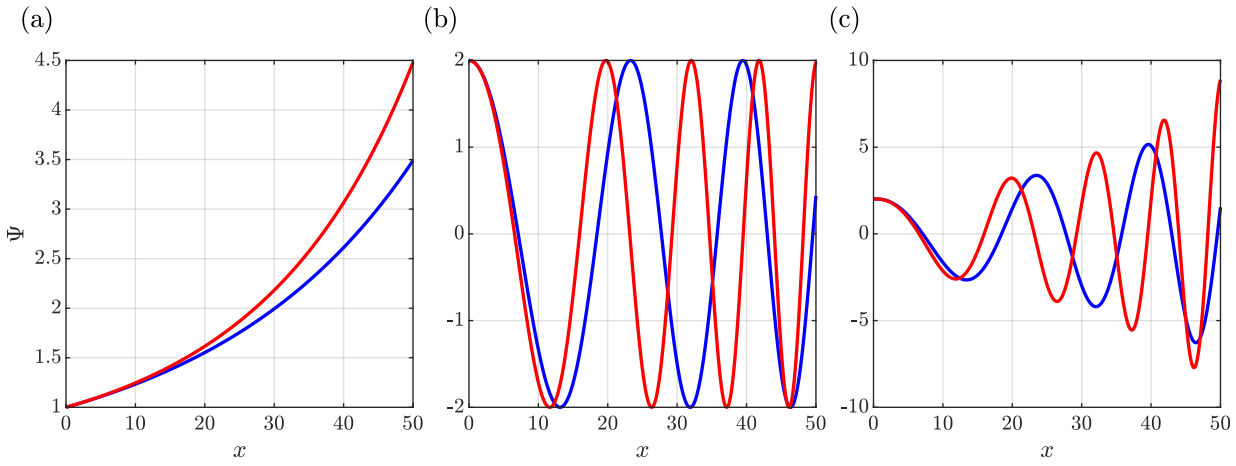

Figure 4.1: Plot of x variation of Ψ = (a) $2\mathrm{Re}(e^{-\alpha_i x})$ (red), $2\,\mathrm{Re}(e^{-\int_0^x \alpha_i ds})$ (blue), (b) $2\,\mathrm{Re}(e^{i\alpha_r x})$ (red), $2\,\mathrm{Re}(e^{i\int_0^x \alpha_r ds})$ (blue), and (c) $2\,\mathrm{Re}(e^{i(\alpha_r+i\alpha_i)x})$ (red), $2\,\mathrm{Re}(e^{i\int_0^x(\alpha_r+i\alpha_i)ds})$ (blue).

results of stationary crossflow instability interaction with an FFS in Casacuberta et al. (2021). To capture such effects, it is essential that each component is allowed to grow at a different growth rate, which leads to the HLNS ansatz, expressed as

$$u'_k = \tilde{u}_k(x,y)\, e^{i\beta z}. \tag{4.9}$$

Here, $\tilde{u}_k(x,y)$ is a complex field which captures growth and phase variation in xy plane. The z periodicity, represented by $e^{i\beta z}$, is common across all perturbation components. The complex field of $\tilde{u}_k(x,y)$ can be decomposed into terms responsible for phase variation and magnitude, and rewritten as

$$u'_k = |\tilde{u}_k|\, e^{i(\phi_k+\beta z)}, \tag{4.10}$$

where $|\tilde{u}_k|$ is the perturbation amplitude function. Its x variation captures the growth or decay of a perturbation. Whereas its y variation at a fixed x station normalized by the maxima of the amplitude function at the same station represents the shape function. On the other hand, ϕ_k represents the xy phase dependency, which controls perturbation tilt in the xy plane and the direction of lines of constant phase in the xz plane.

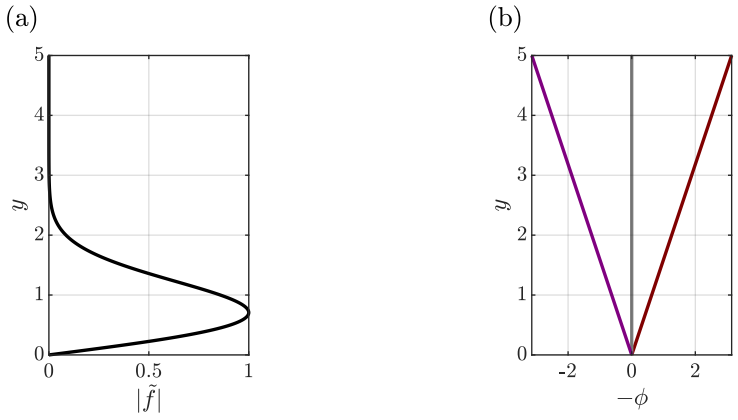

Figure 4.2: Wall-normal variation of (a) $|\tilde{f}|$ and (b) $-\phi$, where $\phi = 2y$ (purple), 0 (grey), and $-2y$ (brown).

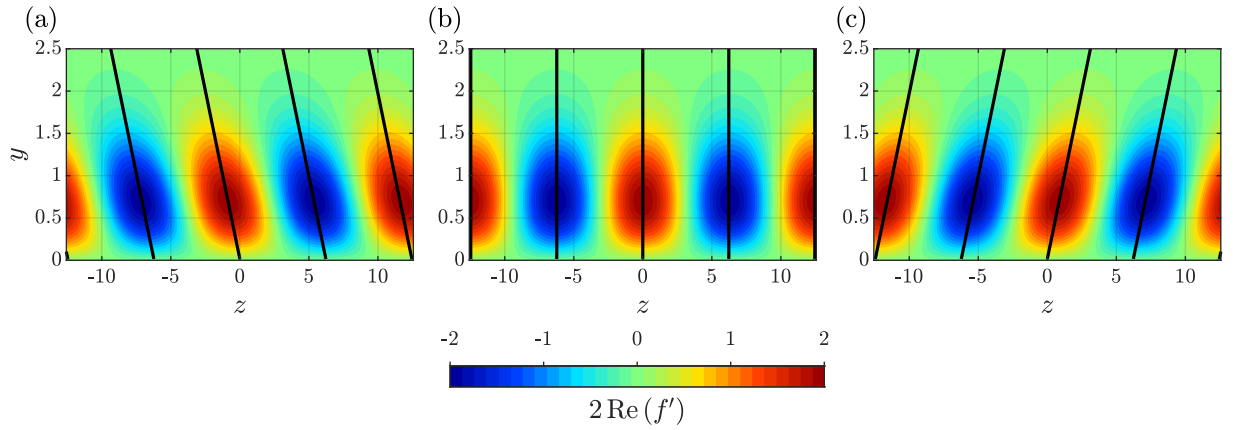

Figure 4.3: Representation of Re(f') on yz planes when (a) $\phi = 2y$, (b) $\phi = 0$, and (c) $\phi = -2y$; black lines denote lines of constant phase.

Perturbation tilt is of prime interest as it can possibly demonstrate the Orr Mechanism (refer Section 1.7.1 and Section 1.8). Hence, artificial fields are constructed to demonstrate how the variation of ϕ influences perturbation tilt. An arbitrary yz field $f' = |\tilde{f}|e^{\mathrm{i}(\phi+\beta z)}$ is considered, whose amplitude function is given by $|\tilde{f}| = ye^{-y^2}/\max(ye^{-y^2})$. The variation of $|\tilde{f}|$ is plotted in Figure 4.2 (a), approximately resembling the u' shape function of clean case crossflow modes. Three different distributions of ϕ ($\phi(y) = 2y, 0, -2y$) are tested for a fixed value of $\beta = 2$ to understand the effect of ϕ distribution on tilt, as shown in Figure 4.2 (b). The real-valued field of f' is expressed by

$$\mathrm{Re}(f') = \mathrm{Re}\left(|\tilde{f}|\, e^{\mathrm{i}(\theta+\beta z)}\right) = |\tilde{f}|\cos(\phi + \beta z). \tag{4.11}$$

The lines of constant phase for this field in the yz plane are obtained by $\phi + \beta z = C$, as shown in Figure 4.3. It is noted that the variation of ϕ with y directly relates to the direction of tilt of the perturbation as it controls the lines of phase in the yz plane. Tilt (m) can be quantified by the slope of the lines of constant phase with respect to the y axis given by

$$m = -\frac{1}{\beta}\frac{\partial \phi}{\partial y}. \tag{4.12}$$

A leftward tilt in Figure 4.3 (a) is noted for the distribution of $\phi(y) = 2y$, owing to the negative slope as per Equation 4.12. A rightward tilt in Figure 4.3 (c) corresponds to the distribution of $\phi(y) = -2y$, owing to the positive slope as per Equation 4.12. Generalizing, since β is a positive constant, the value of $-\partial\phi/\partial y$ directly determines the direction in which the real-valued field of perturbation is tilted.

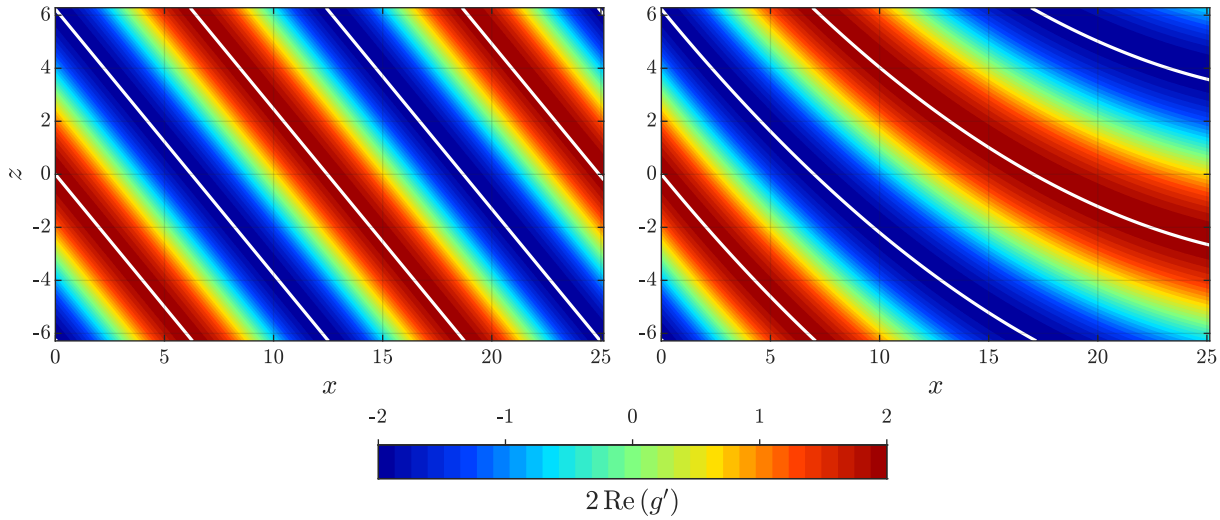

Figure 4.4: Representation of Re(g') on xz planes when (a) $\phi = 0.5$ and (b) $\phi = 0.5 - 0.2x/25$; white lines denote lines of constant phase.

The xz lines of constant phase on the other hand are relevant since the wavenumber vector is in a direction perpendicular to these lines of constant phase. The control of lines of constant phase in xz planes is shown by constructing artificial fields $g' = e^{\mathrm{i}(\phi+\beta z)}$, whose lines of constant phase are given by $\phi+\beta z = C$. β takes a value of 0.5 and two different values of ϕ are tested. The first value of ϕ is the constant value of 0.5, which results in straight lines of constant phase (Figure 4.4 (a)). Whereas when ϕ varies in x, linearly spaced between 0.5 and 0.3 through the domain, curved lines of constant phase are obtained (Figure 4.4 (b)). The angle θ made by the line of constant phase and the x axis can be computed by differentiating the equation of lines of constant phase with respect to x and taking its arctan to yield

$$\theta = \mathrm{atan}\left(-\frac{1}{\beta}\frac{\partial \phi}{\partial x}\right). \tag{4.13}$$

In problems of perturbation evolution, ϕ is a parameter varying with both x and y direction. If the ϕ variation with y remains constant with the change of x station, it implies that ϕ_x does not change with wall-normal height, further implying that the direction of lines of constant phase in xz plane are invariant with height considered. One characteristic line of constant phase can be defined in such a scenario. This would correspond to the assumptions of ILST, which presumably considers the definition of one line of constant phase ($\alpha_r x + \beta z = C$) perpendicular to the wavenumber direction throughout the entire wall-normal height as representative of perturbation lines of constant phase at any height. Whereas, if the variation of ϕ with y changes with the change of x station, it implies that ϕ_x changes with wall-normal height, further implying that the lines of constant phase at two different levels would be aligned in different directions. No common line of constant phase in xz plane can be identified, casting doubt on whether a direction of wavenumber vector can be identified.

4.3.2. Incompressible Local Stability Equations and Solver

The disturbance equations stated in Equation 4.3 and Equation 4.6 can be simplified further by substituting Equation 4.7 into the perturbation equations and assuming parallel flow. Parallel flow implies that the base flow is just a function of y, and the wall-normal velocity is zero. The perturbation derivatives and second derivatives in various directions after the substitution of the ILST ansatz (Equation 4.7) read

$$\frac{\partial u'_k}{\partial x} = \mathrm{i}\alpha \hat{u}_k e^{\mathrm{i}(\alpha x+\beta z)}, \tag{4.14}$$

$$\frac{\partial u'_k}{\partial y} = \frac{\partial \hat{u}_k}{\partial y} e^{\mathrm{i}(\alpha x+\beta z)}, \tag{4.15}$$

$$\frac{\partial u'_k}{\partial z} = \mathrm{i}\beta \hat{u}_k e^{\mathrm{i}(\alpha x+\beta z)}, \tag{4.16}$$

$$\frac{\partial^2 u'_k}{\partial x^2} = -\alpha^2 \hat{u}_k e^{\mathrm{i}(\alpha x+\beta z)}, \tag{4.17}$$

$$\frac{\partial^2 u'_k}{\partial y^2} = \frac{\partial^2 \hat{u}_k}{\partial y^2} e^{\mathrm{i}(\alpha x+\beta z)}, \tag{4.18}$$

$$\frac{\partial^2 u'_k}{\partial z^2} = -\beta^2 \hat{u}_k e^{\mathrm{i}(\alpha x+\beta z)}. \tag{4.19}$$

Similar expressions hold for pressure perturbation and aren't repeated. Substituting these derivatives (Equation 4.14 to Equation 4.19) into the linearized perturbation equations (Equation 4.3 and Equation 4.6), and factoring out common exponentials with parallel flow assumptions give

$$\mathrm{i}\alpha\hat{u} + \frac{\partial \hat{v}}{\partial y} + \mathrm{i}\beta\hat{w} = 0, \tag{4.20}$$

$$\mathrm{i}U_B\alpha\hat{u} + \mathrm{i}W_B\beta\hat{u} + \hat{v}\frac{\partial U_B}{\partial y} = -\frac{\mathrm{i}}{\rho}\alpha\hat{p} + \nu\left(\frac{\partial^2\hat{u}}{\partial y^2} - (\alpha^2+\beta^2)\hat{u}\right), \tag{4.21}$$

$$\mathrm{i}U_B\alpha\hat{v} + \mathrm{i}W_B\beta\hat{v} = -\frac{1}{\rho}\frac{\partial \hat{p}}{\partial y} + \nu\left(\frac{\partial^2\hat{v}}{\partial y^2} - (\alpha^2+\beta^2)\hat{v}\right), \tag{4.22}$$

$$\mathrm{i}U_B\alpha\hat{w} + \mathrm{i}W_B\beta\hat{w} + \hat{v}\frac{\partial W_B}{\partial y} = -\frac{\mathrm{i}}{\rho}\beta\hat{p} + \nu\left(\frac{\partial^2\hat{u}}{\partial y^2} - (\alpha^2+\beta^2)\hat{w}\right). \tag{4.23}$$

These equations together form the Incompressible Local Stability Equations abbreviated as ILST. The ILST system can be non-dimensionalized by non-dimensionalizing perturbation and base flow velocities by U_∞, length scales by a reference length scale (δ_0) and perturbation pressure by ρU_∞^2. The Reynolds number corresponding to this non-dimensionalization is $\mathrm{Re} = U_\infty \delta_0 / \nu$. When Re, β and base flow are known, the non-dimensionalized version of ILST with appropriate boundary conditions takes the form of an eigenvalue problem where α is the eigenvalue and $[\hat{u}, \hat{v}, \hat{w}, \hat{p}]^T$ is the eigenvector. Assuming a fixed value of Reynolds Number, the x station (to obtain the base flow at that particular station) and β can be varied to obtain a contour of real and imaginary values of α. Negative imaginary values of α would correspond to regions of growth, whereas positive regions would correspond to stabilization. Integrating the values of α along x for a fixed value of β helps develop an approximate idea of whether the value of β corresponds to a mode that grows long-term or short-term. Thus, even though ILST uses a parallel flow approximation, it is still usually used in weakly non-parallel flows to select the initial value of mode to be simulated or experimentally observed (Bippes, 1999). Discretization of ILST equations in y direction by Chebyshev polynomials results in a non-uniform grid in y direction as per Malik (1990), onto which the base flow solution at a x station is interpolated. On solving the equations, multiple eigenvalues are obtained. A filtering technique chooses the most physical eigenvalue, motivated by the requirement of the eigenvector to decay exponentially in the freestream region (Groot, 2018).

4.3.3. Linear Parabolized Stability Equations and Solver

The localized nature of ILST without its ability to take into account history effects and streamwise changes of base flow limits its usage in cases where these effects could be significant. The Linearized Parabolic Stability Equations (LPSE) is more preferred in these cases, where the effects of streamwise changes of base flow on perturbation behaviour can be handled to some degree. The perturbation equations are elliptic in nature which makes these equations difficult to solve. But these can be parabolized under certain approximations, which make the equations easier to solve as a downstream marching procedure can be performed ignoring any effects of upstream propagation which would render the system elliptic. To parabolize the perturbation equations, the derivation provided by Westerbeek (2020) is adopted here. The shape function needs to be slowly varying whereas the wave function is allowed to vary fast (Westerbeek, 2020). A slow varying coordinate $\xi = \epsilon x$ is introduced such that $\epsilon = O(Re^{-1})$. The ansatz in Equation 4.8 can be modified as per the modified formulation to read

$$u'_k = \hat{u}_k(\xi, y)\, e^{\mathrm{i}(\int_{x_0}^{x} \alpha ds + \beta z)}. \tag{4.24}$$

The change of $\hat{u}_k$ is given by

$$\frac{\partial \hat{u}_k}{\partial x} = \frac{\partial \xi}{\partial x}\frac{\partial \hat{u}_k}{\partial \xi} \approx \frac{1}{Re}\frac{\partial \hat{u}_k}{\partial \xi}. \tag{4.25}$$

This yields an expression for the first derivative of u'_k which reads

$$\frac{\partial u'_k}{\partial x} \approx \left(\frac{1}{Re}\frac{\partial \hat{u}_k}{\partial \xi} + \mathrm{i}\alpha \hat{u} \right) e^{\mathrm{i}(\int_{x_0}^{x} \alpha ds + \beta z)}. \tag{4.26}$$

The second derivative of u'_k which features in the viscous dissipation terms of the perturbation momentum equation reads

$$\frac{\partial^2 u'_k}{\partial x^2} \approx \left(\frac{1}{Re^2}\frac{\partial^2 \hat{u}_k}{\partial \xi^2} + \frac{2\mathrm{i}\alpha}{Re}\frac{\partial \hat{u}}{\partial \xi} + \frac{\mathrm{i}\hat{u}}{Re}\frac{\partial \alpha}{\partial \xi} - \alpha^2 \hat{u} \right) e^{\mathrm{i}(\int_{x_0}^{x} \alpha ds + \beta z)}. \tag{4.27}$$

The term $\partial^2 \hat{u}_k / \partial \xi^2$ causes the equation to be elliptic (Westerbeek, 2020), and is thus neglected given that the order of magnitude is much lesser than the other terms in the equation (Bertolotti, 1991). This slow varying assumption thus helps parabolize the equations, and this remains valid if streamwise gradients remain small (Bertolotti, 1991; Westerbeek, 2020). Thus, $\partial^2 \hat{u}_k / \partial \xi^2$ is neglected, and the demarcation of chordwise coordinates into slow-varying and fast-varying coordinates is not considered further.

Now, the linearized perturbation equations (Equation 4.3 and Equation 4.6) need to rewritten by substituting the PSE ansatz (Equation 4.8) into the perturbation equations. For this, the first step is deriving expressions for the first and second derivatives of perturbation velocity. The expressions of perturbation velocity first and second derivatives in various directions read

$$\frac{\partial u'_k}{\partial x} = \left(\mathrm{i}\alpha \hat{u}_k + \frac{\partial \hat{u}_k}{\partial x} \right) e^{\mathrm{i}(\int_{x_0}^{x} \alpha ds + \beta z)}, \tag{4.28}$$

$$\frac{\partial u'_k}{\partial y} = \frac{\partial \hat{u}_k}{\partial y} e^{\mathrm{i}(\int_{x_0}^{x} \alpha ds + \beta z)}, \tag{4.29}$$

$$\frac{\partial u'_k}{\partial z} = \mathrm{i}\beta\hat{u}_k e^{\mathrm{i}(\int_{x_0}^{x}\alpha ds+\beta z)}, \tag{4.30}$$

$$\frac{\partial^2 u'_k}{\partial x^2} = \left(\mathrm{i}2\alpha\frac{\partial\hat{u}_k}{\partial x} + \mathrm{i}\hat{u}_k\frac{\partial\alpha}{\partial x} - \alpha^2\hat{u}_k\right)e^{\mathrm{i}(\int_{x_0}^{x}\alpha ds+\beta z)}, \tag{4.31}$$

$$\frac{\partial^2 u'_k}{\partial y^2} = \frac{\partial^2\hat{u}_k}{\partial y^2}e^{\mathrm{i}(\int_{x_0}^{x}\alpha ds+\beta z)}, \tag{4.32}$$

$$\frac{\partial^2 u'_k}{\partial z^2} = -\beta^2\hat{u}_k e^{\mathrm{i}(\int_{x_0}^{x}\alpha ds+\beta z)}. \tag{4.33}$$

Similar expressions hold for pressure perturbation and aren't repeated. These derivatives (Equation 4.28 to Equation 4.33) are substituted into the perturbation equations (Equation 4.3 and Equation 4.6), and the common exponentials are cancelled off to obtain the following equations:

$$\mathrm{i}\alpha\hat{u} + \frac{\partial\hat{u}}{\partial x} + \frac{\partial\hat{v}}{\partial y} + \mathrm{i}\beta\hat{w} = 0, \tag{4.34}$$

$$\mathrm{i}U_B\alpha\hat{u} + U_B\frac{\partial\hat{u}}{\partial x} + V_B\frac{\partial\hat{u}}{\partial\hat{y}} + \mathrm{i}W_B\beta\hat{u} + \hat{u}\frac{\partial U_B}{\partial x} + \hat{v}\frac{\partial U_B}{\partial y} = -\frac{1}{\rho}\left(\frac{\partial\hat{p}}{\partial x} + \mathrm{i}\alpha\hat{p}\right) + \nu\left(\mathrm{i}2\alpha\frac{\partial\hat{u}}{\partial x} + \mathrm{i}\hat{u}\frac{\partial\alpha}{\partial x} + \frac{\partial^2\hat{u}}{\partial y^2} - (\alpha^2+\beta^2)\hat{u}\right), \tag{4.35}$$

$$\mathrm{i}U_B\alpha\hat{v} + U_B\frac{\partial\hat{v}}{\partial x} + V_B\frac{\partial\hat{v}}{\partial\hat{y}} + \mathrm{i}W_B\beta\hat{v} + \hat{u}\frac{\partial V_B}{\partial x} + \hat{v}\frac{\partial V_B}{\partial y} = -\frac{1}{\rho}\frac{\partial\hat{p}}{\partial y} + \nu\left(\mathrm{i}2\alpha\frac{\partial\hat{v}}{\partial x} + \mathrm{i}\hat{v}\frac{\partial\alpha}{\partial x} + \frac{\partial^2\hat{v}}{\partial y^2} - (\alpha^2+\beta^2)\hat{v}\right), \tag{4.36}$$

$$\mathrm{i}U_B\alpha\hat{w} + U_B\frac{\partial\hat{w}}{\partial x} + V_B\frac{\partial\hat{w}}{\partial\hat{y}} + \mathrm{i}W_B\beta\hat{w} + \hat{u}\frac{\partial W_B}{\partial x} + \hat{v}\frac{\partial W_B}{\partial y} = -\frac{\mathrm{i}\beta}{\rho}\hat{p} + \nu\left(\mathrm{i}2\alpha\frac{\partial\hat{u}}{\partial x} + \mathrm{i}\hat{w}\frac{\partial\alpha}{\partial x} + \frac{\partial^2\hat{w}}{\partial y^2} - (\alpha^2+\beta^2)\hat{w}\right). \tag{4.37}$$

These equations can be solved as a parabolic marching problem. The initial condition for this marching procedure is a modal solution obtained from ILST. However, there are two problems that might be encountered while resorting to parabolic marching. One is the upstream propagation of pressure or acoustic modes, which results in elliptic character of the equation. These upstream propagating modes are usually rapidly decaying and weak (Herbert, 1994). Thus, either an appropriately large step size for discretizing the equations can be selected to avoid the influence of such upstream modes or the influence of upstream acoustic modes can be avoided by neglecting the effects of backward propagating modes (Herbert, 1994).

The second problem is that $\hat{u}_k$ is not restricted in the above equations to grow slowly. This is done with a physical norm which enforces the slow change of $\hat{u}_k$ by keeping perturbation energy per component constant at each chordwise location (Herbert, 1994; Westerbeek, 2020), as per

$$\int \hat{u}_k^{\dagger}\frac{\partial\hat{u}_k}{\partial x} = 0. \tag{4.38}$$

The maxima of $|\hat{u}_k^{\dagger}|$ however can still vary from station to station, and might be slightly different from 1 as a result. This means that amplitude purely obtained by growth rate integration might be wrong. Hence, while computing amplitude evolution, the integration of growth rate and the maximum value of $|\hat{u}^{\dagger}|$ are multiplied to cancel out this discrepancy (Westerbeek, 2020).

An in-house LPSE solver the TU Delft Low Speed Lab is used in this thesis. The inflow is initialized using the ILST mode specified in Section 4.1. The no-slip condition is used at the wall, where perturbations go to zero near the freestream. The forward marching procedure in x is conducted using a second-order scheme, wherein the grid is uniform. As for selecting the step size, backward propagating modes are neglected as their consideration leads to an insufficiently resolved grid for resolving perturbation characteristics. The grid in y is generated by discretizing the equations in y using Chebyshev polynomials (Malik, 1990), and the wall-normal derivatives have an accuracy of very high order due to spectral convergence.

4.3.4. Harmonic Linearized Navier Stokes Equations and Solver

Although the PSE accounts for multiple ILST limitations, the method might not predict instability behaviour correctly in regions of high streamwise gradient (Franco et al., 1821). Thus, all terms that cause ellipticity are retained, and an elliptic system of equations are solved using HLNS. To derive the equations to be solved, expressions for the derivatives of perturbation are obtained by substituting the HLNS ansatz (Equation 4.9) in the derivative expansions as follows:

$$\frac{\partial u'_k}{\partial x} = \frac{\partial \tilde{u}_k}{\partial x} e^{\mathrm{i}\beta z}, \tag{4.39}$$

$$\frac{\partial u'_k}{\partial y} = \frac{\partial \tilde{u}_k}{\partial y} e^{\mathrm{i}\beta z}, \tag{4.40}$$

$$\frac{\partial u'_k}{\partial z} = \mathrm{i}\beta \tilde{u}_k e^{\mathrm{i}\beta z}, \tag{4.41}$$

$$\frac{\partial^2 u'_k}{\partial x^2} = \frac{\partial^2 \tilde{u}_k}{\partial x^2} e^{\mathrm{i}\beta z}, \tag{4.42}$$

$$\frac{\partial^2 u'_k}{\partial y^2} = \frac{\partial^2 \tilde{u}_k}{\partial y^2} e^{\mathrm{i}\beta z}, \tag{4.43}$$

$$\frac{\partial^2 u'_k}{\partial z^2} = -\beta^2 \tilde{u}_k e^{\mathrm{i}\beta z}. \tag{4.44}$$

Similar expressions hold for pressure perturbation and aren't repeated. These derivative expressions are substituted into the perturbation continuity and momentum equation to yield

$$\frac{\partial \tilde{u}}{\partial x} + \frac{\partial \tilde{v}}{\partial y} + \mathrm{i}\beta\tilde{w} = 0, \tag{4.45}$$

$$U_B\frac{\partial \tilde{u}}{\partial x} + \tilde{u}\frac{\partial U_B}{\partial x} + V_B\frac{\partial \tilde{u}}{\partial y} + \tilde{v}\frac{\partial U_B}{\partial y} + \mathrm{i}W_B\beta\tilde{u} = -\frac{1}{\rho}\left(\frac{\partial \tilde{p}}{\partial x}\right) + \nu\left(\frac{\partial^2 \tilde{u}}{\partial x^2} + \frac{\partial^2 \tilde{u}}{\partial y^2} - \beta^2\tilde{u}\right). \tag{4.46}$$

$$U_B\frac{\partial \tilde{v}}{\partial x} + \tilde{u}\frac{\partial U_B}{\partial x} + V_B\frac{\partial \tilde{u}}{\partial y} + \tilde{v}\frac{\partial U_B}{\partial y} + \mathrm{i}W_B\beta\tilde{v} = -\frac{1}{\rho}\left(\frac{\partial \tilde{p}}{\partial y}\right) + \nu\left(\frac{\partial^2 \tilde{v}}{\partial x^2} + \frac{\partial^2 \tilde{u}}{\partial y^2} - \beta^2\tilde{v}\right). \tag{4.47}$$

$$U_B\frac{\partial \tilde{w}}{\partial x} + \tilde{w}\frac{\partial U_B}{\partial x} + V_B\frac{\partial \tilde{w}}{\partial y} + \tilde{v}\frac{\partial U_B}{\partial y} + \mathrm{i}W_B\beta\tilde{w} = -\frac{1}{\rho}\left(\frac{\partial \tilde{p}}{\partial z}\right) + \nu\left(\frac{\partial^2 \tilde{w}}{\partial x^2} + \frac{\partial^2 \tilde{w}}{\partial y^2} - \beta^2\tilde{w}\right). \tag{4.48}$$

These equations are fully elliptic. Hence they are not solved as a marching problem. Instead, the solution at all grid points is simultaneously solved by casting the discretized form of the above equations into a matrix form.

An in-house HLNS solver developed at the TU Delft Low Speed Lab is used in this thesis. A uniform discretisation is used in the chordwise direction, and derivatives in this direction are computed using a fourth-order central differencing scheme. Chebyshev polynomials generated using methods proposed by Malik (1990) are used to discretize the equations in y direction, resulting in a non-uniform grid in y direction. The inflow is initialized with an ILST solution. The outflow conditions have to be specified such that unphysical information from the unknown outflow does not propagate backwards. In the Navier Stokes equations, viscous terms and pressure terms allow for the backward propagation of information (Streett & Macaraeg, 1989). Similarly, in the perturbation equations systems, perturbation pressure and viscous terms can enhance the backward propagation of information from the outflow boundary. These terms are damped out by applying a buffer (Joslin, 1992) to the chordwise and spanwise perturbation velocities. The wall-normal perturbation velocity and pressure perturbation are also automatically attenuated by means of the continuity equation. The buffer region stretches from 90% of the domain length to the end of the domain. The no-slip condition is satisfied at the wall, whereas the perturbations are forced to damp down to 0 in the freestream. The discretized version of Equation 4.45 to Equation 4.48, accounting for boundary conditions and procedures to calculate derivatives are cast into a matrix system, whose solution yields perturbation velocity and pressure.

4.4. Selection of Method to Model Perturbation Evolution

HLNS is the best-suited method for modelling perturbation evolution through regions of base flow deformation, given that larger wall-normal velocity and streamwise gradients can be expected compared to the clean case. To prove the above statement, the results of ILST, PSE and HLNS are compared when the ILST mode specified in Section 4.1 is initialized upstream of the base flow deformation. The domain (refer Section 4.1) and grid (refer Section 4.5), and are consistent for all methods. The results of amplitude evolution of $|\tilde{u}|$ at its peak ($A_{|\tilde{u}|}$) evaluated using ILST, PSE and HLNS are presented in Figure 4.5 comparing the clean case with the $-2.5p_f\ 30w$ case. For the clean case, HLNS and PSE amplitude evolution show good agreement with each other, but ILST underpredicts amplitude growth compared to these approaches due to its inability to correctly capture perturbation growth rate in weak non-parallel flows like the clean case (Bippes, 1999). For the deformed case, PSE and HLNS amplitude evolution show similar behaviour, but PSE underpredicts amplitude compared to the HLNS. Although the exact reasons for HLNS and PSE amplitude mismatch are hard to pinpoint, an attempt is made to list out potential reasons. It is known that the PSE assumes streamwise variation of flow to be small over disturbance wavelength (Franco et al., 1821). However, streamwise changes in deformed base flow occur at the order of the mean chordwise wavelength of the clean case ($\approx 11\delta_0$), potentially leading to deviation from HLNS results. Also, the effects of ellipticity are neglected in the PSE, which could contribute to differences with respect to the HLNS solution. ILST amplitude evolution trends show some similarity with respect to HLNS and PSE amplitude evolution trends, with a reduction in amplitude growth evident in the vicinity of $x_{st}/\delta_0 = 0$, but underpredicts amplitude evolution to a large extent. Thus, HLNS is selected as the method for all perturbation simulations conducted in this thesis. However, comparison with results of PSE and ILST feature in the discussion of modified modal behaviour in Section 6.4, where the ILST solution, despite chances of being a very idealized representation of perturbation behaviour in the region of rapid base flow deformation, is assumed to be representative of local modal behaviour.

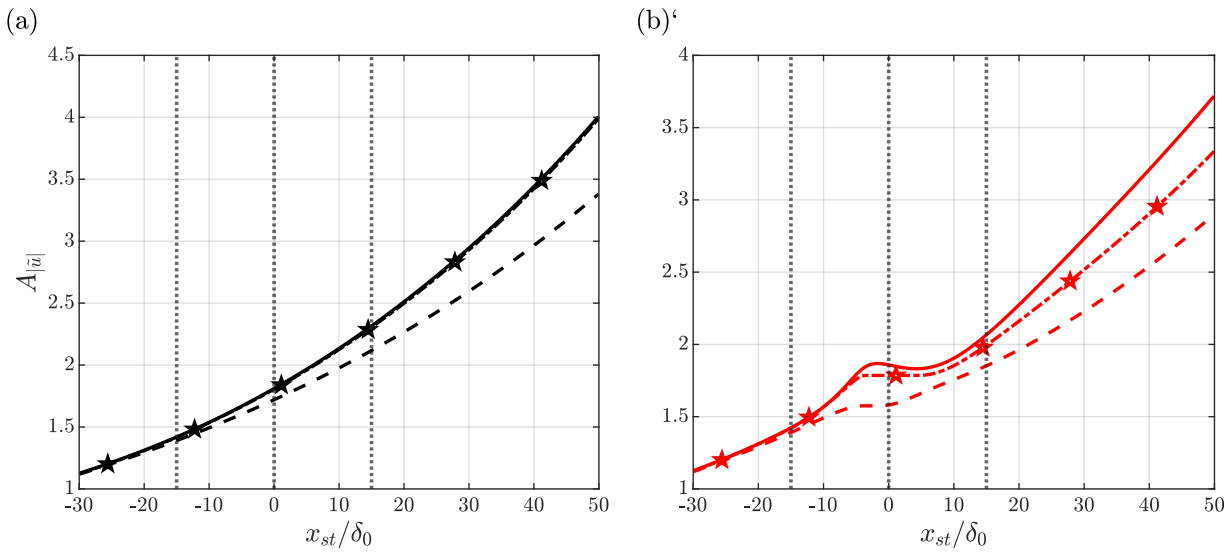

Figure 4.5: Amplitude evolution of u' perturbation in (a) clean case and (b) $-2.5p_f\ 30w$ case, where perturbation evolution is calculated using ILST (dashed), PSE (dash-dotted with stars), and HLNS (solid); black dotted lines at $x_{st}/\delta_0 = -w/2,\ 0,$ and $w/2$ show the region of ΔP imposition.

4.5. Grid for Selected Method

The grid for perturbation analysis has 1500 uniform divisions in x direction and 100 non-uniform divisions in y, such that half the points are placed beneath $y/\delta_0 = 0.2$. The base flow is interpolated onto the perturbation analysis grid before the perturbation equations are solved. To ensure that perturbation behaviour does not change with the grid considered, the number of x and y elements are varied one at a time, testing one grid of lower resolution and one grid of higher resolution. The amplitude evolution of u' perturbation and its shape function at four different locations are evaluated for these grids to present that changing the grid does not influence results. For x-refinement, grids with 1200, 1500 and 1800 divisions are tested, and the results of u' amplitude evolution for a reference deformed case ($-2.5p_f\ 30w$) are shown in Figure 4.6, and u' shape at four different locations are shown in Figure 4.7. The results do not change with the change of grid. Results of refinement in y show similar trends and are attached in Appendix B.5. Thus, the results obtained are not influenced by the grid.

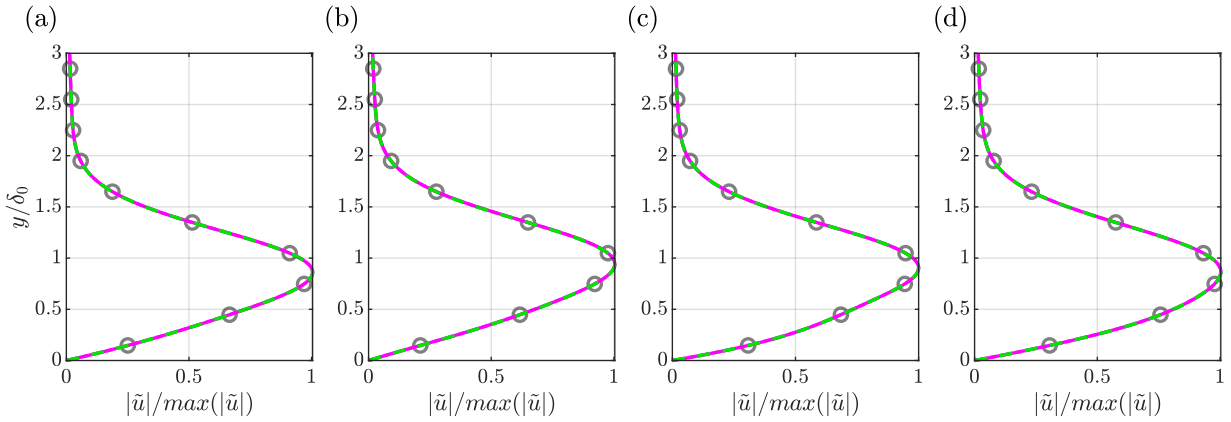

Figure 4.6: Plot of wall-normal variation of normalized amplitude function of u' in $-2.5p_f$ $30w$ case at x_{st}/δ_0 = (a) $-0.6w$, (b) $-0.25w$, (c) $0.25w$, and (d) $0.6w$ when N_x = 1200 (grey circles), 1500 (light green solid), and 1800 (magenta dashed).

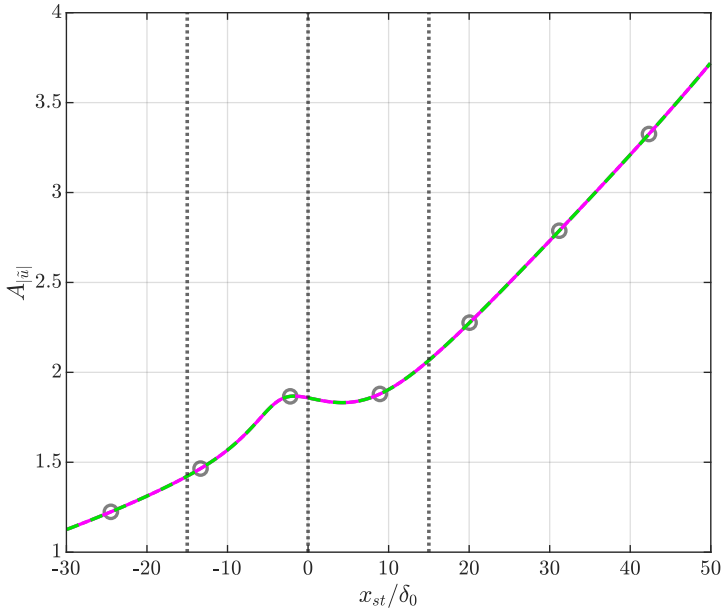

Figure 4.7: Plot of chordwise variation of $|\tilde{u}|$ amplitude in $-2.5p_f$ $30w$ case when N_x = 1200 (grey circles), 1500 (light green solid), and 1800 (magenta dashed); black dotted lines at $x_{st}/\delta_0 = -w/2,\ 0,$ and $w/2$ show the region of ΔP imposition.

5

Mathematical Framework to Explain Perturbation Behaviour

The previous chapter addressed methods to identify unstable modes and monitor their evolution. This would provide the result of perturbation amplitude evolution in rapidly deformed boundary layers. However, there exists a vacuum in literature wherein mechanisms to explain trends of amplitude evolution of stationary crossflow instability in rapidly deformed boundary layers are still unclear, especially evident for a base flow deformed by an FFS (as explained in Section 1.8). There appears to be an attempt to correlate growth to the existence of more than one inflection point (Eppink, 2020). This theory appears correlational in nature, and seem better applicable in a LST sense, where inflection points give rise to inviscid instabilities (Rayleigh, 1879). Casacuberta, Hickel, Westerbeek, and Kotsonis (2022) find that correlation of instability growth with crossflow enhancement also does not exist, showing that directional profiles approximately aligned with the crossflow direction in clean case (Mack, 1984; Bippes, 1999), probably do not govern instability evolution in deformed boundary layers. This provides impetus to develop a spatial Reynolds-Orr framework to understand the mechanisms by which perturbations gain or lose energy on interacting with a rapidly deformed base flow. The observation of non-modal effects by Casacuberta, Hickel, Westerbeek, and Kotsonis (2022) in their FFS cases motivates a section on identifying mechanisms and criteria to check if the incoming mode has a tendency to deviate from modal behaviour on interacting with a deformed boundary layer. The analysis remains in the linear framework throughout this section as the scope of this thesis is limited to studying linear perturbation evolution (refer Section 1.8).

5.1. Development of Spatial Reynolds-Orr Analysis

Reynolds-Orr equations are frequently used to study the evolution of 3D perturbations in 2D base flows using temporal framework (Albensoeder et al., 2001), spatial framework (Karp & Hack, 2018), and spatio-temporal framework (Lanzerstorfer & Kuhlmann, 2012) to explain mechanisms of perturbation growth or decay. However, their usage for stationary crossflow instability evolution in a 3D base flow, using the spatial framework has been limited to the visualization of spanwise integrated production term by Casacuberta, Hickel, Westerbeek, and Kotsonis (2022). Although the production term could be indicative of mechanisms by which a perturbation gains or loses energy, it is necessary to derive a full energy budget wherein energy growth in space can be related to the production term, to be sure that the production term is the main term differentiating perturbation growth or decay. Thus, a derivation for the spanwise integrated Reynolds-Orr equation is provided, which is valid in linear regimes of chordwise growing and spanwise periodic perturbations, which can be extended in the future to non-linear regimes. This is followed by the identification of potentially dominant terms, and a decomposition to explain which terms could be more relevant than others.

5.1.1. Preliminary Energy Balance Equation

The spatial momentum equations (Equation 4.6) are rearranged to obtain

$$-\frac{\partial U_{B,k}}{\partial x_j}u'_j - U_{B,j}\frac{\partial u'_k}{\partial x_j} - \nu\left(\frac{\partial^2 u'_k}{\partial x_j^2}\right) + \frac{\partial p'}{\partial x_k} = 0, \tag{5.1}$$

where the index j reads summation over all $j = 1$, 2, and 3 while index k indicates individual components considered one at a time. Another index l is also introduced further down the current section which behaves the same way as k.

Since perturbation energy is a real-valued quantity, the full HLNS ansatz of u'_k (Equation 4.9) is rewritten considering real-valued contributions from u', v' and w', thus requiring a summation of Fourier modes (0,1) and (0,-1) (the first index in brackets indicates ω while the second indicates β, and the (0,1) mode is also called fundamental mode). Decomposing the real-valued u'_k into a xy dependency and a periodic z dependency, the "basic ansatz" can be obtained as

$$u'_k = u'_{k,(0,1)} + u'_{k,(0,-1)} = \tilde{u}_k\, e^{\mathrm{i}\beta z} + \tilde{u}_k^{\dagger}\, e^{-\mathrm{i}\beta z} = \tilde{u}_k\, e^{\mathrm{i}\beta z} + \text{c.c.}. \tag{5.2}$$

The xy dependency of perturbations, $\tilde{u}_k$ (Equation 5.2) can be further simplified into amplitude function and phase dependent parts as $\tilde{u}_k = |\tilde{u}_k| e^{\mathrm{i}\phi_k}$. Substituting this formulation of xy dependency into the ansatz for real u'_k (Equation 5.2), the "resolved ansatz" can be obtained as

$$u'_k = |\tilde{u}_k| e^{\mathrm{i}(\phi_k + \beta z)} + \text{c.c.}. \tag{5.3}$$

The same basic ansatz and resolved ansatz apply for perturbation pressure, and hence the process is not repeated here.

The basic ansatz (Equation 5.2) can be substituted into the perturbation momentum equation (Equation 5.1), and the exponential dependence in spanwise direction can be factored out to obtain a compact version of the momentum equation which reads

$$\left(\mathcal{A}^{\mathcal{I}}{}_{k,(0,1)} + \mathcal{A}^{\mathcal{II}}{}_{k,(0,1)} + \mathcal{F}^{p}{}_{k,(0,1)} + \mathcal{F}^{\upsilon}{}_{k,(0,1)}\right) e^{\mathrm{i}\beta z} + \left(\mathcal{A}^{\mathcal{I}}{}_{k,(0,-1)} + \mathcal{A}^{\mathcal{II}}{}_{k,(0,-1)} + \mathcal{F}^{p}{}_{k,(0,-1)} + \mathcal{F}^{\upsilon}{}_{k,(0,-1)}\right) e^{-\mathrm{i}\beta z} = 0, \tag{5.4}$$

where

$$\mathcal{A}^{\mathcal{I}}{}_{k,(0,1)} = -\frac{\partial U_{B,k}}{\partial x_j}\tilde{u}_j, \tag{5.5}$$

$$\mathcal{A}^{\mathcal{II}}{}_{k,(0,1)} = -\left(U_B \frac{\partial \tilde{u}_k}{\partial x} + V_B \frac{\partial \tilde{u}_k}{\partial y} + W_B \mathrm{i}\beta \tilde{u}_k\right), \tag{5.6}$$

$$\mathcal{F}^{\nu}{}_{k,(0,1)} = -\nu\left(\frac{\partial^2 \tilde{u}_k}{\partial x^2} + \frac{\partial^2 \tilde{u}_k}{\partial y^2} - \tilde{u}_k \beta^2\right), \tag{5.7}$$

$$\mathcal{F}^{p}{}_{1,(0,1)} = \frac{\partial \tilde{p}}{\partial x},\ \mathcal{F}^{p}{}_{2,(0,1)} = \frac{\partial \tilde{p}}{\partial y},\ \mathcal{F}^{p}{}_{3,(0,1)} = \mathrm{i}\beta\tilde{p}. \tag{5.8}$$

Here, $\mathcal{A}^{\mathcal{I}}{}_{k,(0,1)}$ corresponds to the influence of base flow derivatives, $\mathcal{A}^{\mathcal{II}}{}_{k,(0,1)}$ corresponds to the advection of perturbation by base flow, $\mathcal{F}^{\upsilon}{}_{k,(0,1)}$ corresponds to viscous terms and $\mathcal{F}^{p}{}_{1,(0,1)}$ corresponds to influence of perturbation pressure. Noting that the second half of Equation 5.4 is the complex conjugate of the first half, Equation 5.4 can be simplified to

$$\left(\mathcal{A}^{\mathcal{I}}{}_{k,(0,1)} + \mathcal{A}^{\mathcal{II}}{}_{k,(0,1)} + \mathcal{F}^{p}{}_{k,(0,1)} + \mathcal{F}^{\upsilon}{}_{k,(0,1)}\right) e^{\mathrm{i}\beta z} + \text{c.c.} = 0. \tag{5.9}$$

To obtain the evolution equation for perturbation energy contained in each component k, the momentum equation (Equation 5.9) is multiplied by $\tilde{u}_k$ to obtain

$$\left(\tilde{u}_k\, e^{\mathrm{i}\beta z} + \tilde{u}_k^{\dagger}\, e^{-\mathrm{i}\beta z}\right)\left(\mathcal{A}^{\mathcal{I}}{}_{k,(0,1)} + \mathcal{A}^{\mathcal{II}}{}_{k,(0,1)} + \mathcal{F}^{p}{}_{k,(0,1)} + \mathcal{F}^{\upsilon}{}_{k,(0,1)}\right) e^{\mathrm{i}\beta z} + \text{c.c.} = 0. \tag{5.10}$$

Interest is restricted to observing the behaviour of these equations in xy planes so as to capture any energy growth in the chordwise direction. Thus, any spanwise dependencies in the perturbation energy equation (Equation 5.10) can be removed by integrating in the spanwise direction over an interval 0 to $2\pi/\beta$ (corresponding to one spanwise wavelength) to yield

$$\begin{aligned}\int_0^{2\pi/\beta} \left(\left(\left(\tilde{u}_k\, e^{\mathrm{i}\beta z} + \tilde{u}_k^{\dagger}\, e^{-\mathrm{i}\beta z}\right)\left(\mathcal{A}^{\mathcal{I}}{}_{k,(0,1)} + \mathcal{A}^{\mathcal{II}}{}_{k,(0,1)} + \mathcal{F}^{p}{}_{k,(0,1)} + \mathcal{F}^{\upsilon}{}_{k,(0,1)}\right) e^{\mathrm{i}\beta z}\right)\right) dz\ + \\ \int_0^{2\pi/\beta} \left(\left(\left(\tilde{u}_k\, e^{\mathrm{i}\beta z} + \tilde{u}_k^{\dagger}\, e^{-\mathrm{i}\beta z}\right)\left(\mathcal{A}^{\mathcal{I}}{}_{k,(0,-1)} + \mathcal{A}^{\mathcal{II}}{}_{k,(0,-1)} + \mathcal{F}^{p}{}_{k,(0,-1)} + \mathcal{F}^{\upsilon}{}_{k,(0,-1)}\right) e^{-\mathrm{i}\beta z}\right)\right) dz = 0.\end{aligned} \tag{5.11}$$

Equation 5.11 can be grouped into four parts for further simplification as per

$$T_1 + T_2 + T_3 + T_4 = 0, \tag{5.12}$$

where

$$T_1 = \left(\tilde{u}_k (\mathcal{A}^{\mathcal{I}}{}_{k,(0,1)} + \mathcal{A}^{\mathcal{I}\mathcal{I}}{}_{k,(0,1)} + \mathcal{F}^{p}{}_{k,(0,1)} + \mathcal{F}^{\upsilon}{}_{k,(0,1)}) \right) \int_0^{2\pi/\beta} e^{2\mathrm{i}\beta z} dz, \tag{5.13}$$

$$T_2 = \left(\tilde{u}_k^{\dagger} (\mathcal{A}^{\mathcal{I}}{}_{k,(0,1)} + \mathcal{A}^{\mathcal{I}\mathcal{I}}{}_{k,(0,1)} + \mathcal{F}^{p}{}_{k,(0,1)} + \mathcal{F}^{\upsilon}{}_{k,(0,1)}) \right) \int_0^{2\pi/\beta} dz, \tag{5.14}$$

$$T_3 = \left(\tilde{u}_k (\mathcal{A}^{\mathcal{I}}{}_{k,(0,-1)} + \mathcal{A}^{\mathcal{I}\mathcal{I}}{}_{k,(0,-1)} + \mathcal{F}^{p}{}_{k,(0,-1)} + \mathcal{F}^{\upsilon}{}_{k,(0,-1)}) \right) \int_0^{2\pi/\beta} dz, \tag{5.15}$$

$$T_4 = \left(\tilde{u}_k^{\dagger} (\mathcal{A}^{\mathcal{I}}{}_{k,(0,-1)} + \mathcal{A}^{\mathcal{I}\mathcal{I}}{}_{k,(0,-1)} + \mathcal{F}^{p}{}_{k,(0,-1)} + \mathcal{F}^{\upsilon}{}_{k,(0,-1)}) \right) \int_0^{2\pi/\beta} e^{-2\mathrm{i}\beta z} dz. \tag{5.16}$$

Periodic exponentials of the form $e^{-2\mathrm{i}\beta z}$ and $e^{2\mathrm{i}\beta z}$ are composed of sines and cosines, which on integration from 0 to $2\pi/\beta$ yield 0. The integrals in the above equation thus take the form

$$\int_0^{2\pi/\beta} dz = \frac{2\pi}{\beta}, \ \int_0^{2\pi/\beta} e^{-2\mathrm{i}\beta z} dz = 0, \ \int_0^{2\pi/\beta} e^{2\mathrm{i}\beta z} dz = 0. \tag{5.17}$$

Thus, Equation 5.13 and Equation 5.16 simplify to 0, simplifying Equation 5.11 to

$$T_2 + T_3 = 0, \tag{5.18}$$

$$\frac{2\pi}{\beta} \left(\tilde{u}_k^{\dagger} (\mathcal{A}^{\mathcal{I}}{}_{k,(0,1)} + \mathcal{A}^{\mathcal{I}\mathcal{I}}{}_{k,(0,1)} + \mathcal{F}^{p}{}_{k,(0,1)} + \mathcal{F}^{\upsilon}{}_{k,(0,1)}) + \tilde{u}_k (\mathcal{A}^{\mathcal{I}}{}_{k,(0,-1)} + \mathcal{A}^{\mathcal{I}\mathcal{I}}{}_{k,(0,-1)} + \mathcal{F}^{p}{}_{k,(0,-1)} + \mathcal{F}^{\upsilon}{}_{k,(0,-1)}) \right) = 0. \tag{5.19}$$

Equation 5.19 can be decomposed into four terms accounting for production ($\mathcal{P}_k$), transport ($\mathcal{T}_k$), work of viscous forces ($\mathcal{D}_k$) and pressure work ($\mathcal{W}_k$)

$$\mathcal{P}_k + \mathcal{T}_k + \mathcal{D}_k + \mathcal{W}_k = 0, \tag{5.20}$$

$$\mathcal{P}_k = \frac{2\pi}{\beta} \left(\tilde{u}_k^{\dagger} \mathcal{A}^{\mathcal{I}}{}_{k,(0,1)} + \tilde{u}_k \mathcal{A}^{\mathcal{I}}{}_{k,(0,-1)} \right) = \frac{2\pi}{\beta} \tilde{u}_k^{\dagger} \mathcal{A}^{\mathcal{I}}{}_{k,(0,1)} + \text{c.c.}, \tag{5.21}$$

$$\mathcal{T}_k = \frac{2\pi}{\beta} \left(\tilde{u}_k^{\dagger} \mathcal{A}^{\mathcal{I}\mathcal{I}}{}_{k,(0,1)} + \tilde{u}_k \mathcal{A}^{\mathcal{I}\mathcal{I}}{}_{k,(0,-1)} \right) = \frac{2\pi}{\beta} \tilde{u}_k^{\dagger} \mathcal{A}^{\mathcal{I}\mathcal{I}}{}_{k,(0,1)} + \text{c.c.}, \tag{5.22}$$

$$\mathcal{D}_k = \frac{2\pi}{\beta} \left(\tilde{u}_k^{\dagger} \mathcal{F}^{\upsilon}{}_{k,(0,1)} + \tilde{u}_k \mathcal{F}^{\upsilon}{}_{k,(0,-1)} \right) = \frac{2\pi}{\beta} \tilde{u}_k^{\dagger} \mathcal{F}^{\upsilon}{}_{k,(0,1)} + \text{c.c.}, \tag{5.23}$$

$$\mathcal{W}_k = \frac{2\pi}{\beta} \left(\tilde{u}_k^{\dagger} \mathcal{F}^{p}{}_{k,(0,1)} + \tilde{u}_k \mathcal{F}^{p}{}_{k,(0,-1)} \right) = \frac{2\pi}{\beta} \tilde{u}_k^{\dagger} \mathcal{F}^{p}{}_{k,(0,1)} + \text{c.c.}. \tag{5.24}$$

This forms the equation of perturbation energy per component. To obtain the equation of total perturbation energy, the terms are summed over x, y and z components to yield

$$\mathcal{P} + \mathcal{T} + \mathcal{D} + \mathcal{W} = \sum_{k=1}^{3} (\mathcal{P}_k + \mathcal{T}_k + \mathcal{D}_k + \mathcal{W}_k) = 0. \tag{5.25}$$

This partially concludes the spatial Reynolds-Orr energy balance of linearized perturbation equations, with Equation 5.25 called the ”preliminary energy balance equation”. Equation 5.25 appears to be an incomplete version of the Reynolds-Orr equation as the energy derivative in the chordwise direction doesn't appear explicitly anywhere in the equation. Further decomposition can be applied to the transport term to obtain this derivative, to bear resemblance to traditional Reynolds-Orr analysis equations, where the energy derivative in space can be isolated, resembling the approach taken by Karp and Hack (2018). Among terms of Equation 5.25, the production term represents kinetic energy exchange with the base flow (Schmid & Henningson, 2001; Casacuberta, Hickel, Westerbeek, & Kotsonis, 2022), and has the potential of being the primary source of perturbation energy gain and loss, thus potentially being capable of differentiating regimes of perturbation growth and stabilization. Hence its decomposition is considered to understand the physical mechanisms that determine the production term's behaviour. Contribution from the work of pressure is expected to be negligible and is not considered further. The work of viscous force term is expected to have a consistent contribution of draining perturbation energy across clean and deformed base flow cases, and is not expected to be a key differentiating factor between perturbation behaviour in clean and deformed base flow cases. Hence, its decomposition is not considered further. Equation 5.25 is verified in Section 6.3.

5.1.2. Production Term Decomposition

To further simplify the production term, the expression of ${\mathcal{A}^{\mathcal{I}}}_{k,(0,1)}$ from Equation 5.5 is substituted into Equation 5.21 to obtain

$$\mathcal{P}_k = \frac{2\pi}{\beta}\left(\tilde{u}_k^{\dagger}\frac{\partial U_{B,k}}{\partial x}\tilde{u} + \tilde{u}_k^{\dagger}\frac{\partial U_{B,k}}{\partial y}\tilde{v}\right) + \text{c.c.}. \tag{5.26}$$

The production term represents the energy exchange between base flow and perturbation components (Casacuberta, Hickel, Westerbeek, & Kotsonis, 2022). The negative sign of the production term indicates a stabilizing influence on perturbation evolution, whereas a positive sign of the production term indicates a destabilizing influence on perturbation evolution (Albensoeder et al., 2001). The base flow affects perturbation stabilization or destabilization via flow deceleration or acceleration captured by its x derivatives or via shear captured by its y derivatives as seen in Equation 5.26. This motivates a decomposition of the production term along x and y derivatives of base flow, which reads

$$\mathcal{P}_k = \frac{2\pi}{\beta}\left(\tilde{u}_k^{\dagger}\frac{\partial U_{B,k}}{\partial x}\tilde{u} + \text{c.c.}\right) + \frac{2\pi}{\beta}\left(\tilde{u}_k^{\dagger}\frac{\partial U_{B,k}}{\partial y}\tilde{v} + \text{c.c.}\right) = \mathcal{P}_{x_d,k} + \mathcal{P}_{y_d,k}, \tag{5.27}$$

where x_d and y_d denote x and y partial derivative contributions respectively. This decomposition reveals competing mechanisms that influence perturbation behaviour. The total Production term is obtained by summing Equation 5.27 from $k = 1$ to 3 to yield

$$\mathcal{P} = \sum_{k=1}^{3} P_k = \sum_{k=1}^{3}\left(\mathcal{P}_{x_d,k} + \mathcal{P}_{y_d,k}\right) = \mathcal{P}_{x_d} + \mathcal{P}_{y_d}, \tag{5.28}$$

where

$$\mathcal{P}_{x_d} = -\frac{2\pi}{\beta}\sum_{k=1}^{3}\tilde{u}_k^{\dagger}\frac{\partial U_{B,k}}{\partial x}\tilde{u} + \text{c.c.}, \tag{5.29}$$

$$\mathcal{P}_{y_d} = -\frac{2\pi}{\beta}\sum_{k=1}^{3}\tilde{u}_k^{\dagger}\frac{\partial U_{B,k}}{\partial y}\tilde{v} + \text{c.c.}. \tag{5.30}$$

The decomposition of production term carried out here bears resemblance to the analysis of Loiseau, Robinet, Cherubini, and Leriche (2014), although they considered a different instability, conducted a temporal analysis, and also had non-negligible base flow derivatives along z direction resulting in extra terms. Explicit expressions of $\mathcal{P}_{x_d}$ and $\mathcal{P}_{y_d}$ can now be elaborated by substituting the resolved ansatz into Equation 5.29 and Equation 5.30 to obtain

$$\tilde{u}_k^{\dagger}\tilde{u}_l + \text{c.c.} = |\tilde{u}_k|e^{-i\phi_k}|\tilde{u}_l|e^{\mathrm{i}\phi_l} + \text{c.c.} = |\tilde{u}_k||\tilde{u}_l|e^{\mathrm{i}(\phi_l-\phi_k)} + \text{c.c.} = 2|\tilde{u}_k||\tilde{u}_l|\cos(\phi_l-\phi_k), \tag{5.31}$$

$$\mathcal{P}_{x_d} = \sum_{k=1}^{3}\left(\mathcal{P}_{x_d,k}\right) = -\frac{4\pi}{\beta}\left(|\tilde{u}|^2\frac{\partial U_B}{\partial x} + |\tilde{v}||\tilde{u}|\frac{\partial V_B}{\partial x}\cos(\phi_1-\phi_2) + |\tilde{w}||\tilde{u}|\frac{\partial W_B}{\partial x}\cos(\phi_1-\phi_3)\right), \tag{5.32}$$

$$\mathcal{P}_{y_d} = \sum_{k=1}^{3}\left(\mathcal{P}_{y_d,k}\right) = -\frac{4\pi}{\beta}\left(|\tilde{u}||\tilde{v}|\frac{\partial U_B}{\partial y}\cos(\phi_2-\phi_1) + |\tilde{v}|^2\frac{\partial V_B}{\partial y} + |\tilde{w}||\tilde{v}|\frac{\partial W_B}{\partial y}\cos(\phi_2-\phi_3)\right). \tag{5.33}$$

To elaborate the physical understanding of $\mathcal{P}_{x_d}$, the behaviour of $\mathcal{P}_{x_d,1}$ is considered. A positive sign of $\mathcal{P}_{x_d,1}$ represents the transfer of energy to chordwise perturbation when the chordwise base flow decelerates. Considering the total flow, it appears as if the chordwise perturbation component compensates for the energy not needed anymore by the chordwise base flow component due to the continual decrease of chordwise base flow velocity in the chordwise direction. The opposite scenario occurs when the chordwise base flow accelerates, where the chordwise perturbation has the potential to lose energy. Considering the total flow, it appears as though some energy is taken away from the perturbation component to compensate for the acceleration of the base flow component. $\mathcal{P}_{x_d,2}$ is possibly negligible compared to $\mathcal{P}_{x_d,1}$ and $\mathcal{P}_{x_d,3}$ terms as $\partial V_B/\partial x = O(\delta) << \partial U_B/\partial x = O(1)$, and $|\tilde{v}| << |\tilde{u}|$. $\mathcal{P}_{x_d,3}$ has potential of being similar order of $\mathcal{P}_{x_d,1}$, but the value of $\cos(\phi_1-\phi_3)$ could influence the behaviour of $\mathcal{P}_{x_d,3}$. Similarities and differences between the behaviour of $\mathcal{P}_{x_d,1}$ and $\mathcal{P}_{x_d,3}$ are thus elaborated upon while analyzing results in Section 6.3.1.

On the other hand, the physical understanding of $\mathcal{P}_{y_d}$ can be elaborated upon by observing the behaviour of $\mathcal{P}_{y_d,1}$. $\mathcal{P}_{y_d,1}$ physically represents the transfer of momentum from chordwise base flow by wall-normal perturbation to chordwise perturbation. The sign of energy transfer is determined by $\cos(\phi_2 - \phi_1)$ in a non-separated flow, where U_{B_y} is positive throughout. Three scenarios can be considered to understand the effects of signs. The first is $\phi_2 - \phi_1 = \pi$, which represents a positive sign of $\mathcal{P}_{y_d,1}$, which represents the potential for perturbation destabilization as per the scenario shown in Figure 5.1 (a). This represents the scenario where v' brings high momentum base flow downwards to the peak of u', and low momentum base flow upwards to the valley of u'. This results in a constructive interference, such that u' peaks and valleys grow larger, representing the potential for u' to gain energy. The second scenario is $\phi_2 - \phi_1 = 0$ corresponding to v' bringing high chordwise momentum to regions of valleys of u', and low chordwise momentum to regions of peaks of u'. This represents a destructive interference, where u' potentially loses energy and stabilizes as a result, as shown in Figure 5.1 (b). The third scenario corresponds to $\phi_2 - \phi_1 = \pi/2$. Here, the cosine gives a zero value, completely inhibiting the transfer of momentum from base flow to u', as shown in Figure 5.1 (c). $\mathcal{P}_{y_d,2}$ is possibly negligible owing to $\partial V_B/\partial y = O(1) << \partial U_B/\partial y = O(1/\delta)$, and $|\tilde{v}| << |\tilde{u}|$. $\mathcal{P}_{y_d,3}$ has a similar physical interpretation as $\mathcal{P}_{y_d,1}$, wherein v' transfers spanwise base flow momentum to w', resulting in constructive or destructive difference based on phase interference between v' and w' perturbations.

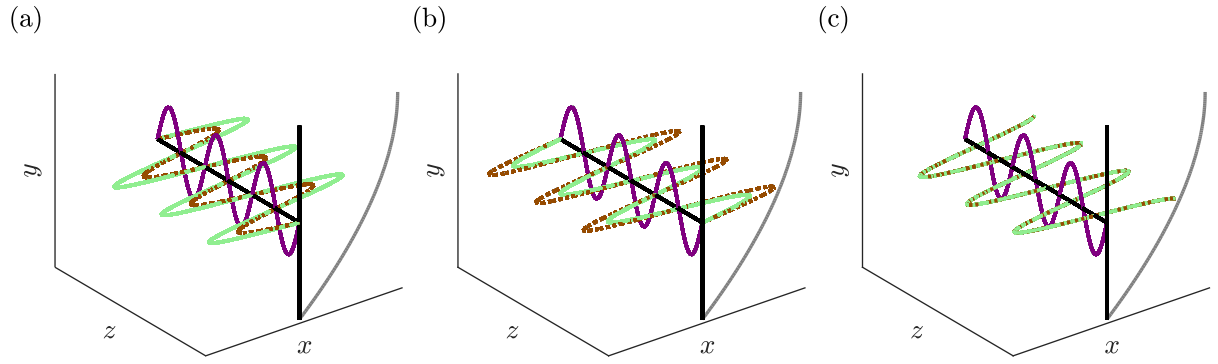

Figure 5.1: Demonstration of v' (purple) transferring momentum from base flow profile (grey) to initial u' (brown dash-dotted) resulting in a new u' profile (green) which (a) increases ($\phi_2 - \phi_1 = \pi$) (b) decreases ($\phi_2 - \phi_1 = 0$), and (c) remains same ($\phi_2 - \phi_1 = \pi/2$) relative to initial u'.

5.1.3. Transport Term Decomposition

The transport term $\mathcal{T}_k$ can be further simplified by first simplifying the expression for ${\mathcal{A}^{\mathcal{II}}}_{k,(0,1)}$. This is done by substituting the resolved ansatz (Equation 5.3) into the expression for ${\mathcal{A}^{\mathcal{II}}}_{k,(0,1)}$ (Equation 5.6) and applying the differentiation chain rule to obtain

$$\frac{\partial \tilde{u}_k}{\partial x_l} = \frac{\partial |\tilde{u}_k| e^{\mathrm{i}\phi_k}}{\partial x_l} = \frac{\partial |\tilde{u}_k|}{\partial x_l} e^{\mathrm{i}\phi_k} + |\tilde{u}_k| \frac{\partial e^{\mathrm{i}\phi_k}}{\partial x_l} = |\tilde{u}_k| e^{\mathrm{i}\phi_k} \left(\frac{1}{|\tilde{u}_k|} \frac{\partial |\tilde{u}_k|}{\partial x_l} + \frac{\partial \phi_k}{\partial x_l} \right) = \tilde{u}_k \left(\frac{1}{|\tilde{u}_k|} \frac{\partial |\tilde{u}_k|}{\partial x_l} + \frac{\partial \phi_k}{\partial x_l}, \right) \tag{5.34}$$

$${\mathcal{A}^{\mathcal{II}}}_{k,(0,1)} = -\tilde{u}_k \left(\frac{U_B}{|\tilde{u}_k|} \frac{\partial |\tilde{u}_k|}{\partial x} + \frac{V_B}{|\tilde{u}_k|} \frac{\partial |\tilde{u}_k|}{\partial y} + \mathrm{i} \left(U_B \frac{\partial \phi_k}{\partial x} + V_B \frac{\partial \phi_k}{\partial y} + W_B \beta \right) \right). \tag{5.35}$$

When this expression of ${\mathcal{A}^{\mathcal{II}}}_{k,(0,1)}$ is substituted into the definition of $\mathcal{T}_k$ (Equation 5.22), the resulting expression is obtained as

$$\tilde{u}_k^\dagger {\mathcal{A}^{\mathcal{II}}}_{k,(0,1)} = -|\tilde{u}_k|^2 \left(\frac{U_B}{|\tilde{u}_k|} \frac{\partial |\tilde{u}_k|}{\partial x} + \frac{V_B}{|\tilde{u}_k|} \frac{\partial |\tilde{u}_k|}{\partial y} + \mathrm{i} \left(U_B \frac{\partial \phi_k}{\partial x} + V_B \frac{\partial \phi_k}{\partial y} + W_B \beta \right) \right), \tag{5.36}$$

$$\mathcal{T}_k = \frac{2\pi}{\beta} \tilde{u}_k^\dagger {\mathcal{A}^{\mathcal{II}}}_{k,(0,1)} + \text{c.c.} = -\frac{4\pi}{\beta} \left(U_B |\tilde{u}_k| \frac{\partial |\tilde{u}_k|}{\partial x} + V_B |\tilde{u}_k| \frac{\partial |\tilde{u}_k|}{\partial x} \right) = -\frac{2\pi}{\beta} \left(U_B \frac{\partial \tilde{E}_k}{\partial x} + V_B \frac{\partial \tilde{E}_k}{\partial y} \right), \tag{5.37}$$

where $\tilde{E}_k$ corresponds to energy contained in each perturbation component $\tilde{u}_k$.

$$\tilde{E}_k = \frac{\tilde{u}_k^2}{2}. \tag{5.38}$$

The transport term physically represents the advection of perturbation energy by the base flow. $\partial\tilde{E}_k/\partial x$ captures growth of perturbation energy per component in the x direction, while $\partial\tilde{E}_k/\partial y$ captures the shear of perturbation energy per component. The total perturbation energy and transport term is obtained by summing over x, y and z contributions to yield

$$\tilde{E} = \frac{1}{2}\sum_{k=1}^{3}|\tilde{u}_k|^2 = \frac{1}{2}\left(|\tilde{u}|^2 + |\tilde{v}|^2 + |\tilde{w}|^2\right) \tag{5.39}$$

$$\mathcal{T} = -\frac{2\pi}{\beta}\sum_{k=1}^{3}\left(U_B|\tilde{u}_k|\frac{\partial|\tilde{u}_k|}{\partial x} + V_B|\tilde{u}_k|\frac{\partial|\tilde{u}_k|}{\partial x}\right) = -\frac{2\pi}{\beta}\left(U_B\frac{\partial\tilde{E}}{\partial x} + V_B\frac{\partial\tilde{E}}{\partial y}\right) \tag{5.40}$$

5.1.4. Final Energy Balance Equation

The final equation for perturbation energy per component can be obtained by substituting the expressions of transport and production terms into Equation 5.20 to obtain

$$\mathcal{P}_{x_d,k} + \mathcal{P}_{y_d,k} - \frac{2\pi}{\beta}\left(U_B\frac{\partial\tilde{E}_k}{\partial x} + V_B\frac{\partial\tilde{E}_k}{\partial y}\right) + \mathcal{D}_k + \mathcal{W}_k = 0. \tag{5.41}$$

Now, the final equation of perturbation energy can be obtained by summing Equation 5.41 over x, y and z components, which reads

$$\mathcal{P}_{x_d} + \mathcal{P}_{y_d} - \frac{2\pi}{\beta}\left(U_B\frac{\partial\tilde{E}}{\partial x} + V_B\frac{\partial\tilde{E}}{\partial y}\right) + \mathcal{D} + \mathcal{W} = 0. \tag{5.42}$$

To obtain a traditional representation of the Reynolds-Orr equation, isolating the spatial perturbation energy derivative to one side along the lines of Karp and Hack (2018), Equation 5.41 and Equation 5.42 are manipulated to obtain

$$\frac{\partial\tilde{E}_k}{\partial x} = \frac{1}{U_B}\left(-V_B\frac{\partial\tilde{E}_k}{\partial y} + \frac{\beta}{2\pi}(\mathcal{P}_{x_d,k} + \mathcal{P}_{y_d,k}) + \frac{\beta}{2\pi}(\mathcal{D}_k + \mathcal{W}_k)\right), \tag{5.43}$$

$$\frac{\partial\tilde{E}}{\partial x} = \frac{1}{U_B}\left(-V_B\frac{\partial\tilde{E}}{\partial y} + \frac{\beta}{2\pi}(\mathcal{P}_{x_d} + \mathcal{P}_{y_d}) + \frac{\beta}{2\pi}(\mathcal{D} + \mathcal{W})\right). \tag{5.44}$$

Perturbation energy growth ($\tilde{E}_x$) is isolated on the left-hand side of Equation 5.44, and the factors affecting it are presented on the right-hand side of Equation 5.44 (also referred as "final energy balance equation"). The production term acts as a source term in Equation 5.44, and is most likely the driving mechanism for perturbation stabilization or destabilization in case pressure work is negligible and work of viscous forces consistently drains perturbation energy across all cases. However, it is important to note that $-V_B\tilde{E}_y$ also exists in Equation 5.44. This can be responsible for perturbation energy advection in the wall-normal direction, such that perturbation energy growth does not directly mimic the effects of the production term, even when the pressure work and the work of viscous forces are less important. The connection of energy growth with production term and the role of $-V_B\tilde{E}_y$ are elaborated upon later in Section 6.3.2. It should be noted that a per-component and total perturbation energy analysis have both been presented here so that either one can be used to elaborate perturbation behaviour depending on whether single component behaviour or perturbation energy behaviour are selected for studying instability evolution (elaborated upon in Section 6.2).

5.2. Modified modal behaviour

As specified in Section 1.7.3, a rapidly changing base flow in the FFS has the potential to modify the behaviour of an incoming mode, such that the usually destabilizing lift-up effect in modal clean case evolution changes character, and criteria in literature indicate the presence of base flow deformed non-modal effects. There is a chance that such effects dictate instability evolution in base flow deformed cases considered in this thesis, and might represent changes with respect to clean case modal evolution. This could hint towards a deviation from modal character and the potential presence of base flow deformed non-modality. In this section, deviation from modal character is examined through the perspective of mechanisms relevant to initial condition driven non-modality, i.e. the lift-up effect and Orr mechanism. Methods to identify these mechanisms are first presented, and their potential to explain the deviation from clean case modal behaviour is examined. The local ILST solution is more representative of local modal behaviour than the behaviour of the clean case. Hence, pointers on comparing the HLNS results and ILST results through the perspective of these mechanisms are then presented. Dissimilar behaviour of the HLNS and ILST solutions in deformed cases from the mechanism perspective would hint towards deviation from local modal behaviour. In case evidence of such deviations is found, criteria are presented that can test the presence of base flow deformed non-modality.

5.2.1. Mechanisms

Lift-up effect

As stated in Section 1.7.3. the lift-up effect in base flow deformed cases can be analyzed by decomposing the perturbation into base flow tangential (u'_t) and normal (u'_n) fields, decomposing the production term based on these perturbation fields, and observing the behaviour of the I_2 component (Albensoeder et al., 2001; Lanzerstorfer & Kuhlmann, 2012; Loiseau et al., 2016; Picella et al., 2018; Casacuberta, Hickel, & Kotsonis, 2022). Physically, the base flow tangential field represents streaky structures, whereas the base flow normal field represents counter-rotating rollers (Picella et al., 2018). The I_2 term represents the transport of base flow momentum to streaky structures via counter-rotating rollers (Picella et al., 2018). In the clean case where the wall-normal base flow is negligible, the base flow normal and wall-normal perturbation components can be assumed to be the same, whereas the tangential field is a vector sum of the chordwise and spanwise perturbation fields. However, a deformed base flow is associated with significant values of wall-normal base flow velocity, which tilts the base flow streamlines upwards or downwards, thus implying that the base flow tangential and normal perturbation field are no longer similar to the clean case. Hence, a detailed derivation of base flow tangential and normal perturbation fields adapted from the work of Casacuberta, Hickel, Westerbeek, and Kotsonis (2022) is first considered. The fundamental perturbation field in vector notation is given by

$$\boldsymbol{v}'_{(0,1)} = u'_{(0,1)}\,\hat{\mathbf{i}} + v'_{(0,1)}\,\hat{\mathbf{j}} + w'_{(0,1)}\,\hat{\mathbf{k}}, \tag{5.45}$$

where $\boldsymbol{v}'_{(0,1)}$ is the fundamental total perturbation vector field and $u'_{(0,1)}$, $v'_{(0,1)}$ and $w'_{(0,1)}$ are the complex fundamental perturbation fields in x, y, and z, respectively. $\boldsymbol{v}'_{(0,1)}$ can now be decomposed into a component following the base flow ($\boldsymbol{v}'_{t,(0,1)}$) and another component orthogonal to it ($\boldsymbol{v}'_{n,(0,1)}$) as per

$$\boldsymbol{v}'_{(0,1)} = \boldsymbol{v}'_{t,(0,1)} + \boldsymbol{v}'_{n,(0,1)}. \tag{5.46}$$

The derivation of the base flow tangential perturbation field is first considered, which can be written in terms of a complex-valued perturbation component ($\tau'_{(0,1)}$) and the base flow tangential direction unit vector ($\hat{\mathbf{t}}$) as

$$\boldsymbol{v}'_{t,(0,1)} = \tau'_{(0,1)}\hat{\mathbf{t}}. \tag{5.47}$$

The unit vector aligned along the base flow vector can be obtained as

$$\hat{\mathbf{t}} = \frac{\mathbf{V}_B}{||\mathbf{V}_B||}, \tag{5.48}$$

where $\mathbf{V}_B$ is the vector field of base flow, given by

$$\mathbf{V}_B = U_B\,\hat{\mathbf{i}} + V_B\,\hat{\mathbf{j}} + W_B\,\hat{\mathbf{k}}. \tag{5.49}$$

Now the focus shifts to obtaining $\tau'_{(0,1)}$. The standard expression for projecting vectors onto one another can be used to obtain

$$\tau'_{(0,1)} = \frac{\mathrm{Re}(\boldsymbol{v}'_{(0,1)}) \cdot \mathbf{V}_B}{||\mathbf{V}_B||} + 1\mathrm{i}\frac{\mathrm{Im}(\boldsymbol{v}'_{(0,1)}) \cdot \mathbf{V}_B}{||\mathbf{V}_B||}. \tag{5.50}$$

To write $\tau'_{(0,1)}$ in simpler notation, an operator $\boxtimes$ can be defined such that

$$\boldsymbol{v}'_{(0,1)} \boxtimes \mathbf{V}_B = \mathrm{Re}(\boldsymbol{v}'_{(0,1)}) \cdot \mathbf{V}_B + 1\mathrm{i}\,\mathrm{Im}(\boldsymbol{v}'_{(0,1)}). \tag{5.51}$$

The basic ansatz (Equation 5.2) can be substituted into Equation 5.51 to obtain

$$\boldsymbol{v}'_{(0,1)} \boxtimes \mathbf{V}_B = (\tilde{u}U_B + \tilde{v}V_B + \tilde{w}W_B)e^{\mathrm{i}\beta z} \tag{5.52}$$

The definition presented in Equation 5.52 can be substituted in Equation 5.50 to get a simplified expression for $\tau'_{0,1}$ which reads

$$\tau'_{(0,1)} = \frac{1}{||\mathbf{V}_B||}\left(\boldsymbol{v}'_{(0,1)} \boxtimes \mathbf{V}_B\right) = \frac{\tilde{u}U_B + \tilde{v}V_B + \tilde{w}W_B}{||\mathbf{V}_B||}e^{\mathrm{i}\beta z} = \tilde{\tau}e^{\mathrm{i}\beta z}, \tag{5.53}$$

where $\tilde{\tau}$ is the xy dependency of $\tau'_{(0,1)}$. Now, the final expression for the tangential perturbation field can be obtained by substituting the expressions of $\tau'_{(0,1)}$ (Equation 5.53) and $\hat{\mathbf{t}}$ (Equation 5.48) into Equation 5.47 to obtain

$$\boldsymbol{v}'_{t,(0,1)} = \frac{U_B\tilde{\tau}}{||\mathbf{V_B}||}e^{\mathrm{i}\beta z}\,\hat{\mathbf{i}} + \frac{V_B\tilde{\tau}}{||\mathbf{V_B}||}e^{\mathrm{i}\beta z}\,\hat{\mathbf{j}} + \frac{W_B\tilde{\tau}}{||\mathbf{V_B}||}e^{\mathrm{i}\beta z}\,\hat{\mathbf{k}}. \tag{5.54}$$

Rewriting Equation 5.54 in Einstein convention,

$$u'_{k,t,(0,1)} = \frac{U_{B,k}\tilde{\tau}}{||\mathbf{V_B}||}e^{\mathrm{i}\beta z} = \tilde{u}_{k,t}e^{\mathrm{i}\beta z}, \tag{5.55}$$

where $\tilde{u}_{k,t}$ represents the xy dependency of the k^{th} component of base flow tangential perturbation field.

Subtracting the tangential perturbation vector field from the perturbation vector field yields the normal perturbation vector field, expressed as

$$\boldsymbol{v}'_{n,(0,1)} = \boldsymbol{v}'_{(0,1)} - \boldsymbol{v}'_{t,(0,1)}. \tag{5.56}$$

In Einstein convention, the xy dependency of the k^{th} component of the base flow normal perturbation field can be expressed by cancelling all z dependencies in Equation 5.56 to obtain

$$\tilde{u}_{k,n} = \tilde{u}_k - \tilde{u}_{k,t}. \tag{5.57}$$

This concludes the derivation of base flow normal and tangential perturbation fields.

Now, to decompose the production term to obtain I_2, the expression of $\mathcal{P}$ (Equation 5.28) is rewritten as

$$\mathcal{P} = -\frac{2\pi}{\beta}\sum_{k=1}^{3}\tilde{u}_k^\dagger\frac{\partial U_{B,k}}{\partial x_j}\tilde{u}_j + \text{c.c.}, \tag{5.58}$$

where contributions from $j = 3$ terms are zero due to spanwise derivatives of base flow being zero. $\tilde{u}_k$ can be written as $\tilde{u}_{k,n} + \tilde{u}_{k,t}$ as per Equation 5.57, and substituted into Equation 5.58 to yield another decomposition of the production term which reads

$$\mathcal{P} = I_1 + I_2 + I_3 + I_4, \tag{5.59}$$

where

$$I_1 = -\frac{2\pi}{\beta}\sum_{k=1}^{3}\tilde{u}_{k,n}^\dagger\frac{\partial U_{B,k}}{\partial x_j}\tilde{u}_{j,n} + \text{c.c.} \tag{5.60}$$

$$I_2 = -\frac{2\pi}{\beta}\sum_{k=1}^{3}\tilde{u}_{k,n}^\dagger\frac{\partial U_{B,k}}{\partial x_j}\tilde{u}_{j,t} + \text{c.c.} \tag{5.61}$$

$$I_3 = -\frac{2\pi}{\beta}\sum_{k=1}^{3}\tilde{u}_{k,t}^\dagger\frac{\partial U_{B,k}}{\partial x_j}\tilde{u}_{j,n} + \text{c.c.} \tag{5.62}$$

$$I_4 = -\frac{2\pi}{\beta}\sum_{k=1}^{3}\tilde{u}_{k,t}^\dagger\frac{\partial U_{B,k}}{\partial x_j}\tilde{u}_{j,t} + \text{c.c.} \tag{5.63}$$

The I_2 term represents the lift-up effect. A term-by-term decomposition of I_2 can be conducted to obtain

$$I_2 = -\frac{2\pi}{\beta}\left(\tilde{u}_t^\dagger\frac{\partial U_B}{\partial x}\tilde{u}_n + \tilde{u}_t^\dagger\frac{\partial U_B}{\partial y}\tilde{v}_n + \tilde{v}_t^\dagger\frac{\partial V_B}{\partial x}\tilde{u}_n + \tilde{v}_t^\dagger\frac{\partial V_B}{\partial y}\tilde{v}_n + \tilde{w}_t^\dagger\frac{\partial W_B}{\partial x}\tilde{u}_n + \tilde{w}_t^\dagger\frac{\partial W_B}{\partial y}\tilde{v}_n\right) + \text{c.c.} \tag{5.64}$$

As per observations of Casacuberta, Hickel, and Kotsonis (2022), the second and sixth terms of Equation 5.64 added to their complex conjugates are dominant, and mimic each other's behaviour in the FFS cases. Similarities could be expected in the cases simulated in this thesis, and the signs of these terms can help determine whether the lift-up effect acts destabilizing like the clean case or acts in a stabilizing sense. The second term of Equation 5.64 can be denoted $I_{2,b}$ and expressed as

$$I_{2,b} = -\frac{2\pi}{\beta}\left(\tilde{u}_t^\dagger\frac{\partial U_B}{\partial y}\tilde{v}_n\right) + \text{c.c.} = -\frac{4\pi}{\beta}\frac{\partial U_B}{\partial y}|\tilde{u}_t||\tilde{v}_n|\cos(\phi_{2,n} - \phi_{1,t}). \tag{5.65}$$

Whereas, the sixth term of Equation 5.64 can be denoted $I_{2,f}$ and expressed as

$$I_{2,f} = -\frac{2\pi}{\beta}\left(\tilde{w}_t^\dagger\frac{\partial W_B}{\partial y}\tilde{v}_n\right) + \text{c.c.} = -\frac{4\pi}{\beta}\frac{\partial W_B}{\partial y}|\tilde{w}_t||\tilde{v}_n|\cos(\phi_{2,n} - \phi_{3,t}). \tag{5.66}$$

Signs of $\cos(\phi_{2,n} - \phi_{1,t})$ and $\cos(\phi_{2,n} - \phi_{3,t})$ can thereby reveal the sign of $I_{2,b}$ and $I_{2,f}$, since U_{B_y} and $-W_{B_y}$ are positive throughout. The sign of I_2 can be determined by observing either component if $I_{2,b}$ and $I_{2,f}$ behave similarly as in the cases considered by Casacuberta, Hickel, and Kotsonis (2022). Any stabilization encountered while considering the lift-up effect would be indicative of deviation from modal clean case behaviour. To check whether this translates to deviation from the local modal solution, indicators are provided in Section 5.2.1.

Orr mechanism

In initial condition driven non-modality, the Orr mechanism corresponds to tilting of perturbation streamfunction or vorticity fields to generate growth of perturbation. These effects are easier to explain in 2D flows via the vorticity analogue, where perturbation vorticity in one direction is conserved (Lindzen, 1988), or by expressing the production term in terms of stream function, where the stream function can easily be calculated and perturbation tilt can be related to growth (Butler & Farrell, 1992) (refer Section 1.7.1). Since the evolution of an initially modal 3D perturbation is considered, where all perturbation components grow simultaneously, a constant perturbation vorticity component is impossible to find. The definition of a three-dimensional streamfunction presents significant difficulty, and recasting the production term into streamfunction components is challenging. Thus, instead of choosing either of these approaches, the tilt of the perturbation velocity field is observed, which has been linked to the Orr mechanism by Tempelmann et al. (2010) and Lucas (2014) in the case of three-dimensional initial condition driven non-modality (refer subsection 1.7.1), wherein the downstream streak fields were tilted in an opposite direction to the upstream inviscidly aligned vortex field when observed on the crossflow plane. Instead of choosing the crossflow plane, observations of tilt are conducted in the yz plane, with the assumption that shears would affect tilt in any plane considered. The tilt of perturbation in the yz planes can easily be considered by noting the difference of wall-normal variation of ϕ at various x stations as explained in Section 4.3.1. Contour plots on yz planes can further provide conclusive evidence of this behaviour. Any changes in the tilt of perturbation with a change of spatial location can be potentially linked to the Orr mechanism, with changing base flow shear being a candidate to cause such changes. In this thesis, emphasis is placed on observing the tilt of chordwise perturbation, one of the main contributors to perturbation energy in cases of stationary crossflow instability. A framework can be developed to understand the factors that can influence perturbation tilt, and its potential consequences that can help explain deviation from modal behaviour. The momentum equation is reconsidered as per Equation 4.6, which reads

$$-\frac{\partial U_{B,k}}{\partial x_j}u'_j - U_{B,j}\frac{\partial u'_k}{\partial x_j} - \nu\left(\frac{\partial^2 u'_k}{\partial x_j^2}\right) + \frac{\partial p'}{\partial x_k} = 0. \tag{5.67}$$

Here, the fact that both (0,1) and (0,-1) perturbation simultaneously satisfy the perturbation momentum equation is exploited (as stated in Section 4.3). The basic ansatz of (0,1) perturbation is substituted in Equation 5.1 to yield the first half of the compact version of momentum equation (Equation 5.9) given by

$$\left(\mathcal{A}^{\mathcal{I}}{}_{k,(0,1)} + \mathcal{A}^{\mathcal{I}\mathcal{I}}{}_{k,(0,1)} + \mathcal{F}^{p}{}_{k,(0,1)} + \mathcal{F}^{\upsilon}{}_{k,(0,1)}\right)e^{\mathrm{i}\beta z} = 0. \tag{5.68}$$

Equation 5.68 is now multiplied by the (0,-1) component, following which the spanwise periodic term cancels off yielding

$$\tilde{u}_k^{\dagger}\left(\mathcal{A}^{\mathcal{I}}{}_{k,(0,1)} + \mathcal{A}^{\mathcal{I}\mathcal{I}}{}_{k,(0,1)} + \mathcal{F}^{p}{}_{k,(0,1)} + \mathcal{F}^{\upsilon}{}_{k,(0,1)}\right) = 0. \tag{5.69}$$

Here, $\tilde{u}_k^{\dagger}\mathcal{A}^{\mathcal{I}\mathcal{I}}{}_{k,(0,1)}$ is expanded in more detail by substituting the expression of $\mathcal{A}^{\mathcal{I}\mathcal{I}}{}_{k,(0,1)}$ derived in Equation 5.6 to yield

$$\tilde{u}_k^{\dagger}\mathcal{A}^{\mathcal{I}\mathcal{I}}{}_{k,(0,1)} = -|\tilde{u}_k|^2\left(U_B\frac{1}{|\tilde{u}_k|}\frac{\partial|\tilde{u}_k|}{\partial x} + V_B\frac{1}{|\tilde{u}_k|}\frac{\partial|\tilde{u}_k|}{\partial y} + \mathrm{i}\left(U_B\frac{\partial\phi_k}{\partial x} + V_B\frac{\partial\phi_k}{\partial y} + W_B\beta\right)\right), \tag{5.70}$$

Here, it is noted that the imaginary part of $\tilde{u}_k^{\dagger}\mathcal{A}^{\mathcal{I}\mathcal{I}}{}_{k,(0,1)}$ contains details of the evolution of ϕ_k in chordwise direction. Hence, the aim would now be to take the imaginary parts of each of the terms of Equation 5.69, and obtain an evolution equation for ϕ_k which reads

$$-U_B\frac{\partial\phi_k}{\partial x} - V_B\frac{\partial\phi_k}{\partial y} - W_B\beta + \frac{1}{|\tilde{u}_k|^2}\mathrm{Im}\left(\mathcal{A}^{I}_{k,(0,1)} + \tilde{u}_k^{\dagger}\mathcal{F}^{p}{}_{k,(0,1)} + \tilde{u}_k^{\dagger}\mathcal{F}^{\upsilon}{}_{k,(0,1)}\right) = 0. \tag{5.71}$$

Rearranging Equation 5.71, ϕ_k can be isolated on one side to obtain

$$\frac{\partial\phi_k}{\partial x} = -\frac{W_B}{U_B}\beta - \frac{V_B}{U_B}\frac{\partial\phi_k}{\partial y} + \frac{1}{U_B|\tilde{u}_k|^2}\mathrm{Im}\left(\tilde{u}_k^{\dagger}\mathcal{A}^{I}_{k,(0,1)} + \tilde{u}_k^{\dagger}\mathcal{F}^{p}{}_{k,(0,1)} + \tilde{u}_k^{\dagger}\mathcal{F}^{\upsilon}{}_{k,(0,1)}\right) = 0 \tag{5.72}$$

Now, the focus is placed only on the evolution of ϕ_1. To obtain a more detailed version of the evolution equation for ϕ_1, $\mathrm{Im}(\tilde{u}_1^{\dagger}\mathcal{A}^{I}_{1,(0,1)})$ can be simplified by substituting the expression of $\mathcal{A}^{I}_{1,(0,1)}$ in Equation 5.5 to obtain

$$\mathrm{Im}\Big(\tilde{u}_1^{\dagger}\mathcal{A}^{\mathcal{I}}{}_{1,(0,1)})\Big) = -\mathrm{Im}\left(|\tilde{u}|^2\left(\frac{\partial U_B}{\partial x} + \frac{\partial U_B}{\partial y}\frac{|\tilde{v}|}{|\tilde{u}|}e^{\mathrm{i}(\phi_2-\phi_1)}\right)\right) = -|\tilde{u}|^2\left(\frac{\partial U_B}{\partial y}\frac{|\tilde{v}|}{|\tilde{u}|}\sin(\phi_2-\phi_1)\right), \tag{5.73}$$

The viscous and pressure terms are not simplified further since their detailed analysis doesn't yield simplified terms. Now, substituting Equation 5.73 into Equation 5.71 with $k = 1$ yields

$$\frac{\partial \phi_1}{\partial x} = -\frac{W_B}{U_B}\beta - \frac{V_B}{U_B}\frac{\partial \phi_1}{\partial y} - \frac{\partial U_B}{\partial y}\frac{|\tilde{v}|}{U_B|\tilde{u}|}\sin(\phi_2 - \phi_1) + \frac{1}{U_B|\tilde{u}|^2}\mathrm{Im}\left(\tilde{u}_1^\dagger {\mathcal{F}^p}_{1,(0,1)} + \tilde{u}_1^\dagger {\mathcal{F}^v}_{1,(0,1)}\right) = 0. \tag{5.74}$$

Equation 5.74 is verified in Section 6.4.2. Monitoring ϕ_{1_x} and the terms in its evolution equation at different wall-normal levels can provide insight into why a particular perturbation could tilt differently for different base flows. If the tilt observed at various x stations is similar, it implies that ϕ_{1_x} remains constant across any wall-normal level considered. Equation 5.74 evaluated at different wall-normal levels would then yield an understanding of what terms help keep ϕ_{1_x} the same at different levels, revealing reasons for nearly constant perturbation tilt. Since ϕ_{1_x} determines the angle a xz line of constant phase makes with the x axis (as shown in subsection 4.3.1), its constant value across different wall-normal levels would imply that a single xz line of constant phase is representative for the entire u' perturbation field (refer subsection 4.3.1). A wavenumber vector direction can be identified in such cases, perpendicular to the representative line of constant phase. The lines of constant phase in traditional modal evolution would lie within degrees of the inviscid streamline (Bippes, 1999). However, if the tilt of ϕ_1 were to rapidly change with the change of x station, ϕ_{1_x} would vary with wall-normal height. Equation 5.74 evaluated at different wall-normal levels would then yield an understanding of what terms potentially force different values of ϕ_{1_x} at different levels, forcing the perturbation to tilt differently at different x stations. If ϕ_{1_x} is not found to be similar at different levels, there is no single representative line of constant phase (refer subsection 4.3.1), which raises doubts about the existence of a wavenumber direction in such a scenario. This would potentially indicate a deviation from modal behaviour.

Thus, if the tilt of u' changes with the change of x location, and a single representative line of constant phase can't be defined, it is counted as a manifestation of the Orr mechanism, deviating from traditionally observed modal behaviour of the identification of one representative line of constant phase perpendicular to wavenumber vector. The presence of a base flow shear term influencing perturbation tilt ratifies the link to the Orr mechanism since its manifestation in initial condition driven non-modality entails the tilting of perturbation under the influence of base flow shear (Section 1.7.1). There is also a similarity between the shear term and $\mathcal{P}_{y_d,1}/(U_B|\tilde{u}|^2)$, where the sine and cosine are interchanged, which shows that the identification of the Orr mechanism might have some indirect influence on energy exchange mechanisms between base flow and perturbation. This lead is however not considered further.

Comparison between ILST and HLNS results

The potential observation of stabilized lift-up effect in deformed cases and its comparison with the destabilizing tendency of the lift-up effect in the clean case might not provide sufficient evidence of deviation from modal behaviour. In a regime of rapid deformation, the underlying change of base flow might change the behaviour of the local crossflow mode, which could deviate from the behaviour of a clean case crossflow mode. Although it is challenging to define a local mode in deformed base flow, an ILST solution is considered to be an approximation of local modal behaviour. ILST solutions neglect streamwise derivatives and wall-normal velocity, which significantly affect perturbation behaviour in deformed base flow, and could lead to the different behaviour of the lift-up effect compared to the more accurate description of the HLNS solution. However, the aim here is not to check how accurate or inaccurate the ILST solution is, but instead to find if the lift-up effect observed through an ILST solution varies in stabilizing or destabilizing character from the HLNS solution. If for instance, I_2 computed using the HLNS and ILST solutions both provide a stabilizing influence, the stabilizing observation of the lift-up effect would not correspond to a deviation from locally observed modal behaviour. Whereas, if I_2 computed for HLNS provides a stabilizing influence when the I_2 computed for ILST provides a destabilizing influence, this can be counted as a deviation from locally observed modal behaviour.

The computation of I_2 for ILST requires casting the ILST ansatz Equation 4.7 back into the HLNS ansatz Equation 4.9. This involves removing the z influences and equating the rest of the ILST ansatz to $\tilde{u}_k$ to yield

$$\tilde{u}_k = \hat{u}_k(y)\, e^{\mathrm{i}\alpha(x-x_0)}, \tag{5.75}$$

where x_0 is subtracted from x to account for a non-zero initial position of stability computation. This value of $\tilde{u}_k$ can be used to compute I_2 by the procedure shown in Section 5.2.1. However, there remains doubt on whether to consider or neglect the contributions of V_B while calculating base flow and tangential perturbation fields, which is neglected while computing ILST solutions. This issue can be relevant as it determines whether the base flow tangential component in the wall-normal direction exists or not (refer Equation 5.55). Thus, two different versions of I_2 are computed, one which would not account for V_B, and one which would account for V_B. This also helps evaluate the effect of the influence of V_B

on the I_2 term. While comparing HLNS results with ILST results, PSE can act as a helpful intermediary. Proximity of the I_2 term computed with the PSE solution towards the I_2 term of HLNS solution instead of the ILST solution would suggest that the neglect of streamwise derivatives, wall-normal velocity or history effects in the ILST ansatz would be the potential cause of the difference in ILST and HLNS I_2 observations. Whereas in case the I_2 term computed by PSE matches the I_2 term computed with ILST better than the I_2 term computed by HLNS solution, ellipticity effects and different growth rates across components could potentially be attributed to observations of difference in ILST and HLNS I_2 observations. The computation of I_2 using PSE requires the PSE ansatz to be recasted into the HLNS ansatz by equating spanwise independent terms to $\tilde{u}_k$ which yields

$$\tilde{u}_k = \hat{u}_k(x, y)\, e^{\mathrm{i}(\int_{x_0}^{x} \alpha ds)}. \tag{5.76}$$

Following this, the values of tangential and normal perturbation can be computed and the value of I_2 can be obtained as per the procedure shown in Section 5.2.1.

On the other hand, the observation of Orr mechanism can directly explain the departure from modal character, be it local or clean case behaviour. This occurs since the ILST ansatz prescribes the existence of a unique value of α_r at any given chordwise station, which would indicate a preferred direction of lines of constant phase in xz plane given by

$$\alpha_r(x - x_0) + \beta z = C, \tag{5.77}$$

which is perpendicular to the wavenumber vector. The variation of phase in the wall-normal direction is assumed to be a local effect, and assumed not to have an effect on the computation of these lines of constant phase. PSE lines of constant phase can once again be plotted to check if the behaviour bears more similarity to either HLNS or ILST by recasting the PSE ansatz into the HLNS ansatz.

5.2.2. Criteria

If evidence of deviation from modal behaviour is obtained, the next step would be to test if non-modal effects could govern instability evolution in regions of deformed base flow. Casacuberta, Hickel, Westerbeek, and Kotsonis (2022) present criteria to identify non-modal character in the form of difference in growth rate of base flow tangential and total perturbation vector fields at the location of fundamental perturbation peak. They evaluate the growth rate of these quantities by using the standard growth rate expressions given by

$$\alpha_{i,\xi} = -\frac{1}{A_\xi}\frac{\partial A_\xi}{\partial x}, \tag{5.78}$$

where $\alpha_{i,\xi}$ is the growth rate of a quantity ξ, which is either the amplitude function of τ' or the norm of $\boldsymbol{v}'_{(0,1)}$, and A_ξ represents the value of ξ at its primary peak. If the growth rates are dissimilar, Casacuberta, Hickel, Westerbeek, and Kotsonis (2022) claim that non-modal effects could play a role in governing instability evolution.

In addition to the difference in growth rates, Casacuberta, Hickel, Westerbeek, and Kotsonis (2022) suggest that perturbation vector misalignment with the base flow can provide evidence of non-modal effects being active. Casacuberta, Hickel, Westerbeek, and Kotsonis (2022) monitor the angle between total and base flow tangential perturbation vector to quantify misalignment. Standard methods for finding an angle between real vector fields fail here as a clear definition of dot products between complex and real spaces lacks definition. Thus, Casacuberta, Hickel, Westerbeek, and Kotsonis (2022) state that the angle between the perturbation velocity vector field and the base flow is equivalent to the angle between the former and the component of perturbation velocity vector field tangential to base flow, which is expressed as

$$\cos\left(\zeta_{(0,1)}\right) = \frac{\boldsymbol{v}'_{(0,1)} \cdot \boldsymbol{v}'_{t,(0,1)}}{||\boldsymbol{v}'_{(0,1)}||\,||\boldsymbol{v}'_{t,(0,1)}||}, \tag{5.79}$$

where a dot product in complex space is defined by the Hermitian dot product (Scharnhorst, 2001). It should be noted that

$$\boldsymbol{v}'_{(0,1)} \cdot \boldsymbol{v}'_{t,(0,1)} = (\boldsymbol{v}'_{t,(0,1)} + \boldsymbol{v}'_{n,(0,1)}) \cdot \boldsymbol{v}'_{t,(0,1)} = \boldsymbol{v}'_{t,(0,1)} \cdot \boldsymbol{v}'_{t,(0,1)} = ||\boldsymbol{v}'_{t,(0,1)}||^2, \tag{5.80}$$

which simplifies the expression of Equation 5.79 to

$$\cos\left(\zeta_{(0,1)}\right) = \frac{||\boldsymbol{v}'_{t,(0,1)}||}{||\boldsymbol{v}'_{(0,1)}||}. \tag{5.81}$$

A value of $\cos\left(\zeta_{(0,1)}\right)$ close to one would indicate that the total perturbation vector and perturbation vector tangential to base flow are aligned with each other, and thus suggest the dominance of modal mechanisms. Values away from one would suggest misalignment and the presence of non-modal effects. Casacuberta, Hickel, Westerbeek, and Kotsonis (2022) also further decompose the expression of Equation 5.81 to find that that misalignment of total perturbation vector and base flow can directly be linked to the growth rates of tangential and total perturbation being different from each other.

6

Perturbation Response to Base Flow Deformation

This chapter considers the interaction of stationary crossflow instability with a base flow deformed via a two-way pressure variation imposed on the clean case pressure distribution which possesses a favourable pressure gradient. Relevant features of base flow that potentially affect perturbation behaviour are first investigated. This is followed by an investigation of perturbation behaviour via observation of its normalized amplitude function and its amplitude evolution. The spanwise integrated Reynold Orr framework developed in Section 5.1 is then used to explain the trends of amplitude evolution. The focus then shifts to identifying the lift-up effect and the Orr mechanism as prescribed in Section 5.2.1. The action of these mechanisms on actual perturbation evolution and ILST solution evolution (representative of local modal behaviour) are compared to find traces of deviation of perturbation from modal character. Criteria specified in Section 5.2.2 are then examined to claim whether the identified deviation from modal character translates to the development of non-modal character.

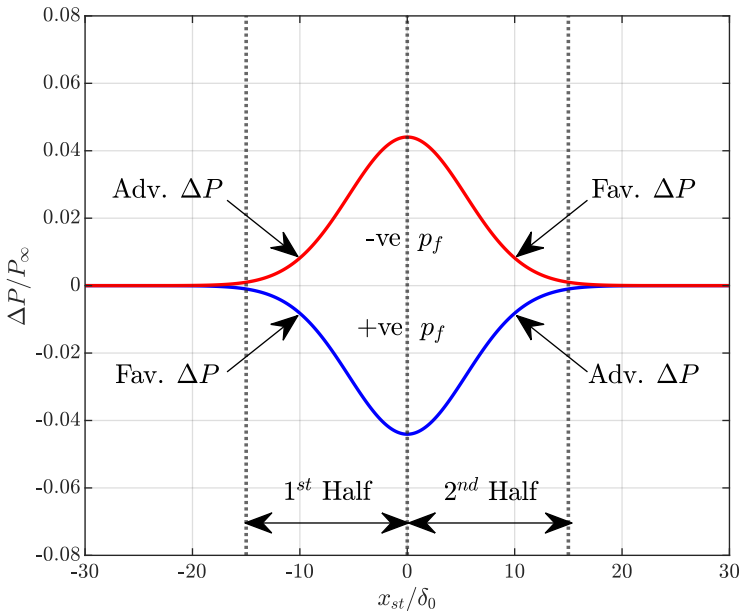

Figure 6.1: ΔP distribution of $2.5p_f$ $30w$ (blue) and $-2.5p_f$ $30w$ (red) cases, denoting first and second half of pressure variation, and adverse (abbreviated as adv.) and favourable (abbreviated as fav.) ΔP regimes; black dotted lines at $x_{st}/\delta_0 = -w/2,\ 0,$ and $w/2$ show the region of ΔP imposition.

Before beginning the discussion on base flow characteristics, the nomenclature used in this chapter is considered. To ease the interpretation of results, the region where ΔP is imposed is divided into the first half of deformation demarcated

by the region between $x_{st} = -w/2$ and $x_{st} = 0$, and the second half of deformation demarcated by the region between $x_{st} = 0$ and $x_{st} = w/2$, as shown in Figure 6.1. A region of positive slope of ΔP v/s x is called adverse, approximately corresponding to a region of reduced effective pressure gradient (less negative or positive) than the clean case. Whereas, a region of negative slope of ΔP v/s x is called favourable, approximately corresponding to a region of higher negative effective pressure gradient than the clean case (noting that effective pressure gradient, external pressure gradient and base flow pressure gradient are synonymous for boundary layer solver base flows). The first half in positive p_f and second half in negative p_f cases corresponds to a favourable ΔP region, whereas the first half in negative p_f and second half in positive p_f cases corresponds to an adverse ΔP region. The favourable and adverse ΔP regions are marked in Figure 6.1. Throughout the chapter, a comparison of the results of clean, $2.5p_f$ $30w$, and $-2.5p_f$ $30w$ cases proposed in Section 2.4 are primarily presented through contours and plots. These are referred to as "reference cases", with the latter two cases being referred to as "reference deformed cases", and their selection is grounded in the width scale being the average width scale and the pressure factor being the highest, making changes of base flow and perturbation behaviour easily perceptible. Similarities and differences with the behaviour of medium (± 1.5) and lowest (± 2.5) p_f $30\delta_0$ cases and cases of other width scales are occasionally highlighted when necessary.

6.1. Base Flow Characteristics

In the boundary layer solver, the modification of external pressure distribution is directly taken into account by the variation of external velocity via the Bernoulli equation. The external velocity profiles for the $30\delta_0$ cases are shown in Figure 6.2 (a). The external velocity increases at a rate faster than the clean case through most of the favourable ΔP region due to the deformed case possessing a relatively more favourable effective pressure gradient compared to the clean case. On the other hand, the external velocity grows slower than the clean case or starts decreasing through most of the adverse ΔP region due to the deformed case possessing a relatively less favourable or adverse effective pressure gradient compared to the clean case. The term "most" is used as the external pressure gradient of the clean case has a negative pressure gradient, implying that any ΔP distribution superposed on the clean case external profile will result in slightly asymmetrical acceleration or deceleration of external velocity in the region of deformation. The changes in external velocity profiles relative to the clean case are higher for higher p_f values, owing to the increase in strength of pressure variation imposed.

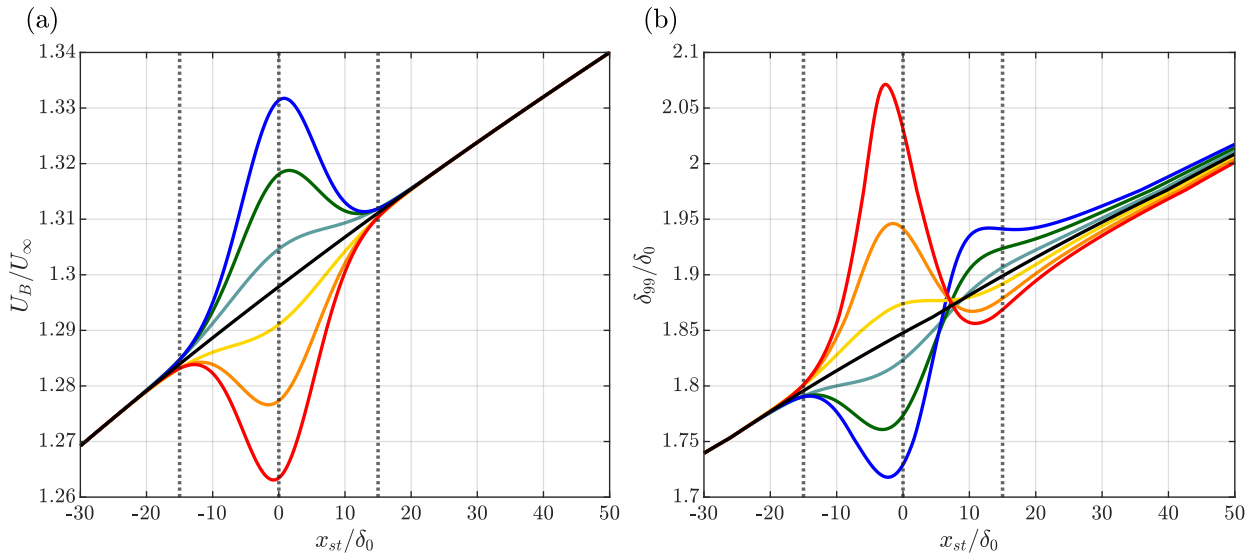

Figure 6.2: Chordwise evolution of (a) External Velocity and (b) Boundary layer thickness in $30\delta_0$ cases; $-2.0p_f$ (red), $-1.5p_f$ (orange), $-0.5p_f$ (yellow), $0.5p_f$ (cyan), $1.5p_f$ (dark green), $2.5p_f$ (blue), and clean case (black); black dotted lines at $x_{st}/\delta_0 = -w/2$, 0, and $w/2$ show the region of ΔP imposition in deformed cases.

A visualization of boundary layer thickness in Figure 6.2 (b) elucidates how the changes in inviscid flow deform the boundary layer. The clean case possesses a gradually thickening boundary layer. Before the region of pressure change, all flows have the same boundary layer thickness, as evidence of the parabolicity of boundary layer solvers only affecting changes downstream of the imposed pressure change. In positive p_f cases, through most of the first half of deformation, the boundary layer thickness reduces relative to the clean case. This can be explained with the z vorticity analogue (Abernathy, 1968; Vos & Farokhi, 2015), where viscosity potentially has lesser time to diffuse z vorticity due to higher external velocity

relative to the clean case, leading to a thinner boundary layer. Note that even though the external velocity increases in the clean case and the first half of $0.5p_f\ 30w$ case, its boundary layer does not decrease in an absolute sense, showing that the decrease of boundary layer thickness in an absolute sense only occurs when the change of external velocity occurs sufficiently fast over a short width scale (close to the orders of boundary layer thickness). On the other hand, in most of the first half of negative p_f cases, a thicker boundary layer is observed relative to the clean case, potentially due to the increased time available to viscosity to spread z vorticity as a consequence of lower external velocity relative to the clean case. It is noted that the increase of boundary layer thickness relative to the clean case occurs even for the $-0.5p_f\ 30w$ case, where the effective pressure gradient is fully favourable. This highlights that explaining results in terms of the nature of ΔP region, which approximately indicates whether the effective pressure gradient is more negative or less negative (or positive) than the clean case, is more appropriate than commenting on results based on the adverse or favourable nature of effective pressure gradient. The behaviour of boundary layer thickness reverses on approaching the end of the first half of deformation through the second half of deformation in the deformed cases i.e. a boundary layer initially thicker than the clean case in the first half of deformation eventually falls beneath clean case boundary layer thickness in the second half of deformation and vice versa. This is potentially due to the change in behaviour of external velocity in the second half relative to the first half of deformation, which potentially dictates boundary layer thickness behaviour by virtue of viscosity having more or less time to spread z vorticity in the second half relative to the first half of deformation. At the end of the second half of deformation, the boundary layer thickness starts saturating to values close to those of the clean case, showing the localization of imposed deformation. The same trends are observed across the p_f cases of different width scales as shown in Appendix C.1. The local increase or decrease of boundary layer thickness implies a change in the near-wall chordwise momentum distribution, motivating an investigation of the underlying chordwise velocity field.

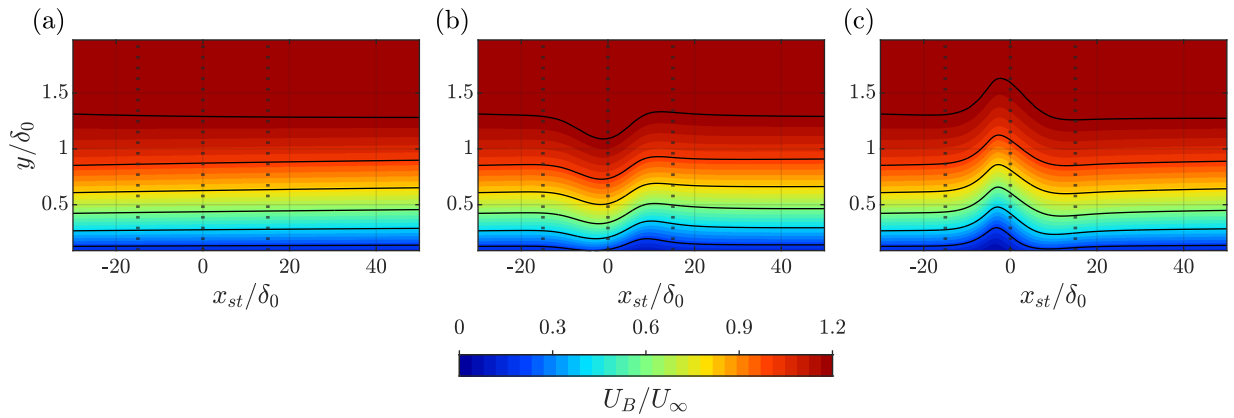

Figure 6.3: Contours of chordwise velocity in (a) clean case, (b) $2.5p_f\ 30w$ case, and (c) $-2.5p_f\ 30w$ case; black solid lines show constant velocity contour lines; black dotted lines at $x_{st}/\delta_0 = -w/2,\ 0,$ and $w/2$ show the region of ΔP imposition in deformed cases.

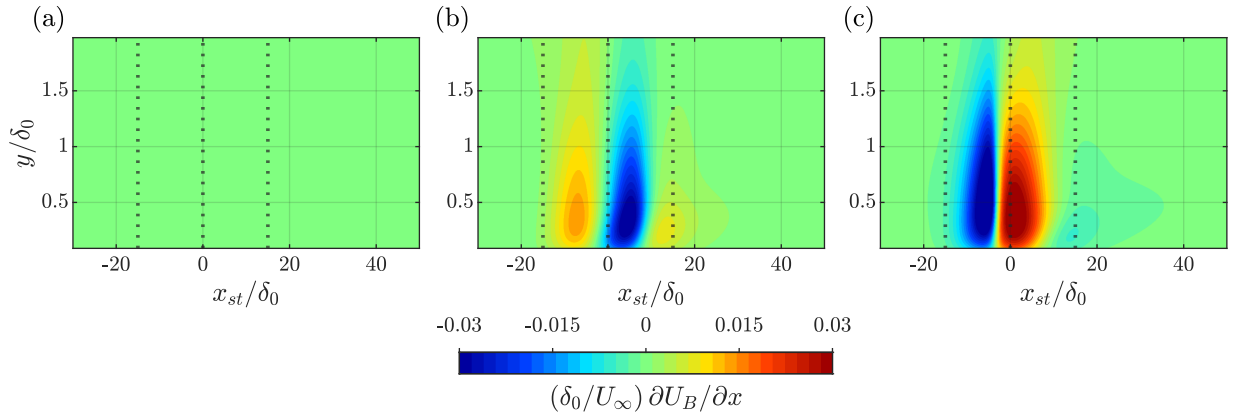

Figure 6.4: Contours of chordwise derivative of chordwise velocity in (a) clean case, (b) $2.5p_f\ 30w$ case, and (c) $-2.5p_f\ 30w$ case; black dotted lines at $x_{st}/\delta_0 = -w/2,\ 0,$ and $w/2$ show the region of ΔP imposition in deformed cases.

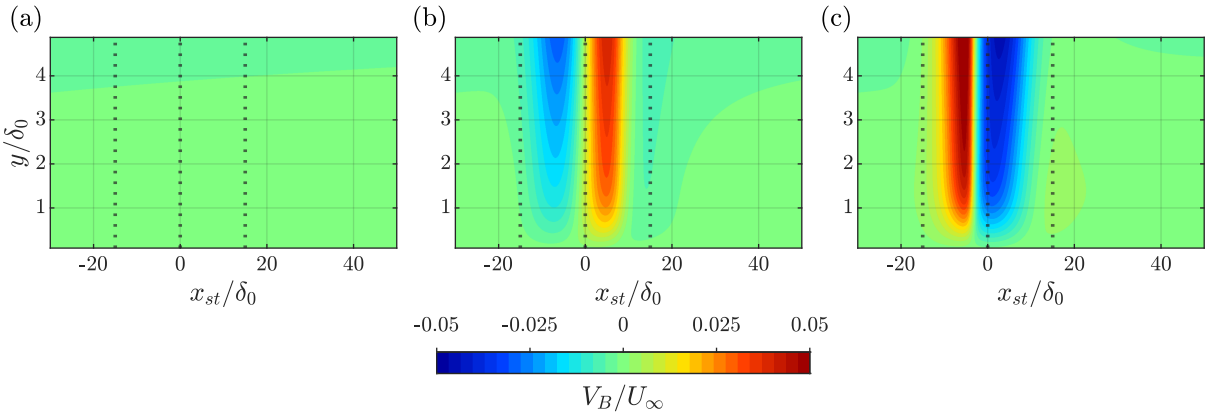

Figure 6.5: Contours of wall-normal velocity in (a) clean case, (b) $2.5p_f\ 30w$ case, and (c) $-2.5p_f\ 30w$ case; black dotted lines at $x_{st}/\delta_0 = -w/2,\ 0,$ and $w/2$ show the region of ΔP imposition in deformed cases.

In the clean case, a mildly favourable pressure gradient accelerates near-wall chordwise velocity. However, the effect of a gradually increasing boundary layer counters the effect of this acceleration, reducing the chordwise velocity at near-wall levels. The competition of these effects results in the constant contour lines of chordwise velocity almost remaining horizontal in the near-wall region in the clean case as observed in Figure 6.3 (a) relative to the behaviour of constant contour lines in deformed cases, resulting in negligible values of U_{B_x} as seen in Figure 6.4 (a). In positive p_f cases, a more negative effective pressure gradient relative to the clean case in most of the favourable ΔP region forces the chordwise velocity to accelerate as seen for the reference case in Figure 6.4 (b). This causes a downward deflection of constant contour lines of U_B, as seen for the reference case in Figure 6.3 (b), bringing more momentum to the near-wall region, consistent with the effect of a contracting boundary layer. The effect of boundary layer size appears to complement the effect of pressure gradient in terms of influencing U_{B_x} behaviour in deformed cases, unlike the clean case. Whereas, in a negative p_f case, a positive effective pressure gradient (or a less negative effective pressure gradient relative to the clean case for the lowest negative p_f case) in most of the adverse ΔP region forces the chordwise velocity to decelerate as seen for the reference case in Figure 6.4 (b). This causes an upward deflection of constant contour lines of U_B as seen for the reference case in Figure 6.3 (b), taking away momentum from near-wall regions. From the end of the first half of deformation through most of the second half of deformation, the behaviour of effective pressure gradient changes relative to its behaviour in most of the first half of deformation, causing a change in the behaviour of U_{B_x} (observed in Figure 6.4 (b) and (c)) and deflection of U_B constant contour lines (observed in Figure 6.3 (b) and (c)). There remains a third region of non-negligible U_{B_x} at the end of the second half of deformation, most prominent in the highest positive and negative p_f cases, evidenced in Figure 6.4 (b) and (c). This is attributed to the eventual relaxation of the deformed boundary layer to characteristics of the clean boundary layer. The sign of U_{B_x} in this region resembles the sign of U_{B_x} in the first half of deformation, although its magnitude is much reduced compared to the first half of deformation. Decreasing the p_f for a fixed width decreases the magnitude of U_{B_x} as a consequence of a weaker change of effective pressure, as shown in Appendix C.3. However, the value of U_{B_x} is much higher than the clean case for all deformed cases, making it a key feature of a "rapid" base flow deformation. The behaviour of U_B and U_{B_x} influences V_B and U_{B_y}, which are subsequently considered.

The behaviour of V_B can directly be interpreted from the behaviour of U_{B_x} by integrating the continuity equation (Equation 3.6) to obtain

$$V_B = -\int_0^y \frac{\partial U_B}{\partial x} dy + V_B(y=0) = -\int_0^y \frac{\partial U_B}{\partial x} dy, \tag{6.1}$$

since V_B is zero at the wall by means of the no-slip condition. Relative to the deformed cases, the clean case has much smaller values of U_{B_x}, resulting in negligible values of V_B as shown in Figure 6.5 (a). For the deformed cases, U_{B_x} can be assumed to have a consistent sign at a given chordwise position in regions of deformation, as seen for the reference cases in Figure 6.4 (b) and (c). Thus, via Equation 6.1, a region of positive U_{B_x} corresponds to a region of downwash, and a region of negative U_{B_x} corresponds to a region of upwash, as seen for the reference cases by comparing Figure 6.4 (b) and (c) with Figure 6.5 (b) and (c). V_B magnitude reduces with a reduction of p_f due to the reduction of U_{B_x} magnitude for a given width scale, as shown in Appendix C.3, but remains much higher than clean case values, making it another key feature of a rapid base flow deformation.

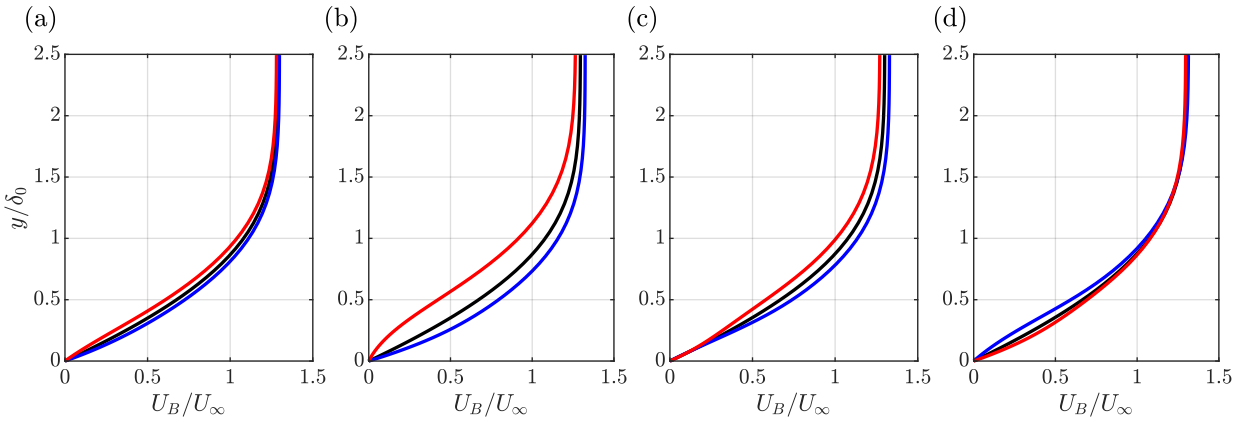

Figure 6.6: Wall-normal variation of chordwise velocity in clean case (black), $2.5p_f$ $30w$ case (blue), and $-2.5p_f$ $30w$ case (red) at x_{st}/δ_0 = (a) -0.3w, (b) -0.1w, (c) 0.1w, and (d) 0.3w.

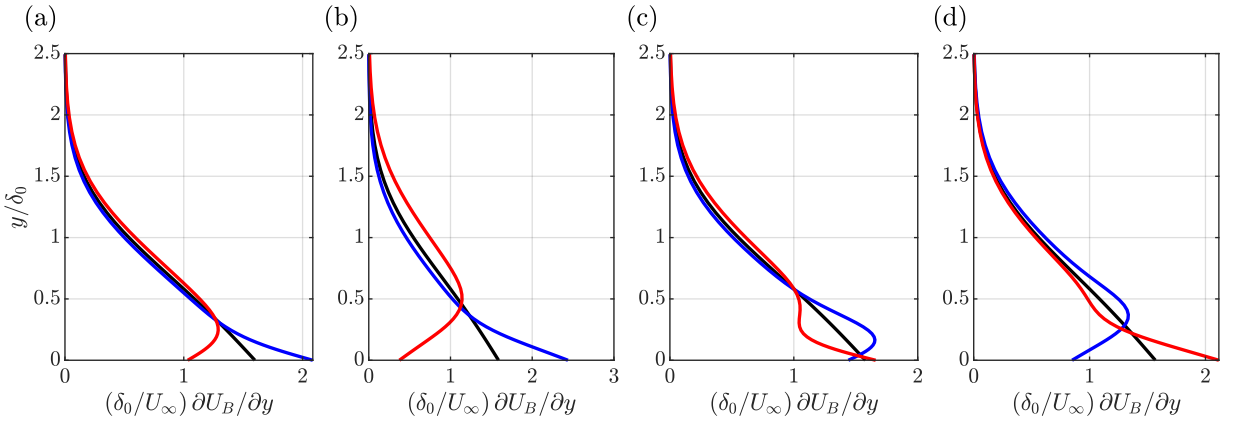

Figure 6.7: Wall-normal variation of chordwise velocity shear in clean case (black), $2.5p_f$ $30w$ case (blue), and $-2.5p_f$ $30w$ case (red) at x_{st}/δ_0 = (a) -0.3w, (b) -0.1w, (c) 0.1w, and (d) 0.3w.

The behaviour of chordwise velocity shear depends on the chordwise momentum near the wall. Higher near-wall chordwise momentum results in a larger y derivative of U_B, resulting in higher chordwise velocity shear and vice versa. Plots of wall-normal variation of chordwise velocity and chordwise shear are shown at four different locations in Figure 6.6 and Figure 6.7, respectively, for the reference cases to demonstrate these trends, wherein the first two locations are in the first half of deformation and the latter two locations are in the second half of deformation. In positive p_f cases, the increase of near-wall momentum relative to the clean case in the first half of deformation leads to an increase of chordwise velocity shear. The subsequent decrease of near-wall momentum in the second half relative to the first half of deformation leads to a reduction of chordwise velocity shear. The behaviour of chordwise velocity shear can similarly be interpreted for negative p_f cases, with reduced shear in the first half of deformation relative to the clean case due to reduced near-wall momentum, and increased shear in the second half relative to the first half of deformation due to increased near-wall momentum. For the same width scale, the extent of reduction or increase of shear is lower for lower p_f cases relative to higher p_f cases in regions of deformation, as shown in Appendix C.4, due to the weaker deformation of baseflow. Development of inflection points in the U_B distribution are evidenced by observing that the U_{B_y} distribution peaks at a location other than $y/\delta_0 = 0$ in adverse ΔP regions of both reference positive and negative p_f cases. This occurs due to the boundary layer being subjected to an adverse effective pressure gradient. However, these inflection points do not develop in the lowest p_f cases due to the consistently favourable nature of pressure gradient, as observed in Appendix C.4. The existence or absence of inflection points is of significance, as it is used by Eppink (2020) to justify instability amplification in regions where multiple inflection points exist.

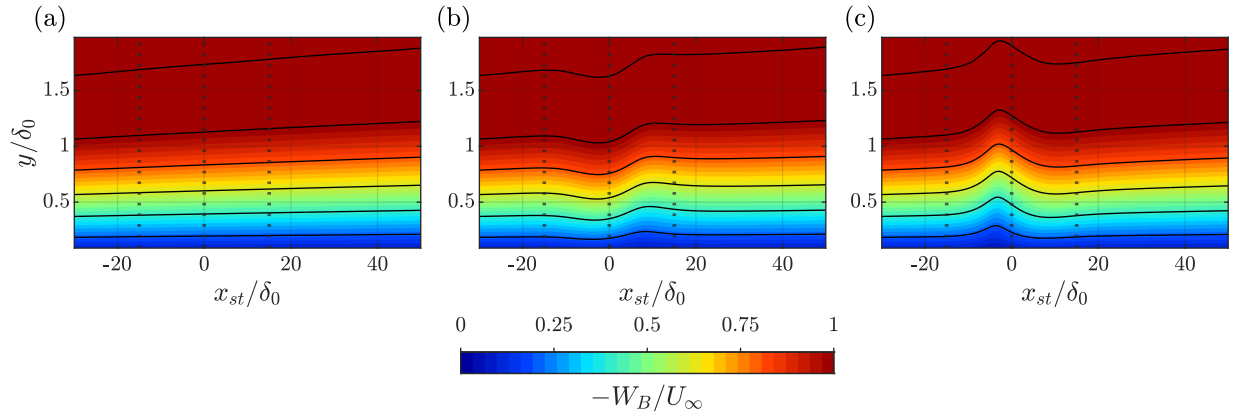

Figure 6.8: Contours of spanwise velocity in (a) clean case, (b) $2.5p_f$ $30w$ case, and (c) $-2.5p_f$ $30w$ case; black solid lines show constant velocity contour lines; black dotted lines at $x_{st}/\delta_0 = -w/2,\ 0,$ and $w/2$ show the region of ΔP imposition in deformed cases.

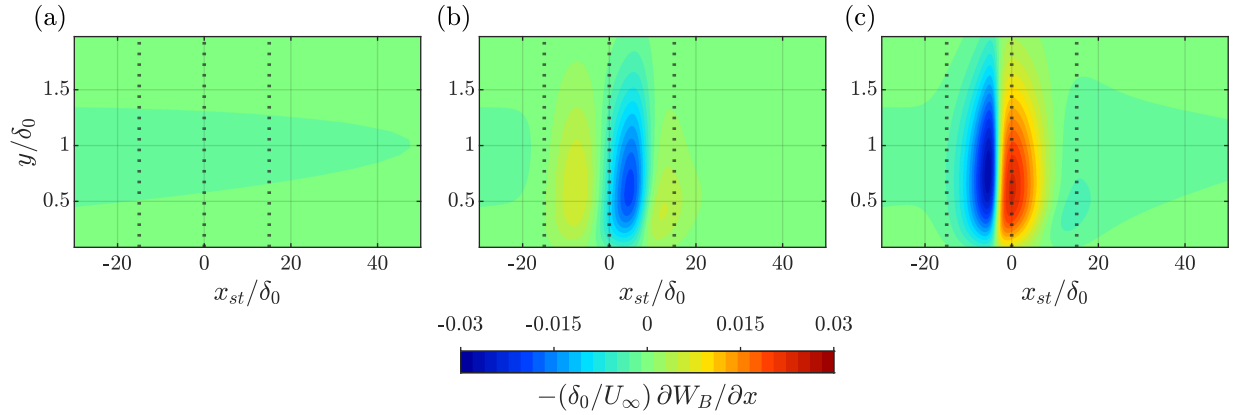

Figure 6.9: Contours of chordwise derivative of spanwise velocity in (a) clean case, (b) $2.5p_f$ $30w$ case, and (c) $-2.5p_f$ $30w$ case; black dotted lines at $x_{st}/\delta_0 = -w/2,\ 0,$ and $w/2$ show the region of ΔP imposition in deformed cases.

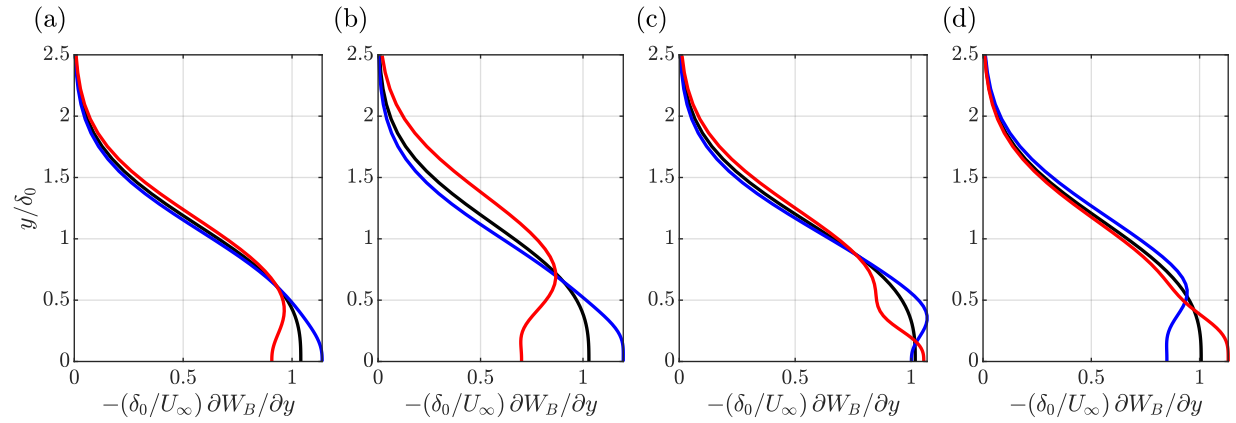

Figure 6.10: Wall-normal variation of spanwise velocity shear of clean case (black), $2.5p_f$ $30w$ case (blue), and $-2.5p_f$ $30w$ case (red) at x_{st}/δ_0 = (a) -0.3w, (b) -0.1w, (c) 0.1w, and (d) 0.3w.

The field of U_B and V_B together influence the field of W_B, as a pressure gradient is absent in the z direction. To elucidate mechanisms that might influence the chordwise evolution of spanwise velocity, the base flow z-momentum equation is

rearranged to bring W_{B_x} to the left-hand side to obtain

$$\frac{\partial W_B}{\partial x} = \underbrace{-\frac{V_B}{U_B}\frac{\partial W_B}{\partial y}}_{\mathcal{V}_w} + \underbrace{\frac{\nu}{U_B}\frac{\partial^2 W_B}{\partial y^2}}_{\mathcal{D}_w}. \tag{6.2}$$

An illustration of plots of Equation 6.2 on two different wall-normal levels for reference cases in Figure 6.11 shows that $\mathcal{V}_w$ drives the development of W_{B_x} in the deformed region. The sign of $\mathcal{V}_w$ depends directly on the sign of V_B (which in turn is related to the sign of U_{B_x}) since W_{B_y} has a negative sign negating the other negative sign. A region of chordwise velocity deceleration corresponds to a region of upwash, which makes $\mathcal{V}_w$ positive, resulting in a positive value of W_{B_x}, which implies a deceleration of the spanwise component (since W_e is negative). The vice versa is true for a region of downwash or chordwise velocity acceleration. Thus, the trends of $-W_{B_x}$ in clean and deformed cases (shown for reference cases in Figure 6.9) match the trends of U_{B_x} (shown for reference cases in Figure 6.4). This in turn results in the upward and downward movement of constant contour lines of spanwise velocity in the majority of adverse ΔP and favourable ΔP near-wall regions, respectively, as observed for reference deformed cases in Figure 6.8 (b) and (c). The reduction of spanwise near-wall momentum goes hand in hand in hand with a reduction of $-W_{B_y}$ and vice versa, as observed in Figure 6.10. The extent of reduction or increase of W_B, magnitude of sign changed W_{B_x}, and change of W_{B_y} behaviour in lower p_f cases occur to a reduced degree compared to the reference positive and negative p_f cases due to weaker deformation of base flow, as shown in Appendix C.2, Appendix C.3, and Appendix C.4, respectively. The behaviour of W_{B_x} is the third key feature differentiating a rapidly deformed base flow from clean case base flow behaviour (the first two features being U_{B_x} and V_B).

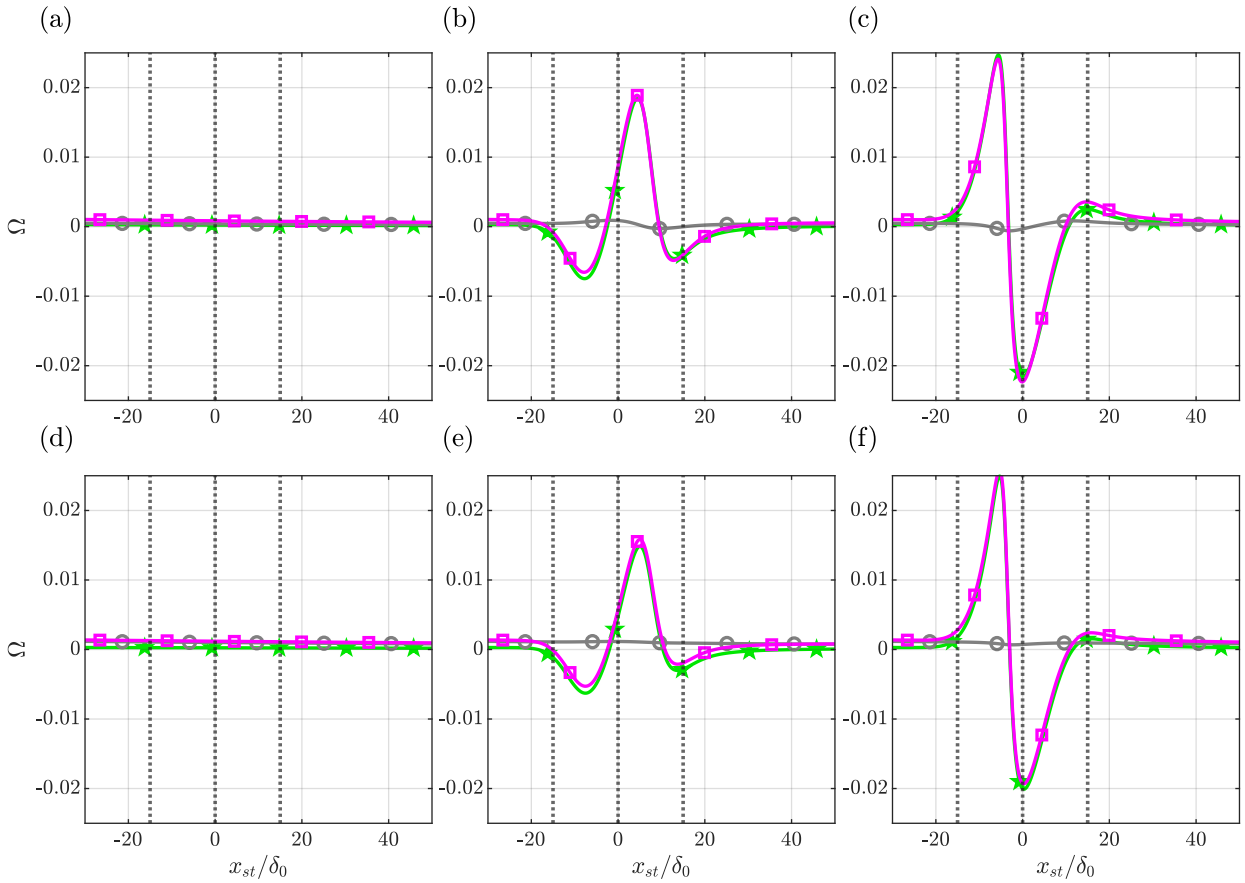

Figure 6.11: Plot of the evolution of terms in Equation 6.2, $\Omega = W_{B_x}$ (magenta with squares), $\mathcal{V}_w$, (green with stars), and $\mathcal{D}_w$ (grey with circles) of clean case (a,d), $2.5p_f$ $30w$ case (b,e), and $-2.5p_f$ $30w$ case (c,f) at $y/\delta_0 = 0.5$ (top) and $y/\delta_0 = 1$ (bottom); black dotted lines at $x_{st}/\delta_0 = -w/2,\ 0,$ and $w/2$ show the region of ΔP imposition in deformed cases.

With the understanding of U_B, V_B and W_B fields, an investigation of near-wall streamlines can be conducted since a large streamline deflection has the potential of forcing an initially modal perturbation not to follow the base flow anymore.

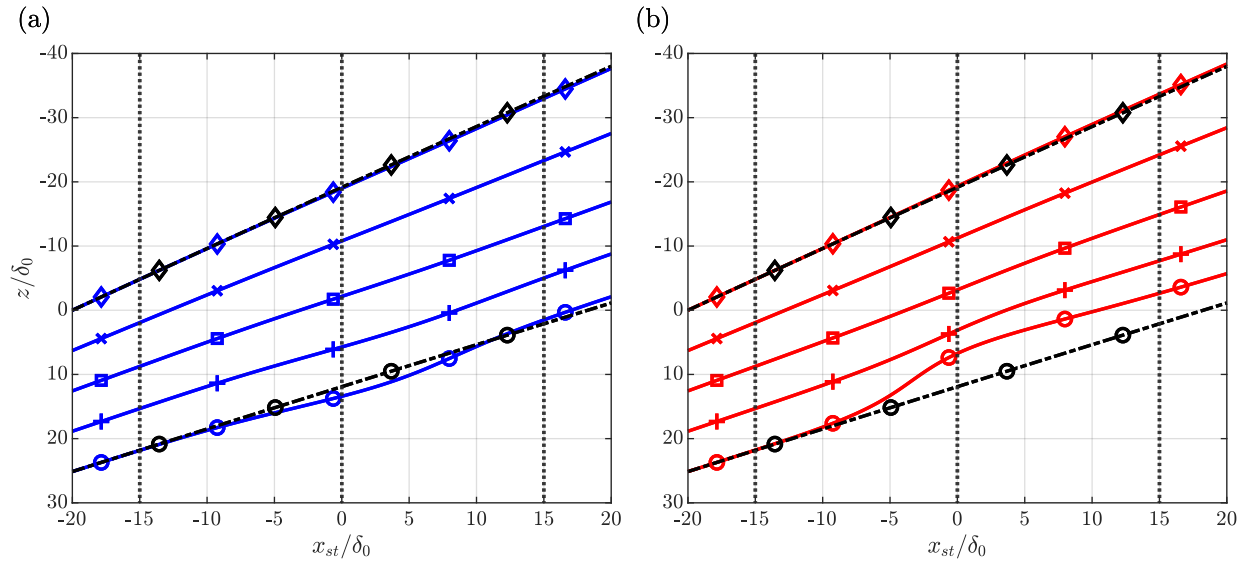

Figure 6.12: Plot of xz projection of 3D streamlines seeded at $y/\delta_0, z/\delta_0$ = (i) $0.05, 8\pi$ (circle), (ii) $0.25, 6\pi$ (plus), (iii) $0.5, 4\pi$ (square), (iv) $1, 2\pi$ (cross), and (v) $2, 0$ (diamond) in (a) $2.5p_f$ $30w$ case and (b) $-2.5p_f$ $30w$ case; black dash-dotted lines show clean case near-wall streamline and far-wall streamline; black dotted lines at $x_{st}/\delta_0 = -w/2,\ 0,$ and $w/2$ show the region of ΔP imposition in deformed cases.

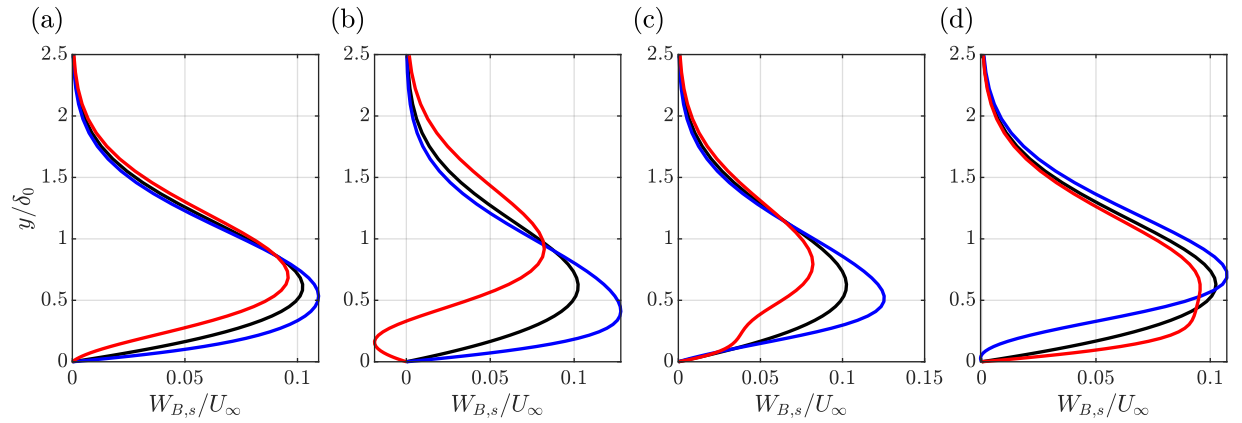

Figure 6.13: Wall-normal variation of crossflow velocity in clean case (black), $2.5p_f$ $30w$ case (blue), and $-2.5p_f$ $30w$ (red) case at x_{st}/δ_0 = (a) $-0.3w$, (b) $-0.1w$, (c) $0.1w$, and (d) $0.3w$.

This could in turn result in non-modal effects similar to those observed by Casacuberta, Hickel, Westerbeek, and Kotsonis (2022). Near-wall streamlines for reference deformed cases (shown in Figure 6.12) show an outboard deflection in the adverse ΔP region and an inboard deflection in the favourable ΔP region, potentially due to the stronger adverse and favourable pressure gradient regimes compared to the clean case. The outboard and inboard turn of near-wall streamlines in regions of local adverse and favourable pressure gradient, respectively, are also observed by Casacuberta, Hickel, Westerbeek, and Kotsonis (2022). The lowest p_f cases hardly show any streamline deflection in the near-wall region potentially due to the effective pressure gradient not undergoing a sign change. Whereas the medium p_f cases show similar behaviour with reduced extent when compared with the highest p_f cases of same sign due to reduced extent of base flow deformation. The observed trends of streamline deflection have consequences for crossflow velocity behaviour, whose investigation is relevant since the crossflow profiles are aligned within a few degrees of clean case directional profiles (Bippes, 1999), which govern modal growth characteristics (Mack, 1984). The crossflow velocity ($W_{B,s}$) is expressed by

$$W_{B,s} = W_B \cos(\theta_s) - U_B \sin(\theta_s), \tag{6.3}$$

where the inviscid streamline angle is given by

$$\theta_s = \arctan\left(\frac{W_\infty}{U_e}\right). \tag{6.4}$$

For the clean case, in the coordinate conventions considered here, the crossflow component is consistently positive. Deformed base flows present a chance for deviation from clean case crossflow properties, wherein a region of local adverse pressure gradient has been related to crossflow reversal and a region of stronger favourable pressure gradient than clean case has been related to crossflow enhancement in the studies of FFS base flow (Eppink, 2020; Rius-Vidales & Kotsonis, 2021). In the first half of deformation of the reference positive p_f case, the inboard turn of streamlines results in enhanced crossflow compared to the clean case as observed in Figure 6.13 (a) and (b), possibly due to the more negative effective pressure gradient. On the other hand, the outboard turn of streamlines in the first half of the reference negative p_f case results in reduced crossflow than the clean case, which eventually reverses direction, possibly due to the adverse effective pressure gradient. In the second half of deformation, crossflow enhancement is noted in the reference negative p_f case and crossflow reduction in the reference positive p_f case, relative to the first half of deformation, possibly due to the change in behaviour of effective pressure gradient in the second half of deformation. The region where crossflow enhancement and reduction occurs remains the same for the same sign of p_f, with the extent of enhancement and reduction curtailed due to the weaker pressure deformation, as shown in Appendix C.5. Crossflow does not reverse in the lowest positive and negative p_f cases potentially due to a fully favourable pressure gradient distribution. Crossflow also does not reverse in the medium positive and negative p_f cases potentially due to a weaker adverse pressure gradient than the highest positive and negative p_f case, and might have reversed had the same adverse pressure gradient region existed over a larger width scale.

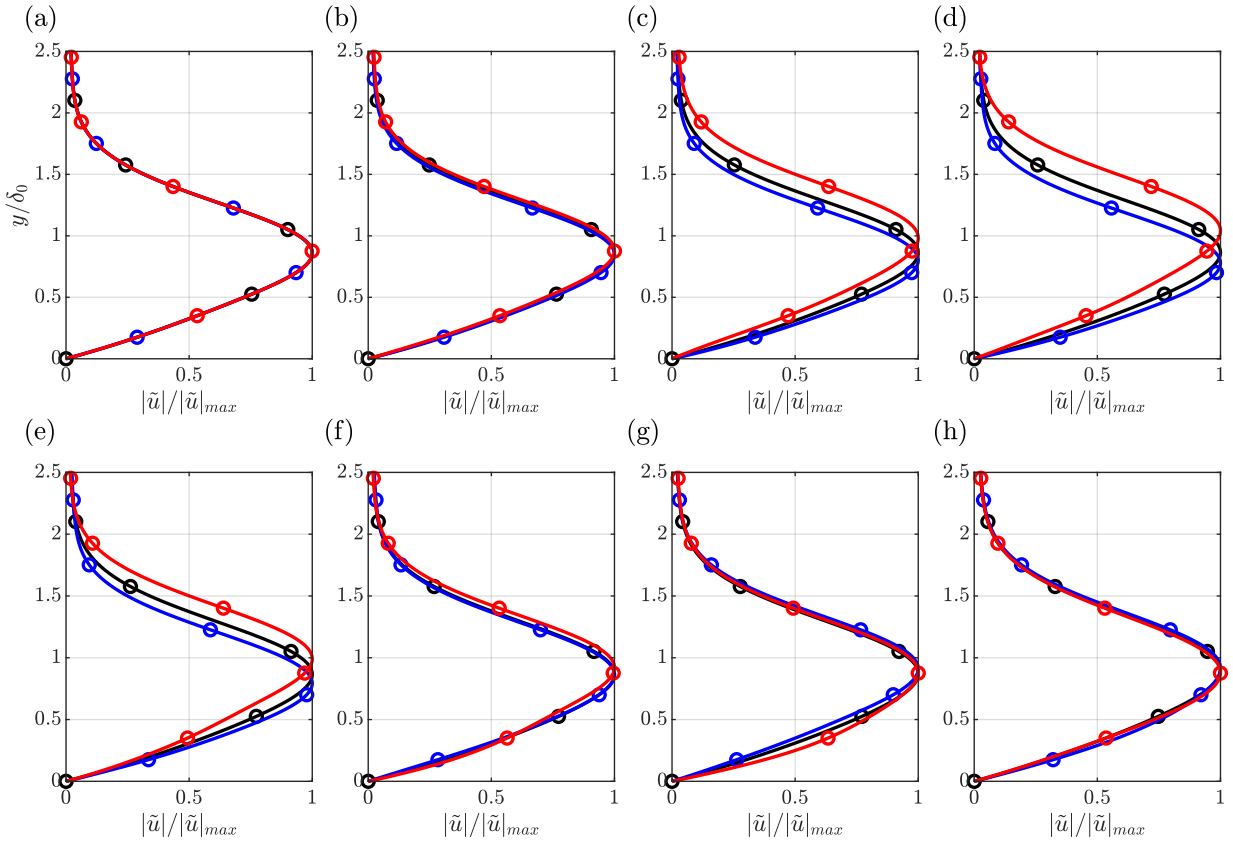

Figure 6.14: Wall-normal variation of normalized amplitude function of u' in clean case (black), $2.5p_f$ $30w$ case (blue), and $-2.5p_f$ $30w$ case (red) at $x_{st}/\delta_0 =$ (a) $-0.75w$, (b) $-0.4w$, (c) $-0.2w$, (d) $-0.05w$, (e) $0.05w$, (f) $0.2w$, (g) $0.4w$, and (h) $0.75w$.

6.2. Perturbation Evolution

The amplitude function of perturbations is first examined to identify if secondary peaks are present in the amplitude function of u', and to find which perturbation components are dominant contributors to total perturbation energy. Secondary peaks are associated with near-wall streaks by Casacuberta, Hickel, Westerbeek, and Kotsonis (2022), and the authors claim that amplitude evolution at the primary peak is more representative of the behaviour of crossflow instability, even when the $|\tilde{u}|$ value at the secondary peak is higher than its value at primary peak. Wall-normal variation of $|\tilde{u}|$ normalized perturbation amplitude function (defined as perturbation amplitude function at a chordwise location normalized by maxima of $|\tilde{u}|$ at that location), shown for reference cases at various locations in the first and second half

of deformation in Figure 6.14, show that secondary peaks do not develop when the u' perturbation evolves through the reference deformed base flow considered here, meaning additional near-wall streaks are absent. Secondary peaks are also not observed when the perturbation evolves through non-reference deformed base flows, as shown for the $30\delta_0$ cases in section D.1. In addition, the normalized amplitude function peak stays approximately at a constant height in the clean case, whereas it undergoes an upward motion in the adverse ΔP half and a downward motion in the favourable ΔP half in deformed base flow cases, with movement increasing with an increase of p_f magnitude, as seen in section D.1. The w' normalized amplitude function does not develop secondary peaks, and also shows the upward and downward trends of peak movement noted for u' normalized amplitude function. The value of w' amplitude function peak is comparable to that of the u' amplitude function peak (shown in Appendix D.1). Examination of v' normalized amplitude function (shown in Appendix D.1) reveals that v' is a much smaller perturbation component than u' with values of amplitude less than 10% of the amplitude of u' perturbation at any given chordwise location. The appearance of secondary peaks makes a trend for v' peaks difficult to identify clearly. Thus, u' and w' bear the bulk of perturbation energy. A potential explanation for the upward and downward movement of peaks of u' and w' in the region of base flow deformation is provided later in Section 6.3.2.

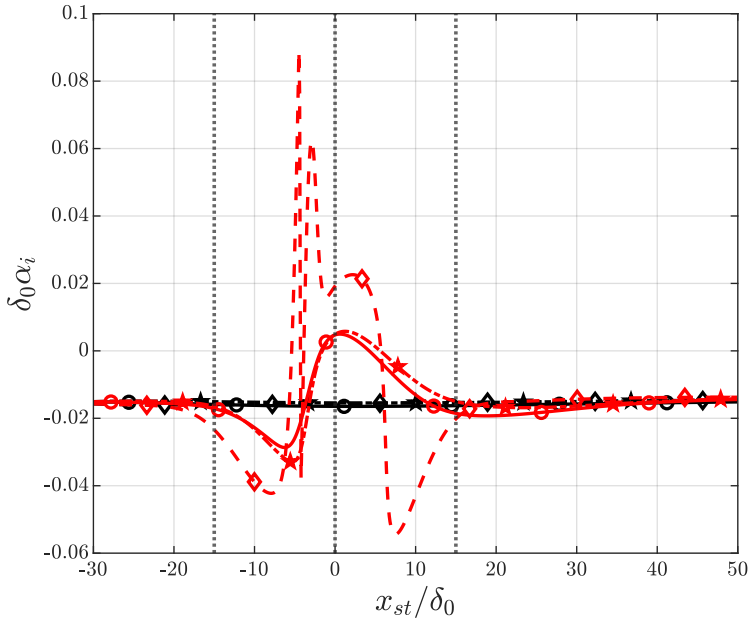

Figure 6.15: Chordwise evolution of growth rate of u' (solid with circles), v' (dashed with diamonds), and w' (dash-dotted with stars) in clean case (black) and $-2.5p_f$ $30w$ case (red); black dotted lines at $x_{st}/\delta_0 = -w/2,\ 0,$ and $w/2$ show the region of ΔP imposition in the deformed case.

The growth rate of a perturbation component ($\alpha_{i,k}$) can be calculated at its amplitude function maxima ($A_{k,max}$ at the wall-normal location "max") by

$$\alpha_{i,k} = -\frac{1}{A_{k,max}} \frac{dA_{k,max}}{dx}, \tag{6.5}$$

In analysis of modal growth with tools such as ILST, all perturbation components are assumed to grow with the same growth rate. In case of the propagation of a stationary crossflow instability in a weakly non-parallel boundary layer like the clean case, the assumption of similar growth rates across all components is valid, as shown in Figure 6.15. However, in a deformed boundary layer like the reference negative p_f case, the growth rate of u', v' and w' have potential to differ from each other, as shown in Figure 6.15. This is also evidenced in the FFS step cases of Casacuberta et al. (2021). Even though v' accounts for very little perturbation energy as presented earlier, representing growth rate and amplitude based on the norm of total perturbation vector ($|\tilde{u}_{\text{tot}}| = \sqrt{|\tilde{u}|^2 + |\tilde{v}|^2 + |\tilde{w}|^2} = \sqrt{2\tilde{E}}$) is better suited for deformed cases (whose trends would be dominated by the growth rate and amplitude of u' and w' perturbation, since these components contain the bulk of perturbation energy). This metric has also been used to quantify growth and amplitude evolution by Casacuberta et al. (2021) and Casacuberta, Hickel, Westerbeek, and Kotsonis (2022) in their FFS cases, thus ratifying its choice.

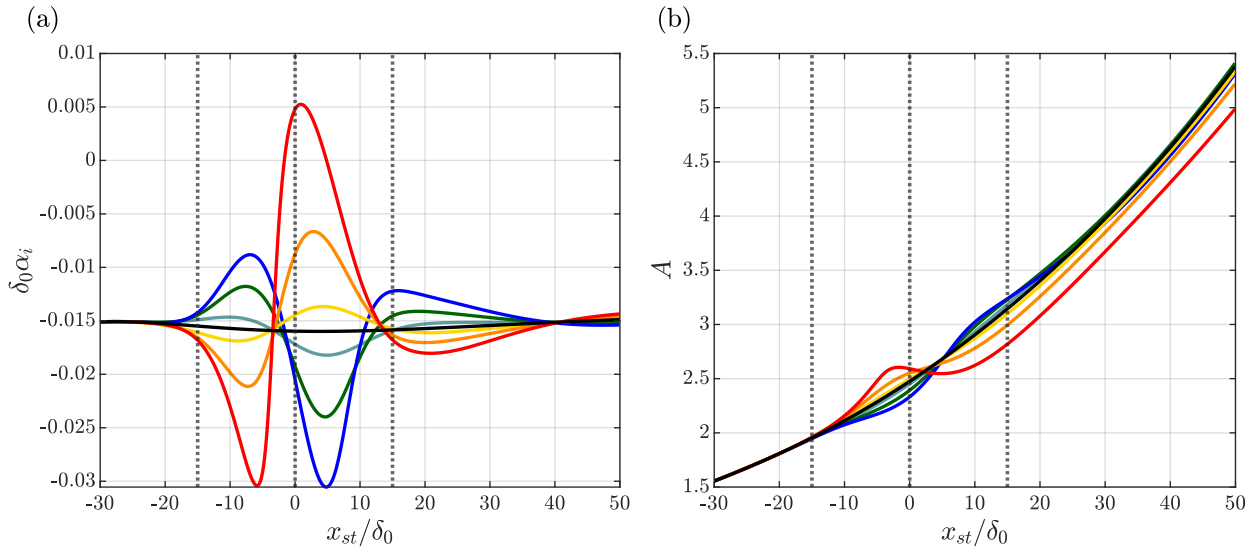

Figure 6.16: Chordwise evolution of (a) growth rate and (b) Amplitude in $30\delta_0$ cases; $-2.5p_f$ (red), $-1.5p_f$ (orange), $-0.5p_f$ (yellow), $0.5p_f$ (cyan), $1.5p_f$ (dark green), $2.5p_f$ (blue), and clean case (black); black dotted lines at $x_{st}/\delta_0 = -w/2,\ 0,$ and $w/2$ show the region of ΔP imposition in deformed cases.

The evolution of growth rate (α_i) and Amplitude (A) of $|\tilde{u}_{\text{tot}}|$ are presented in Figure 6.16 (a) and (b), respectively, for the $30\delta_0$ cases. A negative growth rate corresponds to destabilization and a positive growth rate corresponds to stabilization. The clean case has a negative growth rate with minor variation along the chordwise direction. For the deformed cases, the growth rate originally has the same value as the clean case, and starts deviating slightly upstream of the first half of deformation. Comparing α_i in positive p_f cases against α_i in the clean case, less negative values are observed in the first half of deformation, followed by more negative values from the end of the first half through most of the second half of deformation, followed by less negative values at the end of the second half of deformation. Comparing α_i in negative p_f cases against α_i in the clean case, more negative values are observed in the first half of deformation, followed by less negative values (or positive values) from the end of the first half through most of the second half of deformation, followed by more negative values at the end of the second half of deformation. Similar trends of growth rate are observed for larger and smaller width scale cases as shown in Appendix D.2, indicating that the explanation of trends for $30\delta_0$ cases would apply to cases of other width scales. The amplitude evolution trends show that the change of growth rate in deformation hardly has any long-term increase or reduction of amplitude beyond regions of base flow deformation in positive p_f cases. However, considerable long-term amplitude reduction is observed in the highest negative p_f case due to a positive growth rate in some parts of the deformation. Even though the lower negative p_f cases don't have a change in sign of growth rate, minor long-term amplitude stabilization is observed due to the considerably reduced growth rate compared to the clean case from the end of the first half to the second half of deformation.

Some of the results qualitatively match the behaviour noted by Casacuberta, Hickel, Westerbeek, and Kotsonis (2022) in a region of local adverse pressure gradient sufficiently upstream of the FFS, where secondary structures do not appear in the u' amplitude function. They observe that perturbations grow linearly and faster than the clean case. The best comparison with their results would be in the form of comparing the -2.5 p_f cases, where local regions of effective adverse pressure gradient are imposed in the first ΔP half. In this case, an initial increase in amplitude is noted compared to the clean case in the adverse effective pressure gradient region, similar to the results of Casacuberta, Hickel, Westerbeek, and Kotsonis (2022) in their FFS upstream region. Now, the challenge remains to understand what mechanism could potentially cause the perturbation growth rate and amplitude to behave in the manner shown in Figure 6.16. While it appears appealing to directly correlate the trends seen in the simulated cases to the nature of directional profiles or the appearance of inflection points, the next section elucidates why such theories would not work in the cases considered here, and thus leads to the demonstration of an energy framework to understand mechanisms influencing perturbation amplitude evolution.

6.3. Mechanisms Governing Perturbation Evolution

Two theories traditionally used to explain the behaviour of crossflow instability are the behaviour of directional profile (Mack, 1984) and the appearance of multiple inflection points (Eppink, 2020; Hosseinverdi & Fasel, 2016). In the clean case, the directional profile roughly matches the crossflow profile (Casacuberta, Hickel, Westerbeek, & Kotsonis,

2022). Regions of enhanced crossflow are correlated with higher growth of crossflow instability in Falkner-Skan-Cooke boundary layers by Mack (1984). In deformed cases, a directional profile can be difficult to obtain, as explained later in Section 6.4.2. Thus, an attempt is made to directly correlate perturbation behaviour with the nature of crossflow profiles to prove that this approach wouldn't work in the cases considered here. In the favourable ΔP region of the positive p_f cases considered in this study, lower growth of instability is observed compared to the clean case (Figure 6.16) in a region of enhanced crossflow (Figure 6.13). Similarly, in the adverse ΔP region of negative p_f cases, enhanced instability growth in comparison with the clean case (Figure 6.16) occurs in a region of reduced crossflow (Figure 6.13). This suggests that the correlation of crossflow instability characteristics with local crossflow enhancement or decay would not be a suitable way to describe instability growth or decay in a region of rapidly deformed base flow, reaffirming the doubts expressed by Casacuberta, Hickel, Westerbeek, and Kotsonis (2022) in using such an approach in their FFS cases.

The second theory involves finding if an additional inflection point appears in the U_B profile in addition to the inflection point already existing in the crossflow profile, to correlate additional destabilization with respect to the clean case to the appearance of the new inflection point in the U_B profile in addition to the already existing inflection point in the crossflow profile (Hosseinverdi & Fasel, 2016; Eppink, 2020). The results of - $0.5p_f\ 30w$ case wherein perturbation amplitude experiences enhanced growth relative to the clean case in the adverse ΔP half, without the appearance of any additional inflection points in the U_B profile (refer Section 6.1), casts doubt on whether the increase of inflection points can actually be correlated to additional growth of the crossflow instability. Hence, the energy balance framework presented in Section 5.1 is considered to explain mechanisms of perturbation behaviour in regions of deformed flow. Only the results of reference cases are shown here, with the occasional mention of results in non-reference $30\delta_0$ cases.

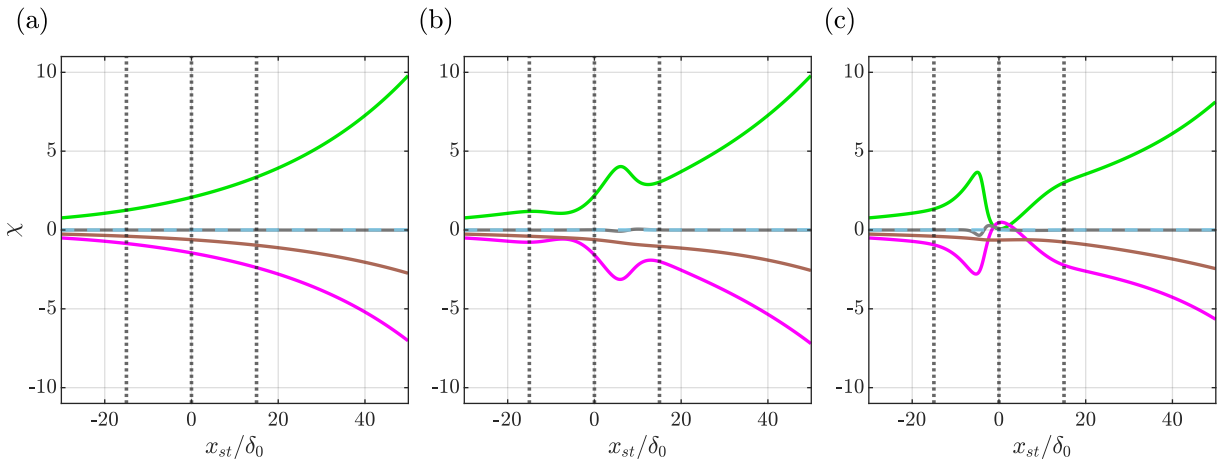

Figure 6.17: Budget of Reynold Orr Equation Equation 5.25, $\chi = \int \mathcal{P} dy$ (light green), $\int \mathcal{T} dy$ (magenta), $\int \mathcal{D} dy$ (brown), $\int \mathcal{W} dy$ (grey), and $\int (\mathcal{P} + \mathcal{T} + \mathcal{D} + \mathcal{W}) dy$ (sky blue dashed) of (a) clean case, (b) $2.5p_f\ 30w$ case, (c) $-2.5p_f\ 30w$ case; black dotted lines at $x_{st}/\delta_0 = -w/2,\ 0,$ and $w/2$ show the region of ΔP imposition in deformed cases.

The preliminary energy balance equation given by Equation 5.25 is reconsidered. Whether the sum of terms in Equation 5.25 sums to zero needs to be verified. For this purpose, the wall-normal integrated production, transport, work of viscous forces, work of pressure, and their total sum are presented for reference cases in Figure 6.17. It can be noted that the total sums to zero showing that the derived analysis (Equation 5.25) is correct. The work of pressure takes negligible values and thus is not analyzed further. The work of viscous forces acts as a means for perturbation to lose energy uniformly throughout all cases, without a perceptible change in character for deformed and clean cases, thus justifying the choice not to study its behaviour further. On the other hand, the production term which acts as a source for perturbation stabilization or destabilization, and the transport term which contains terms indicating energy growth rates, have comparable magnitudes. Comparing the production integral with the transport integral of individual cases shows that the transport integral appears to mirror the character of the production integral in regions where the latter is positive, with a reduced extent due to some energy lost to the work of viscous forces. These terms also have differing behaviour in clean and deformed cases, and have the potential to explain the differences in perturbation amplitude evolution between clean and deformed cases. Hence, they are decomposed as per Section 5.1.2 and Section 5.1.3, and considered in further detail.

6.3.1. Analysis of Production Term Evolution

The production term for the clean case shown in Figure 6.18 (a) remains positive and shows a monotonically increasing trend in chordwise direction, representing a consistent destabilizing tendency (refer subsection 5.1.2). Although the production term remains destabilizing in the positive p_f cases, it loses its monotonic behaviour as shown for the reference positive p_f case in Figure 6.18 (b). In the lower negative p_f cases, the production term remains positive and non-monotonic like the positive p_f cases. However, the reference negative p_f case shows a region of negative production term, which represents a large potential for perturbation stabilization, as seen in Figure 6.18 (c). An explanation for the trends of the production term is not readily evident, and hence $\mathcal{P}$ is decomposed into $\mathcal{P}_{x_d}$ and $\mathcal{P}_{y_d}$ as described in Section 5.1.2, to first understand their trends.

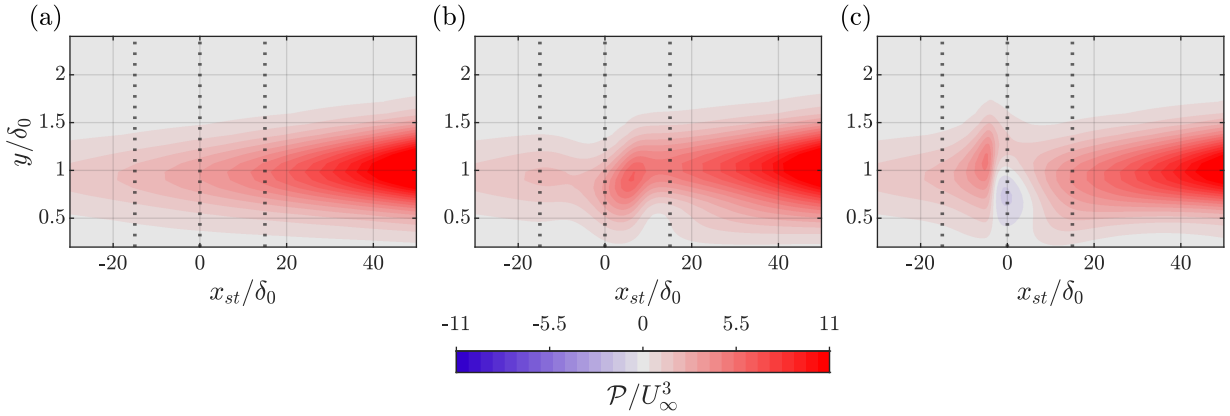

Figure 6.18: Contours of production term in (a) clean case, (b) $2.5p_f$ $30w$ case, and (c) $-2.5p_f$ $30w$ case; black dotted lines at $x_{st}/\delta_0 = -w/2,\ 0,$ and $w/2$ show the region of ΔP imposition in deformed cases.

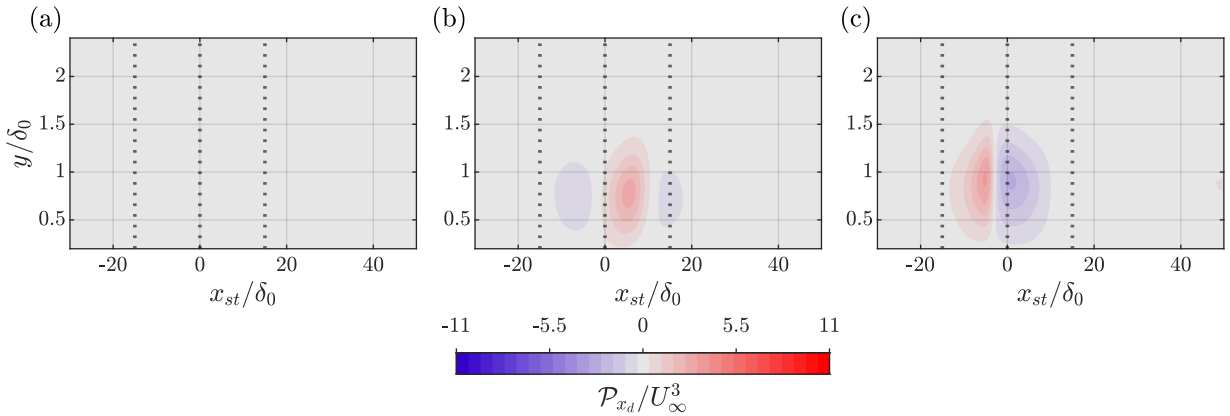

Figure 6.19: Contours of $\mathcal{P}_{x_d}$ in (a) clean case, (b) $2.5p_f$ $30w$ case, and (c) $-2.5p_f$ $30w$ case; black dotted lines at $x_{st}/\delta_0 = -w/2,\ 0,$ and $w/2$ show the region of ΔP imposition in deformed cases.

To understand the trends of $\mathcal{P}_{x_d}$, shown for reference cases in Figure 6.19, its decomposition is considered as per Equation 5.32, which reads

$$\mathcal{P}_{x_d} = \underbrace{-\frac{4\pi}{\beta}\left(|\tilde{u}|^2\frac{\partial U_B}{\partial x}\right)}_{\mathcal{P}_{x_d,1}} \underbrace{-\frac{4\pi}{\beta}\left(|\tilde{v}||\tilde{u}|\frac{\partial V_B}{\partial x}\cos(\phi_1-\phi_2)\right)}_{\mathcal{P}_{x_d,2}} \underbrace{-\frac{4\pi}{\beta}\left(|\tilde{w}||\tilde{u}|\frac{\partial W_B}{\partial x}\cos(\phi_1-\phi_3)\right)}_{\mathcal{P}_{x_d,3}}. \tag{6.6}$$

The contribution of $\mathcal{P}_{x_d,2}$ is negligible compared to the contribution of $\mathcal{P}_{x_d,1}$ and $\mathcal{P}_{x_d,3}$ in this balance as shown by wall-normal integrated terms in Figure 6.20, possibly by means of the order of magnitude argument stated in Section 5.1.2. Thus, the character of $\mathcal{P}_{x_d}$ is determined by $\mathcal{P}_{x_d,1}$ and $\mathcal{P}_{x_d,3}$, whose wall-normal integrals behave similarly in Figure 6.20. The sign of $\mathcal{P}_{x_d,1}$ is directly determined by $-U_{B_x}$. On the other hand, the sign of $\mathcal{P}_{x_d,3}$ is determined by $-W_{B_x}$ and $\cos(\phi_1-\phi_3)$. The latter remains -1 throughout regions relevant for energy transfer mechanisms as seen in Figure 6.21 for reference cases and in Appendix D.3.1 for non-reference cases. Since $-W_{B_x}$ and U_{B_x} have the same sign throughout

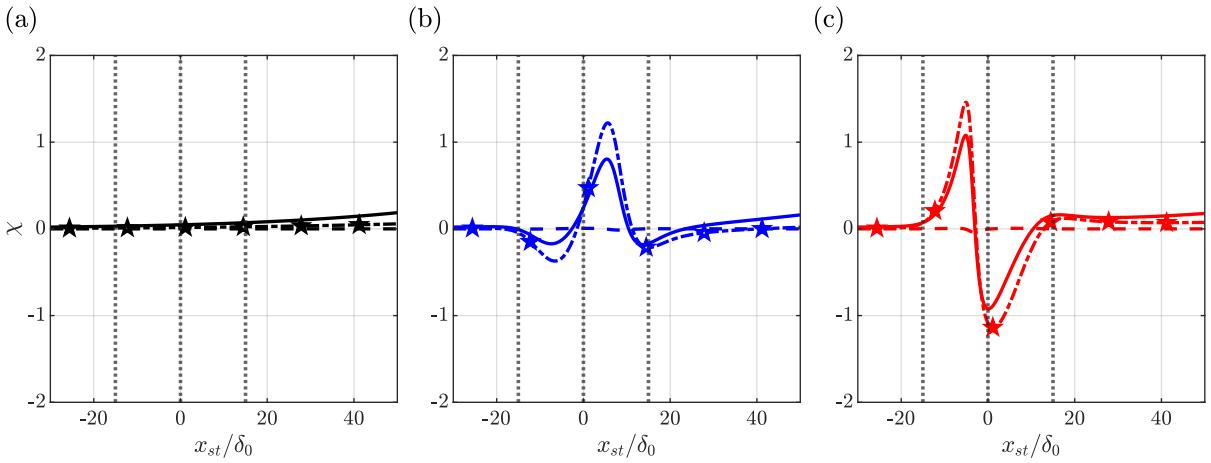

Figure 6.20: Evolution of $\chi = \int \mathcal{P}_{x_d,1} dy$ (dash-dotted with stars), $\int \mathcal{P}_{x_d,2} dy$ (dashed), and $\int \mathcal{P}_{x_d,3} dy$ (solid) in (a) clean case, (b) $2.5p_f$ $30w$ case, and (c) $-2.5p_f$ $30w$ case; black dotted lines at $x_{st}/\delta_0 = -w/2,\ 0,$ and $w/2$ show the region of ΔP imposition in deformed cases.

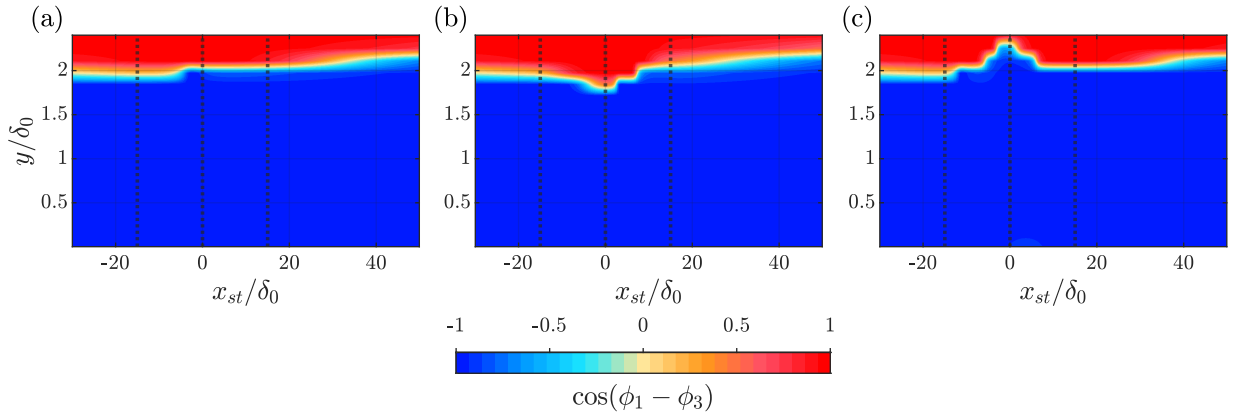

Figure 6.21: Contours of $\cos(\phi_1 - \phi_3)$ in (a) clean case, (b) $2.5p_f$ $30w$ case, and (c) $-2.5p_f$ $30w$ case; black dotted lines at $x_{st}/\delta_0 = -w/2,\ 0,$ and $w/2$ show the region of ΔP imposition in deformed cases.

regions of deformation (refer Figure 6.9 and Figure 6.4), $\mathcal{P}_{x_d,1}$ and $\mathcal{P}_{x_d,3}$ constructively interfere with each other (as shown in Figure 6.20). Hence, trends of $\mathcal{P}_{x_d}$ can be explained by examining either of the two terms, motivating an investigation of the trends of $\mathcal{P}_{x_d,1}$ (which is influenced by the sign of U_{B_x} seen in Equation 6.6).

U_{B_x} is negligible in the clean case resulting in negligible $\mathcal{P}_{x_{d,1}}$, explaining the negligible values of $\mathcal{P}_{x_d}$ seen in Figure 6.19 (a). In the deformed cases, wall-tangential base flow x derivatives have higher magnitudes than the clean case in three regions, the first region spanning most of the first half of deformation, the second region spanning the end of the first half through the second half of deformation, and the third region starting at the end of second half spanning through a short chordwise distance post the second half of deformation as shown for reference cases in Figure 6.4 and Figure 6.9. Thus $\mathcal{P}_{x_{d_1}}$ is non-zero in these three regions taking the exact same sign of $-U_{B,x}$, resulting in non-zero values of $\mathcal{P}_{x_d}$ in these regions, as shown for reference deformed cases in Figure 6.19 (b) and (c). It should be noted that the values in the third region are invisible in the contour plot of reference negative p_f case in Figure 6.19 (c), as the third region has much lower values of U_{B_x} and W_{B_x} compared to the first two regions, as can be noted in Figure 6.4 (c) and Figure 6.9 (c). Positive values of $\mathcal{P}_{x_d}$ physically imply that the perturbation has the potential to take up the energy not needed by the wall-tangential base flow when it decelerates in the chordwise direction, resulting in the potential for perturbation destabilization. Whereas, negative values of $\mathcal{P}_{x_d}$ imply that the perturbation has the potential to lose energy when the base flow accelerates, resulting in the potential for perturbation stabilization.

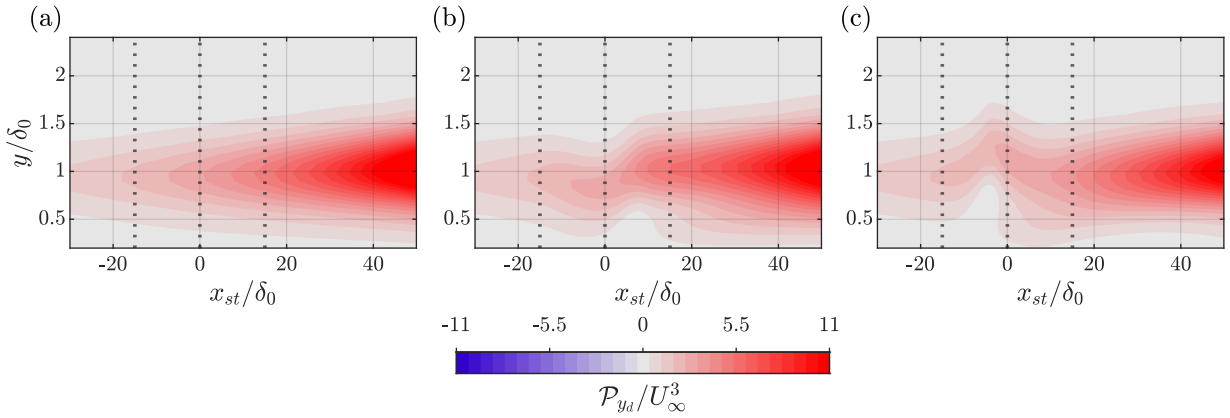

Figure 6.22: Contours of $\mathcal{P}_{y_d}$ in (a) clean case, (b) $2.5p_f$ $30w$ case, and (c) $-2.5p_f$ $30w$ case; black dotted lines at $x_{st}/\delta_0 = -w/2,\ 0,$ and $w/2$ show the region of ΔP imposition in deformed cases.

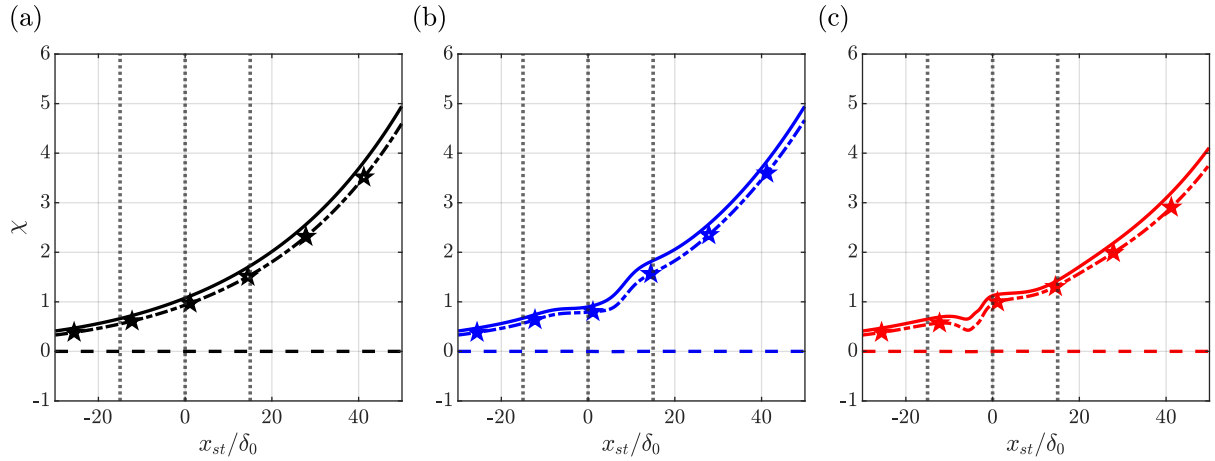

Figure 6.23: Evolution of $\chi = \int \mathcal{P}_{y_d,1} dy$ (dash-dotted with stars), $\int \mathcal{P}_{y_d,2} dy$ (dashed), and $\int \mathcal{P}_{y_d,3} dy$ (solid) in (a) clean case, (b) $2.5p_f$ $30w$ case, and (c) $-2.5p_f$ $30w$ case; black dotted lines at $x_{st}/\delta_0 = -w/2,\ 0,$ and $w/2$ show the region of ΔP imposition in deformed cases.

Now, the trends of $\mathcal{P}_{y_d}$ are analyzed, whose contours in reference cases are shown in Figure 6.22. To understand the terms controlling its behaviour, its decomposition is considered, given by Equation 5.33, which reads

$$\mathcal{P}_{y_d} = \underbrace{-\frac{4\pi}{\beta}\left(|\tilde{u}||\tilde{v}|\frac{\partial U_B}{\partial y}\cos(\phi_2-\phi_1)\right)}_{\mathcal{P}_{y_d,1}} \underbrace{-\frac{4\pi}{\beta}\left(|\tilde{v}|^2\frac{\partial V_B}{\partial y}\right)}_{\mathcal{P}_{y_d,2}} \underbrace{-\frac{4\pi}{\beta}\left(|\tilde{w}||\tilde{v}|\frac{\partial W_B}{\partial y}\cos(\phi_2-\phi_3)\right)}_{\mathcal{P}_{y_d,3}} \tag{6.7}$$

The terms $\mathcal{P}_{y_d,1}$ and $\mathcal{P}_{y_d,3}$ dominate over $\mathcal{P}_{y_d,2}$ as shown by visualizing the evolution of their wall-normal integrated values in Figure 6.23. This dominance is potentially explained by order of magnitude arguments provided in Section 5.1.2. $\mathcal{P}_{y_d,3}$ behaves in a manner similar to $\mathcal{P}_{y_d,1}$ as evidenced in Figure 6.23, due to three reasons. The first reason is the similarity of behaviour of $-W_{B_y}$ and U_{B_y}, wherein these shears reduce in adverse ΔP regions due to movement of wall-tangential momentum away from the wall, and increase in favourable ΔP regions due to movement of wall-tangential momentum towards the wall as shown in Figure 6.7 and Figure 6.10. The second reason is the similarity in behaviour of $|\tilde{u}|$ and $|\tilde{w}|$ evolution. The third reason is similar behaviour of $\cos(\phi_2-\phi_1)$ and $-\cos(\phi_2-\phi_3)$ in regions relevant for energy transfer, since the value of $\cos(\phi_1-\phi_3)$ is -1 in these regions, as observed in Appendix D.3.1. Hence, studying the behaviour of $\mathcal{P}_{y_d,1}$ is enough to comment upon the behaviour of $\mathcal{P}_{y_d}$. Since $\mathcal{P}_{y_d,1}$ depends on multiple parameters, commenting upon its increase or decrease relative to previous positions when the sign doesn't change is challenging and thus not considered in detail. However, there exists a potential for sign change which is explored further.

The sign of $\mathcal{P}_{y_d,1}$ is determined by $\cos(\phi_2-\phi_1)$ since U_{B_y} does not change sign throughout the cases considered here, due to absence of separation in cases considered. The contours of $\cos(\phi_2-\phi_1)$ for reference cases are plotted in

Figure 6.24. A negative sign of this quantity would provide a destabilizing contribution whereas a positive sign would provide a stabilizing contribution. In the clean case, in the region where $\mathcal{P}_{y_d}$ is active (approximately $0.5<y/\delta_0<1.5$, refer Figure 6.22 (a)), a value close to -1 is noted. The physical implication is that the v' perturbation has a phase difference close to 180 degree with u' perturbation, meaning that u' has peaks where v' transfers high base flow momentum downwards and u' has valleys where v' transfers low momentum upwards, thus providing potential for u' to grow as explained earlier in Figure 5.1. In the vicinity of $y/\delta_0 = 2$, the sign of cosine changes, and its behaviour indicates $\mathcal{P}_{y_{d,1}}$ has the potential to be stabilizing. These correspond to regions where v' valleys don't align with u' peaks, but rather in a phase-shifted manner such that u' has the potential to lose energy. However, these are located in the vicinity where $\mathcal{P}_{y_d}$ and $\mathcal{P}$ have negligible values possibly due to lower values of U_{B_y} in these regions, thus not leading to any significant stabilization, as seen in Figure 6.22 (a).

In deformed cases, constant contour lines of $\cos(\phi_2 - \phi_1)$ tend to take a downward trajectory in the favourable ΔP region and an upward trajectory in the adverse ΔP region, as shown for reference cases in Figure 6.24 (b) and (c), and for non-reference cases in Appendix D.3.1. The upward and downward deflection of $\cos(\phi_2 - \phi_1)$ constant contour lines appear to increase with the increase of p_f for a given width scale, as seen in Appendix D.3.1, hinting that this deflection is influenced by the strength of base flow deformation. The value of cosine monotonically increases in y till a level of about $y/\delta_0 = 0.75$ (the exact level varies from case to case as seen for reference cases in Figure 6.24 (b) and (c)), implying that any downward deflection of $\cos(\phi_2 - \phi_1)$ contour lines in this region would correspond to an increase of $\cos(\phi_2 - \phi_1)$ and vice versa. Thus in the near-wall region, an adverse ΔP region corresponds to a reduction of $\cos(\phi_2 - \phi_1)$ and a favourable ΔP region corresponds to an increase of $\cos(\phi_2 - \phi_1)$, as shown with line plots for further clarity in Appendix D.3.1. Furthermore, in some parts of the near-wall region of adverse ΔP regions, the reduction of $\cos(\phi_2 - \phi_1)$ exposes near-zero sign changed values. In these regions, U_{B_y} itself is not negligible meaning that the near-zero positive values of $\cos(\phi_2 - \phi_1)$ result in much-reduced values of $\mathcal{P}_{y_d}$ relative to the clean case. This is clearly visible in the reference cases by reduced values of $\mathcal{P}_{y_d}$ in the adverse ΔP region in Figure 6.22 (b) and (c) at the level $y/\delta_0 = 0.5$, where the clean case had stronger positive $\mathcal{P}_{y_d}$ values, as observed in Figure 6.22 (a).

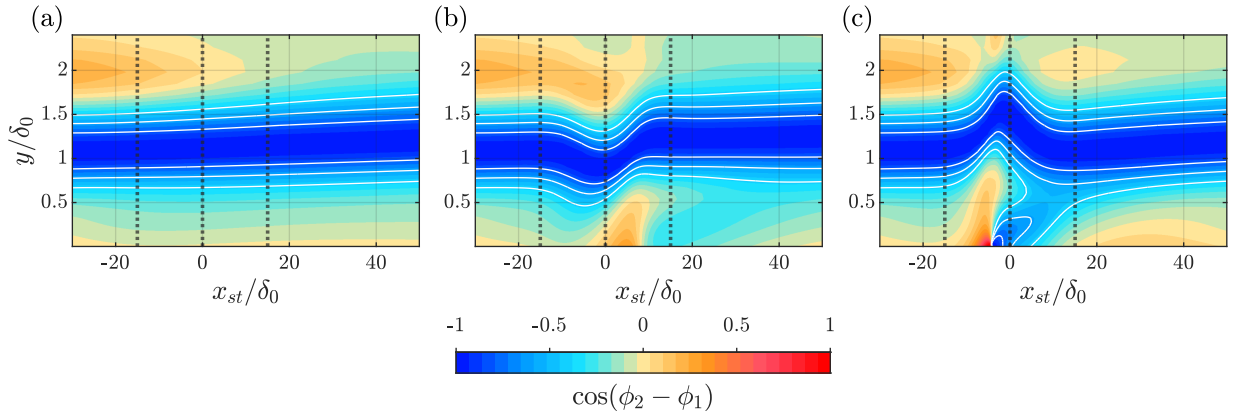

Figure 6.24: Contours of $\cos(\phi_2 - \phi_1)$ in (a) clean case, (b) $2.5p_f$ $30w$ case, and (c) $-2.5p_f$ $30w$ case; white solid lines show constant cosine contour lines in the range -1 to -0.4; black dotted lines at $x_{st}/\delta_0 = -w/2,\ 0,$ and $w/2$ show the region of ΔP imposition in deformed cases.

Since the effects of $\mathcal{P}_{x_d}$ and $\mathcal{P}_{y_d}$ have been considered individually, their combination is now studied at two different heights $y/\delta_0 = 0.5$ and $y/\delta_0 = 1$ (here on referred as lower and higher height respectively), for reference cases in Figure 6.25 to draw final comments on the behaviour of the Production term. The different heights studied correspond to the different behaviour of $\mathcal{P}_{y_d}$ terms in regions of deformed flow where $\mathcal{P}$ is active. For instance, in Figure 6.22 (c), $\mathcal{P}_{y_d}$ appears to reduce along a line drawn along $y/\delta_0 = 0.5$ and does not appear to change significantly along $y/\delta_0 = 1$. Concrete comments can only be made about the sign of $\mathcal{P}_{x_d}$ and $\mathcal{P}_{y_d}$. "Potential reasons" can be provided accounting for their increase or decrease when their signs are consistent, which are speculative to some degree.

In the clean case, $\mathcal{P}_{x_d}$ is negligible as seen in Figure 6.25 (a) and (d), and all contributions to the production term occur through $\mathcal{P}_{y_d}$, which is destabilizing throughout the considered region of evolution as seen in Figure 6.25 (b) and (e). The negligible value of $\mathcal{P}_{x_d}$ occurs due to the negligible values of U_{B_x} and W_{B_x} in the clean case. In the deformed cases, the influence of $\mathcal{P}_{x_d}$ becomes prominent in the region where pressure change is imposed, and it has similar orders of magnitude compared to the $\mathcal{P}_{y_d}$ term. A potential explanation of matching orders can be obtained by examining the orders

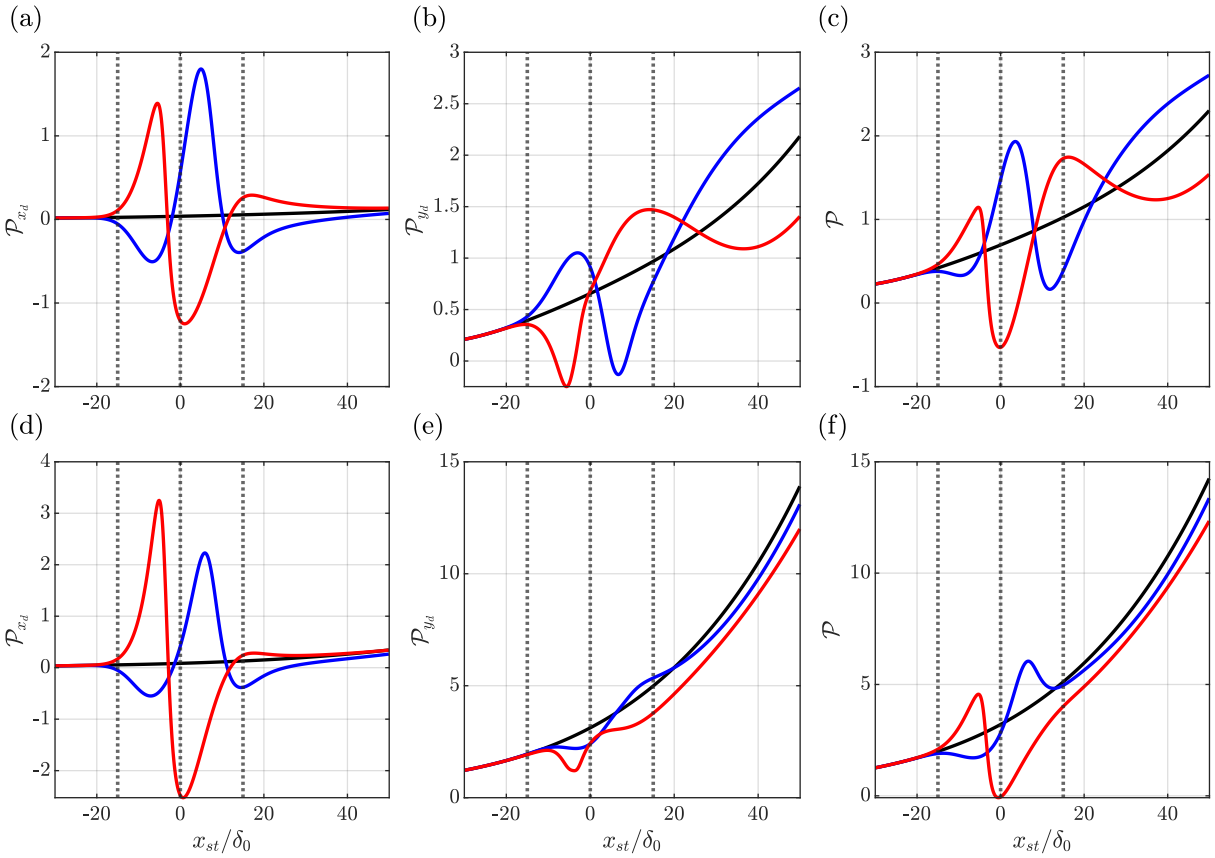

Figure 6.25: Evolution of $\mathcal{P}_{x_d}$ (a,d), $\mathcal{P}_{y_d}$ (b,e), $\mathcal{P}$ (c,f) in clean case (black), $2.5p_f\ 30w$ case (blue), and $-2.5p_f\ 30w$ (red) at $y/\delta_0 = 0.5$ (top) and $y/\delta_0 = 1$ (bottom); black dotted lines at $x_{st}/\delta_0 = -w/2,\ 0,$ and $w/2$ show the region of ΔP imposition in deformed cases.

of magnitude of the uncommon terms in $\mathcal{P}_{x_d,1}$ and $\mathcal{P}_{y_d,1}$, and noting the order of $\cos(\phi_2 - \phi_1)$ to be $O(1)$. Even though U_{B_x} is approximately 10 orders of magnitude lesser than U_{B_y}, the fact that $|\tilde{u}|$ is about 10 times $|\tilde{v}|$ potentially ensures that

$$O\left(\frac{\partial U_B}{\partial x}|\tilde{u}|\right) \approx O\left(\frac{\partial U_B}{\partial y}|\tilde{v}|\right), \tag{6.8}$$

resulting in similar orders of $\mathcal{P}_{x_d,1}$ and $\mathcal{P}_{y_d,1}$ in regions of deformed flow. The same can be said for $\mathcal{P}_{x_d,3}$ and $\mathcal{P}_{y_d,3}$, and thus $\mathcal{P}_{x_d}$ and $\mathcal{P}_{y_d}$ have comparable orders.

At both heights in the deformed cases, positive values of $\mathcal{P}_{x_d}$ are obtained in regions of wall-tangential base flow deceleration, and negative values are obtained in regions of wall-tangential base flow acceleration, as seen for reference deformed cases in Figure 6.25 (a) and (d). At the lower height, $\mathcal{P}_{y_d}$ approximately appears to fall below clean case levels in adverse ΔP regions, and appears to rise over clean case levels in favourable ΔP regions, as observed for reference deformed cases in Figure 6.25 (b), potentially triggered by the decrease and increase of $\cos(\phi_2 - \phi_1)$ (and $-\cos(\phi_2 - \phi_3)$) in adverse and favourable ΔP regions, respectively. The sign changed values of $\mathcal{P}_{y_d}$ are also noted in adverse ΔP regions of reference deformed cases due to the sign change of $\cos(\phi_2 - \phi_1)$ (and $-\cos(\phi_2 - \phi_3)$). Beyond these two regions of deformation, $\mathcal{P}_{y_d}$ does not take similar values as the clean case. This could potentially be due to the changed values of $\cos(\phi_2 - \phi_1)$ taking some chordwise length to return back to clean case levels and the values of $|\tilde{u}|$ and $|\tilde{v}|$ changing permanently beyond the deformation. At the higher height, $\mathcal{P}_{y_d}$ remains destabilizing like the clean case, as seen by comparing deformed case trends with clean case trends for reference cases in Figure 6.25 (e). The behaviour of $\mathcal{P}$ in the first and second half of deformation, although influenced both by $\mathcal{P}_{x_d}$ and $\mathcal{P}_{y_d}$, reduces beneath clean case levels approximately in regions of negative $\mathcal{P}_{x_d}$ or wall-tangential base flow acceleration, and increases above clean case levels approximately in regions of positive $\mathcal{P}_{x_d}$ or wall-tangential base flow deceleration, as seen for reference cases in Figure 6.25 (c) and (f) and for non-reference $30\delta_0$ cases in Appendix D.3.2. The reduction of $\mathcal{P}$ to near zero values or to negative values in the vicinity of the lower height is stronger when a region of wall-tangential base flow deceleration precedes a region of wall-tangential base flow acceleration. This is evidenced by negative values at the beginning of the

second half of deformation in the reference negative p_f case and near-zero values near the second half of deformation in the reference positive p_f case in Figure 6.25 (c). This occurs since $\mathcal{P}_{y_d}$ already reduces compared to the clean case in the adverse ΔP region at the lower height (approximately in a region of wall-tangential flow deceleration), and it doesn't recover to clean case levels by the location at which wall-tangential flow acceleration sets in, allowing a negative $\mathcal{P}_{x_d}$ to significantly reduce or change the sign of $\mathcal{P}$. Post the two halves of deformation, the behaviour of $\mathcal{P}$ is governed solely by the behaviour of $\mathcal{P}_{y_d}$.

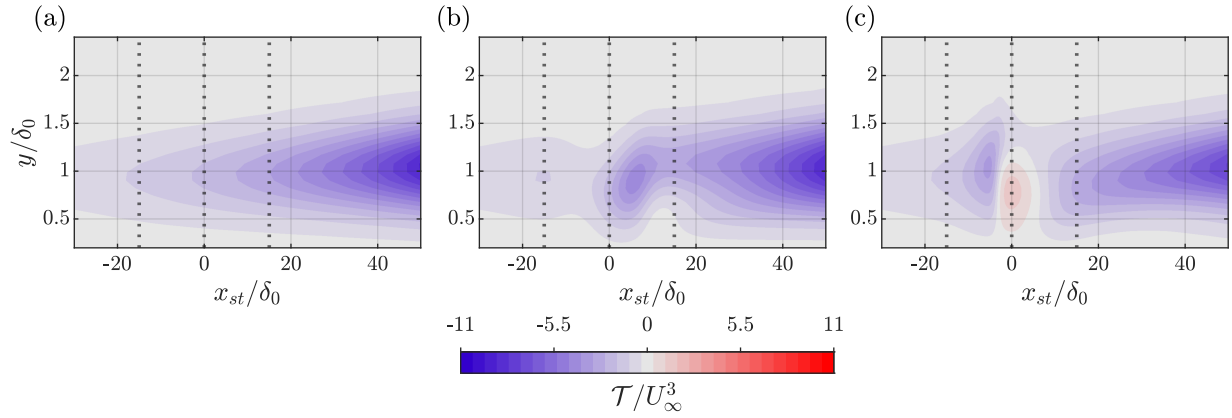

Figure 6.26: Contours of transport term in (a) clean case, (b) $2.5p_f$ $30w$ case, and (c) $-2.5p_f$ $30w$ case; black dotted lines at $x_{st}/\delta_0 = -w/2,\ 0,$ and $w/2$ show the region of ΔP imposition in deformed cases.

6.3.2. Analysis of Transport Term Evolution

The transport term shown in Figure 6.26 shows a mirrored behaviour compared to the production term shown in Figure 6.18 for each of the individual cases. When $\mathcal{P}$ is positive, the effect of the production term is distributed among the work of viscous forces and the transport term as per the preliminary energy balance equation, thereby ensuring that the magnitude of the transport term would be lesser than the magnitude of production term. The vice versa is true when $\mathcal{P}$ is negative, where the transport term magnitude is larger than the production term magnitude since it contributes to loss of energy to both the production and work of viscous force term. The decomposition of the transport term shown in Equation 5.40 is given by

$$\mathcal{T} = \underbrace{-\frac{2\pi}{\beta}\left(U_B\frac{\partial\tilde{E}}{\partial x}\right)}_{\mathcal{T}_{x_c}}\underbrace{-\frac{2\pi}{\beta}\left(V_B\frac{\partial\tilde{E}}{\partial y}\right)}_{\mathcal{T}_{y_c}}, \tag{6.9}$$

where x_c and y_c denote x and y contributions, respectively. To understand the behaviour of $\tilde{E}_x$, which contains valuable information on perturbation energy growth trends in regions of deformed flow, the behaviour of $\mathcal{T}_{y_c}$ needs to be interpreted first, since

$$\tilde{E}_x = -\frac{\beta}{2\pi U_B}(\mathcal{T} - \mathcal{T}_{y_c}). \tag{6.10}$$

$\mathcal{T}_{y_c}$ depends on V_B, which is negligible in the clean case, thus resulting in near-zero values of $\mathcal{T}_{y_c}$ as shown in Figure 6.27 (a). $\mathcal{T}_{y_c}$ is non-negligible in deformed cases when significant values of V_B are encountered. The non-negligible values occur in three regions (like U_{B_x}), the first region spanning most of the first half of deformation, the second region spanning the end of the first half through the second half of deformation, and the third region starting at the end of second half spanning through a short chordwise distance post the second half of deformation (the trends of V_B in these three regions follow a negative-positive-negative behaviour in positive p_f cases and a positive-negative-positive behaviour in negative p_f cases, as seen for reference cases in Figure 6.5 (b) and (c)). $\mathcal{T}_{y_c}$ also depends on the shears of perturbation energy, which are likely to resemble the behaviour of shears of $|\tilde{u}|$ and $|\tilde{w}|$, since the contribution of $|\tilde{v}|$ to perturbation energy is much smaller than $|\tilde{u}|$ and $|\tilde{w}|$. An observation of the normalized amplitude function of $|\tilde{u}|$ (refer Figure 6.14) for instance can help understand the trends of perturbation energy shear. The shear is positive until the peak wherein $|\tilde{u}|$ increases with y and negative from the point of peak upwards, wherein $|\tilde{u}|$ reduces with y. To fully understand the behaviour of $\mathcal{T}_{y_c}$, two regions can be considered by $y/\delta_0 < 1$ and $y/\delta_0 > 1$, where perturbation energy shear is approximately positive and negative, respectively. In regions of upwash, $\mathcal{T}_{y_c}$ takes away energy from the lower region and transports it to the higher region, and

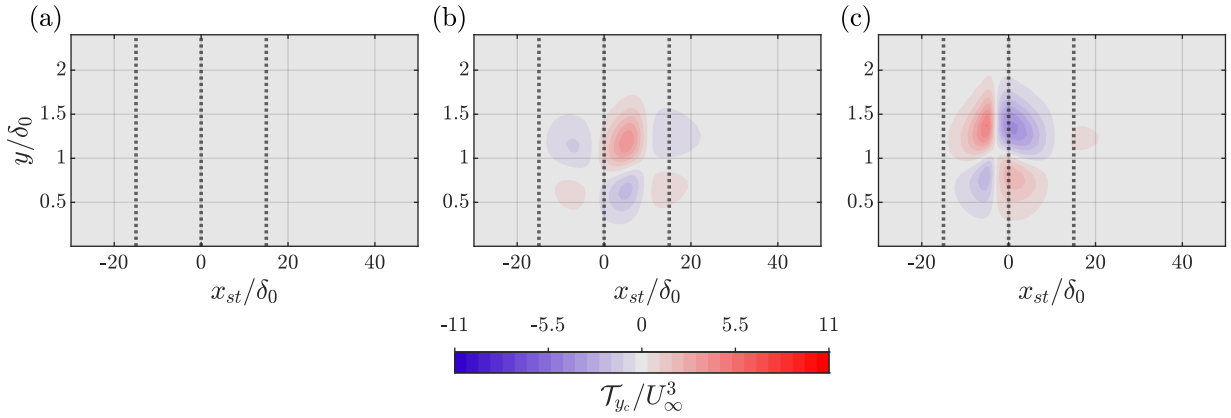

Figure 6.27: Contours of $\mathcal{T}_{y_c}$ in (a) clean case, (b) $2.5p_f\ 30w$ case, and (c) $-2.5p_f\ 30w$ case; black dotted lines at $x_{st}/\delta_0 = -w/2,\ 0,$ and $w/2$ show the region of ΔP imposition in deformed cases.

in regions of downwash, $\mathcal{T}_{y_c}$ takes away energy from the higher region and transports it to the lower region (explaining the alternating behaviour seen in top and bottom region through regions of different V_B behaviour in Figure 6.27 (b) and (c)). $\mathcal{T}_{y_c}$, earlier referred to as an agent for advection of energy in the wall-normal direction in Section 5.1.3, physically acts as an energy redistributor, wherein it takes away energy from a region of negative $\mathcal{T}_{y_c}$ and pushes energy to a region of positive $\mathcal{T}_{y_c}$. The close correspondence of upwash to an adverse ΔP region potentially explains why the peaks of u' and w' perturbation amplitude function shift upwards in these regions since energy is taken away from the wall in a region of upwash. By similar reasoning, downward moving peaks of u' and w' peaks can be explained in a favourable ΔP region, closely corresponding to a region of downwash, where energy is transported to near-wall heights.

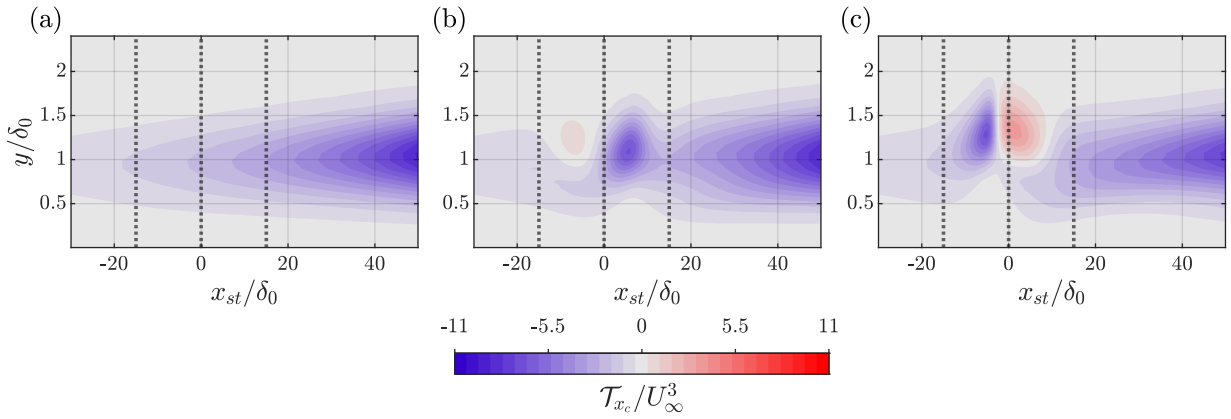

Figure 6.28: Contours of $\mathcal{T}_{x_c}$ in (a) clean case, (b) $2.5p_f\ 30w$ case, and (c) $-2.5p_f\ 30w$ case; black dotted lines at $x_{st}/\delta_0 = -w/2,\ 0,$ and $w/2$ show the region of ΔP imposition in deformed cases.

Since $\mathcal{T}_{y_c}$ locally acts as a redistributor, the behaviour of $\mathcal{T}_{x_c}$ corresponds to the behaviour of $\mathcal{T}$ modulated by $\mathcal{T}_{y_c}$. The behaviour of $\tilde{E}_x$ (shown for reference cases in Figure 6.29) closely corresponds to the mirrored behaviour of $\mathcal{T}_{x_c}$ (shown for reference cases in Figure 6.28) since U_B does not change sign. The final energy balance equation (Equation 5.44) is reconsidered to explain trends of $\tilde{E}_x$ which reads

$$\frac{\partial \tilde{E}}{\partial x} \approx \frac{1}{U_B}\left(\frac{\beta}{2\pi}(\mathcal{P}_{x_d} + \mathcal{P}_{y_d}) - V_B\frac{\partial \tilde{E}}{\partial y} + \frac{\beta}{2\pi}\mathcal{D}\right), \tag{6.11}$$

where work of pressure is neglected due to its negligible value. In the clean case, the production term dominated by the behaviour of $\mathcal{P}_{y_d}$ acts as a source for energy growth wherein the base flow provides energy to the perturbation through the action of $\mathcal{P}_{y_d,1}$. Some of this source energy is lost to the work of viscous forces, but the rest of the energy is utilized by the perturbation to grow monotonically as evidenced in Figure 6.29 (a). Since $\mathcal{T}_{y_c}$ is negligible, $\tilde{E}_x$ mimics the behaviour of $\mathcal{P}$. In the deformed cases, the production term does not increase monotonically in the chordwise direction, and its regions of

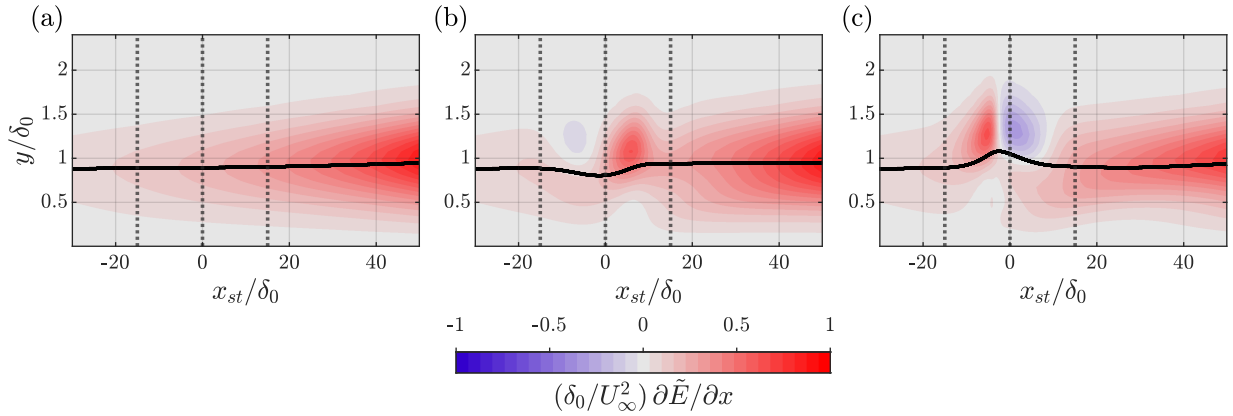

Figure 6.29: Contours of chordwise derivative of perturbation energy in (a) clean case, (b) $2.5p_f$ $30w$ case, and (c) $-2.5p_f$ $30w$ case; black solid lines shows location of "max"; black dotted lines at $x_{st}/\delta_0 = -w/2,\ 0,$ and $w/2$ show the region of ΔP imposition in deformed cases.

increase and decrease with respect to clean case approximately correspond to regions of flow deceleration and acceleration, respectively, as shown in Section 6.3.1. When the production term is positive (and higher than the magnitude of work of viscous forces), as is the case in the reference positive p_f case and most regions of the reference negative p_f case (refer Figure 6.18), the base flow acts as a source of energy such that some of the provided energy is lost by work of viscous forces. Some energy is redistributed among layers by the action of $\mathcal{T}_{y_c}$. A region which receives redistributed energy has a positive value of $\tilde{E}_x$ corresponding to the perturbation energy experiencing strong growth. A region which loses energy due to redistribution has a reduced positive value of $\tilde{E}_x$ compared to the former region or a negative value of $\tilde{E}_x$, resulting in a non-uniform wall-normal behaviour of $\tilde{E}_x$. On the other hand when the production term is negative (or lower than the magnitude of work of viscous forces), as seen in some regions of the reference negative p_f case (refer Figure 6.18 (c)), the perturbation taps into its already existing energy, such that energy after being redistributed between layers is lost to work of viscous forces and to the base flow by the production term, causing the perturbation to lose energy in the wall-normal region post its perturbation energy wall-normal distribution peak. In deformed cases, a chordwise section of reduced or negative production term compared to the clean case (approximately corresponding to a chordwise section of wall-tangential base flow acceleration) corresponds well with a chordwise section of less positive or negative $\tilde{E}_x$, which further corresponds well with a region of less negative growth rate compared to the clean case or positive growth rate, as observed for the reference cases by comparing Figure 6.18, Figure 6.29, and Figure 6.16 (a). Similarly, a region of higher production term (approximately corresponding to a chordwise section of wall-tangential base flow deceleration) with respect to the clean case corresponds well with a region of more negative growth rate compared to the clean case. It is evident from these trends that the production term is the differentiating factor between regions of perturbation growth or loss. Thus, mechanisms of perturbation amplitude evolution are primarily controlled by the behaviour of the production term. The large stabilization occurring in the amplitude of the reference negative p_f case can be attributed to a region of negative production term.

6.3.3. Potential Pitfalls

Potential pitfalls in this analysis include the usage of an idealized base flow to simulate perturbation evolution. The order of chordwise derivatives of wall-tangential base flow, which primarily differentiate the synthetic deformed base flows from the clean case, are different for the idealized BLS base flow compared to the full Navier Stokes representation. Thus, relative orders of U_{B_x} and U_{B_y} in the synthetic deformation cases simulated by BLS could be different from those imposed by a natural base flow deformation. This would result in idealized predictions of perturbation behaviour, and mechanisms influencing its amplitude evolution depending on the balance of $\mathcal{P}_{x_d}$ and $\mathcal{P}_{y_d}$ may also only be applicable to idealized cases. The movement of constant contour lines of $\cos(\phi_2 - \phi_1)$ which influences the sign of $\mathcal{P}_{y_d}$ could also just be an artefact of an idealized base flow. Thus, Chapter 7 examines if the order of chordwise derivatives of wall-tangential base flow and mechanisms governing instability amplitude evolution in a natural base flow deformation (i.e. an FFS case) bear resemblance to those in a synthetic base flow deformation with similar pressure characteristics.

6.4. Deviation from Modal Character

The analysis presented in the above sections shows that a deformed base flow affects the methods by which a stationary crossflow perturbation grows or decays. This brings into question on whether a stationary instability growing via modal mechanisms retains its original modal character on interacting with a base flow. Mechanisms such as the lift-up effect and

Orr mechanism are usually associated with non-modal character in the case of an initial condition driven non-modality in 3D flows (refer subsection 1.7.2), wherein an initially modal perturbation with non-modal growth characteristics gets modified to a perturbation with modal growth characteristics for the underlying base flow. Thus, the perturbation can be interpreted to initially have non-modal character with respect to the underlying base flow before it shows modal character at a downstream location. It can be hypothesized that a base flow deformation presents an opportunity to view this from an alternative perspective, i.e. an incoming mode interacts with a rapid base flow, and thus has the potential to deviate from modal character. Mechanisms such as the lift-up effect and Orr mechanism have the potential of being active in the region of base flow deformation, and their identification (as per subsection 5.2.1 and Equation 5.2.1) can provide insight into deviation from local modal character (identified as per Equation 5.2.1). The results presented conclude with a discussion of criteria in literature (as per subsection 5.2.2) to claim if the perturbation has traces of non-modal character.

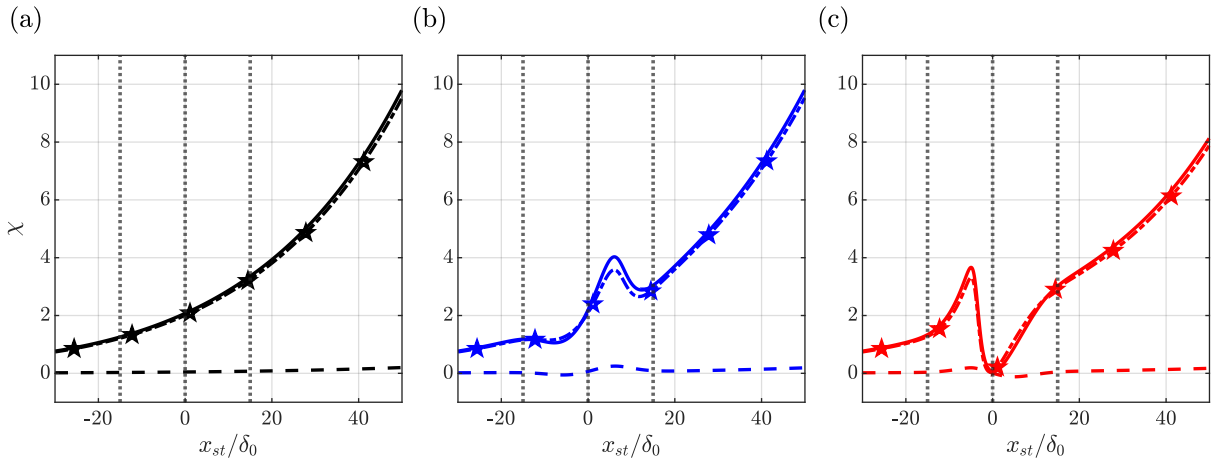

Figure 6.30: Evolution of $\chi = \int \mathcal{P} dy$ (solid), $\int I_2 dy$ (dash-dotted with stars), and $\int (I_1 + I_3 + I_4) dy$ (dashed) in (a) clean case, (b) $2.5p_f$ $30w$ case, and (c) $-2.5p_f$ $30w$ case; black dotted lines at $x_{st}/\delta_0 = -w/2,\ 0,$ and $w/2$ show the region of ΔP imposition in deformed cases.

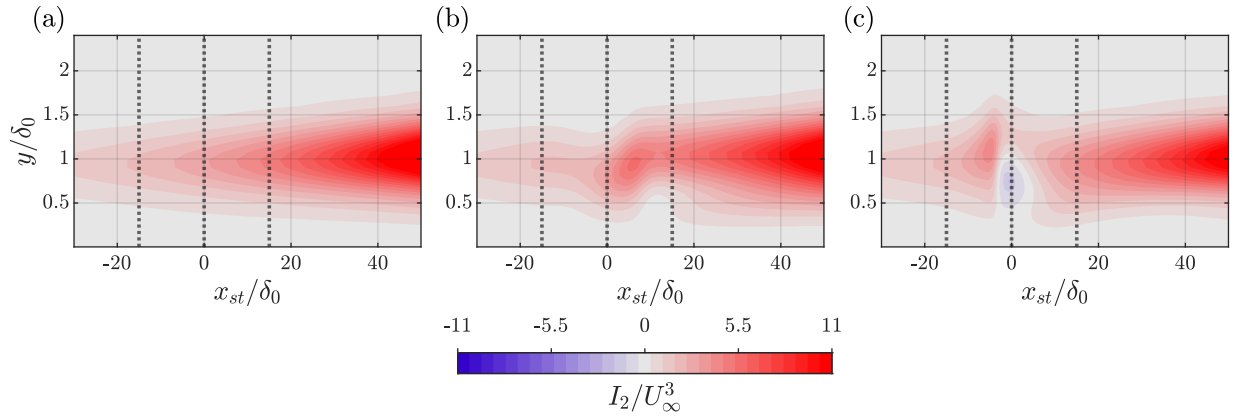

Figure 6.31: Contours of I_2 in (a) clean case, (b) $2.5p_f$ $30w$ case, and (c) $-2.5p_f$ $30w$ case; black dotted lines at $x_{st}/\delta_0 = -w/2,\ 0,$ and $w/2$ show the region of ΔP imposition in deformed cases.

6.4.1. Lift-up Effect

The I_2 component of production term decomposition, as per Section 5.2.1 denotes the influence of the lift-up effect (Casacuberta, Hickel, & Kotsonis, 2022; Lanzerstorfer & Kuhlmann, 2012). Thus, the production term is decomposed in base flow normal-tangential coordinates to understand the influence of I_2 as per the procedure suggested by Casacuberta, Hickel, Westerbeek, and Kotsonis (2022) (shown in Section 5.2.1). It is noted that I_2 is the dominant component and almost resembles the production term evolution across all cases, implying that the lift-up effect is the dominant mechanism in the cases considered here, as shown for reference cases in Figure 6.30. Thus, I_2 mimics the behaviour of $\mathcal{P}$ when its contours are plotted in Figure 6.31. The lift-up effect has a destabilizing tendency in the modal clean case. However, it has a stabilizing influence in the deformed cases as noted in Figure 6.31 (c). This mimics behaviour noted by Casacuberta, Hickel, and Kotsonis (2022), where they claim that the ”reverse lift-up effect” has a stabilizing influence as opposed

to the conventional lift-up effect which has a destabilizing influence. The change of behaviour of the lift-up effect can thereby provide a preliminary indication of deviation from modal behaviour, which needs to be compared with local modal behaviour to draw any final conclusions (as discussed in Section 5.2). To understand why a sign change of I_2 can occur, I_2 is decomposed to its 6 components as per Equation 5.64, which reads

$$I_2 = -\frac{2\pi}{\beta}\left(\tilde{u}_t^\dagger \frac{\partial U_B}{\partial x}\tilde{u}_n + \tilde{u}_t^\dagger \frac{\partial U_B}{\partial y}\tilde{v}_n + \tilde{v}_t^\dagger \frac{\partial V_B}{\partial x}\tilde{u}_n + \tilde{v}_t^\dagger \frac{\partial V_B}{\partial y}\tilde{v}_n + \tilde{w}_t^\dagger \frac{\partial W_B}{\partial x}\tilde{u}_n + \tilde{w}_t^\dagger \frac{\partial W_B}{\partial y}\tilde{v}_n\right) + \text{c.c.}. \tag{6.12}$$

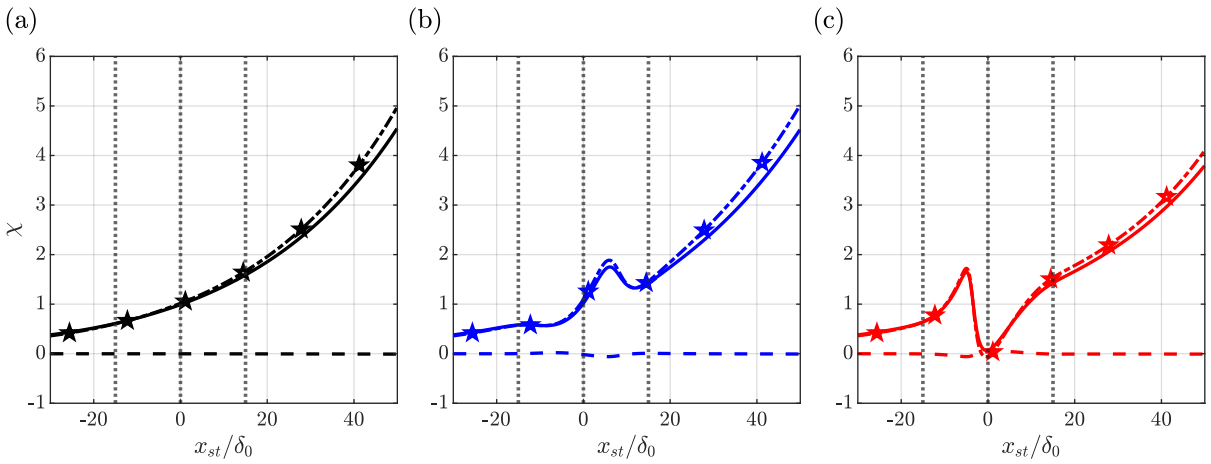

Figure 6.32: Evolution of $\chi = \int I_{2,b}dy$ (dash-dotted with stars), $\int I_{2,f}dy$ (solid) and $\int(I_2 - I_{2,b} - I_{2,f})dy$ (dashed) in (a) clean case, (b) $2.5p_f$ $30w$ case, and (c) $-2.5p_f$ $30w$ case; black dotted lines at $x_{st}/\delta_0 = -w/2,\ 0,$ and $w/2$ show the region of ΔP imposition in deformed cases.

The dominant terms in the evolution of I_2 are found to be $I_{2,b}$ and $I_{2,f}$, which are the second and sixth terms added to their corresponding complex conjugates in Equation 6.12. This is evidenced by integrating the various components of I_2 in the y direction and comparing their influence in Figure 6.32. The dominance of $I_{2,b}$ and $I_{2,f}$ is consistent with results of Casacuberta, Hickel, and Kotsonis (2022) in their FFS cases. The behaviour of I_2 can thus be explained by explaining the behaviour of either $I_{2,b}$ or $I_{2,f}$. Hence, an attempt is made to explain the behaviour of $I_{2,b}$, especially from the sign perspective, to understand why the lift-up effect might have a stabilizing influence. $I_{2,b}$ can be expressed as

$$I_{2,b} = -\frac{2\pi}{\beta}\left(\tilde{u}_t^\dagger \frac{\partial U_B}{\partial y}\tilde{v_n}\right) + \text{c.c.} = -\frac{4\pi}{\beta}\left(|\tilde{u}_t||\tilde{v}_n|\frac{\partial U_B}{\partial y}\cos(\phi_{2,n} - \phi_{1,t})\right) \tag{6.13}$$

The sign of this quantity can be determined by $\cos(\phi_{2,n} - \phi_{1,t})$, since U_{B_y} is consistently positive throughout the cases considered here. Despite base flow tangential and base flow normal components having physical significance as fields representative of streaks and rollers, respectively (Picella et al., 2018), the direct interpretation of their phase difference is difficult due to the convoluted nature of mathematics that goes into deriving their expressions. The key to understanding the behaviour of $\cos(\phi_{2,n} - \phi_{1,t})$ is to relate the phase difference of $\tilde{v}_n$ and $\tilde{u}_t$ to the phase difference between $\tilde{v}$ and $\tilde{u}$, whose behaviour has already presented in Figure 6.24. To find this relation, an expression for $\tilde{u}_t^\dagger \tilde{v}_n$ is written as

$$\tilde{u}_t^\dagger \tilde{v}_n = \tilde{u}_t^\dagger(\tilde{v} - \tilde{v}_t) = \tilde{u}_t^\dagger \tilde{v} - \tilde{u}_t^\dagger \tilde{v}_t, \tag{6.14}$$

where the relation between $\tilde{v}_n$, $\tilde{v}_t$ and $\tilde{v}$ is given by Equation 5.57. Referring to Equation 5.58, the term $\tilde{u}_t^\dagger \tilde{v}_t$ in Equation 6.14 can be expressed as

$$\tilde{u}_t^\dagger \tilde{v}_t = \frac{U_B\tau^\dagger V_B\tau}{||\mathbf{V}_B||^2} = \frac{U_B V_B|\tau|^2}{||\mathbf{V}_B||^2} = |\tilde{u}_t|\frac{V_B|\tau|}{||\mathbf{V}_B||}. \tag{6.15}$$

Rewriting the rest of the terms of equation Equation 6.14 in terms of exponentials,

$$|\tilde{u}_t||\tilde{v}_n|e^{i(\phi_{2,n}-\phi_{1,t})} = |\tilde{u}_t||\tilde{v}|e^{i(\phi_2-\phi_{1,t})} - |\tilde{u}_t|\frac{V_B|\tau|}{||\mathbf{V}_B||}. \tag{6.16}$$

Uniformly cancelling $|\tilde{u}_t|$ in Equation 6.16,

$$|\tilde{v}_n|e^{i(\phi_{2,n}-\phi_{1,t})} = |\tilde{v}|e^{i(\phi_2-\phi_{1,t})} - \frac{V_B|\tau|}{||\mathbf{V}_B||}. \tag{6.17}$$

Taking the real part of Equation 6.17,

$$|\tilde{v}_n|\cos(\phi_{2,n} - \phi_{1,t}) = |\tilde{v}|\cos(\phi_2 - \phi_{1,t}) - \frac{V_B|\tau|}{||\mathbf{V}_B||}. \tag{6.18}$$

Equation 6.18 makes it easier to interpret the behaviour of $\cos(\phi_{2,n} - \phi_{1,t})$. $\cos(\phi_2 - \phi_{1,t})$ represents a term similar to $\cos(\phi_2 - \phi_1)$, which played a role in determining the sign of the production term. ϕ_1 and $\phi_{1,t}$ take similar values potentially due to the base flow normal component in x direction being extremely small, i.e.

$$\tilde{u}_t = \tilde{u} - \tilde{u}_n \approx \tilde{u}, \tag{6.19}$$

$$\phi_{1,t} \approx \phi_1. \tag{6.20}$$

The similarity in values of ϕ_1 and $\phi_{1,t}$ is evidenced in the field of $\cos(\phi_{1,t} - \phi_1)$ and $\sin(\phi_{1,t} - \phi_1)$ shown in Appendix D.4, which take values close to one and zero, respectively, in both clean and deformed cases. Thus

$$\cos(\phi_2 - \phi_{1,t}) \approx \cos(\phi_2 - \phi_1). \tag{6.21}$$

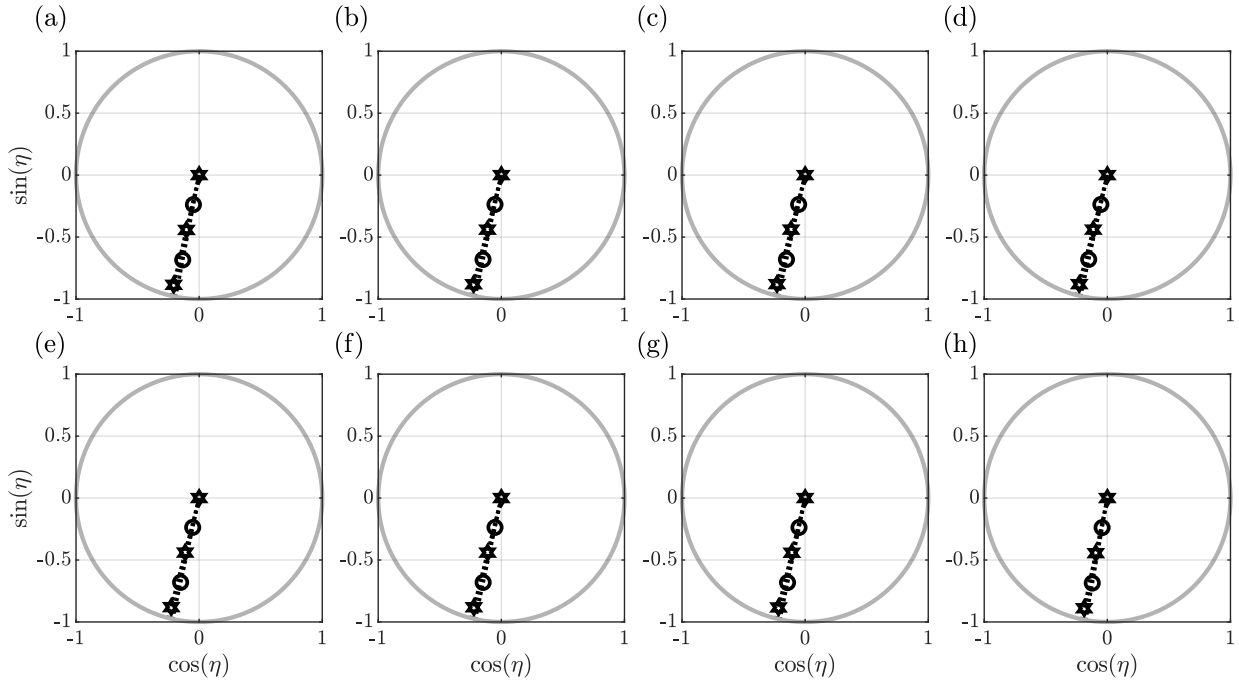

Figure 6.33: Phase plots of $\eta = \phi_2 - \phi_1$ (dotted with circles) and $\phi_{2,n} - \phi_{1,t}$ (dotted with stars) in the clean case at x_{st}/δ_0 = (a) $-0.75w$, (b) $-0.4w$, (c) $-0.2w$, (d) $-0.05w$, (e) $0.05w$, (f) $0.2w$, (g) $0.4w$, and (h) $0.75w$.

V_B on the other hand behaves in a manner similar to U_{B_x}, wherein it changes signs in regions of base flow deformation, as shown for reference cases in Figure 6.5. Thus, the phase difference between v'_n and u'_t leads or lags the phase difference between v' and u' based on the influence of V_B. This presents the picture that the I_2 term can capture the influence of sign of $\mathcal{P}_{y_d}$ terms via $\cos(\phi_2 - \phi_1)$ and that of $\mathcal{P}_{x_d}$ terms via V_B effects, providing insight into why I_2 fully captures the behaviour of $\mathcal{P}$. An examination of the relation between $\cos(\phi_2 - \phi_1)$ and $\cos(\phi_{2,n} - \phi_{1,t})$, and its connection to V_B is confirmed by examining plots of phase of $\phi_2 - \phi_1$ and $\phi_{2,n} - \phi_{1,t}$ for the clean and reference negative p_f case as shown in Figure 6.33 and Figure 6.34, respectively, at a level $y/\delta_0 = 0.5$, a level where stabilization is encountered in the I_2 terms of the reference negative p_f case.

In the clean case, $\cos(\phi_2 - \phi_1)$ and $\cos(\phi_{2,n} - \phi_{1,t})$ take close negative values as seen in Figure 6.33, due to the negligible influence of V_B. Negative sign of $\cos(\phi_{2,n} - \phi_{1,t})$ denotes a destabilizing tendency of the lift-up effect. In the reference negative p_f case, $\cos(\phi_{2,n} - \phi_{1,t})$ lags $\cos(\phi_2 - \phi_1)$ through most of the adverse ΔP region as V_B is positive, as seen in Figure 6.34 (a), (b), and (c). $\cos(\phi_{2,n} - \phi_{1,t})$ appears to be negative and thus, I_2 is destabilizing. This lagging tendency changes to a leading tendency at the end of the adverse ΔP region through most of the favourable ΔP region as

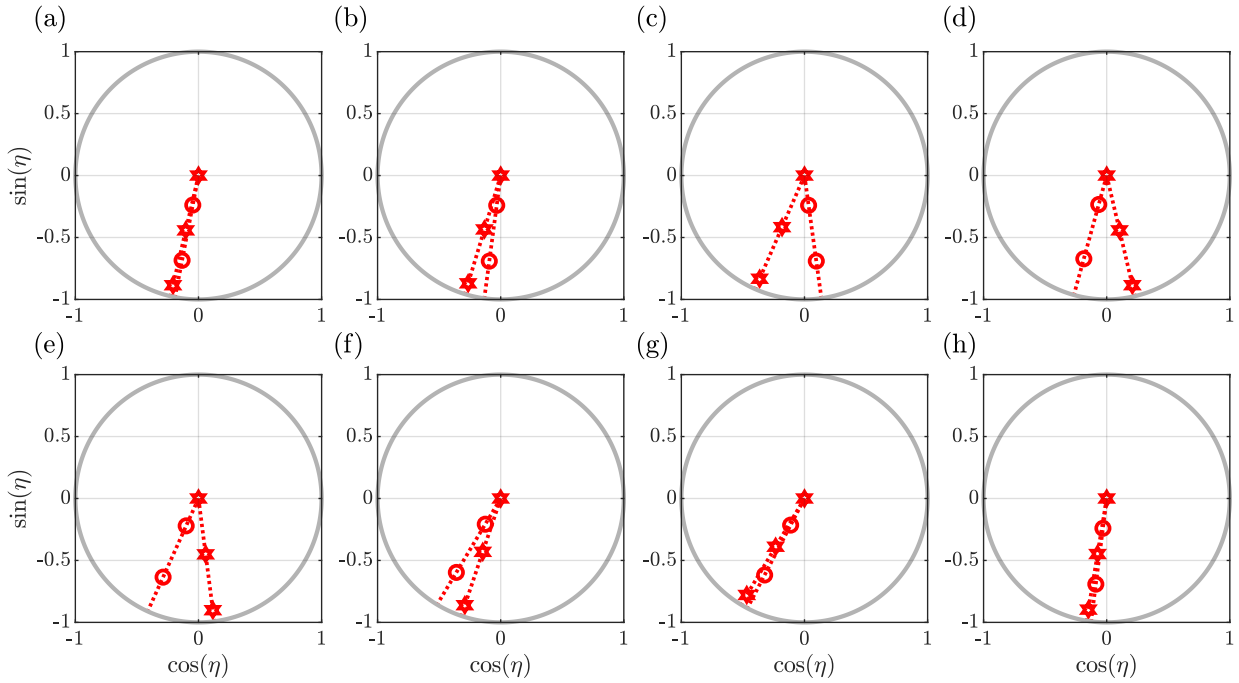

Figure 6.34: Phase plots of $\eta = \phi_2 - \phi_1$ (dotted with circles) and $\phi_{2,n} - \phi_{1,t}$ (dotted with stars) in the $-2.5p_f$ $30w$ case at x_{st}/δ_0 = (a) $-0.75w$, (b)$-0.4w$, (c) $-0.2w$, (d) $-0.05w$, (e) $0.05w$, (f) $0.2w$, (g) $0.4w$, and (h) $0.75w$.

seen in Figure 6.34 (d), (e), and (f) due to the change of sign of V_B, before both $\cos(\phi_2 - \phi_1)$ and $\cos(\phi_{2,n} - \phi_{1,t})$ take similar values towards the end of the deformation as observed in Figure 6.34 (g) and (h). During the transition from lag to lead of $\cos(\phi_{2,n} - \phi_{1,t})$ with respect to $\cos(\phi_2 - \phi_1)$, Figure 6.34 (d) and (e) show a positive value of $\cos(\phi_{2,n} - \phi_{1,t})$ even when $\cos(\phi_2 - \phi_1)$ is negative due to the action of changed V_B direction, thus yielding a stabilization of I_2, amounting to the observation of the reverse lift-up effect. This stabilizing influence only occurs in the reference negative p_f case but not in the reference positive p_f case since I_2 directly captures the effects of the production term, which only stabilizes in the former and not in the latter. I_2 stabilizes only in the cases where the production term becomes negative, and it can be claimed that those particular cases show preliminary hints of deviation from modal character. Whether the stabilizing tendency of the lift-up effect seen here translates to deviation from modal character is explored in Section 6.4.3, where comparisons against local modal behaviour provide a final conclusion on this matter.

6.4.2. Orr Mechanism

As stated in Section 5.2.1, conventional observations of the Orr mechanism in terms of observing tilt of streamfunction or constant vorticity are difficult in the framework of initially modal 3D perturbations. Hence, observation of u' perturbation tilt, given by the slope of wall-normal variation of ϕ_1 is considered here (Section 4.3.1), and in case their wall-normal variation differs with the change of chordwise station, the Orr mechanism is presumed to be active (Section 5.2.1). In case the tilt differs at different x stations, phase variation on different y levels are evaluated to conclude that there is no existence of a unique line of constant phase in xz plane, perpendicular to wavenumber direction, which is a property of modal evolution (as explained in Section 5.2.1). With the above approach in mind, the wall-normal variation of ϕ_1 is observed at three chordwise stations, one prior to the imposed deformation, another in the first half of deformation and another in the second half of deformation, as shown for reference cases in Figure 6.35, and the manifestation of ϕ_1 tilt is shown in yz plane contours of the real-valued u' field for further clarity in Figure 6.36.

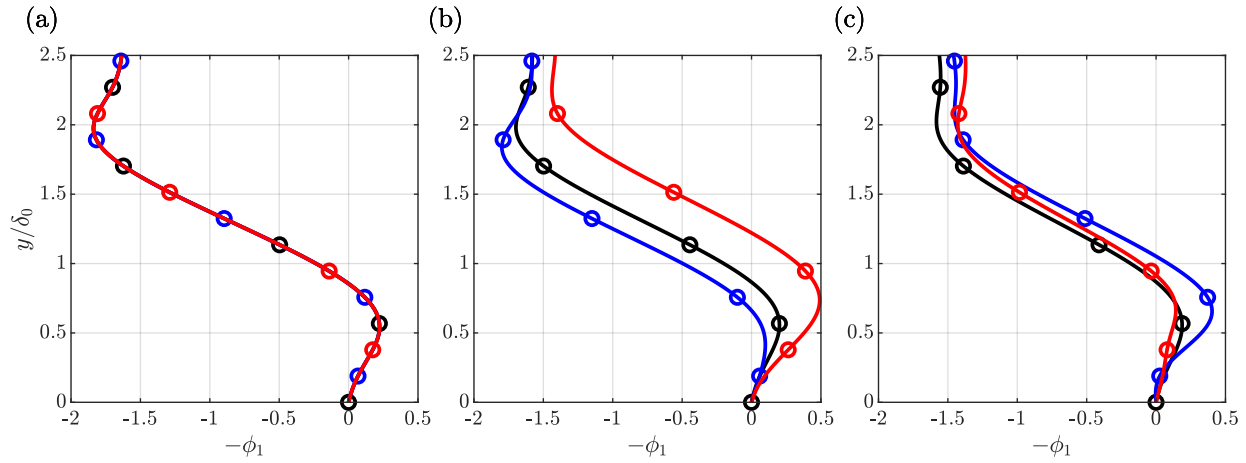

Figure 6.35: Wall-normal variation of $-\phi_1$ (solid with circles) in clean case (black), $2.5p_f$ $30w$ case (blue), and $-2.5p_f$ $30w$ case (red) at x_{st}/δ_0 = (a) $-0.75w$, (b) $-0.2w$, and (c) $0.4w$.

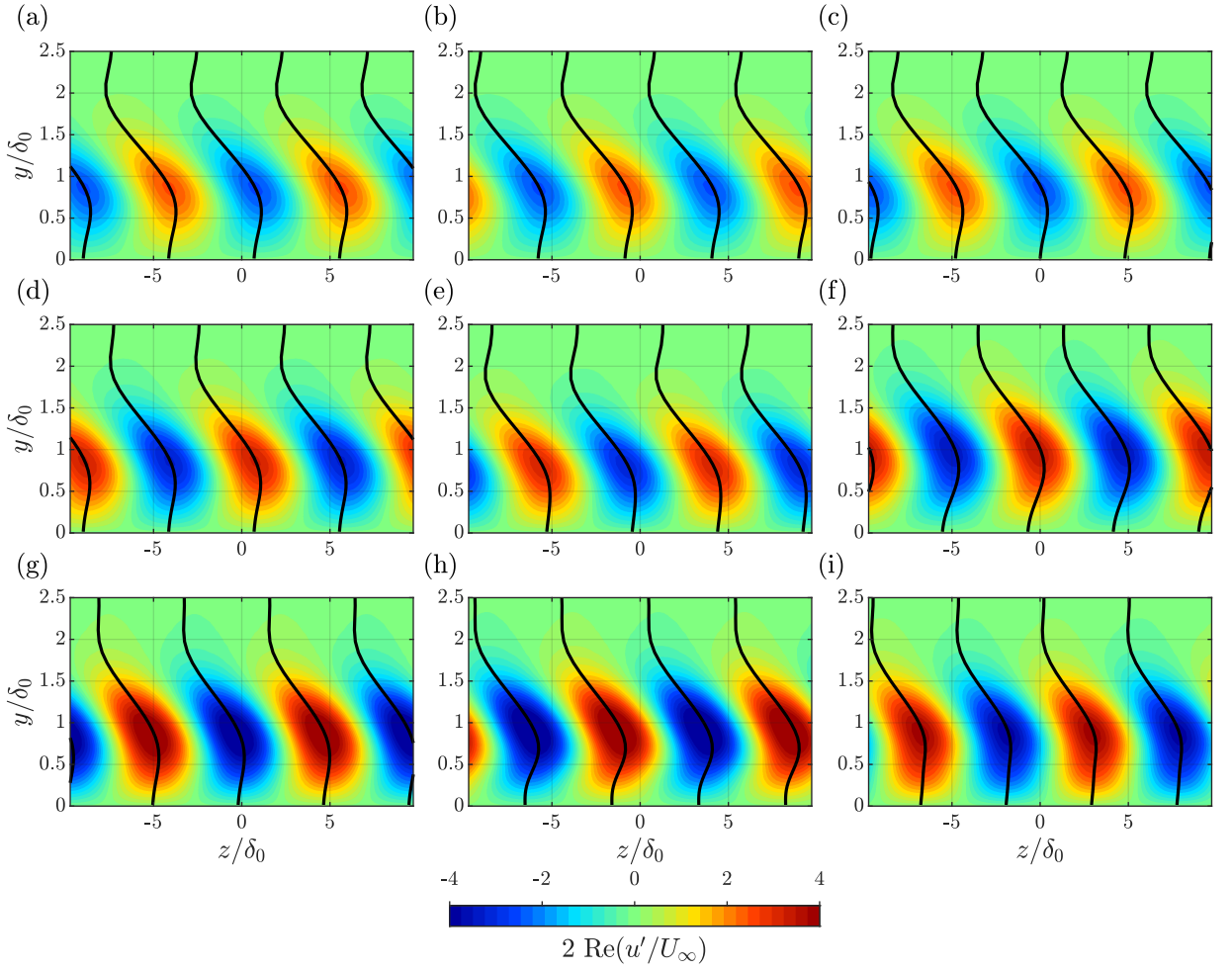

Figure 6.36: Contours of real-valued u' on yz planes for clean case (a,d,g), $2.5p_f$ $30w$ case (b,e,h), and $-2.5p_f$ $30w$ case (c,f,i) at $x_{st}/\delta_0 = -0.75w$ (top), $-0.2w$ (middle), and $0.4w$ (bottom); black dotted lines at $x_{st}/\delta_0 = -w/2,\ 0,$ and $w/2$ show the region of ΔP imposition in deformed cases.

At the first station, Figure 6.35 (a) shows the same wall-normal variation of ϕ_1 throughout all cases. Thus, the u' tilt is the same across all reference cases, as shown in Figure 6.36 (a) to (c), where there is virtually no difference in perturbation tilt. At the second station located within the first half of pressure deformation, the wall-normal variation of ϕ_1 is no longer

the same across clean and deformed cases as shown in Figure 6.35 (b), indicating that perturbation tilt is different for each case. An attempt is made to differentiate these based on how tilted the ϕ_1 distributions appear; more tilt corresponds to a higher gradient of ϕ_1 with y at a particular station. Also, the behaviour of ϕ is studied in two different regions; one near the wall ($y/\delta_0 \approx 0.5$) and one slightly further from the wall ($y/\delta_0 \approx 1.0$). ϕ_1 is tilted more in the near-wall region for the negative p_f cases compared to the clean case, whereas the ϕ_1 distribution is tilted less in case of the positive p_f cases compared to the clean case. In a region slightly further away from the wall, the ϕ_1 distributions appear with similar slopes, phase shifted from each other. Thus, in the contour plots of chordwise perturbation, it can be noted that the near-wall region corresponds to differences in ϕ_1 tilt between clean and deformed cases, whereas the region slightly further from wall appears to have a similar ϕ_1 tilt, as seen in Figure 6.36 (d) to (f).

In the second half of the pressure deformation, an opposite behaviour is noted in the near-wall region, evidenced in Figure 6.35 (c) and Figure 6.36 (g) to (i). The reference positive p_f case has a higher tilt compared to the previous station, whereas the reference negative p_f case exhibits a lower tilt compared to the previous station, as seen by comparing Figure 6.35 (c) with (b). Again, in the region further from the wall the differences in tilt are minor. This opposing behaviour for positive and negative p_f cases suggests a link with the nature of the base flow in adverse and favourable ΔP regions. It appears as though perturbations have a tendency to tilt more in adverse ΔP regions, whereas they have a tendency to tilt less in the favourable ΔP region, also evidenced for non-reference cases in Appendix D.5.

An attempt to explain the above-observed behaviour is made by considering the evolution equation of ϕ_1 (Equation 5.74) and evaluating it at two different levels $y/\delta_0 \approx 0.5$ and $y/\delta_0 \approx 1$. The evolution equation of ϕ_1 (Equation 5.74) reads

$$\frac{\partial \phi_1}{\partial x} = \underbrace{-\frac{W_B}{U_B}\beta}_{\mathcal{B}_A} \underbrace{-\frac{V_B}{U_B}\frac{\partial \phi_1}{\partial y}}_{\mathcal{P}_S} \underbrace{-\frac{\partial U_B}{\partial y}\frac{|\tilde{v}|}{U_B|\tilde{u}|}\sin(\phi_2-\phi_1)}_{\mathcal{B}_S} + \underbrace{\frac{1}{U_B|\tilde{u}|^2}\mathrm{Im}\left(\tilde{u}^{\dagger}\mathcal{F}^{p}{}_{1,(0,1)} + \tilde{u}^{\dagger}\mathcal{F}^{v}{}_{1,(0,1)}\right)}_{\mathcal{V}_P}. \tag{6.22}$$

The evolution of ϕ_{1_x} captured by finite difference is found to be the same as the evolution of ϕ_{1_x} captured by summing the terms on the right-hand side of Equation 6.22, as shown for the reference cases in Figure 6.37, thus verifying the equation. The abbreviations in Equation 6.22 are explained in more detail. $\mathcal{B}_A$ denotes the influence of base flow angle, as the base flow projected onto a xz plane at a fixed wall-normal height makes an angle $\theta_B = \mathrm{atan}(W_B/U_B)$ with the x axis. $\mathcal{P}_S$ denotes perturbation phase shear influence, which is likely to play a role when V_B has a considerable value in deformed regions. $\mathcal{B}_S$ denotes base flow shear influence and depends upon the shear of base flow, the phase difference between chordwise and wall-normal perturbations, and their respective amplitude functions. In a region slightly far from wall ($y/\delta_0 \approx 1$), the influence of $\mathcal{B}_S$ would be negligible as $\phi_2 - \phi_1$ is close to π, evidenced by values of $\cos(\phi_2 - \phi_1) = -1$ in Figure 6.24, leading to negligible values of $\sin(\phi_2 - \phi_1)$. But in a region closer to the wall, $\mathcal{B}_S$ should play a more important role as $\phi_2 - \phi_1$ deviates from π. $\mathcal{V}_P$ denotes the influence of perturbation pressure and viscous terms. As explained in Section 4.3.1, if ϕ_{1_x} has similar values for all levels, it implies that the ϕ_1 wall-normal distribution at any location would be a replication of the initial ϕ_1 wall-normal distribution. On the other hand, if ϕ_{1_x} is different in two different levels, it would indicate that the perturbation tilt changes with respect to its initial alignment.

The results of Equation 6.22 evaluated for reference clean and base flow deformed cases at the two different levels mentioned above are shown in Figure 6.37. In the clean case at a higher height shown in Figure 6.37 (d), it is noted that ϕ_{1_x} almost matches $\mathcal{B}_A$ due to the values of $\mathcal{B}_S$ tending to zero by virtue of $\sin(\phi_2 - \phi_1) \approx 0$. This implies that

$$\frac{1}{\beta}\frac{\partial \phi_1}{\partial x} \approx -\frac{W_B}{U_B}, \tag{6.23}$$

$$\theta_P = \mathrm{atan}\left(-\frac{1}{\beta}\frac{\partial \phi_1}{\partial x}\right) \approx \mathrm{atan}\left(\frac{W_B}{U_B}\right) = \theta_B, \tag{6.24}$$

where θ_P corresponds to the angle made by the lines of constant phase of u' in the xz plane with the x axis (refer subsection 4.3.1 for a detailed explanation). This implies that the stationary crossflow instability follows the base flow at this particular level. At the lower height (shown in Figure 6.37 (a)), it is noted that in addition to $\mathcal{B}_A$, $\mathcal{B}_S$ also determines ϕ_{1_x} behaviour. However, ϕ_{1_x} appears to have the same value across both higher and lower levels. It appears as though $\mathcal{B}_S$ compensates for the effect of base flow angle not being the same at two different heights through a non-negligible value of $\sin(\phi_2 - \phi_1)$ at the lower level. Variations of ϕ_1 with x remain similar at other heights to the variation observed at these two different heights, implying that the change of phase distribution in y would not change significantly when moving from one x station to another. This is evidenced by the above observation of ϕ_1 distributions having similar tilt across

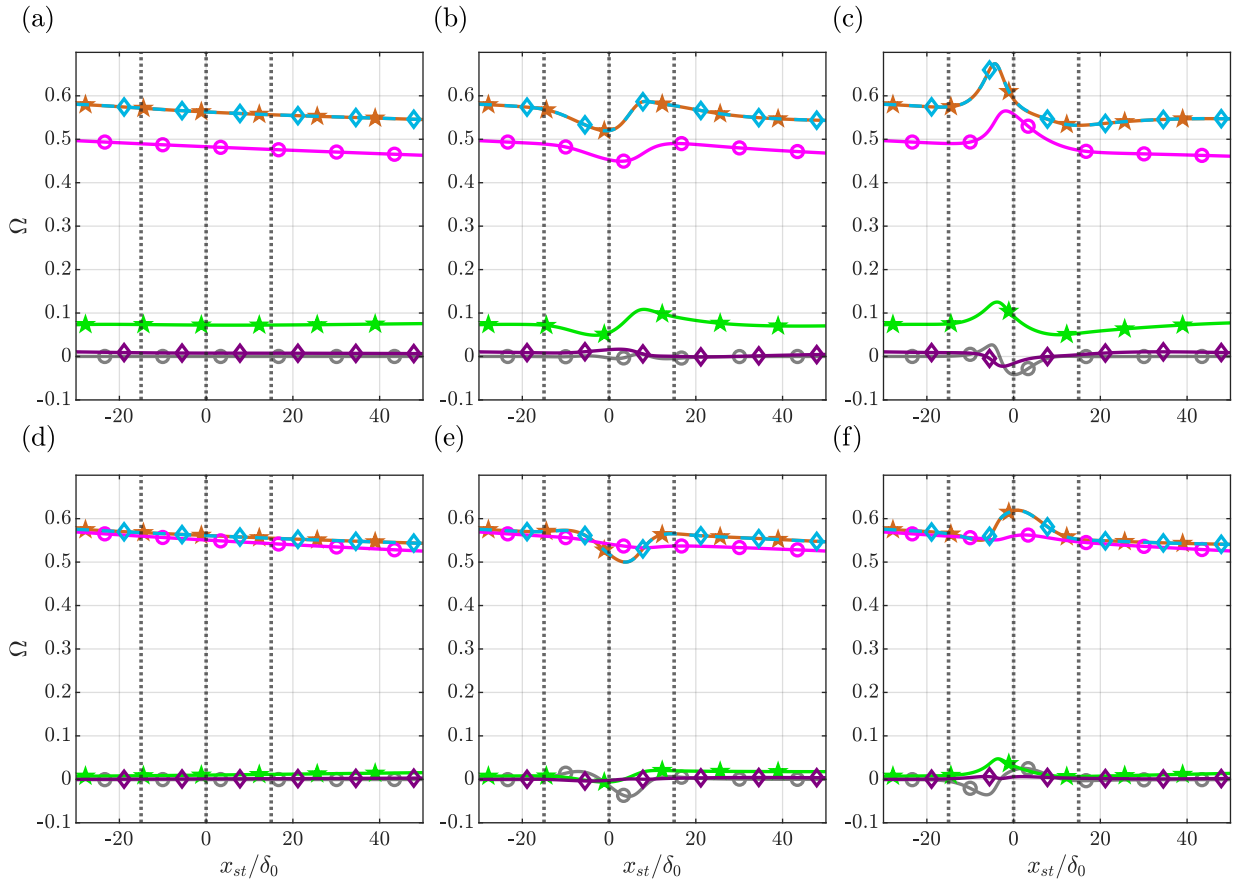

Figure 6.37: Budget of ϕ_1 evolution equation (Equation 6.22), $\Omega = \phi_{1_x}$ (orange solid with stars; calculated by finite difference), $\mathcal{B}_A$ (magenta solid with circles), $\mathcal{B}_S$ (light green solid with stars), $\mathcal{P}_S$ (grey solid with circles), $\mathcal{V}_P$ (purple solid with diamonds), and ϕ_{1_x} (sky blue dashed with diamonds; calculated evaluating Equation 5.74) of (a) clean case, (b) $2.5p_f$ $30w$ case, (c) $-2.5p_f$ $30w$ case at $y/\delta_0 = 0.5$ (top) and $y/\delta_0 = 1$ (bottom); black dotted lines at $x_{st}/\delta_0 = -w/2,\ 0,$ and $w/2$ show the region of ΔP imposition in deformed cases.

all x stations considered in Figure 6.35. In the deformed cases, the behaviour of similar evolution of ϕ_{1_x} at two different levels does not occur, evidenced by comparing its values for the reference positive p_f case in Figure 6.37 (b) and (e), and the reference negative p_f case in Figure 6.37 (c) and (f). The exact cause for this phenomenon is difficult to identify since the non-unique behaviour at different levels of all terms in the right-hand side of Equation 6.22 seem to affect ϕ_{1_x} to some extent or the other. The difference of ϕ_{1_x} at two different levels within the region of deformation explains that the wall-normal variation of ϕ_1 would not be the same at two different x stations considered within the deformation, as evidenced in Figure 6.37 (b), (c), (e), and (f). Thus, the perturbation has a tendency to tilt when observed in the yz plane. The issue of higher or lower tilt at the lower height can be addressed by observing the rate of perturbation phase change at $y/\delta_0 = 0.5$. At the lower height, for deformed cases, $\mathcal{B}_A$ and $\mathcal{B}_S$ have the same influence of slowing ϕ_{1_x} in favourable ΔP regions and enhancing ϕ_{1_x} in adverse ΔP regions with respect to clean case behaviour. Thus, at $y/\delta_0 = 0.5$ in the reference positive p_f case (seen in Figure 6.37 (b)), ϕ_1 appears slowed down initially and then enhanced compared to the clean case whereas the vice versa occurs in the reference negative p_f case (seen in Figure 6.37 (c)). A similar trend occurs for all heights below $y/\delta_0 = 0.5$ in both reference and non-reference cases (not shown here explicitly), contributing to ϕ_1 uniformly being slowed down below $y/\delta_0 = 0.5$ in a favourable ΔP region, leading to the decrease of tilt. The opposite occurs for an adverse ΔP region leading to the increase of tilt.

The different evolution of ϕ_1 at different heights implies that lines of constant phase in the xz plane do not remain in the same direction with a change of wall-normal height, as would be expected in the clean case. This leads to doubts about whether the lines of constant phase would remain aligned with the inviscid flow, as observed in the conventional modal evolution of crossflow instability (Bippes, 1999). The difference between the inviscid streamline angle and local angle of lines of constant phase (denoted ϕ_d) at a given height is shown in Figure 6.38 to elaborate on this observation. In Figure 6.38 (a), it is noted that the clean case has a nearly constant ϕ_d of approximately 2.5 degrees, whereas the deformed cases have ϕ_d of up to 5 degrees more or less than that of the clean case. The variation of ϕ_d with height in Figure 6.38

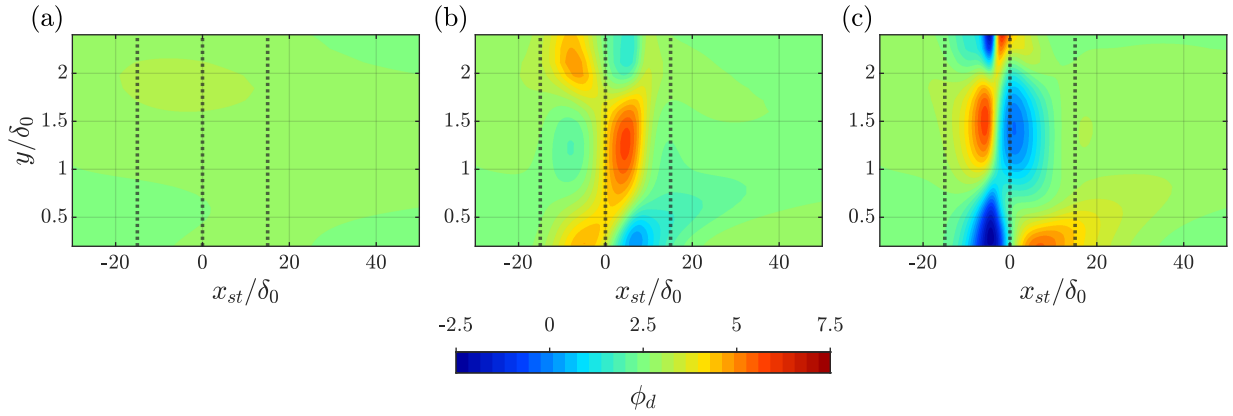

Figure 6.38: Contours of ϕ_d in (a) clean case, (b) $2.5p_f$ $30w$ case, and (c) $-2.5p_f$ $30w$ case; black dotted lines at $x_{st}/\delta_0 = -w/2,\ 0,$ and $w/2$ show the region of ΔP imposition in deformed cases.

(b) and (c) also shows that lines of constant phase do not remain constant with an increase of height. Thus, whereas no direct evidence is found of the Orr mechanism influencing perturbation energy gain or loss mechanisms, its influence on perturbation lines of constant phase in the xz plane being misaligned or aligned with the inviscid flow is clear. Doubts are expressed as to whether a wavenumber direction can be defined in regions of deformed flow since the perturbation lines of constant phase of u' perturbation in xz plane can't be replaced by a single representative line of constant phase in xz plane. Thus, the observation of the difference in direction of propagation of lines of constant phase in xz planes in deformed regions of flow hints towards a deviation from traditionally observed modal behaviour. The deviation of lines of constant phase from inviscid flow is most prominent for the highest p_f cases, progressively reducing for lower p_f cases, as shown in Appendix D.5.

6.4.3. Comparison with Local Modal Behaviour

ILST solutions are assumed to provide an estimate of local modal behaviour. The results of HLNS and ILST are compared by the perspective of the lift-up and Orr mechanism with PSE acting as an intermediary to understand the difference of ILST and HLNS results, as explained in Section 5.2.1. The lift-up effect is first evaluated, via a representation of the I_2 term, to check whether I_2 generated via the ILST and PSE solutions show a reverse lift-up effect in regions where I_2 generated via the HLNS solution becomes negative. To calculate the I_2 term, all perturbation results are cast into the HLNS ansatz as per Equation 5.2.1. It is observed that PSE and HLNS predict similar I_2 evolution across all cases, including those where I_2 stabilizes, as evidenced by comparing the I_2 evolution for reference cases generated by PSE shown in Figure 6.39 (g), (h), and (i) with those generated by HLNS in Figure 6.31. This highlights that the action of the dominant mechanism in the tangential-normal decomposition of production term, given by I_2, has the same character for HLNS and PSE even though the amplitude values don't fully match for both methods in deformed cases, as shown in Section 4.4.

There remains some ambiguity on the consideration of V_B while computing I_2 terms for ILST solutions, since V_B itself is neglected when ILST solves for eigenmodes. Thus, the effect of considering V_B while computing I_2 (shown for reference cases in Figure 6.39 (a), (b), and (c)) and neglecting V_B while computing I_2 (shown for reference cases in Figure 6.39 (d), (e), and (f)) are evaluated separately for ILST. I_2 calculations for ILST solutions including V_B effects seem to approximately match the trends of I_2 predicted by PSE and HLNS, as seen for the reference cases by comparing the bottom two rows of Figure 6.39. The most surprising result is that the ILST computations of I_2 including wall-normal velocity give a stabilizing value of lift-up effect in the reference negative p_f case shown in Figure 6.39 (f), in a region very similar to the region of stabilization seen in PSE (shown in Figure 6.39 (h)) and HLNS. The reason for such stabilization can be understood by first considering the I_2 computation that neglects V_B for the reference negative p_f case (shown in Figure 6.39 (c)). Here the sign of I_2 is just governed by $\cos(\phi_2 - \phi_1)$, since $v'_n = v'$ when $V_B = 0$ (refer Equation 5.55). The field of $\cos(\phi_2 - \phi_1)$, visualized for reference cases in Figure 6.40, shows upward and downward movement of constant contour levels in regions of adverse and favourable ΔP, respectively, similar to observations in the contours of $\cos(\phi_2 - \phi_1)$ in both PSE (Figure 6.40) and HLNS (Figure 6.24). The change in sign of the ILST $\cos(\phi_2 - \phi_1)$ field in the adverse ΔP region is observed at a very high height compared to the PSE $\cos(\phi_2 - \phi_1)$ field, exposing larger regions of positive $\cos(\phi_2 - \phi_1)$, subsequently leading to some degree of stabilization in I_2 seen in Figure 6.39 (c). On considering the effects of wall-normal velocity, there is a phase difference between v'_n and v' attributed to non-zero wall-normal velocity (as demonstrated in subsection 5.2.1), which leads to additional stabilization.

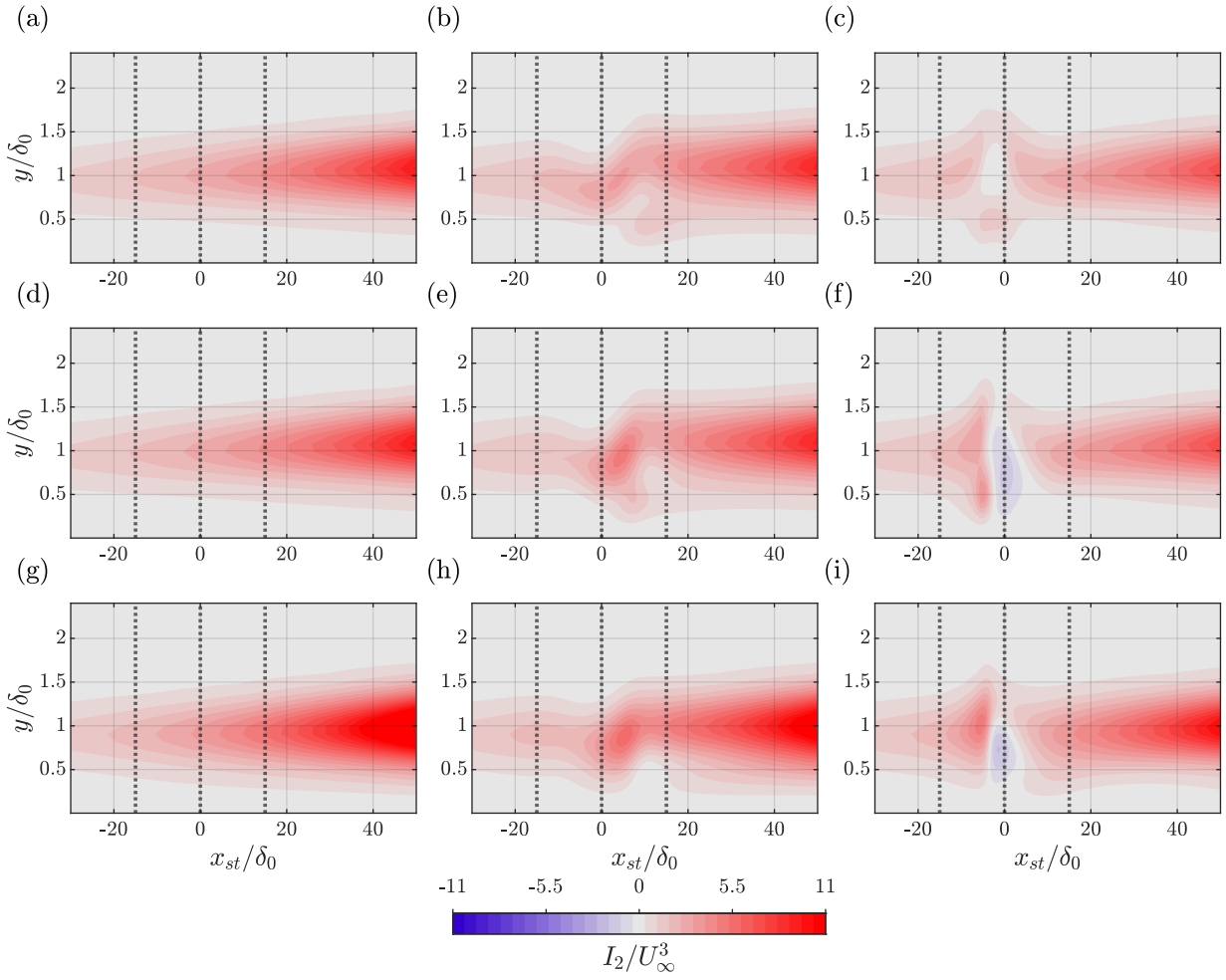

Figure 6.39: Contours of I_2 in clean case (a,d,g), $2.5p_f$ $30w$ case (b,e,h), and $-2.5p_f$ $30w$ case (c,f,i) generated using solutions of ILST ignoring V_B (top), ILST considering V_B (top), and PSE (bottom); black dotted lines at $x_{st}/\delta_0 = -w/2,\ 0,$ and $w/2$ show the region of ΔP imposition in deformed cases.

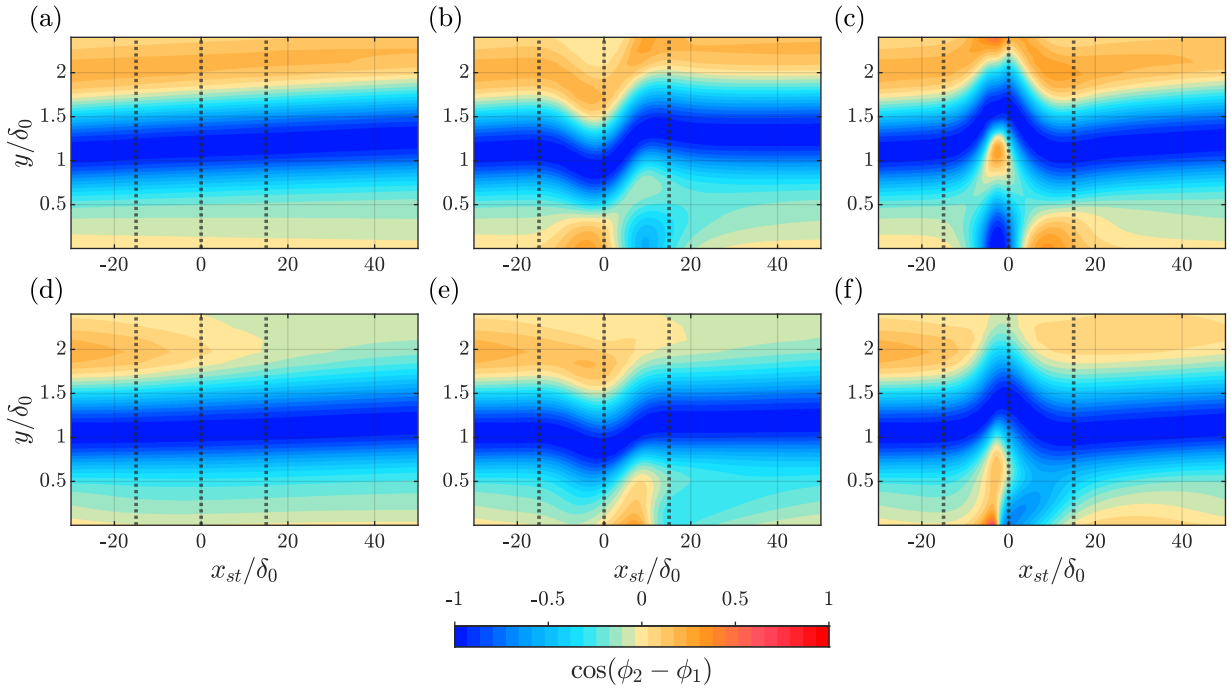

Figure 6.40: Contours of $\cos(\phi_2 - \phi_1)$ in clean case (a,d), $2.5p_f$ $30w$ case (b,e), and $-2.5p_f$ $30w$ case (c,f) solved using ILST (top) and PSE (bottom); black dotted lines at $x_{st}/\delta_0 = -w/2,\ 0,$ and $w/2$ show the region of ΔP imposition in deformed cases..

Thus, the local modal descriptions can capture some extent of lift-up driven stabilization without considering wall-normal base flow velocity, but the full extent of stabilization can only be captured by considering the effects of wall-normal base flow velocity. The effects of the reference positive p_f and clean case aren't considered in further detail as the lift-up effect is uniformly destabilizing in both cases. The consistent stabilization of I_2 across results of all solvers considered here with varying levels of approximation in the reference negative p_f case hints that the reversal of the lift-up effect is not an indication of deviation from local modal behaviour.

From the perspective of the Orr mechanism, perturbation tilt is very similar across ILST, PSE and HLNS solutions for the clean case seen by comparing Figure 6.42 (a), (d), and (g). However, the ϕ_1 distributions tilt similarly for HLNS and PSE solutions but differently for ILST solutions in regions of deformation in positive and negative p_f cases, as seen by observing the trends of reference positive and negative p_f case in the second and third column of Figure 6.42, respectively. A potential reason cannot be pinpointed since an evolution equation for ϕ_{1_x} is impossible to formulate using ILST as it is a local method, but it can be hypothesized that the neglect of upstream information and neglect of strong streamwise derivatives could result in deviations in deformed cases. Perturbation tilt in yz planes and lines of constant phase in xz planes potentially have nothing to do with each other in ILST solutions, as ILST predicts a single representative line of constant phase (given by $\alpha_r x + \beta z = C$) perpendicular to the wavenumber vector. Whereas in PSE and HLNS, the different yz plane tilt in different x stations leads to different values of ϕ_{1_x} at different wall-normal levels, which in turn leads to the absence of a unique line of constant phase with the change of wall-normal height. A comparison of the angle made between the lines of constant phase in xz plane and inviscid flow (their difference denoted ϕ_d) provides more insight into the behaviour of xz lines of constant phase across solvers. ILST, PSE, and HLNS solutions show the same behaviour of ϕ_d evolution in the clean case evidenced by comparing Figure 6.41 (a) and (c), implying the existence of a unique line of constant phase in xz plane, aligned almost to the direction of inviscid flow. In the deformed cases, ILST predicts some differences in ϕ_d evolution compared to the clean case (as evidenced for reference deformed cases in Figure 6.41 (b) and (c)), but these are minor compared to ϕ_d predicted by HLNS and PSE solutions (as evidenced for PSE solutions of reference deformed cases in Figure 6.41 (e) and (f), noting PSE and HLNS both predict very similar ϕ_d evolution trends). Thus, the observation of the Orr mechanism is linked to deviation from local modal behaviour, as lines of constant phase do not tend to align with the inviscid flow to the extent the representative line of constant phase of the local modal solution aligns with the inviscid flow. The direction of a local wavenumber vector also seems difficult to perceive in the HLNS and PSE solutions in deformed regions of flow due to the inability to find a representative xz line of constant phase, but can easily be constructed for the ILST solution in deformed regions of flow. The idea of a "directional profile" thus potentially collapses in regions of highly deformed base flow.

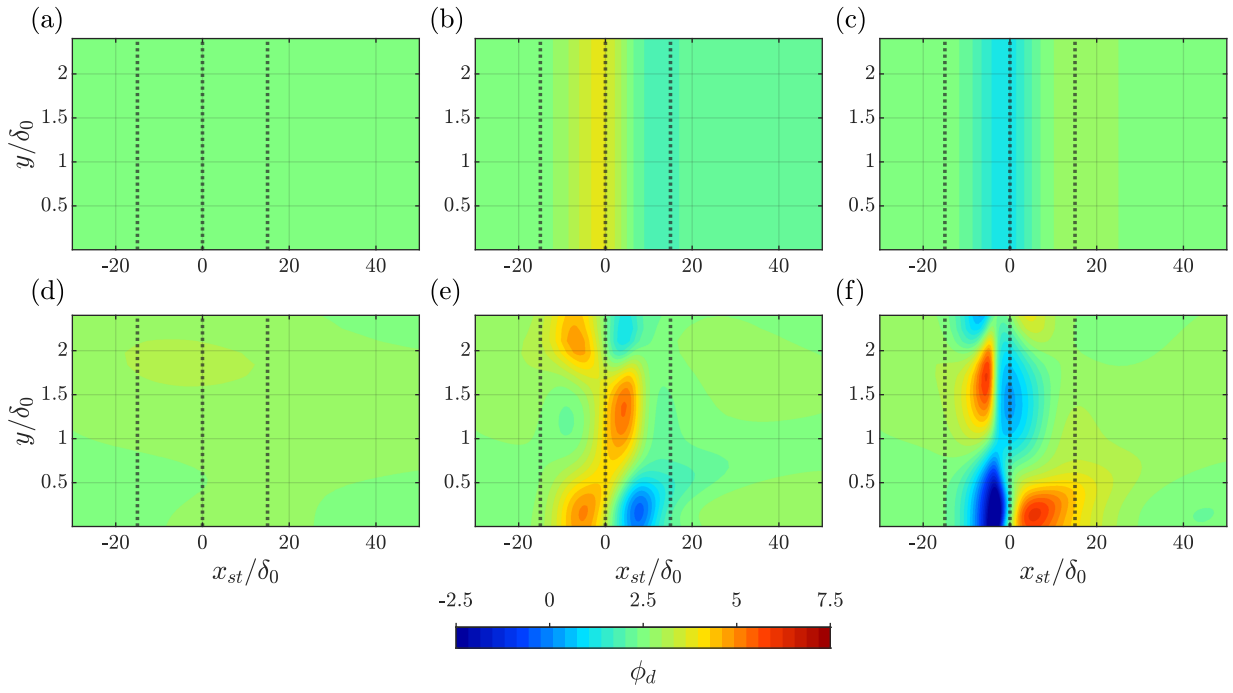

Figure 6.41: Contours of ϕ_d in clean case (a,d), $2.5p_f$ $30w$ case (b,e), and $-2.5p_f$ $30w$ case (c,f) generated using ILST data (top) and PSE data (bottom); black dotted lines at $x_{st}/\delta_0 = -w/2,\ 0,$ and $w/2$ show the region of ΔP imposition in deformed cases.

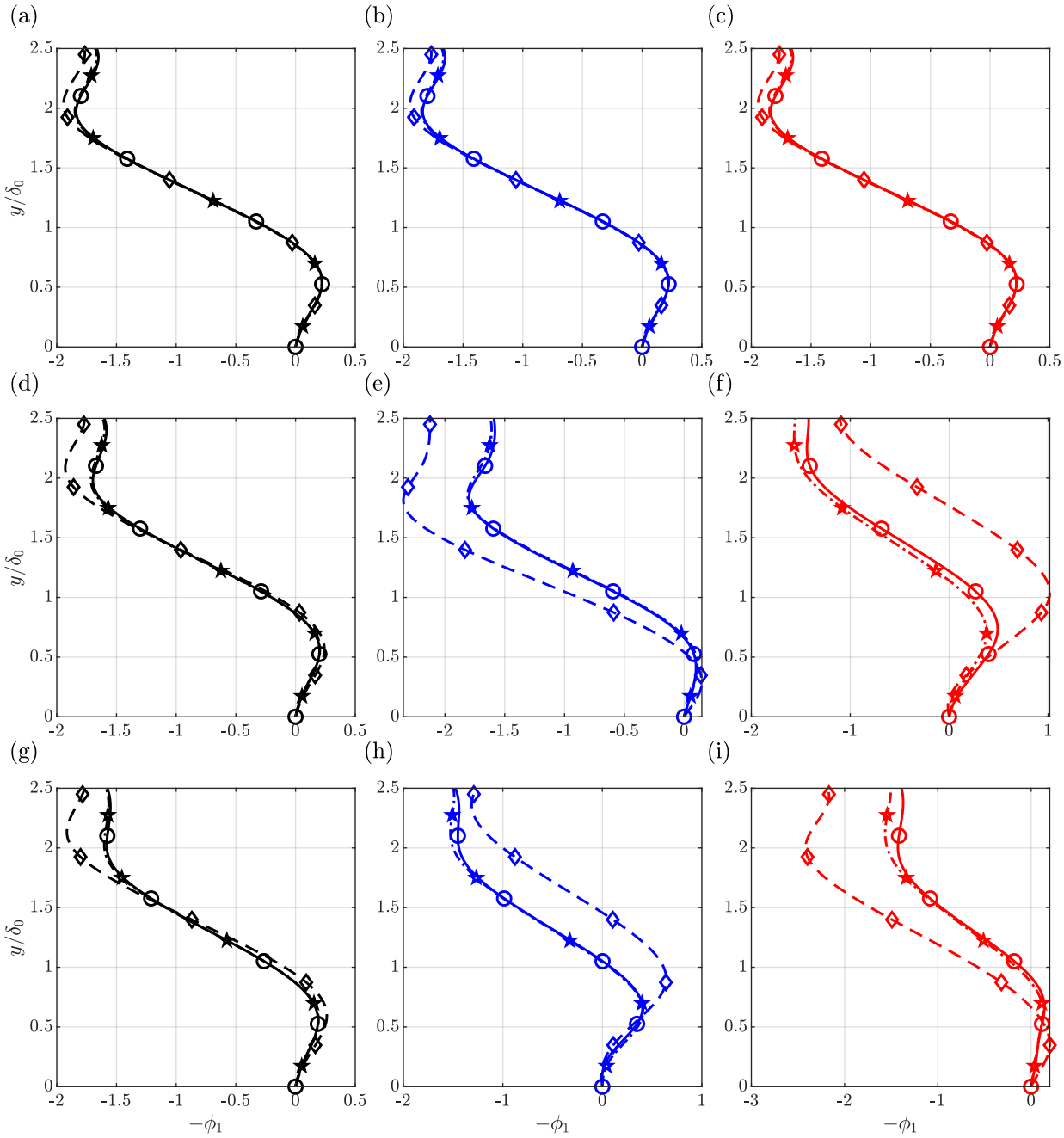

Figure 6.42: Wall-normal variation of $-\phi_1$ in clean case (a,d,g), $2.5p_f$ $30w$ case (b,e,h), and $-2.5p_f$ $30w$ case (c,f,i) at $x_{st}/\delta_0 = -0.75w$ (top), $-0.2w$ (middle), and $0.4w$ (bottom) generated using HLNS data (solid with circles), PSE data (dash-dotted with stars), and ILST data (dashed with diamonds).

6.4.4. Non-modal Behaviour Criteria

As there is evidence of the action of the Orr mechanism in deformed base flows resulting in a potential deviation from modal behaviour, non-modal behaviour criteria prescribed in Section 5.2.2 are evaluated in this section to find whether non-modal effects could govern instability evolution in regions of base flow deformation. The comparison of the growth rate of base flow tangential and total perturbation of reference cases are presented in Figure 6.43, where the growth rates are computed at the "max" location since no secondary peaks appear in the amplitude function of τ' or the norm of $\boldsymbol{v}'_{(0,1)}$. The growth rates superpose on each other through clean and deformed cases, indicating that non-modal effects are absent. The comparison of the cosine of the angle between base flow tangential and total perturbation vector for reference cases at the max level of τ', shown in Figure 6.44, also yields a value very close to one across deformed and clean cases, indicating that these vectors are also aligned with each other. This further suggests that non-modal effects aren't observed in the cases considered here. Casacuberta, Hickel, Westerbeek, and Kotsonis (2022) find that the misalignment of total perturbation

vector with tangential perturbation vector depends on growth rates of tangential and normal perturbation being different from each other. Since the growth rates are similar at max level, $\cos(\zeta_{(0,1)})$ at max level show negligible difference among clean and deformed cases. Only at a location extremely close to the wall given by $y/\delta_0 = 0.05$, some angular difference is noted between the evolution of deformed and clean cases. A potential reason for this is the strong streamline deflection seen at these levels as shown in Figure 6.12. However, these heights are not relevant for energy exchange mechanisms, as observed in Figure 6.18 since the values of production term are negligible beneath $y/\delta_0 \approx 0.2$. Hence, it can be concluded that non-modal character is not observed in the current cases considered here.

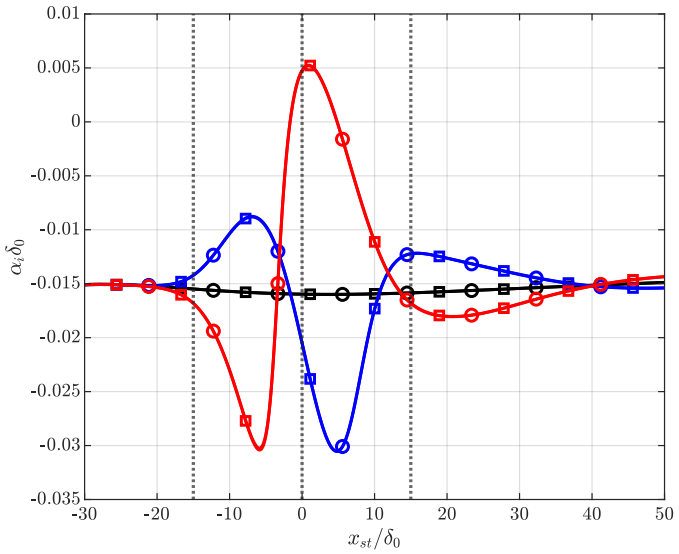

Figure 6.43: Chordwise variation of growth rate of base flow tangential perturbation (solid with circles) and total perturbation (solid with squares) in (a) clean case (black), (b) $2.5p_f$ $30w$ case (blue), and (c) $-2.5p_f$ $30w$ case (red); black dotted lines at $x_{st}/\delta_0 = -w/2,\ 0,$ and $w/2$ show the region of ΔP imposition in deformed cases.

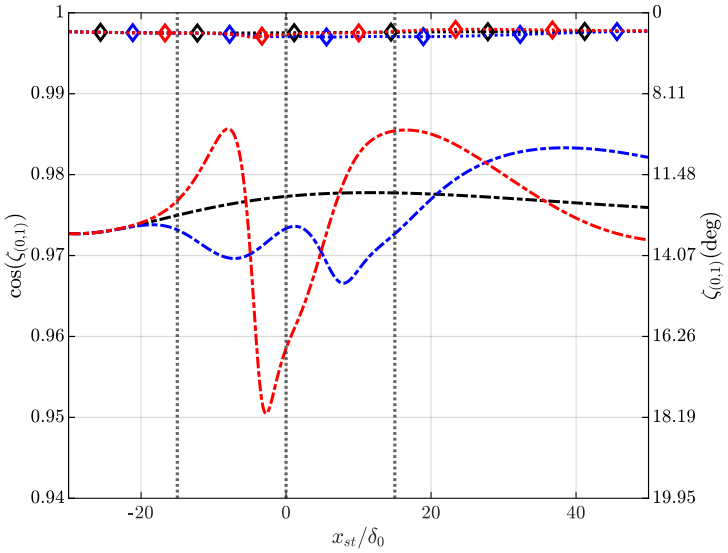

Figure 6.44: Chordwise variation of $\zeta_{(0,1)}$ at max (dotted with diamonds) and $y/\delta_0 = 0.05$ (solid) in (a) clean case (black), (b) $2.5p_f$ $30w$ case (blue), and (c) $-2.5p_f$ $30w$ case (red); black dotted lines at $x_{st}/\delta_0 = -w/2,\ 0,$ and $w/2$ show the region of ΔP imposition in deformed cases.

7

Comparison with the FFS

As mentioned in Section 3.5, boundary layer solvers manage to provide a local near-wall base flow pressure change at the expense of providing wall-normal velocity and wall-tangential base flow chordwise derivative fields totally different from the full Navier Stokes representation given by DNS. The idealization of base flow implies that the perturbation evolution trends through this base flow might also end up being an idealization (refer subsection 6.3.3), and might be unrepresentative of perturbation behaviour observed in instances of natural base flow deformation such as an FFS. Hence, this chapter first aims to critically examine if characteristics of base flow influencing mechanisms of perturbation evolution (i.e. the production term) in an FFS bear resemblance to a synthetic three-way base flow deformation with similar pressure characteristics. The chapter then aims to compare perturbation evolution in the region of base flow deformation, with an emphasis on production term behaviour, to comment on whether a synthetic base flow deformation can capture the influence of an FFS on perturbation evolution. All three synthetic three-way cases show similar observations of base flow and perturbation behaviour, and hence only the details of the highest p_f case are primarily considered here i.e. the $2.5p_f\ 30w \times 2$ case (also denoted reference synthetic three-way case). Results generated using the data of the medium FFS height simulated by Casacuberta, Hickel, Westerbeek, and Kotsonis (2022) are primarily considered here, with this FFS case being termed as the "reference FFS case". The base flow and perturbation behaviour of the reference FFS case and lowest height FFS simulated by Casacuberta, Hickel, Westerbeek, and Kotsonis (2022) show similar trends. Although the base flow characteristics of the largest FFS case and reference FFS are similar, the perturbation shows different behaviour in the FFS downstream region, possibly due to the very strong base flow deformation it imposes and is hence only mentioned while considering recommendations for future work (Section 8.2).

7.1. Base Flow Comparison

The character of ΔP i.e. adverse or favourable was used in Chapter 6 to split the base flow deformation into parts for ease of interpreting behaviour trends in each of these parts. Thus, values of ΔP for the reference three-way and step cases are shown in Figure 7.1 (a) and (d). In the synthetic cases, ΔP is imposed at the top and propagates down to the wall. Whereas in the FFS case, the local pressure differences w.r.t to the clean case (also termed ΔP) are naturally generated by the presence of a sharp geometrical discontinuity in the form of an FFS. The ΔP distribution of the FFS case is more powerful than the synthetically imposed ΔP distribution, and shows wall-normal variation, reducing gradually away from the wall, as opposed to the uniform synthetically imposed ΔP distribution. Both the three-way and FFS cases have a three-way ΔP distribution, as demonstrated in Figure 2.6 and Figure 2.1, respectively. The FFS cases have a much shorter region of favourable ΔP (approximately at $x_{st}/\delta_0 = 0$) in comparison with the $2.5p_f\ 30w \times 2$ case, flanked by two adverse ΔP regions of similar width.

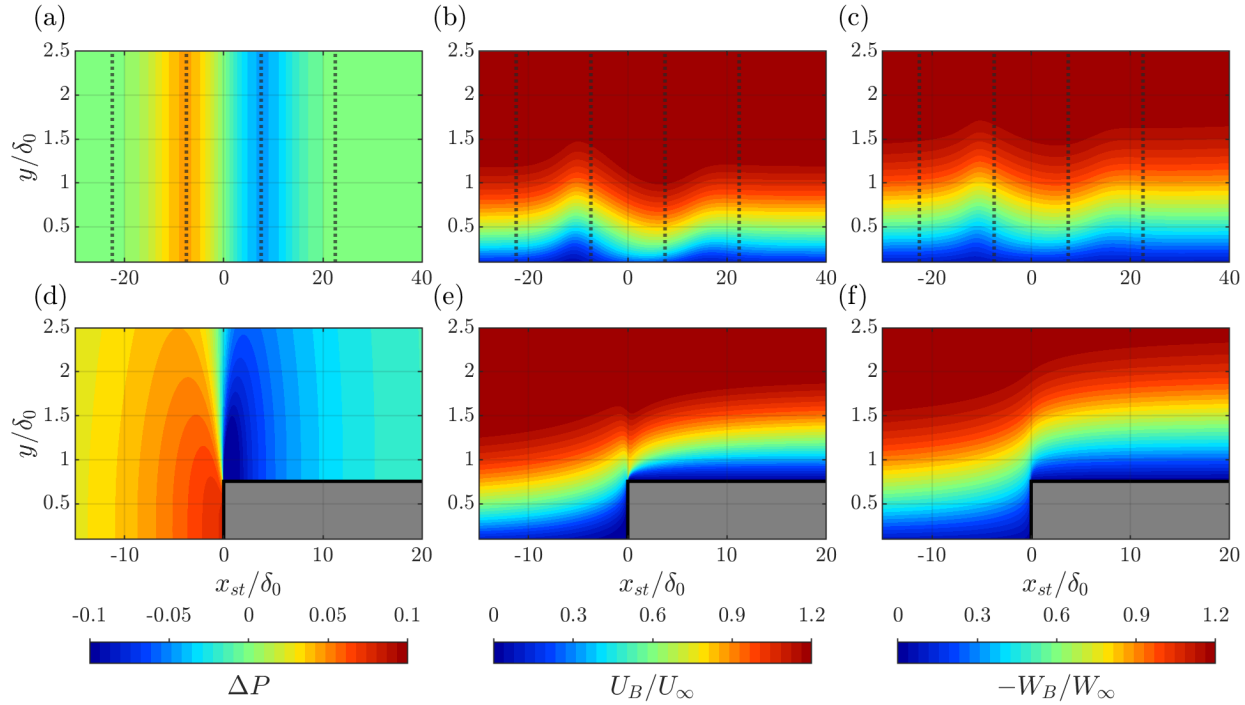

Figure 7.1: Contours of ΔP (a,d), U_B (b,e), and W_B (c,f) in the $2.5p_f$ $30w \times 2$ case (top) and the reference FFS case (bottom); black dotted lines at $x_{st}/\delta_0 = -3w/4,\ -w/4,\ w/4,$ and $3w/4$ show the region of ΔP imposition.

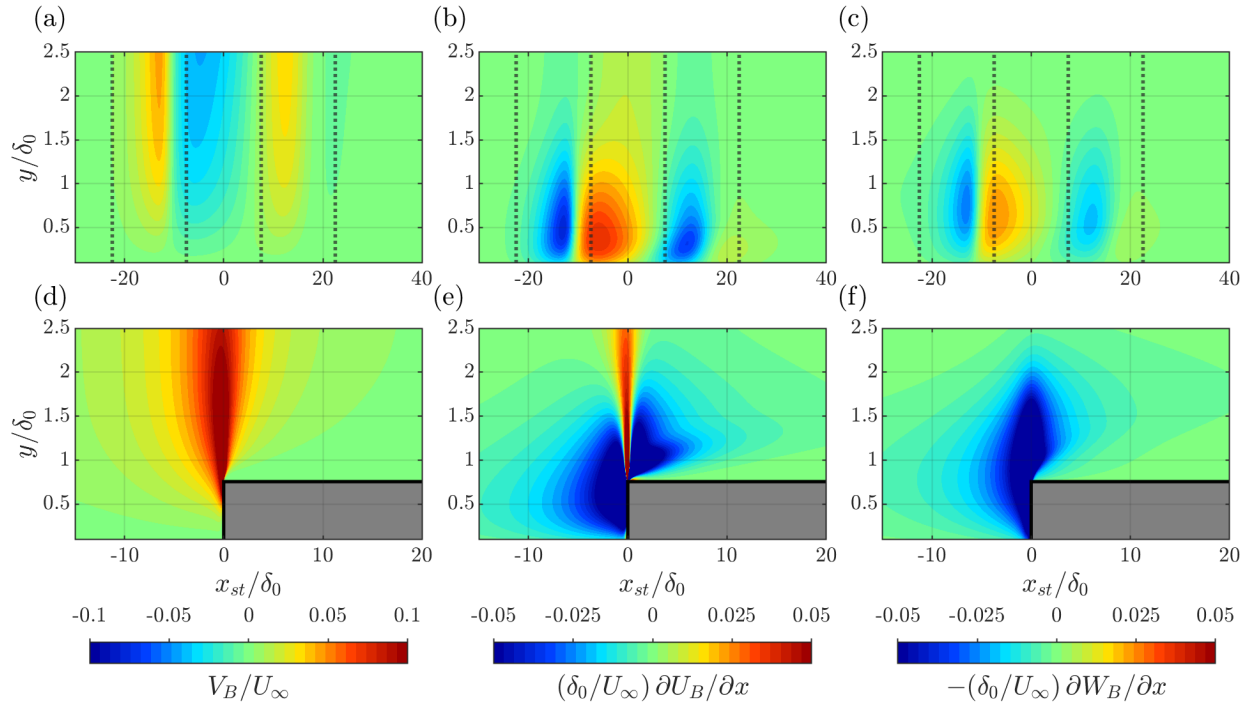

Figure 7.2: Contours of V_B (a,d), U_{B_x} (b,e), and $-W_{B_x}$ (c,f) in the $2.5p_f$ $30w \times 2$ case (top) and the reference FFS case (bottom); black dotted lines at $x_{st}/\delta_0 = -3w/4,\ -w/4,\ w/4,$ and $3w/4$ show the region of ΔP imposition.

The ΔP distributions affect the base flow in deformed regions with mechanisms similar to those explained in Section 6.1. In the reference cases, the adverse ΔP region results in a chordwise deceleration of chordwise base flow, as shown in Figure 7.2 (b) and (e), and subsequent upward movement of contour levels, as shown in Figure 7.1 (b) and (e), due to a local adverse pressure gradient in this region. Whereas a favourable ΔP region in the reference case results in chordwise acceleration of chordwise base flow, and downward movement of contour levels due to a locally higher favourable base

flow pressure gradient in reference cases compared to the clean case. It should be noted that behaviour in the non-reference cases can be explained with exactly the same explanation as reference cases with the exception of flow behaviour in the adverse ΔP region of the lowest p_f synthetic three-way case, where flow deceleration occurs due to an effective pressure gradient less favourable than the clean case, instead of an adverse effective pressure gradient. Values of U_{B_x} directly correspond to the opposite sign of V_{B_y} by virtue of the continuity equation (as seen for reference cases comparing Figure 7.3 (a) and (d) with Figure 7.2 (b) and (e)). The behaviour of V_B follows from the behaviour of -U_{B_x}, wherein an upwash persists in regions of decelerated chordwise base flow, by means of the integrated continuity equation (Equation 6.1) argument stated in Section 6.1), as seen for reference cases by comparing Figure 7.2 (a) and (d) with Figure 7.2 (b) and (e). Although a downwash persists in regions of accelerated chordwise base flow in synthetic deformations, an upwash is noted in regions of accelerated chordwise base flow in the FFS base flows. In the FFS case, the geometrical obstruction induces upwash upstream of the step in the adverse ΔP, which does not change sign in the favourable ΔP region. Instead, the peak of positive V_B undergoes an abrupt shift very near to the wall on encountering the step (Eppink, 2018), by means of which V_{B_y} remains negative throughout the wall-normal height post the V_B peak. This results in a positive U_{B_x} in wall-normal heights post the V_B peak even when V_B is positive. Such behaviour doesn't occur in the favourable ΔP region of the reference synthetic three-way case where V_B gradually increases with the increase of wall-normal height, thus mimicking the sign of $-U_{B_x}$.

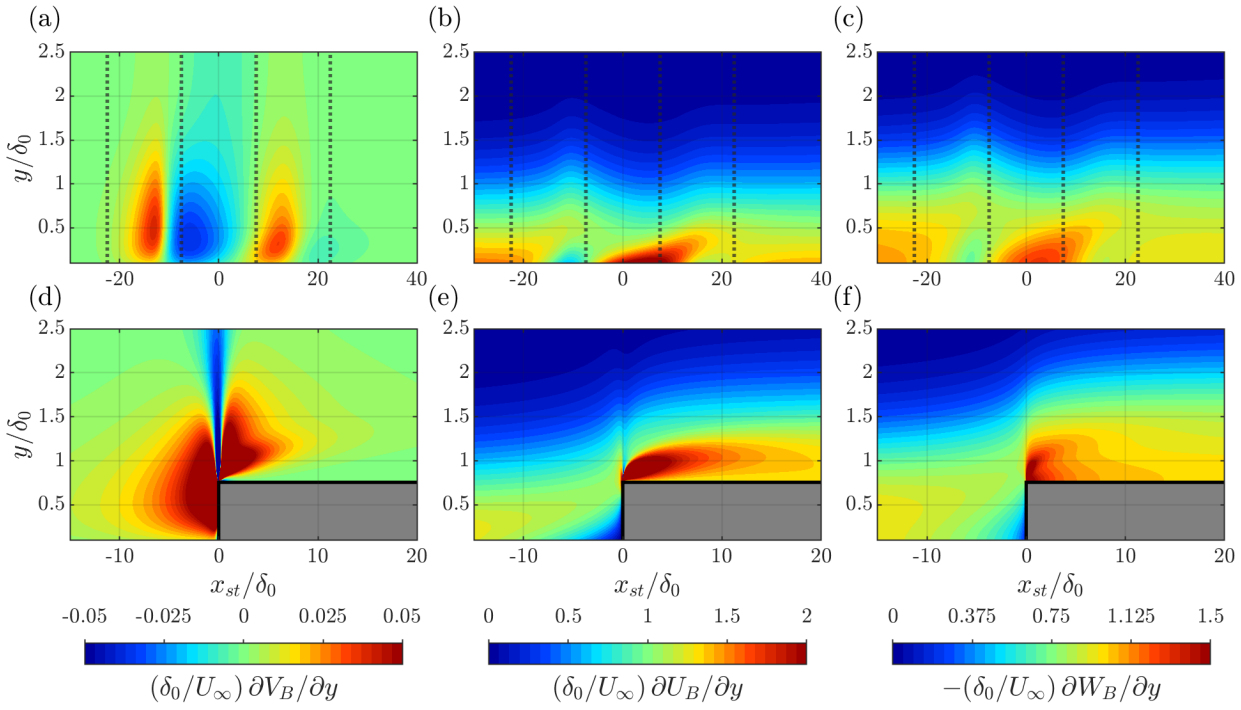

Figure 7.3: Contours of V_{B_y} (a,d), U_{B_y} (b,e), and $-W_{B_y}$ (c,f) in the $2.5p_f$ $30w \times 2$ case (top) and the reference FFS case (bottom); black dotted lines at $x_{st}/\delta_0 = -3w/4,\ -w/4,\ w/4$, and $3w/4$ show the region of ΔP imposition.

The character of V_B primarily plays a role in determining the sign of W_{B_x} as explained in Section 6.1 through Equation 6.2 (assuming that $W_{B_{xx}}$ is much lower than $W_{B_{yy}}$). In the synthetic three-way case, $-W_{B_x}$ and U_{B_x} assume a similar character in both adverse and favourable ΔP regions, as regions of accelerated chordwise base flow co-exist with regions of downwash, which in turn induces spanwise velocity acceleration (and vice versa for regions of decelerated chordwise base flow), as seen for the reference synthetic case in Figure 7.2 (c). However, since V_B remains positive throughout the adverse and favourable ΔP regions of the FFS case (as seen for the reference FFS in Figure 7.2 (e)), $-W_{B_x}$ only takes a positive sign throughout (as seen for the reference FFS in Figure 7.2 (f)). This in turn influences the behaviour of the W_B contours, as shown for reference cases in Figure 7.1 (f), wherein the contour levels keep rising without any downward movement in FFS cases owing to continuous deceleration. Whereas characteristic up-down-up movement of constant contour levels is seen in the synthetically deformed three-way cases due to the chordwise deceleration-acceleration-deceleration behaviour of spanwise base flow velocity component, as observed for the reference synthetic cases in Figure 7.1 (c).

The characteristic upward and downward movement of U_B and W_B momentum in the near-wall region evidenced by contour level movement in their respective contour plots were used to explain the behaviour of shears of these profiles

in Section 6.1. This explanation works in adverse ΔP regions of both FFS and synthetic deformation cases, with a progressive reduction of shear in the chordwise direction in both the reference three-way synthetic and FFS case, as evidenced in reference case contours of U_{B_y} (Figure 7.3 (b) and (e)), and $-W_{B_y}$ (Figure 7.3 (c) and (f)). However, at the step location in the FFS cases, the abrupt geometrical obstruction causes an abrupt concentration of chordwise and spanwise momentum at the step location relative to the upstream location prior to the step, leading to a large enhancement in the shear of U_B and W_B, as evidenced in their contours for the reference FFS case in Figure 7.3 (e) and (f), respectively. The shear distribution in the favourable ΔP region of synthetic cases can be explained by the increase of chordwise and spanwise momentum in the near-wall region due to the downward movement of constant contour levels, as evidenced in the shear contours in Figure 7.3 (b) and (c). Even though the reference synthetic three-way and FFS cases have very different sources of ΔP, multiple similarities have been identified in the features of base flow. Remarkably, the order of wall-tangential base flow x derivatives in both the FFS and synthetic three-way case are similar, with higher magnitude values in the FFS due to a stronger ΔP. The wall-tangential base flow shear terms also have similar orders in both the reference FFS and synthetic three-way case, but this result is more expected, as these are close to orders experienced in the clean case. The similarity in orders of chordwise derivatives and shears of wall-tangential base flow implies that there is a chance that $\mathcal{P}_{x_d}$ and $\mathcal{P}_{y_d}$ terms could have similarities in order when perturbation equations are evaluated for both cases. Some degree of similarity in the trends of synthetic deformation and FFS is also found in terms of increase and decrease of wall-tangential shear, and acceleration and deceleration of U_B in favourable and adverse ΔP regions, respectively, implying that once the perturbation behaviour is evaluated, $\mathcal{P}_{x_d}$ and $\mathcal{P}_{y_d}$ might bear similar trends for both cases.

7.2. Perturbation Evolution Comparison

The perturbation data are generated using linear HLNS for synthetic three-way cases and non-linear DNS for FFS cases, where the behaviour of perturbation in the step upstream region is linear (Casacuberta, Hickel, Westerbeek, & Kotsonis, 2022). In case of an FFS, when the perturbation evolves through the region of base flow deformation, its u' amplitude function develops secondary peaks upstream of the step, which remains active for a short region downstream of the step. These secondary peaks are not observed when the perturbation evolves through a synthetically deformed base flow (refer Appendix E). Since secondary peaks are associated with near-wall streaks (Casacuberta, Hickel, Westerbeek, & Kotsonis, 2022), and carry different physical significance compared to the primary peak itself, their absence implies that the synthetic cases cannot fully capture the effects of an FFS on perturbation evolution. A possible reason for the lack of these secondary peaks in the synthetically deformed cases is the lack of separation, whose presence can cause a much stronger base flow deformation. Furthermore, the appearance of non-linear effects downstream of step location implies that its direct comparison with linear perturbation evolution through the synthetic base flow deformation might not be appropriate, as these harmonics could eventually influence the behaviour of the fundamental mode (sum of (0,1) and (0,-1)). However, the production term evolution of the fundamental mode would still play an important role in governing the mechanisms by which the fundamental perturbation grows or decays, and can thus be compared for the synthetic and FFS case. This would also demonstrate the effectiveness of the $\mathcal{P}_{x_d}$ and $\mathcal{P}_{y_d}$ decomposition in explaining trends of $\mathcal{P}$ for an instance of naturally deformed base flow. The step upstream region entails linear perturbation evolution approximately till the point secondary peaks appear. Hence, the behaviour of perturbation growth rate in this regime can be directly compared to the first adverse ΔP region of synthetic base flow deformations. In both the synthetic deformation and the FFS, perturbations are found to grow faster than the clean case in the first adverse ΔP region, and an investigation of the production term behaviour relative to the clean case elucidates why this occurs (as shown in Section 6.3.2).

Observations of $\mathcal{P}$ (shown for reference cases in Figure 7.4 (a) and (d)) without decomposition lack clarity on the type of base flow parameter distinguishing the production term's regions of stabilizing and destabilizing influence. It is noted that different initial amplitudes result in different magnitudes of $\mathcal{P}$ in synthetically deformed and FFS cases (unit amplitude is assumed in HLNS as its values do not influence linear perturbation evolution). Its decomposition shows that the $\mathcal{P}_{x_d}$ and $\mathcal{P}_{y_d}$ term are both active in the region of ΔP imposition in the synthetic three-way cases and FFS cases, as seen for reference cases in Figure 7.4. This shows that the orders of $\mathcal{P}_{x_d}$ and $\mathcal{P}_{y_d}$ are comparable even in instances of natural base flow deformations, alleviating concerns of idealized behaviour raised in Section 6.3.3. The $\mathcal{P}_{x_d}$ term can further be decomposed to find that $\mathcal{P}_{x_d,1}$ and $\mathcal{P}_{x_d,3}$ are the dominant contributors (as shown for reference cases in Figure 7.5), consistent with trends seen in Section 6.3.1. The sign of U_{B_x} controls the sign of $\mathcal{P}_{x_d,1}$, thus implying destabilizing tendency or positive values in regions of chordwise base flow deceleration and stabilizing tendency in regions of chordwise base flow acceleration, evidenced in the contours of $\mathcal{P}_{x_d,1}$ of reference cases in Figure 7.5 (a) and (d). Since the sign of $\cos(\phi_1 - \phi_3)$ is -1 in both cases in heights relevant for energy transfer mechanisms (as seen for reference cases in Figure 7.6 (a) and (d)), the sign of W_{B_x} controls the sign of $\mathcal{P}_{x_d,3}$. $\mathcal{P}_{x_d,3}$ thus remains destabilizing throughout the upstream and downstream near-step region, as shown for the reference FFS step in Figure 7.5 (f), not fully mimicking the behaviour of $\mathcal{P}_{x_d,1}$ due to difference in the behaviour of U_{B_x} and $-W_{B_x}$ at the FFS location. Whereas, in synthetic three-way cases, the behaviour of $\mathcal{P}_{x_d,3}$ mimics the behaviour of $\mathcal{P}_{x_d,1}$, as shown for the reference case comparing Figure 7.5 (c) and (a).

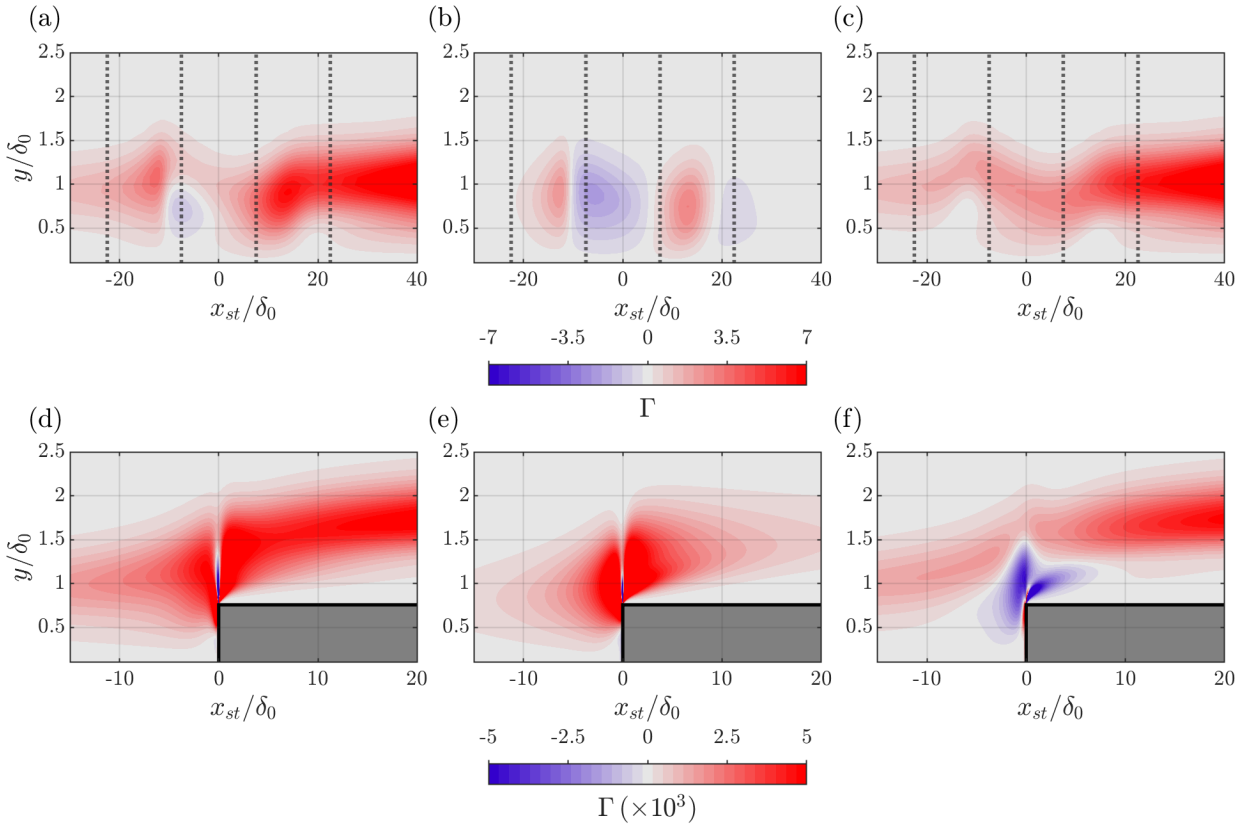

Figure 7.4: Contours of $\Gamma = \mathcal{P}$ (a,d), $\mathcal{P}_{x_d}$ (b,e), and $\mathcal{P}_{y_d}$ (c,f) in the $2.5p_f$ $30w \times 2$ case (top) and the reference FFS case (bottom); black dotted lines at $x_{st}/\delta_0 = -3w/4,\ -w/4,\ w/4$, and $3w/4$ show the region of ΔP imposition.

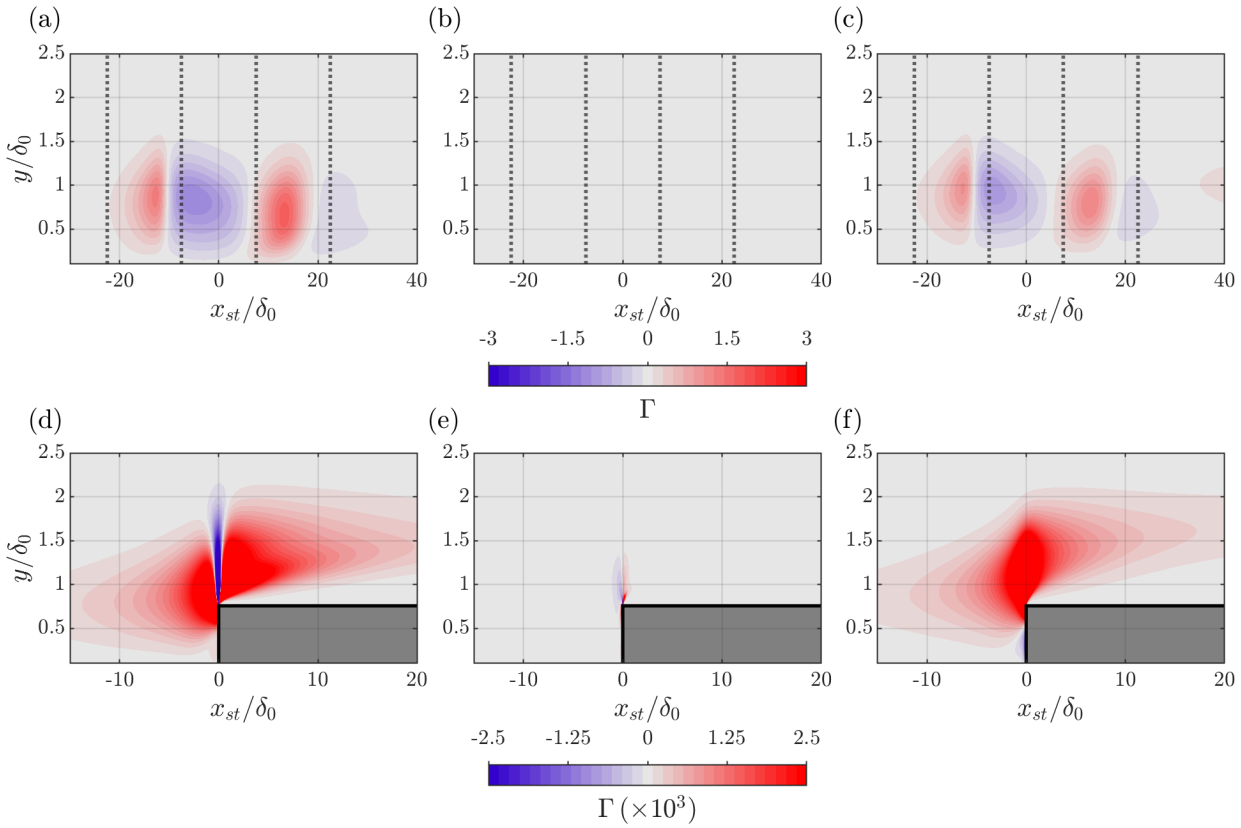

Figure 7.5: Contours of $\Gamma = \mathcal{P}_{x_d,1}$ (a,d), $\mathcal{P}_{x_d,2}$ (b,e), and $\mathcal{P}_{x_d,3}$ (c,f) in the $2.5p_f$ $30w \times 2$ case (top) and the reference FFS case (bottom); black dotted lines at $x_{st}/\delta_0 = -3w/4,\ -w/4,\ w/4$, and $3w/4$ show the region of ΔP imposition.

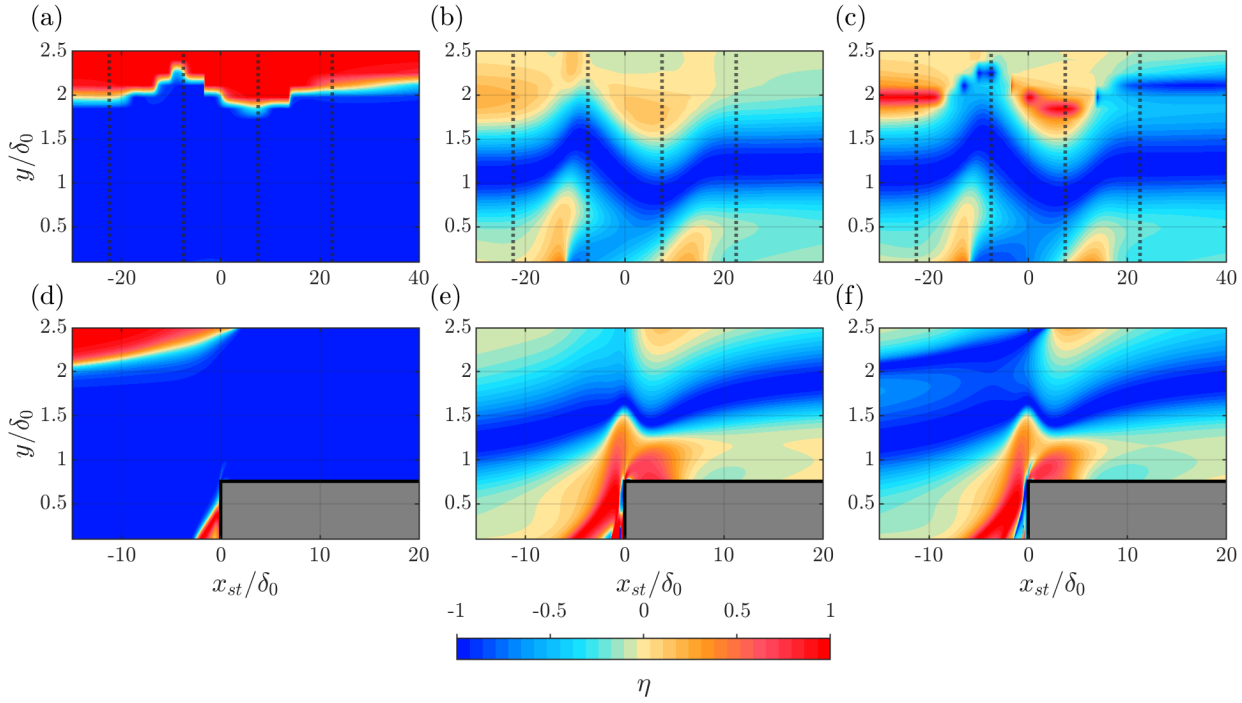

Figure 7.6: Contours of $\eta = \cos(\phi_1 - \phi_3)$ (a,d), $\cos(\phi_2 - \phi_1)$ (b,e), and -$\cos(\phi_2 - \phi_3)$ (c,f) in the $2.5p_f$ $30w \times 2$ case (top) and the reference FFS (bottom) case; black dotted lines at $x_{st}/\delta_0 = -3w/4,\ -w/4,\ w/4$, and $3w/4$ show the region of ΔP imposition.

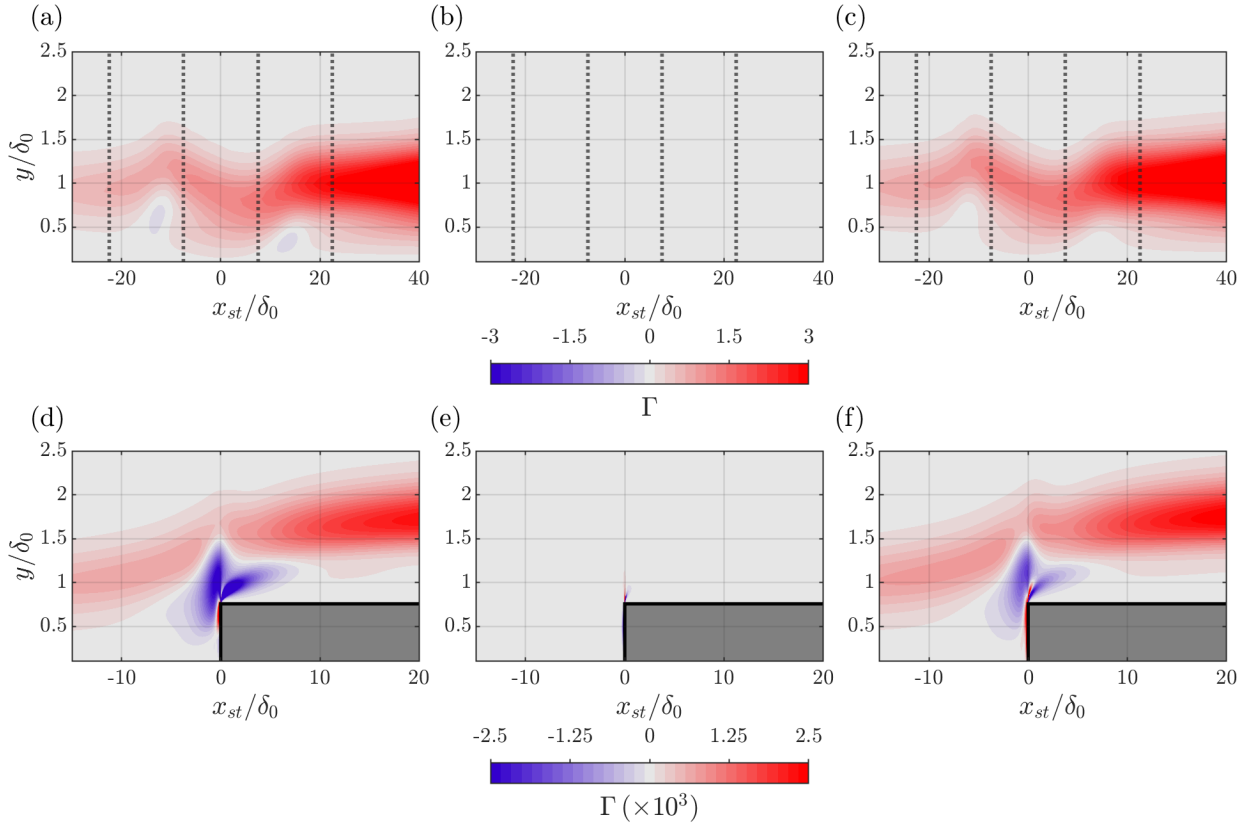

Figure 7.7: Contours of $\Gamma = \mathcal{P}_{y_d,1}$ (a,d), $\mathcal{P}_{y_d,2}$ (b,e), and $\mathcal{P}_{y_d,3}$ (c,f) in the $2.5p_f$ $30w \times 2$ case (top) and the reference FFS case; black dotted lines at $x_{st}/\delta_0 = -3w/4,\ -w/4,\ w/4$, and $3w/4$ show the region of ΔP imposition.

Considering $\mathcal{P}_{y_d}$, its behaviour is controlled by $\mathcal{P}_{y_d,1}$ and $\mathcal{P}_{y_d,3}$ in the synthetic three-way and FFS cases, as seen for the reference cases in Figure 7.7, consistent with trends presented in Section 6.3.1. $\mathcal{P}_{y_d,1}$ and $\mathcal{P}_{y_d,3}$ have very similar trends of evolution, and an attempt to explain $\mathcal{P}_{y_d}$ behaviour can be made explaining the behaviour of either term. Here, $\mathcal{P}_{y_d,1}$ is chosen and appears to be slightly stabilizing towards the end of both adverse ΔP regions in the reference synthetic three-way case but remains destabilizing otherwise. $\mathcal{P}_{y_d,1}$ also appears to be stabilizing in regions near the wall for the FFS cases in the vicinity of the step, and the extent of stabilization seems to be much more than that synthetically deformed cases, evidenced for the reference FFS case by negative values with magnitude comparable to the highest positive values of $\mathcal{P}_{y_d,1}$ in the cropped domain (as seen in Figure 7.7 (b)). The stabilization occurs in regions of positive shear and hence can be attributed to $\cos(\phi_2 - \phi_1)$ changing sign. The contours of $\cos(\phi_2 - \phi_1)$ for the synthetic three-way and FFS case show a characteristic upward and downward trend approximately in adverse and favourable ΔP regions, respectively, as shown for reference cases in Figure 7.6 (a) and (d), respectively. This upward and downward movement of $\cos(\phi_2 - \phi_1)$ contour levels in adverse and favourable ΔP regions for a naturally deformed base flow alleviates concerns of such behaviour being an artefact of an idealized base flow in synthetic cases (mentioned in Section 6.3.3). The upward movement in the first adverse ΔP region exposes regions of sign changed $\cos(\phi_2 - \phi_1)$ in the near-wall region, where the sign changes from negative to positive, explaining stabilizing tendencies in both synthetic three-way and FFS cases as per mechanisms explained in Section 5.1.2. However, the cosines in FFS cases take much larger positive values (much nearer to one) than the synthetically deformed cases in adverse ΔP regions, resulting in a stronger near-wall stabilizing tendency of $\mathcal{P}_{y_d}$.

The behaviour of $\mathcal{P}$ is now considered. Regions of increased and decreased $\mathcal{P}$ with respect to the clean case appear to be approximately correlated with regions of positive and negative $\mathcal{P}_{x_d}$ in the first adverse and favourable ΔP region, as seen for the reference FFS in Figure 7.8. However, this does not hold at the lower height throughout the second adverse ΔP region. The exact extent of increase or reduction of $\mathcal{P}$ with respect to the clean case can only be determined by a balance of $\mathcal{P}_{x_d}$ and $\mathcal{P}_{y_d}$. The trends of $\mathcal{P}$ for synthetic cases are presented in Appendix E, showing an increase with respect to clean case approximately in regions of wall-tangential base flow deceleration and vice versa. Since the production term is identified as the source of linear perturbation growth in Section 6.3.2, it can be concluded that in the linear region of growth upstream of the step, where secondary structures in perturbation shape function are absent, the extra amplification with respect to the clean case can be attributed to a region of decelerated wall-tangential base flow. Similar behaviour is also captured in the first adverse ΔP region of synthetic three-way cases, wherein the increase of $\mathcal{P}$ relative to clean case closely corresponds to the region of positive $\mathcal{P}_{x_d}$ or wall-tangential base flow deceleration, resulting in an increase of amplitude relative to the clean case (amplitude trends are shown in Appendix E). This also shows the effectiveness of decomposing $\mathcal{P}$ into $\mathcal{P}_{x_d}$ and $\mathcal{P}_{y_d}$ terms in identifying wall-tangential base flow acceleration or deceleration as a base flow property that can demarcate regions of perturbation stabilization or destabilization when it evolves linearly.

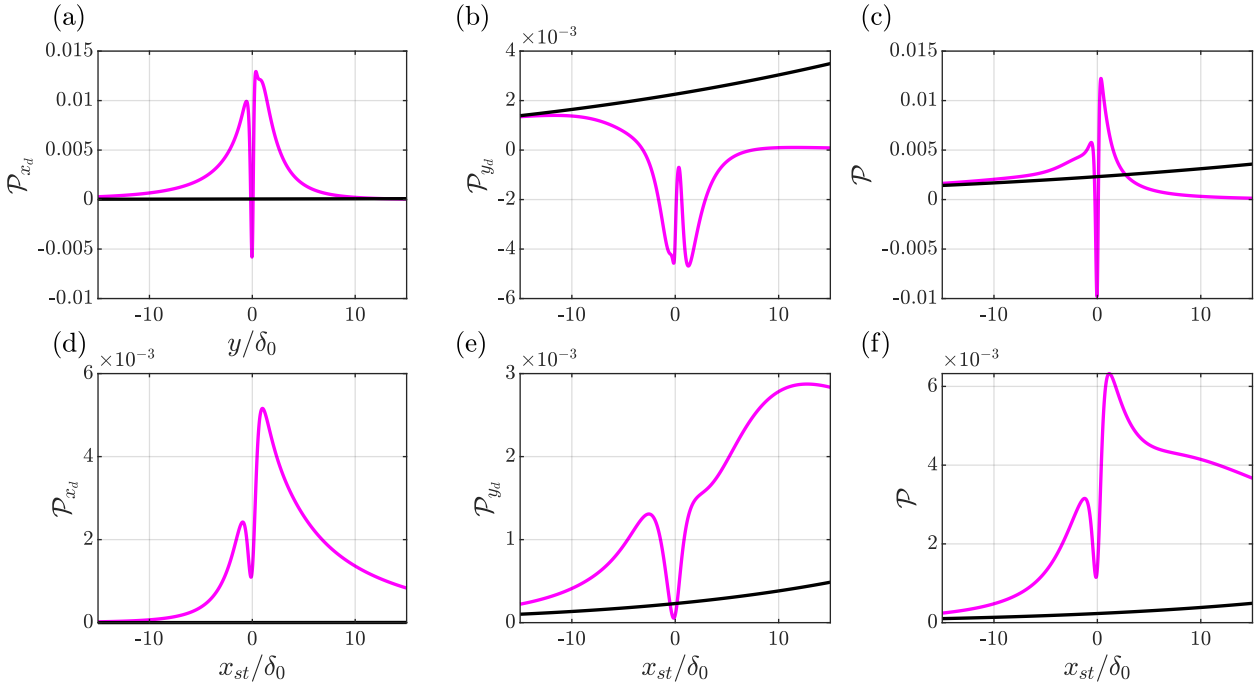

Figure 7.8: Evolution of $\mathcal{P}_{x_d}$ (a,d), $\mathcal{P}_{y_d}$ (b,e), $\mathcal{P}$ (c,f) in reference FFS case (magenta) and clean case (black) at $y/\delta_0 = 1$ (top) and $y/\delta_0 = 1.5$ (bottom)

8

Conclusion and Recommendations for Future Work

8.1. Conclusion

In literature, there is confusion surrounding mechanisms governing the interaction of an incoming crossflow mode with a rapid base flow deformation such as an FFS placed on a swept wing or a swept flat plate. This motivates the current thesis, where the evolution of primary stationary crossflow instability in its linear phase is studied in a spanwise invariant, synthetically generated, rapid base flow deformation. In the FFS, a local pressure change over a chordwise length scale (of orders of boundary layer thickness) much smaller than the scale of pressure change of the favourable pressure gradient region of a swept flat plate (also referred to as the clean case), contributes to the development of a rapid base flow deformation. Inspired by the FFS, a synthetic rapid base flow deformation is devised by imposing a Gaussian-like pressure variation (ΔP) on the external pressure gradient of the clean case, and propagating the resulting effective pressure distribution down to the wall. The Gaussian-like pressure variation is parametrized by three parameters. The first parameter is the width, which is assumed to be of the order of $10\delta_0$ (where δ_0 is the δ_{99} at the inlet) to ensure the base flow pressure changes over a much shorter width scale than the clean case. The second parameter is the pressure factor, which provides a simplified method to quantify the gradient of the ΔP distribution. An increase in the magnitude of p_f results in a stronger pressure variation. A positive sign of p_f results in a region of negative ΔP (favourable) followed by positive ΔP (adverse) and a negative sign of p_f results in a region of adverse ΔP followed by favourable ΔP. Relative to the clean case, the imposition of a positive p_f ΔP distribution results in an effective pressure distribution with a region of more negative pressure gradient followed by a region of less negative (or positive) pressure gradient. The opposite trend is followed for negative p_f cases, where the effective pressure distribution consists of a region of less negative (or positive) pressure gradient followed by a region of more negative pressure gradient. The third parameter is the location of ΔP imposition which is chosen to be the FFS location considered by Casacuberta, Hickel, Westerbeek, and Kotsonis (2022). The boundary layer solver is found to be the best base flow solution technique to ensure that the developed effective pressure distributions propagate unaltered to the wall, thus resulting in a rapid base flow deformation within the boundary layer. However, the results of the boundary layer solver are valid under boundary layer theory approximations, which do not hold for the full Navier Stokes equation solution wherein base flow pressure is not found to be invariant with y. This implies that the synthetic deformations developed in this thesis are "idealized".

Characteristics of the BLS base flow such as boundary layer thickness are found to be better characterised by the nature of effective pressure distribution relative to the clean case rather than the effective pressure gradient itself being favourable or adverse. The most convenient way to characterize base flow properties is thus in terms of favourable and adverse ΔP regions, which approximately correspond to regions of relatively more negative and relatively less negative (or positive) effective pressure gradient compared to the clean case, respectively. The base flow deformation is divided into halves based on the halves of the Gaussian-like ΔP, with each half spanning $w/2$ on either side of the location of ΔP imposition. The chordwise base flow accelerates in most of the favourable ΔP region owing to a higher favourable pressure gradient compared to the clean case and decelerates in most of the adverse ΔP region owing to a lower favourable pressure gradient compared to the clean case or adverse pressure gradient depending on the case considered. Thus, in positive p_f cases, most of the favourable ΔP half has positive valued U_{B_x}, followed by negative valued U_{B_x} in the region spanning the end of the favourable ΔP half through most of the adverse ΔP half. Whereas in negative p_f cases, most of the adverse ΔP half has negative valued U_{B_x}, followed by positive valued U_{B_x} from the region spanning the end of the adverse ΔP half

through most of the favourable ΔP half. Towards the end of the second half of base flow deformation, another region of accelerated or decelerated base flow exists, with the same sign of U_{B_x} in the first half of pressure deformation. The chordwise and wall-normal extent of this region is short and it is associated with the relaxation back to the clean case pressure gradient after the region of deformation. A region of accelerated chordwise base flow closely corresponds to a region of downwash (explained via integrating the continuity equation) and accelerated spanwise base flow (explained via analysis of the z base flow momentum equation), with the vice versa applicable for a region of decelerated chordwise base flow. The higher magnitudes of chordwise derivatives of wall-tangential base flow components and wall-normal velocity in regions of base flow deformation compared to clean case values differentiate a rapid base flow deformation from a smooth base flow evolution represented by the clean case. Regions of chordwise base flow acceleration and deceleration also correspond to regions of increased and decreased near-wall chordwise momentum, leading to an increase and decrease of shear, respectively. The decrease of chordwise base flow shear leads to the development of inflection points in case the effective pressure gradient is adverse. Regions of spanwise base flow acceleration and deceleration similarly correspond to regions of increased and decreased near-wall spanwise velocity shear. The behaviour of U_B, V_B, and W_B together determine the behaviour of near-wall streamlines and crossflow. Near-wall streamlines tend to take an inboard turn in regions of favourable effective pressure gradient more negative than the clean case and an outboard turn in regions of adverse effective pressure gradient, with no perceptible change in behaviour of near-wall streamlines when the sign of effective pressure gradient does not change. Crossflow changes behaviour in deformed cases, reducing approximately in regions of adverse ΔP and increasing approximately in regions of favourable ΔP, potentially linked to the effect of reduced and increased effective pressure gradient compared to the clean case in adverse and favourable ΔP halves, respectively. The strongest base flow deformations also lead to negative crossflow (opposite to the consistent positive crossflow noted in the clean case), and this reversal is linked to the strong nature of adverse effective pressure gradient.

To study the response of stationary crossflow instability to the above-described synthetically deformed base flow, the instability is initialized as a 7.5 mm spanwise periodic mode, and its linear evolution is simulated using HLNS, due to its ability to solve the system of elliptic perturbation equations without a range of assumptions common in PSE and ILST. As for the structure of instability, chordwise and spanwise perturbation amplitude functions do not develop secondary peaks, whereas the wall-normal velocity perturbation develops secondary peaks. The growth rates of u', v' and w' do not match, leading to the usage of a total perturbation vector norm for characterizing perturbation growth and amplitude evolution. In the clean case, the growth rate almost remains constant and negative, leading to a consistent increase in amplitude. Whereas in deformed cases, regions of favourable ΔP approximately correspond to growth rate becoming less negative than the clean case, whereas regions of adverse ΔP approximately correspond to regions of growth rate more negative than the clean case. The growth rate is also found to increase or decrease with respect to the clean case in a short region at the end of the second half of deformation, as per behaviour in the first half of deformation. The growth rate changes sign for strong negative p_f base flow deformations (an example being the $-2.5p_f30w$ case), leading to amplitude stabilization in the region of positive growth rate, which appears to contribute to a long-term reduction of amplitude compared to the clean case post the deformation. To explain the trends of amplitude evolution, a correlation to the nature of crossflow profile and double inflection point criteria are both tested, and they do not explain trends in all cases, casting doubt on the universality of these theories. This leads to the development of an energy balance framework to understand mechanisms by which a perturbation grows or decays.

The energy balance equation is derived in a spanwise integrated sense to focus only on energy growth in the x direction, inspired by the work of Karp and Hack (2018). The growth of energy in the chordwise direction is governed by

$$\frac{\partial \tilde{E}}{\partial x} \approx \frac{1}{U_B}\left(\frac{\beta}{2\pi}\underbrace{(\mathcal{P}_{x_d}+\mathcal{P}_{y_d})}_{\mathcal{P}}\underbrace{-V_B\frac{\partial \tilde{E}}{\partial y}}_{\mathcal{R}}+\frac{\beta}{2\pi}\mathcal{D}\right), \tag{8.1}$$

where the work of pressure forces is neglected due to its negligible contribution. As per Equation 8.1, in case $\mathcal{P}$ (the production term) is positive and greater than the magnitude of $\mathcal{D}$ (the work of viscous forces), the base flow provides energy to the perturbation by $\mathcal{P}$. Some of this energy is lost to the work of viscous forces, while some of the energy is redistributed (through $\mathcal{R}$) in the boundary layer depending on the action of V_B. Redistribution is negligible in the clean case due to negligible values of V_B but is active in regions of deformed flow, predominantly transferring energy away from the wall in regions of upwash and transferring energy towards the wall in regions of downwash. In wall-normal levels where there is surplus energy, the perturbation absorbs energy resulting in energy growth. However, there also exists some wall-normal levels from where energy is taken away by the redistribution term, resulting in reduced energy growth or decay compared to the wall-normal levels where the redistribution term injects energy. On the other hand, when $\mathcal{P}$ is negative (or positive but lower than the magnitude of $\mathcal{D}$), the perturbation taps into a part of its own energy reserves, some of which gets redistributed by $\mathcal{R}$ in the boundary layer, following which the redistributed energy is lost to the work

of viscous forces and the base flow (via production). This results in perturbation energy stabilization, especially strong in wall-normal levels where the redistribution term takes energy away. The change of sign of production term acts as a differentiating factor between chordwise stations at which a perturbation gains or loses energy, and its behaviour governs perturbation amplitude evolution. Understanding its trends is thus critical, and decomposing it into contributions from base flow x derivative ($\mathcal{P}_{x_d}$), and y derivative terms ($\mathcal{P}_{y_d}$) greatly aids this process.

$\mathcal{P}_{x_d}$ represents the potential for perturbations to gain energy not required by the wall-tangential base flow when it decelerates or to lose energy when the wall-tangential base flow accelerates. In the clean case, the contribution of $\mathcal{P}_{x_d}$ to the production term is negligible whereas it makes a significant contribution to the production term in deformed cases within the region of deformation where chordwise derivatives of wall-tangential base flow are active. Whereas $\mathcal{P}_{y_d}$ represents the potential of v' to transfer wall-tangential base flow momentum to wall-tangential perturbation components. The sign of $\mathcal{P}_{y_d}$ in regions of positive U_{B_y} (or W_{B_y}) is determined by the sign of cos(ϕ_2-ϕ_1) (or -cos(ϕ_2-ϕ_3)) i.e. the cosine of the phase difference between v' and u' (or $-w'$) perturbations in the synthetic deformation. Destabilizing tendency occurs when v' and u' (or -w') are phase shifted between $\pi/2$ and π implying that downward action of v' brings high base flow momentum to regions near peaks of u' (or -w'), thereby providing the potential to enhance u' (or -w'). Stabilizing tendency occurs when the phase of v' differs from the phase of u' (or -w') by values between 0 and $\pi/2$, where the downward action of v' brings high base flow momentum to regions near valleys of u' (or -w'), thereby providing the potential to stabilize u' (or -w'). In the clean case, the destabilizing behaviour of the production term is owed to the destabilizing behaviour of $\mathcal{P}_{y_d}$ due to a consistent negative value of cos(ϕ_2-ϕ_1) in regions where energy transfer mechanisms are active, leading to a consistent positive $\tilde{E}_x$ or gain of energy, subsequently leading to a consistent negative growth rate. In majority of the deformation in positive and negative p_f cases, the behaviour of $\mathcal{P}_{y_d}$ is destabilizing aided by cos(ϕ_2-ϕ_1) being negative. At wall-normal heights with $y/\delta_0 < 0.5$, $\mathcal{P}_{y_d}$ increases with respect to the clean case in favourable ΔP regions and reduces with respect to the clean case in adverse ΔP regions, potentially due to cos(ϕ_2-ϕ_1) becoming more negative in favourable ΔP regions and less negative adverse ΔP regions at these heights. In adverse ΔP regions of large p_f cases, cos(ϕ_2-ϕ_1) changes sign to positive values very near zero, resulting in a mild stabilizing tendency of $\mathcal{P}_{y_d}$ at these heights ($y/\delta_0 < 0.5$). Although both $\mathcal{P}_{y_d}$ and $\mathcal{P}_{x_d}$ determine the behaviour of $\mathcal{P}$, the increase and decrease of $\mathcal{P}$ with respect to the clean case approximately corresponds to regions where $\mathcal{P}_{x_d}$ is positive and negative, respectively. This implies that the perturbation gains energy at a slower rate than the clean case or loses energy approximately in regions of wall-tangential base flow acceleration, and gains energy at a faster rate than the clean case approximately in regions of wall-tangential base flow deceleration. This corresponds well with the trends of growth rate (Figure 6.16 (a)) where enhanced or reduced growth rate in deformed cases with respect to the clean case occur in three regions, with enhanced growth rate observed in regions of wall-tangential base flow deceleration and reduced growth observed in regions of wall-tangential base flow acceleration. The potential for perturbation stabilization is maximised while switching from a region of wall-tangential base flow deceleration to a region of wall-tangential base flow acceleration. At wall-normal heights close to $y/\delta_0 < 0.5$, the former region contributes to reduced values of $\mathcal{P}_{y_d}$ (potentially due to reduction of cos(ϕ_2-ϕ_1) in an adverse ΔP region), which do not recover to clean case $\mathcal{P}_{y_d}$ levels by the beginning of the latter region. At the beginning of the latter region, a negative $\mathcal{P}_{x_d}$ exploits the reduced values of $\mathcal{P}_{y_d}$ to push $\mathcal{P}$ to negative values (or positive values very close to zero).

The change in the method by which the perturbation exchanges energy with the base flow in regions of deformed base flow brings into question whether the perturbation deviates from modal character on interacting with regions of base flow deformation. Deviation from modal behaviour is first evaluated through the identification of mechanisms prevalent in initial condition driven non-modality (refer Section 1.7.3) and finding whether these mechanisms show a difference when evaluated using the HLNS solution with respect to the ILST solution in regions of deformation. Observation of the lift-up effect involves decomposition of the perturbation into base flow tangential and normal components, representative of streaks and rollers respectively, and the computation of I_2, which physically captures the growth of streaks via transfer of base flow momentum by rollers (Picella et al., 2018). Even after decomposing the production term into I_1 to I_4, I_2 appears to capture production term evolution fully. The lift-up effect thus appears to be destabilizing in the clean case and positive p_f cases but stabilizing in those negative p_f cases where regions of negative production term can be identified, thus behaving differently from the classic lift-up effect which is destabilizing. The stabilization is attributed to the sign change of the phase difference between the representative field of rollers and streaks. This sign change is explained by relating this phase difference to the phase difference of v' and u', wherein it is found that the effects of a negative wall-normal base flow velocity cause the phase difference between rollers and streaks to take a value in the fourth quadrant (stabilizing), leading the phase difference of u' and v' which lies in the third quadrant (destabilizing), in the transition region from the end of adverse ΔP to the beginning of the favourable ΔP region where V_B changes sign. However, the stabilization of the lift-up effect is also noted for the local ILST solution (computed for the negative p_f base flow that shows negative $\mathcal{P}$), exactly in regions where the HLNS solution stabilizes. The stabilization encountered shows that the

stabilized lift-up effect is possibly just a manifestation of a stabilized mode in regions of deformed base flow.

The Orr mechanism is evaluated next via the observation of tilt of ϕ_1 i.e. the xy variation of u' phase, quantified by its wall-normal gradient. The clean case shows consistent tilt throughout different x stations. This implies that ϕ_{1_x} is constant for different wall-normal heights. ϕ_{1_x} determines the angle made by a line of constant phase on the xz plane with the x axis, and its constant value across wall-normal heights implies that lines of constant phase in any xz plane follow a unique direction, which is almost aligned with the inviscid streamline (approximately 2.5 degrees) and perpendicular to the wavenumber direction. Whereas in deformed cases, perturbation tilt does not remain the same in the deformed region, with a tendency of increased tilt in near-wall regions on encountering an adverse ΔP region and a tendency of decreased tilt in near-wall regions on encountering a favourable ΔP region. The change of tilt in regions of deformed flow is assumed to be a manifestation of the Orr mechanism, possibly triggered to some degree by the change of base flow direction and the change of shears of chordwise base flow. The lack of consistent tilt in ϕ_1 across x stations implies that ϕ_{1_x} is not constant at every height considered, further implying that lines of constant phase in the xz plane do not have a unique direction. Comparing the angle difference between the direction of lines of constant phase in xz planes at different heights and the direction of inviscid flow further shows that the angle difference (ϕ_d) is relatively larger in some regions of base flow deformation than the 2.5 degree value obtained for clean case, with ϕ_d values found to be closer to the clean case value with reduction of p_f. This counts as a deviation from modal behaviour wherein the instability is expected to be almost aligned with the inviscid streamline (Bippes, 1999). The characteristic xz line of constant phase of the ILST solution assumed to be defined by $\alpha_r x + \beta z = C$, in a direction perpendicular to the wavenumber vector, are found to follow inviscid streamlines much better than the HLNS solution. Thus, the HLNS solution which is representative of actual perturbation behaviour presents hints of deviation from local modal behaviour from the perspective of the Orr mechanism. However, none of the criteria suggested by Casacuberta, Hickel, Westerbeek, and Kotsonis (2022) to find signs of non-modal character are satisfied in the cases simulated here leading to the conclusion that the instability is an instance of a base flow deformed mode, with hints of deviation from local modal behaviour via the action of the Orr mechanism.

Unfortunately, the idealized BLS solution generated for synthetically deformed base flows predicts different orders of magnitude of U_{B_x} and V_B compared to the full Navier Stokes solution generated using DNS. The major reason for the mismatch of results is the assumption of y momentum equation being reduced to $P_{B_y} = 0$ in BLS base flows, which does not hold in DNS base flows, potentially due to changes in external flow being imposed in the orders of boundary layer thickness. The difference in orders of magnitude of chordwise derivatives of wall-tangential base flow between a BLS and DNS base flow calls into question if $\mathcal{P}$, responsible for predicting linear perturbation evolution trends, is actually driven by a balance of $\mathcal{P}_{x_d}$ and $\mathcal{P}_{y_d}$ terms, as these terms have similar orders only due to the significant increase in the order of chordwise derivatives of wall-tangential base flow in the region of deformation in BLS base flows. This motivates a validation study comparing combinations of two two-way cases resulting in synthetic three-way cases with the data of FFS cases from Casacuberta, Hickel, Westerbeek, and Kotsonis (2022). Synthetic three-way and FFS cases both have a region of favourable ΔP flanked on either side by a region of adverse ΔP. The orders of magnitude of chordwise derivatives and shears of wall-tangential base flow in regions of base flow deformation are found to be similar in both the synthetic three-way and FFS case, with higher magnitude noted in FFS cases due to the strength of base flow deformation. Some degree of similarity in the trends of synthetic deformation and FFS is also found in terms of the increase and decrease of wall-tangential shear, and the acceleration and deceleration of U_B approximately in favourable and adverse ΔP regions, respectively. The underlying similarities in base flow result in $\mathcal{P}_{x_d}$ and $\mathcal{P}_{y_d}$ being of similar orders for both synthetic three-way and FFS cases, providing evidence that their balance is not an artefact of an idealized base flow. The stabilizing or destabilizing influence of $\mathcal{P}_{y_d}$ is determined by the sign of $\cos(\phi_2 - \phi_1)$. Across synthetically deformed and two FFS cases of lower height, the constant contours levels of $\cos(\phi_2 - \phi_1)$ show upward and downward movement in adverse and favourable ΔP regions, respectively, leading to its local near-wall decrease and increase. This shows that the local near-wall increase and decrease of $\cos(\phi_2 - \phi_1)$, also observed in two-way synthetically deformed cases, is also not an artefact of an idealized base flow. Multiple similarities are found in the evolution of $\mathcal{P}_{x_d}$ and $\mathcal{P}_{y_d}$ between the synthetic base flow deformation and FFS, but perturbation evolution through the former does not give rise to secondary peaks in u' amplitude function present in the latter, possibly due to the lack of separation, whose presence generates a much more rapid base flow deformation in the FFS cases. Nevertheless, there exists a region upstream of the FFS where a perturbation grows linearly without the development of secondary structures. Perturbations grow faster than the clean case in this step upstream region. Perturbation amplitude also increases with respect to the clean case in the first adverse ΔP region of synthetic three-way cases. This behaviour in both the FFS and synthetic three-way cases is attributed to a positive $\mathcal{P}_{x_d}$ due to wall-tangential base flow deceleration, which results in enhanced production term with respect to the clean case even when $\mathcal{P}_{y_d}$ shows stabilizing behaviour in certain parts of the considered region. Thus, the effect of an FFS on an incoming stationary crossflow instability in the step upstream region is captured to a good extent by a synthetic base flow deformation.

Considering the broader outlook, this thesis provides a direction to develop natural manifestations of base flow deformation which do not deform the flow as much as a step, but somewhere close to the negative p_f synthetic deformations, which can damp the linear primary phase of perturbation growth through mechanisms proposed here. This can possibly lead to the delayed growth of subsequent stages, thereby potentially leading to the development of new transition delay techniques for stationary crossflow instability induced transition.

8.2. Recommendations for Future Work

- The evolution of stationary crossflow instability through swept wing boundary layers deformed via a natural source such as a hump should be tested, and the mechanisms of perturbation evolution could be studied using frameworks similar to those developed in this thesis. The hump for instance could potentially have a region of wall-tangential base flow deceleration followed by a region of wall-tangential base flow acceleration if its velocity fields are viewed in the xy Cartesian coordinate system (similar to the reference negative p_f case shown in Figure 6.3 (C)), which might help stabilize the crossflow instability via the results found here. The energy balance procedure can either be adapted to the curvilinear coordinate system in which perturbation equations are usually solved by accounting for a boundary layer with curved obstacles. Or, the energy balance procedure can be performed on a fine Cartesian grid, wherein the results on this grid are obtained as a result of coordinate transformation and interpolation from the curvilinear coordinate system. In either approach, the production term behaviour needs to be explicitly related to the energy partial derivative in the desired direction, which should then be able to ratify the trends of perturbation growth or decay. A surface indentation can also be tested, although its effectiveness in damping an incoming stationary crossflow mode might not be as strong since it would potentially entail a region of wall-tangential base flow acceleration followed by wall-tangential base flow deceleration when viewed in the Cartesian xy coordinate system (similar to the reference positive p_f case shown in Figure 6.3 (b)).
- An extension of the spanwise integrated Reynolds-Orr tool to model non-linear terms in primary instability evolution could be undertaken. A potential use case would be the study of an FFS to understand how the harmonics, prominent in step downstream regions, gain energy and how their growth affects the development of the fundamental perturbation. Studies on the effects of varying initial amplitude can also be conducted, starting from a small amplitude and increasing to a large amplitude, since this parameter would also play a major role in governing the extent of non-linear effects.
- The behaviour of $\cos(\phi_2 - \phi_1)$ needs to be studied in detail in future studies since an exact reason explaining its near-wall increase and decrease in base flow deformed regions could not be found in this thesis. Understanding the behaviour of this parameter is important since its decrease plays a role in aiding stabilization when a decelerating base flow starts accelerating. The first step would be to understand the behaviour of $\cos(\phi_2 - \phi_1)$ in the clean case for different wavelengths. Since $\cos(\phi_2 - \phi_1)$ takes negative values causing consistent destabilization in the clean case of 7.5 mm wavelength, there is a chance that the behaviour is dependent on whether the crossflow mode is itself a growing or decaying mode, with a locally stable mode possibly yielding positive values of $\cos(\phi_2 - \phi_1)$. The variation of $\cos(\phi_2 - \phi_1)$ with spanwise wavelength in clean cases can be studied via ILST solutions since ILST, PSE, and HLNS all predict the same field of $\cos(\phi_2 - \phi_1)$ for the single wavelength simulated in the clean case. The second step would be to study the evolution of $\cos(\phi_2 - \phi_1)$ by seeding stationary crossflow instabilities of different spanwise wavelengths and studying the linear evolution of each of these through the synthetic deformed base flows developed in this thesis. This will help understand if the tendency of upward and downward movement of their constant contour lines, resulting in reduction and increase in near-wall regions in adverse ΔP and favourable ΔP regions, respectively, are universal for all spanwise wavelengths considered. Even if a fully mathematical explanation can't be worked out, a correlation relating the behaviour of $\cos(\phi_2 - \phi_1)$ possibly to parameters of base flow such as boundary layer change with respect to the clean case could be formulated. Once the behaviour of $\cos(\phi_1 - \phi_2)$ is understood, the behaviour of $\mathcal{P}_{y_d}$ will be understood to a much better extent. Asymmetric ΔP distributions can then be tried out, varying the size of regions of base flow acceleration and deceleration, to understand if these asymmetric distributions work more effectively than symmetric distributions in stabilizing incoming perturbations.
- A study on understanding potential reasons for secondary peaks appearing in u' amplitude function in the FFS (but not in the synthetic deformations simulated here) needs to be undertaken. The emergence of secondary peaks might be related to the behaviour of $\cos(\phi_2 - \phi_1)$. Regions where $\cos(\phi_2 - \phi_1)$ takes high positive values close to one, are close to regions of secondary peak appearance in FFS cases, which could to some extent be correlated to the presence of a very strong adverse pressure gradient upstream and downstream of the step, which deforms the flow much more than the synthetic deformations tested here. The strong stabilization seen in the production term of the highest FFS case simulated by Casacuberta, Hickel, Westerbeek, and Kotsonis (2022) occurs in the second adverse ΔP region, in a region not only close to the presence of secondary peaks but also in the region of decay of these secondary peaks, providing further evidence that the study of the behaviour of these peaks is extremely important. The stabilization of $\mathcal{P}$ in the largest FFS case can be attributed to a sudden reversal of $\cos(\phi_2 - \phi_1)$ sign from negative to positive

(the stabilization of $\mathcal{P}_{y_d}$ terms is so strong that even when the $\mathcal{P}_{x_d}$ terms are destabilizing, $\mathcal{P}$ stabilizes). The full energy balance considering the x derivative of energy, instead of just the production term, would perhaps yield an understanding of how the reversal of $\cos(\phi_2 - \phi_1)$ sign affects the development of secondary peaks. Also in the case of competing primary and secondary peaks, it would be more instructive to integrate the perturbation amplitude function in the wall-normal direction, while checking if the perturbation grows or decays in x. A good use case to study secondary peak development could be the study of crossflow instability evolution over a separation bubble similar to the setup used by Hosseinverdi and Fasel (2016), where separation would possibly trigger secondary peak development.

References

Abernathy, F. (1968). *Fundamentals of boundary layers*. National Committee for Fluid Mechanics Films., Education Development Center., & Encyclopaedia Britannica Educational Corporation.

Albensoeder, S., Kuhlmann, H., & Rath, H. (2001). Three-dimensional centrifugal-flow instabilities in the lid-driven-cavity problem. *Physics of fluids*, *13*(1), 121–135. doi: 10.1063/1.1329908

Anderson, J. D. (2011). *Fundamentals of aerodynamics*. McGraw-Hill.

Andersson, P., Berggren, M., & Henningson, D. S. (1999). Optimal disturbances and bypass transition in boundary layers. *Physics of Fluids*, *11*(1), 134-150. doi: 10.1063/1.869908

Anger, A. (2010). Including aviation in the European emissions trading scheme: Impacts on the industry, carbon dioxide emissions and macroeconomic activity in the eu. *Journal of Air Transport Management*, *16*(2), 100-105. (Selected Papers from the Air Transport Research Society Conference Athens, 2008) doi: 10.1016/j.jairtraman.2009.10.009

Anscombe, A., & Illingworth, L. N. (1956). *Wind-tunnel observations of boundary-layer transition on a wing at various angles of sweepback.* ARC R MN 2968.

Beck, N., Landa, T., Seitz, A., Boermans, L., Liu, Y., & Radespiel, R. (2018). Drag reduction by laminar flow control. *Energies*, *11*(1). doi: 10.3390/en11010252

Bertolotti, F. P. (1991). *Linear and nonlinear stability of boundary layers with streamwise varying properties* (Unpublished doctoral dissertation).

Bertolotti, F. P., Herbert, T., & Spalart, P. R. (1992). Linear and nonlinear stability of the Blasius boundary layer. *Journal of Fluid Mechanics*, *242*, 441–474. doi: 10.1017/S0022112092002453

Bippes, H. (1999). Basic experiments on transition in three-dimensional boundary layers dominated by crossflow instability. *Progress in Aerospace Sciences*, *35*(4), 363-412. doi: 10.1016/S0376-0421(99)00002-0

Boiko, A. V., Dovgal, A. V., Grek, G. R., & Kozlov, V. V. (2011). *Physics of transitional shear flows: Instability and laminar–turbulent transition in incompressible near-wall shear layers* (Vol. 98). Springer Science & Business Media.

Brandt, L. (2014). The lift-up effect: The linear mechanism behind transition and turbulence in shear flows. *European Journal of Mechanics - B/Fluids*, *47*, 80-96. (Enok Palm Memorial Volume) doi: 10.1016/j.euromechflu.2014.03.005

Butler, K. M., & Farrell, B. F. (1992). Three dimensional optimal perturbations in viscous shear flow. *Physics of Fluids A: Fluid Dynamics*, *4*(8), 1637-1650. doi: 10.1063/1.858386

Byström, M. G. (2007). *Optimal disturbances in boundary layer flows* (Unpublished doctoral dissertation). KTH, Mechanics.

Casacuberta, J., Groot, K. J., Hickel, S., & Kotsonis, M. (2022). Secondary instabilities in swept-wing boundary layers: Direct numerical simulations and biglobal stability analysis. In *Aiaa scitech 2022 forum* (p. 2330). doi: 10.2514/6.2022-2330

Casacuberta, J., Hickel, S., & Kotsonis, M. (2021). Mechanisms of interaction between stationary crossflow instabilities and forward-facing steps. In *Aiaa scitech 2021 forum* (p. 0854).

Casacuberta, J., Hickel, S., & Kotsonis, M. (2022). Passive stabilisation of crossflow instabilities via a reverse lift-up effect. *Under consideration for publication in Journal of Fluid Mechanics*.

Casacuberta, J., Hickel, S., Westerbeek, S., & Kotsonis, M. (2022). Direct numerical simulation of interaction between a stationary crossflow instability and forward-facing steps. *Journal of Fluid Mechanics*, *943*. doi: 10.1017/jfm.2022.456

Corbett, P., & Bottaro, A. (2001). Optimal linear growth in swept boundary layers. *Journal of Fluid Mechanics*, *435*, 1–23. doi: 10.1017/S0022112001003627

Dörr, P., & Kloker, M. (2015). Stabilisation of a three-dimensional boundary layer by base-flow manipulation using plasma actuators. *Journal of Physics D: Applied Physics*, *48*(28), 285205. doi: 10.1088/0022-3727/48/28/285205

Ellingsen, T., & Palm, E. (1975). Stability of linear flow. *The Physics of Fluids*, *18*(4), 487-488. doi: 10.1063/1.861156

Eppink, J. L. (2018). The effect of forward-facing steps on stationary crossflow instability growth and breakfown. In *2018 aiaa aerospace sciences meeting* (p. 0817).

Eppink, J. L. (2020). Mechanisms of stationary cross-flow instability growth and breakdown induced by forward-facing steps. *Journal of Fluid Mechanics*, *897*, A15. doi: 10.1017/jfm.2020.367

Fjørtoft, R. (1950). *Application of integral theorems in deriving criteria of stability for laminar flows and for the baroclinic circular vortex* (Vol. 17). Grøndahl & søns boktr., I kommisjon hos Cammermeyers boghandel.

Franco, J., Hein, S., & Valero, E. (1821). Effect of humps and indentations on boundary-layer transition of compressible flows using the ahlns methodology. *Proc. 6th ECCM–7th ECFD, Paper*, *2018*.

Gill, M. (2016). Aviation benefits beyond borders. *Air Transport Action Group (ATAG)*, *1*(1), 1–76.

Goldstein, S. (1948). On laminar boundary-layer flow near a position of separation. *The Quarterly Journal of Mechanics and Applied Mathematics*, *1*(1), 43–69.

Gray, W. (1952). The effect of wing sweep on laminar flow. *Rae Tm Aero*, *227*, 1952.

Groot, K. (2018). *Biglobal stability of shear flows spanwise & streamwise analyses* (Unpublished doctoral dissertation). Delft University of Technology.

Haberman, R. (1983). *Elementary applied partial differential equations* (Vol. 987). Prentice Hall Englewood Cliffs, NJ.

Haglind, F., Hasselrot, A., & Singh, R. (2006). Potential of reducing the environmental impact of aviation by using hydrogen Part I: Background, prospects and challenges. *The Aeronautical Journal*, *110*(1110), 533–540. doi: 10 .1017/S000192400000141X

Hansen, H. (2010). Laminar flow technology–the airbus view. In *27th international congress of the aeronautical sciences (icas), nice, france.*

Herbert, T. (1988). Secondary instability of boundary layers. *Annual review of fluid mechanics*, *20*(1), 487–526.

Herbert, T. (1994). Parabolized stability equations. In *Agard report no. 793.*

Hickel, S., & Adams, N. (2008). Implicit les applied to zero-pressure-gradient and adverse-pressure-gradient boundary-layer turbulence. *International Journal of Heat and Fluid Flow*, *29*(3), 626–639. doi: 10.1016/j.ijheatfluidflow .2008.03.008

Hickel, S., Egerer, C. P., & Larsson, J. (2014). Subgrid-scale modeling for implicit large eddy simulation of compressible flows and shock-turbulence interaction. *Physics of Fluids*, *26*(10), 106101. doi: 10.1063/1.4898641

Hosseinverdi, S., & Fasel, H. F. (2016). Direct numerical simulations of laminar-to-turbulent transition in laminar separation bubbles in three-dimensional boundary-layer. In *46th aiaa fluid dynamics conference* (p. 3793).

Howard, L. N. (1961). Note on a paper of john w. miles. *Journal of Fluid Mechanics*, *10*(4), 509–512.

Hultgren, L. S., & Gustavsson, L. H. (1981). Algebraic growth of disturbances in a laminar boundary layer. *The Physics of Fluids*, *24*(6), 1000-1004. doi: 10.1063/1.863490

Joslin, R. D. (1992). *Validation of three-dimensional incompressible spatial direct numerical simulation code: A comparison with linear stability and parabolic stability equation theories for boundary-layer transition on a flat plate* (Vol. 3205). National Aeronautics and Space Administration, Office of Management, Scientific and Technical Information Program.

Karp, M., & Hack, M. P. (2018). Transition to turbulence over convex surfaces. *Journal of Fluid Mechanics*, *855*, 1208–1237. doi: doi:10.1017/jfm.2018.690

Landahl, M. T. (1980). A note on an algebraic instability of inviscid parallel shear flows. *Journal of Fluid Mechanics*, *98*(2), 243–251. doi: 10.1017/S0022112080000122

Lanzerstorfer, D., & Kuhlmann, H. C. (2012). Three-dimensional instability of the flow over a forward-facing step. *Journal of fluid mechanics*, *695*, 390–404. doi: 10.1017/jfm.2012.28

Levin, O., & Henningson, D. S. (2003). Exponential vs algebraic growth and transition prediction in boundary layer flow. *Flow, Turbulence and Combustion*, *70*(1), 183–210. doi: 10.1023/B:APPL.0000004918.05683.46

Lin, C. C. (1944). On the stability of two-dimensional parallel flows. *Proceedings of the National Academy of Sciences*, *30*(10), 316-324. doi: 10.1073/pnas.30.10.316

Lindzen, R. S. (1988). Instability of plane parallel shear flow (toward a mechanistic picture of how it works). *Pure and Applied Geophysics*, *126*. doi: 10.1007/BF00876917

Loiseau, J.-C., Robinet, J.-C., Cherubini, S., & Leriche, E. (2014). Investigation of the roughness-induced transition: global stability analyses and direct numerical simulations. *Journal of Fluid Mechanics*, *760*, 175–211. doi: 10.1017/ jfm.2014.589

Loiseau, J.-C., Robinet, J.-C., & Leriche, E. (2016). Intermittency and transition to chaos in the cubical lid-driven cavity flow. *Fluid Dynamics Research*, *48*(6), 061421. doi: 10.1088/0169-5983/48/6/061421

Lucas, J. (2014). *Spatial optimal perturbations for transient growth analysis in three-dimensional boundary layers* (Unpublished doctoral dissertation). Université de Toulouse.

Luchini, P. (2000). Reynolds-number-independent instability of the boundary layer over a flat surface: optimal perturbations. *Journal of Fluid Mechanics*, *404*, 289–309. doi: 10.1016/0021-9991(90)90106-B

Mack, L. M. (1984). Special course on stability and transition of laminar flow. In *Agard report no. 709.*

Malik, M. R. (1990). Numerical methods for hypersonic boundary layer stability. *Journal of computational physics*, *86*(2), 376–413. doi: 10.1016/0021-9991(90)90106-B

Malik, M. R., Li, F., & Chang, C.-L. (1994). Crossflow disturbances in three-dimensional boundary layers: nonlinear development, wave interaction and secondary instability. *Journal of Fluid Mechanics*, *268*, 1–36. doi: 10.1017/ S0022112094001242

Marxen, O., Lang, M., Rist, U., Levin, O., & Henningson, D. S. (2009). Mechanisms for spatial steady three-dimensional disturbance growth in a non-parallel and separating boundary layer. *Journal of Fluid Mechanics*, *634*, 165–189. doi: 10.1017/S0022112009007149

Mistry, V. I. (2014). *Simulation and control of stationary crossflow vortices* (Unpublished doctoral dissertation). Loughborough University.

Morkovin, M. V. (1969). On the many faces of transition. In C. S. Wells (Ed.), *Viscous drag reduction* (pp. 1–31). Boston, MA: Springer US.

Orr, W. M. (1907). The stability or instability of the steady motions of a perfect liquid and of a viscous liquid. part ii: A viscous liquid. *Proceedings of the Royal Irish Academy. Section A: Mathematical and Physical Sciences*, *27*, 69–138.

Picella, F., Loiseau, J.-C., Lusseyran, F., Robinet, J.-C., Cherubini, S., & Pastur, L. (2018). Successive bifurcations in a fully three-dimensional open cavity flow. *Journal of Fluid Mechanics*, *844*, 855–877. doi: 10.1017/jfm.2018.169

Prandtl, L. (1921). Bemerkungen über die entstehung der turbulenz. *ZAMM-Journal of Applied Mathematics and Mechanics/Zeitschrift für Angewandte Mathematik und Mechanik*, *1*(6), 431–436.

Radeztsky Jr, R. H., Reibert, M. S., & Saric, W. S. (1999). Effect of isolated micron-sized roughness on transition in swept-wing flows. *AIAA journal*, *37*(11), 1370–1377. doi: 10.2514/2.635

Rayleigh, L. (1879, 11). On the Stability, or Instability, of certain Fluid Motions. *Proceedings of the London Mathematical Society*, *s1-11*(1), 57-72. doi: 10.1112/plms/s1-11.1.57

Reddy, S. C., & Henningson, D. S. (1993). Energy growth in viscous channel flows. *Journal of Fluid Mechanics*, *252*, 209–238. doi: 10.1017/S0022112093003738

Reed, H. L., & Saric, W. S. (2014). Attachment-line heating in a compressible flow. *Journal of Engineering Mathematics*, *84*(1), 99–110. doi: 10.1007/s10665-013-9662-5

Reed, H. L., Saric, W. S., & Arnal, D. (1996). Linear stability theory applied to boundary layers. *Annual Review of Fluid Mechanics*, *28*(1), 389-428. doi: 10.1146/annurev.fl.28.010196.002133

Reibert, M., Saric, W., Carrillo, R., Jr, & Chapman, K. (1996). Experiments in nonlinear saturation of stationary crossflow vortices in a swept-wing boundary layer. In *34th aerospace sciences meeting and exhibit* (p. 184).

Reshotko, E. (2008). Transition issues for atmospheric entry. *Journal of Spacecraft and Rockets*, *45*(2), 161-164. doi: 10.2514/1.29777

Rius-Vidales, A. F., & Kotsonis, M. (2020). Influence of a forward-facing step surface irregularity on swept wing transition. *AIAA Journal*, *58*(12), 5243-5253. doi: 10.2514/1.J059566

Rius-Vidales, A. F., & Kotsonis, M. (2021). Impact of a forward-facing step on the development of crossflow instability. *Journal of Fluid Mechanics*, *924*, A34. doi: 10.1017/jfm.2021.497

Rius-Vidales, A. F., & Kotsonis, M. (2022). Unsteady interaction of crossflow instability with a forward-facing step. *Journal of Fluid Mechanics*, *939*, A19. doi: 10.1017/jfm.2022.151

Roy, A., & Govindarajan, R. (2010, 08). An introduction to hydrodynamic stability. In (p. 131-147). doi: 10.1007/978-1-4419-6494-6_6

Roy, A., & Subramanian, G. (2014). An inviscid modal interpretation of the 'lift-up' effect. *Journal of Fluid Mechanics*, *757*, 82–113. doi: 10.1017/jfm.2014.485

Sahoo, S., Zhao, X., & Kyprianidis, K. (2020). A review of concepts, benefits, and challenges for future electrical propulsion-based aircraft. *Aerospace*, *7*(4). doi: 10.3390/aerospace7040044

Saric, W. S., Reed, H. L., & White, E. B. (2003). Stability and transition of three-dimensional boundary layers. *Annual Review of Fluid Mechanics*, *35*(1), 413-440. doi: 10.1146/annurev.fluid.35.101101.161045

Saric, W. S., West, D. E., Tufts, M. W., & Reed, H. L. (2019). Experiments on discrete roughness element technology for swept-wing laminar flow control. *AIAA Journal*, *57*(2), 641–654. doi: 10.2514/1.J056897

Scharnhorst, K. (2001). Angles in complex vector spaces. *Acta Applicandae Mathematica*, *69*(1), 95–103. doi: 10.48550/arXiv.math/9904077

Schlichting, H., & Gersten, K. (2000). *Fundamentals of boundary-layer theory*. Springer.

Schmid, P. J., & Henningson, D. S. (2001). Stability and transition in shear flows. New York, NY: Springer New York. doi: 10.1007/978-1-4613-0185-1_7

Schrauf, G. (2005). Status and perspectives of laminar flow. *The Aeronautical Journal (1968)*, *109*(1102), 639–644. doi: 10.1017/S000192400000097X

Serpieri, J., & Kotsonis, M. (2016). Three-dimensional organisation of primary and secondary crossflow instability. *Journal of Fluid Mechanics*, *799*, 200–245. doi: 10.1017/jfm.2016.379

Sgouridis, S., Bonnefoy, P. A., & Hansman, R. J. (2011). Air transportation in a carbon constrained world: Long-term dynamics of policies and strategies for mitigating the carbon footprint of commercial aviation. *Transportation Research Part A: Policy and Practice*, *45*(10), 1077-1091. (A Collection of Papers:Transportation in a World of Climate Change) doi: 10.1016/j.tra.2010.03.019

Smith, A. M. O., & Gamberoni, N. (1956). Transition, pressure gradient and stability theory. *Douglas Aircraft Co., Report ES 26388*.

Streett, C., & Macaraeg, M. (1989). Spectral multi-domain for large-scale fluid dynamic simulations. *Applied Numerical Mathematics*, *6*(1-2), 123–139. doi: 10.1016/0168-9274(89)90058-5

Tempelmann, D., Hanifi, A., & Henningson, D. S. (2010). Spatial optimal growth in three-dimensional boundary layers. *Journal of Fluid Mechanics*, *646*, 5–37. doi: 10.1017/S0022112009993260

Tempelmann, D., Schrader, L.-U., Hanifi, A., Brandt, L., & Henningson, D. S. (2012). Swept wing boundary-layer receptivity to localized surface roughness. *Journal of Fluid Mechanics*, *711*, 516–544. doi: 10.1017/jfm.2012.405

Tufts, M. W., Reed, H. L., Crawford, B. K., Duncan, G. T., & Saric, W. S. (2017). Computational investigation of step excrescence sensitivity in a swept-wing boundary layer. *Journal of Aircraft*, *54*(2), 602-626. doi: 10.2514/1.C033892

Van Ingen, J. (1956). A suggested semi-empirical method for the calculation of the boundary layer transition region. *Technische Hogeschool Delft, Vliegtuigbouwkunde, Rapport VTH-74*.

Vos, R., & Farokhi, S. (2015). Aerodynamics of non-lifting bodies. In *Introduction to transonic aerodynamics* (pp. 275–366). Dordrecht: Springer Netherlands. doi: 10.1007/978-94-017-9747-4_6

Wassermann, P., & Kloker, M. (2002). Mechanisms and passive control of crossflow-vortex-induced transition in a three-dimensional boundary layer. *Journal of Fluid Mechanics*, *456*, 49–84.

Westerbeek, S. (2020). *Development of a nonlinear parabolized stability equation (npse) analysis tool for spanwise invariant boundary layers* (Unpublished master's thesis). TU Delft.

A

Additional Test Case Details

A.1. Clean Case Pressure Distribution

The clean case external pressure distribution is shown in Figure A.1. The external pressure is propagated uniformly down to the wall, implying invariance of pressure with wall-normal height.

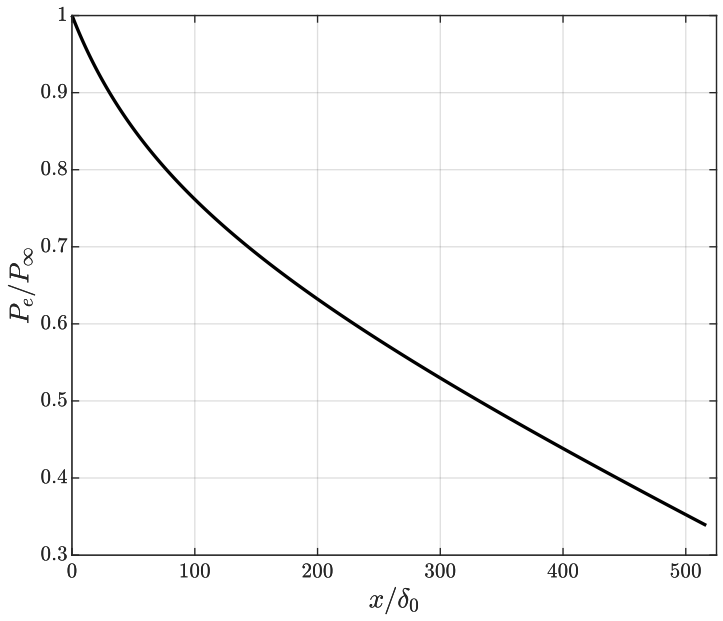

Figure A.1: External pressure distribution of clean case

A.2. Tabulated Test Case Properties

Some additional details of the test-matrix of two-way cases simulated in the thesis are provided here. The gradient of ΔP distributions, and the maximum and minimum values of effective pressure gradient are compared for all two-way pressure variation cases in Table A.1. The values of clean case are presented for reference in the row corresponding to case 19. The maximum values of $d(|\Delta P|)/dx$ lie between 0.5E-3 and 0.9E-3 for the low p_f cases, between 2.2E-3 and 2.9E-3 for the medium p_f cases, and between 4E-3 and 5.3E-3 for the large p_f cases, showing the similarities in the maximum $d(|\Delta P|)/dx$ values for a given value of p_f. The highest p_f cases have maximum favourable pressure gradient of about five times the pressure gradient of clean case, and adverse pressure gradient of about three times the pressure gradient of clean case. Whereas the lowest p_f cases have pressure gradients much nearer to the clean case, with absence of adverse pressure gradient regions evidenced by the negative values of dP_e/dx_{max}.

Case	p_f	w/δ_0	$d(\lvert\Delta P\rvert)/dx_{max}$ $(\delta_0/P_\infty \times 10^3)$	dP_e/dx_{min} $(\delta_0/P_\infty \times 10^3)$	dP_e/dx_{max} $(\delta_0/P_\infty \times 10^3)$
1	0.5	10	0.523	-1.709	-0.642
2	1.5	10	2.231	-3.413	1.063
3	2.5	10	4.131	-5.313	2.962
4	-0.5	10	0.523	-1.688	-0.662
5	-1.5	10	2.231	-3.399	1.048
6	-2.5	10	4.131	-5.300	2.949
7	0.5	30	0.744	-1.942	-0.411
8	1.5	30	2.736	-3.930	1.578
9	2.5	30	4.904	-6.096	3.744
10	-0.5	30	0.744	-1.898	-0.454
11	-1.5	30	2.736	-3.895	1.543
12	-2.5	30	4.904	-6.063	3.711
13	0.5	50	0.826	-2.036	-0.318
14	1.5	50	2.942	-4.146	1.793
15	2.5	50	5.224	-6.426	4.073
16	-0.5	50	0.826	-1.971	-0.383
17	-1.5	50	2.942	-4.091	1.738
18	-2.5	50	4.069	-5.219	2.866
19	0	-	-	-1.262	-1.109

Table A.1: Properties of two-way pressure variation distributions and their corresponding effective pressure distributions.

The ΔP gradient and pressure gradient data for three-way cases are provided in Table A.2. The absolute value of maximum $d(\Delta P)/dx$ is approximately half the absolute value of the minimum $d(\Delta P)/dx$, showing the steeper value of favourable ΔP gradient compared to the adverse ΔP regions, as evident in Figure 2.6. Also, it can be noted that dP_e/dx_{max} never turns positive in the lowest p_f case. As seen in the two-way pressure variation cases, the discrepancy between pressure gradient of deformed cases and the pressure gradient of the clean case increases with an increase of p_f.

Case	p_f	w/δ_0	$(d(\Delta P)/dx_{min}$ $\delta_0/P_\infty \times 10^3)$	$d(\Delta P)/dx_{max}$ $(\delta_0/P_\infty \times 10^3)$	dP_e/dx_{min} $(\delta_0/P_\infty \times 10^3)$	dP_e/dx_{max} $(\delta_0/P_\infty \times 10^3)$
1	0.5	30	-1.484	0.714	-2.660	-0.419
2	1.5	30	-5.092	2.709	-6.267	1.571
3	2.5	30	-8.634	4.877	-9.809	3.739
4	0	-	-	-	-1.262	-1.109

Table A.2: Properties of three-way pressure variation distributions and their corresponding effective pressure distributions.

B

Additional Details on Modelling Base Flow and Perturbation Evolution

B.1. Domain

The domain used for base flow and perturbation computations is shown in Figure B.1. The base flow domain extends from $y/\delta_0 = 0$ to 516. Whereas, the perturbation domain is a cropped version of the base flow domain, extending from extending from $x/\delta_0 = 140$ to 273. The location of pressure variation imposition of the largest deformation width is also shown, and it can be observed that the location of stationary crossflow mode initialization (i.e. the inlet of perturbation domain) is sufficiently upstream of the largest width base flow deformation.

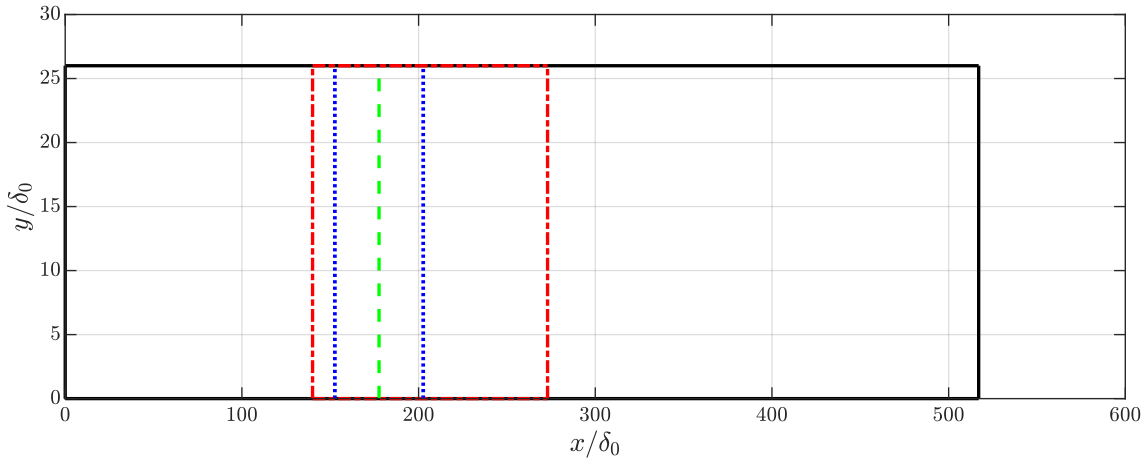

Figure B.1: Domain for baseflow computation (solid black) and domain for perturbation computation (dash-dotted red); location of μ (dashed green) at $x/\delta_0 = 177.62$; location of $x/\delta_0 = \mu - w/2$ and $\mu + w/2$ (dotted blue) when $w = 50$.

B.2. Derivation of Boundary Layer Equations

To obtain the boundary layer equations from the Navier Stokes equations, a number of assumptions need to be applied. A reference is made to Schlichting and Gersten (2000) to derive these assumptions. The original equations were presented for two-dimensional flat plates by the author, but in the current case, the assumptions are extended to three-dimensional swept flat plate boundary layers. The first assumption relates the thickness of boundary layer 'δ' and a characteristic length scale 'l', representative of the swept flat plate by

$$\delta << l. \tag{B.1}$$

Physically this implies that changes in the boundary layer occur over a very thin region (order of δ) compared to the changes in streamwise direction (occuring over l). Emperically, at large Reynolds numbers based on the flat plate length

scale ($\mathrm{Re} = U_\infty l/\nu$), it is found that

$$\frac{\delta}{l} \propto \frac{1}{\sqrt{\mathrm{Re}}}. \tag{B.2}$$

At large Reynolds numbers, the RHS of Equation B.2 tends to a very small number. Thus, Equation B.1 holds in the limit of large Reynolds number. The continuity and momentum equations (Equations Equation 3.1 to Equation 3.4) are non dimensionalized by the length scale of the flat plate l and freestream velocity U_∞ to further study the impact of this assumption, yielding

$$\underbrace{\frac{\partial {U_B}^*}{\partial x^*}}_{O(1)} + \underbrace{\frac{\partial {V_B}^*}{\partial y^*}}_{O(1)} = 0, \tag{B.3}$$

$$\underbrace{{U_B}^*}_{O(1)}\underbrace{\frac{\partial {U_B}^*}{\partial x}}_{O(1)} + \underbrace{{V_B}^*}_{O(\delta^*)}\underbrace{\frac{\partial {U_B}^*}{\partial y}}_{O(1/\delta^*)} = -\frac{\partial {P_B}^*}{\partial x} + \underbrace{\frac{1}{\mathrm{Re}}}_{O(\delta^{*2})}\left(\underbrace{\frac{\partial^2 {U_B}^*}{\partial x^2}}_{O(1)} + \underbrace{\frac{\partial^2 {U_B}^*}{\partial y^2}}_{O(1/\delta^{*2})}\right), \tag{B.4}$$

$$\underbrace{{U_B}^*}_{O(1)}\underbrace{\frac{\partial {V_B}^*}{\partial x}}_{O(\delta^*)} + \underbrace{{V_B}^*}_{O(\delta^*)}\underbrace{\frac{\partial {V_B}^*}{\partial y}}_{O(1)} = -\frac{\partial {P_B}^*}{\partial y^*} + \underbrace{\frac{1}{\mathrm{Re}}}_{O(\delta^{*2})}\left(\underbrace{\frac{\partial^2 {V_B}^*}{\partial x^2}}_{O(\delta^*)} + \underbrace{\frac{\partial^2 {V_B}^*}{\partial y^2}}_{O(1/\delta^*)}\right), \tag{B.5}$$

$$\underbrace{{U_B}^*}_{O(1)}\underbrace{\frac{\partial {W_B}^*}{\partial x}}_{O(1)} + \underbrace{{V_B}^*}_{O(\delta^*)}\underbrace{\frac{\partial {W_B}^*}{\partial y}}_{O(1/\delta^*)} = \underbrace{\frac{1}{\mathrm{Re}}}_{O(\delta^{*2})}\left(\underbrace{\frac{\partial^2 {W_B}^*}{\partial x^2}}_{O(1)} + \underbrace{\frac{\partial^2 {W_B}^*}{\partial y^2}}_{O(1/\delta^{*2})}\right), \tag{B.6}$$

where $x^* = x/l$ and $y^* = y/l = y\delta^*/\delta$. The estimated order of magnitudes of each of the terms in the above equations are also mentioned beneath the terms to allow further simplification of the equations. First, the order of magnitudes in the non-dimensionalized continuity equation (Equation B.4) are considered. ${U_B}^*$ and x^* are ratios of quantities with similar scale and thus have an order of magnitude 1. This implies that $\partial {U_B}^*/\partial x^* = O(1)$. Whereas since y has a length scale comparable to δ, y^* = O(δ^*). In the inviscid limit, δ^* tends to zero. For the continuity equation to not tend to infinity in this limit, ${V_B}^*$ and y^* should have the same order of magnitude. Thus, $V_B = O(\delta^*)$.

The order of magnitudes in the x momentum equation (Equation B.4) are now considered. The order of the x advection term is self-explanatory, knowing the order of U_B and $\partial {U_B}^*/\partial x^*$. In the y advection term, the order of $\partial {U_B}^*/\partial y^*$ is a division of orders of each term resulting in $1/\delta^*$. When multiplied by V_B, the resulting order is $O(1)$ term. On the right hand side, pressure should have an $O(1)$ magnitude to match the order of x^*, leading to an O(1) magnitude for the derivative. Moving to the next term, the effect of viscosity has to be manifested by at least one term to ensure that the inviscid solution and the viscous solution vary from each other. $\partial^2 {U_B}^*/\partial {y^*}^2$ clearly has a much greater order than $\partial^2 {U_B}^*/\partial {x^*}^2$ due to y^* having a much smaller order than x^*. Therefore, its order is balanced off by the Reynolds number which now has to have a O$(\delta^*)^2$ limit, so that the whole viscous term has an order of one, similar to the convection terms of the equation. The treatment of the viscous terms results in the second assumption from order of magnitude analysis which reads

$$\frac{\partial^2 {U_B}^*}{\partial {y^*}^2} >> \frac{\partial^2 {U_B}^*}{\partial {x^*}^2}. \tag{B.7}$$

A similar treatment can be applied to the non-dimensionalized z momentum equation yielding

$$\frac{\partial^2 {W_B}^*}{\partial {y^*}^2} >> \frac{\partial^2 {W_B}^*}{\partial {x^*}^2}. \tag{B.8}$$

Now, the y momentum (Equation B.5) equation is considered. All terms yield an O(δ^*) magnitude using the order of magnitude analysis technique proposed above except the y pressure gradient term, which has O($1/\delta^*$) magnitude. Thus, this is the dominating term in the equation. Removing all lower order terms out results in the third assumption of boundary layer which reads

$$\frac{\partial {P_B}^*}{\partial y^*} = 0. \tag{B.9}$$

This assumption implies that any pressure gradient imposed at the top boundary or in the inviscid flow region is directly felt at the wall. Schlichting and Gersten (2000) explains that this assumption physically corresponds to a particle having no

mass or experiencing no friction while moving in the wall-normal direction in the boundary layer. The resulting equations are brought back to dimensional form, after removing terms omitted by the order of magnitude analysis to yield

$$\frac{\partial U_B}{\partial x} + \frac{\partial V_B}{\partial y} = 0, \tag{B.10}$$

$$U_B \frac{\partial U_B}{\partial x} + V_B \frac{\partial U_B}{\partial y} = -\frac{1}{\rho}\frac{\partial P_B}{\partial x} + \nu \frac{\partial^2 U_B}{\partial y^2}, \tag{B.11}$$

$$\frac{\partial P_B}{\partial y} = 0, \tag{B.12}$$

$$U_B \frac{\partial W_B}{\partial x} + V_B \frac{\partial W_B}{\partial y} = \nu \frac{\partial^2 W_B}{\partial y^2}. \tag{B.13}$$

The pressure in Equation B.11 can be eliminated by considering the conditions of the inviscid layer placed above the boundary layer, where U_{B_y} and $U_{B_{yy}}$ are infinitesimally small, simplifying the equation to the Bernoulli equation in differential form given by

$$U_e \frac{\partial U_e}{\partial x} = -\frac{1}{\rho}\frac{\partial P_e}{\partial x} \tag{B.14}$$

The subscript "e" corresponds to external flow in the inviscid region. Since there is no vartion of pressure in y, $P_B = P_e$. This eliminates pressure from Equation B.11 to yield

$$U_B \frac{\partial U_B}{\partial x} + V_B \frac{\partial U_B}{\partial y} = U_e \frac{\partial U_e}{\partial x} + \nu \frac{\partial^2 U_B}{\partial y^2}. \tag{B.15}$$

B.3. DNS and BLS Base Flow Differences

Additional plots on the differences between the BLS and DNS base flow of the $-2.5p_f30w$ case are shown in this section, whose preliminary results are shown in Section 3.5. P_e and P_B (at $y/\delta_0 = 0.75$) distributions of DNS and BLS base flows are contrasted in Figure B.2 (a) and (b) respectively. V_e and V_B (at $y/\delta_0 = 0.75$) distributions of DNS and BLS base flows are contrasted in Figure B.2 (a) and (b) respectively. U_{e_x} and U_{B_x} (at $y/\delta_0 = 0.75$) distributions of DNS and BLS base flows are contrasted in Figure B.4 (a) and (b) respectively.

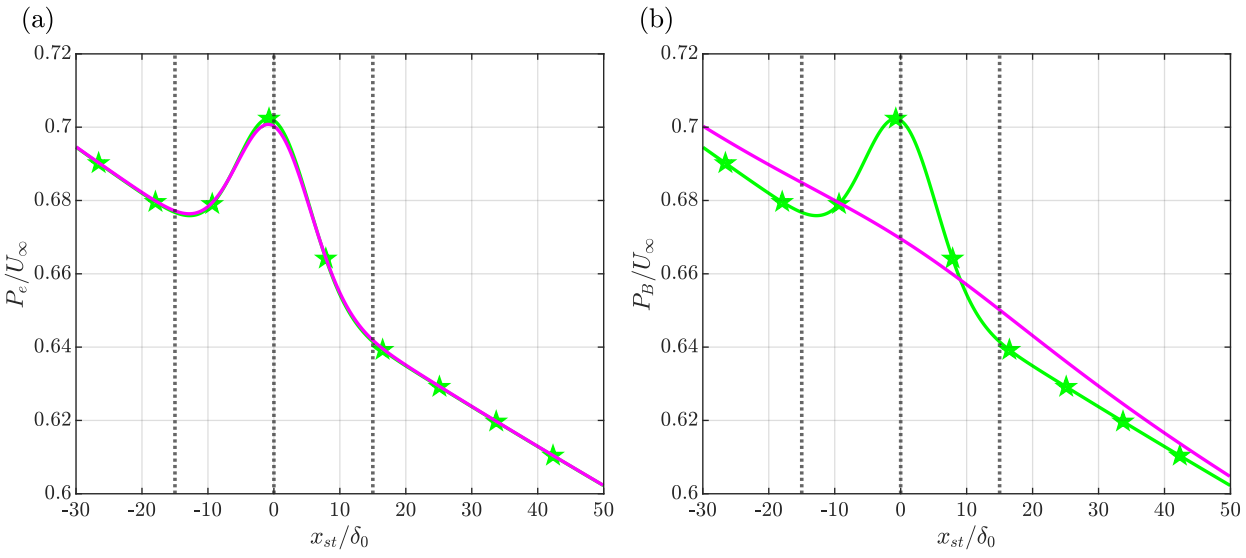

Figure B.2: Chordwise variation of (a) P_e and (b) P_B (at $y/\delta_0 = 0.75$) in the $-2.5p_f30w$ case simulated by DNS (magenta) and BLS (light green); black dotted lines at $x_{st}/\delta_0 = -w/2,\ 0,$ and $w/2$ show region of ΔP imposition.

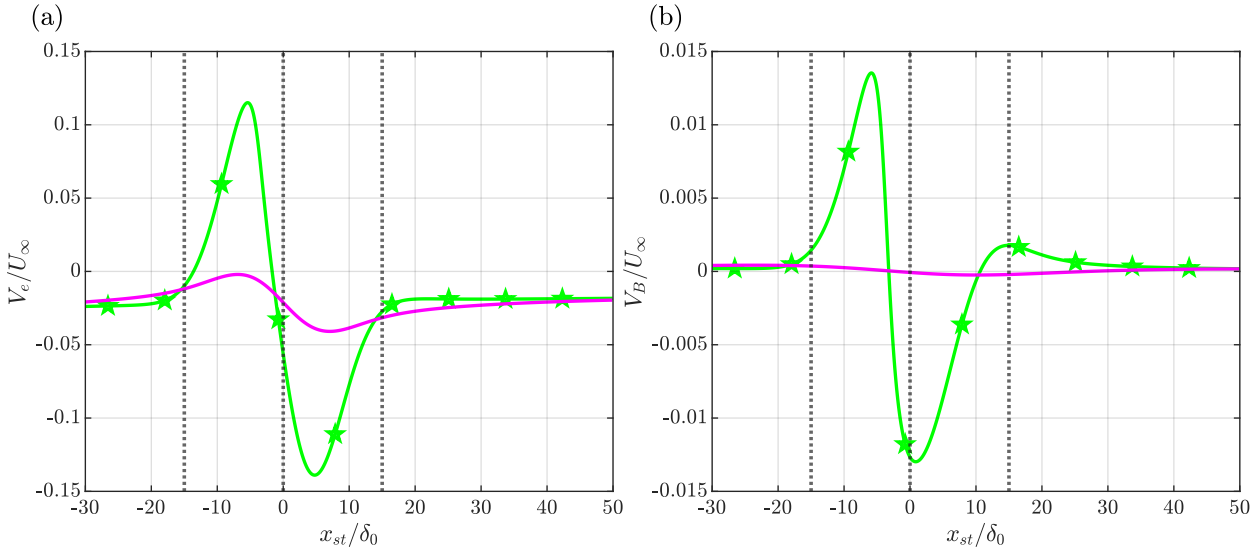

Figure B.3: Chordwise variation of (a) V_e and (b) V_B (at $y/\delta_0 = 0.75$) in the $-2.5p_f30w$ case simulated by DNS (magenta) and BLS (light green); black dotted lines at $x_{st}/\delta_0 = -w/2,\ 0,$ and $w/2$ show region of ΔP imposition.

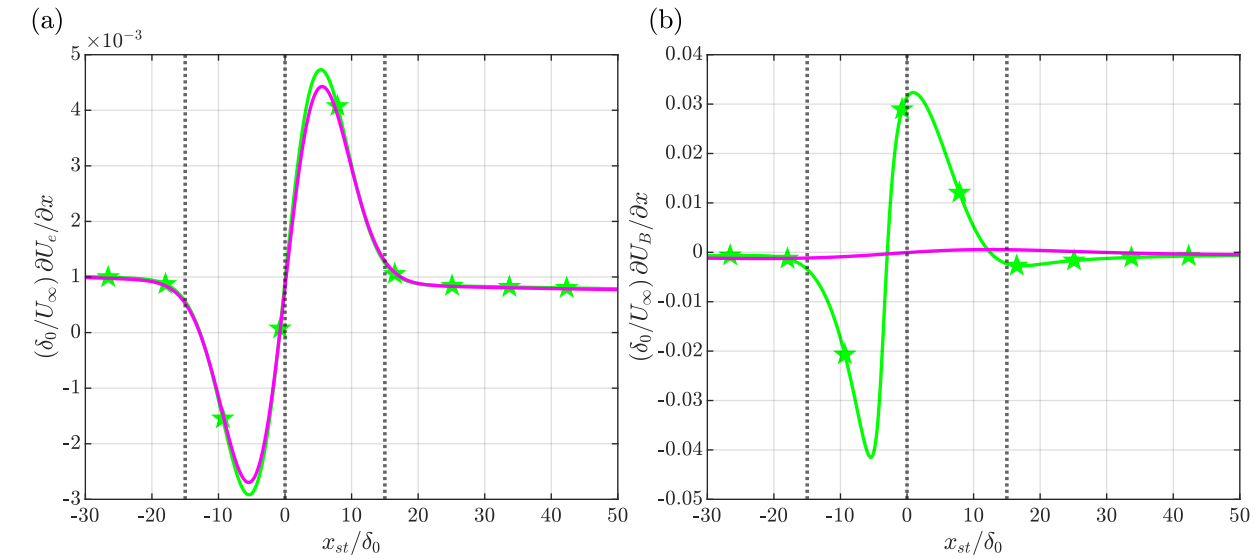

Figure B.4: Chordwise variation of (a) U_{e_x} and (b) U_{B_x} (at $y/\delta_0 = 0.75$) in the $-2.5p_f30w$ case simulated by DNS (magenta) and BLS (light green); black dotted lines at $x_{st}/\delta_0 = -w/2,\ 0,$ and $w/2$ show region of ΔP imposition.

B.4. Wall-normal Grid Independence of BLS Solution

The grid independence in y direction is shown in Figure B.5 and Figure B.6, with three different levels of refinement considered keeping the x discretization constant, $N_x = 15000$.

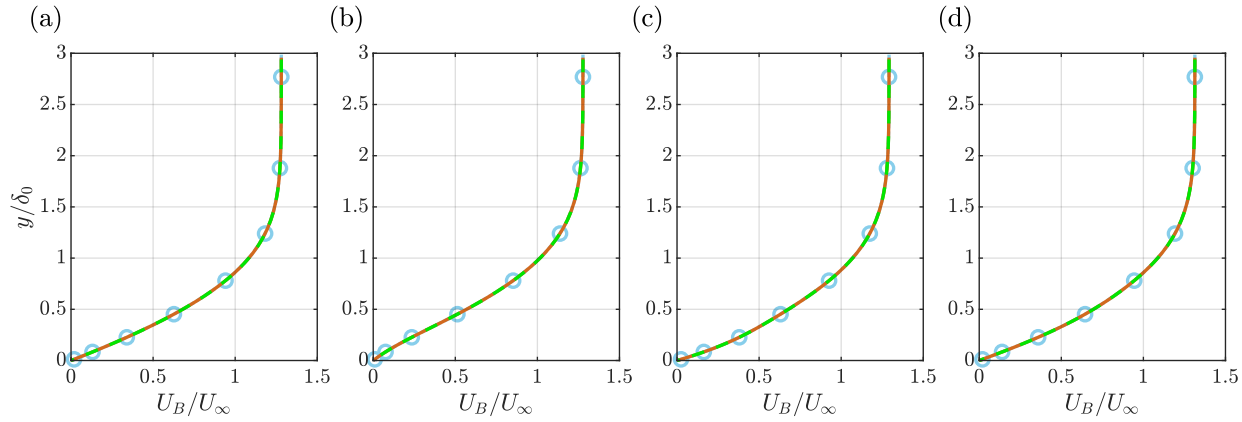

Figure B.5: Plot of wall-normal variation of chordwise velocity in the $-2.5p_f$ $30w$ case at x_{st}/δ_0 = (a) $-0.6w$, (b) $-0.25w$, (c) $0.25w$, and (d) $0.6w$ when N_y = 75 (sky blue with circles), 100 (light green), and 125 (brown).

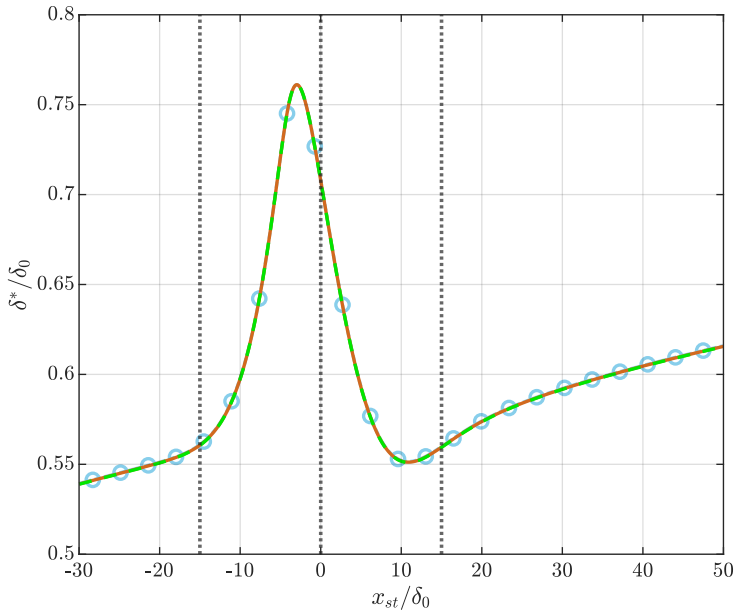

Figure B.6: Plot of chordwise variation of displacement thickness in the $-2.5p_f$ $30w$ case when N_y = 75 (sky blue with circles), 100 (light green), and 125 (brown); black dotted lines at $x_{st}/\delta_0 = -w/2,\ 0,$ and $w/2$ show the region of ΔP imposition.

B.5. Wall-normal Grid Independence of HLNS Solution

The grid independence in y direction is shown in Figure B.7 and Figure B.8, with three different levels of refinement considered keeping the x discretization constant, $N_x = 1500$.

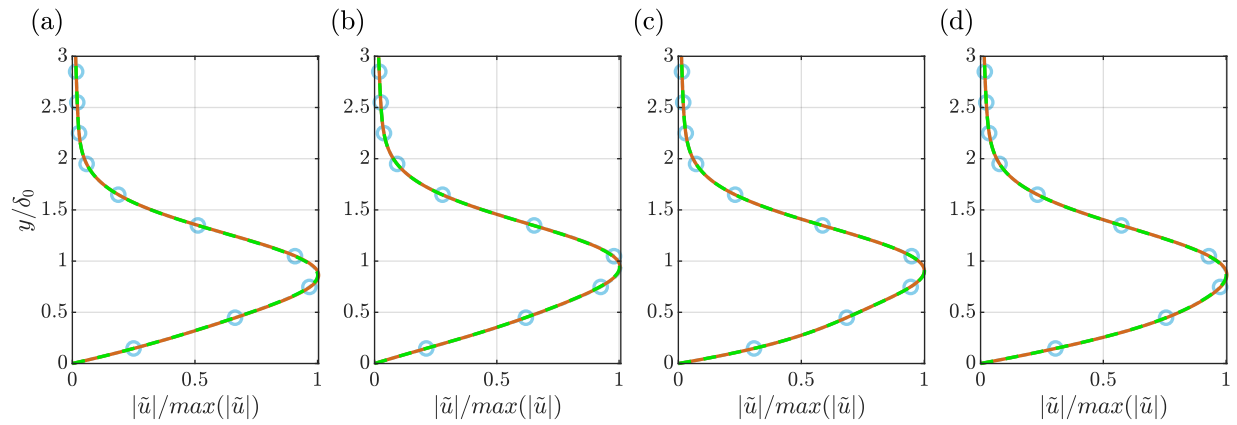

Figure B.7: Plot of wall-normal variation of normalized amplitude function of u' in $-2.5p_f$ $30w$ case at x_{st}/δ_0 = (a) $-0.6w$, (b) $-0.25w$, (c) $0.25w$, and (d) $0.6w$ when N_y = 75 (sky blue with circles), 100 (light green), and 125 (brown).

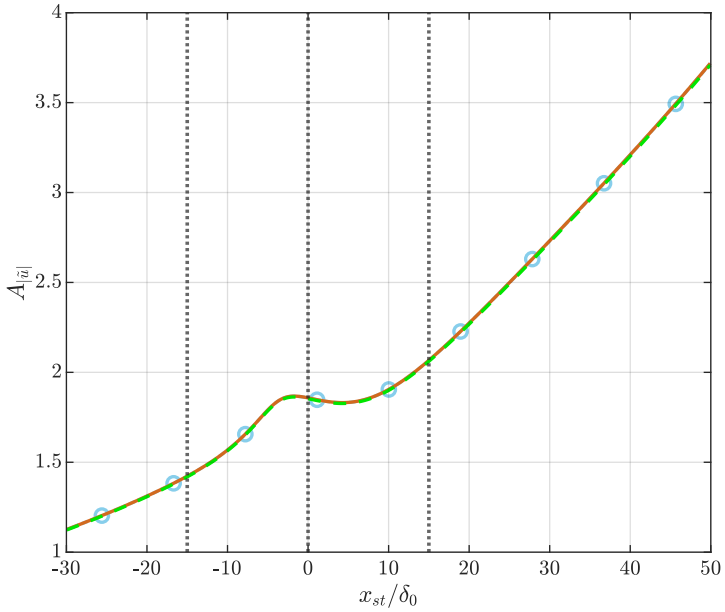

Figure B.8: Plot of chordwise variation of $|\tilde{u}|$ amplitude in $-2.5p_f$ $30w$ case when N_y = 75 (sky blue with circles), 100 (light green), and 125 (brown); black dotted lines at $x_{st}/\delta_0 = -w/2,\ 0,$ and $w/2$ show region of ΔP imposition.

C

Base Flow Properties of Two-way Cases

In this chapter, properties of base flow of non-reference two-way cases are presented. Not that base flows with pressure variation of $w = 30\delta_0$ are simultaneously also denoted as $30\delta_0$ or $30\delta_0$ cases.

C.1. External Velocity and Boundary Layer Properties

The chordwise variation of external velocity and boundary layer size in $10\delta_0$ and $50\delta_0$ cases shown in Figure C.1 and Figure C.2 respectively show the same properties as those noted in $30\delta_0$ cases shown in Figure 6.2. The extent of increase or decrease of external velocity and boundary layer thickness compared to the clean case increases with the increase of width scale for the same p_f, due to a larger exposure to regions of deformed flow in the larger width scale cases.

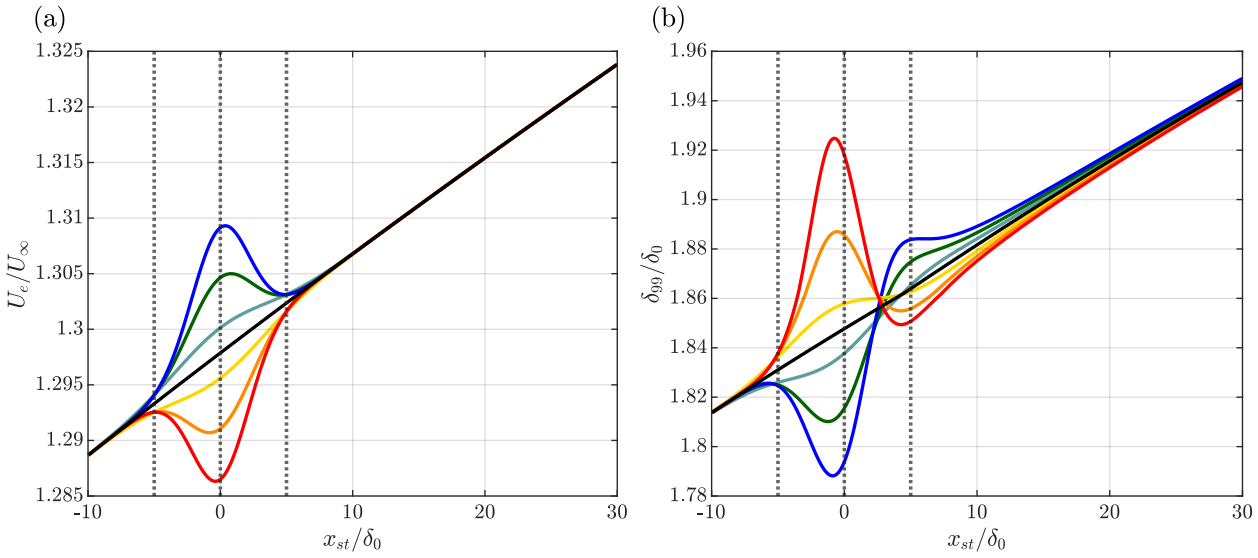

Figure C.1: Chordwise evolution of (a) External Velocity and (b) Boundary layer thickness in $10\delta_0$ cases; $-2.5p_f$ (red), $-1.5p_f$ (orange), $-0.5p_f$ (yellow), $0.5p_f$ (cyan), $1.5p_f$ (dark green), $2.5p_f$ (blue), and clean case (black); black dotted lines at $x_{st}/\delta_0 = -w/2,\ 0,$ and $w/2$ show region of ΔP imposition in deformed cases.

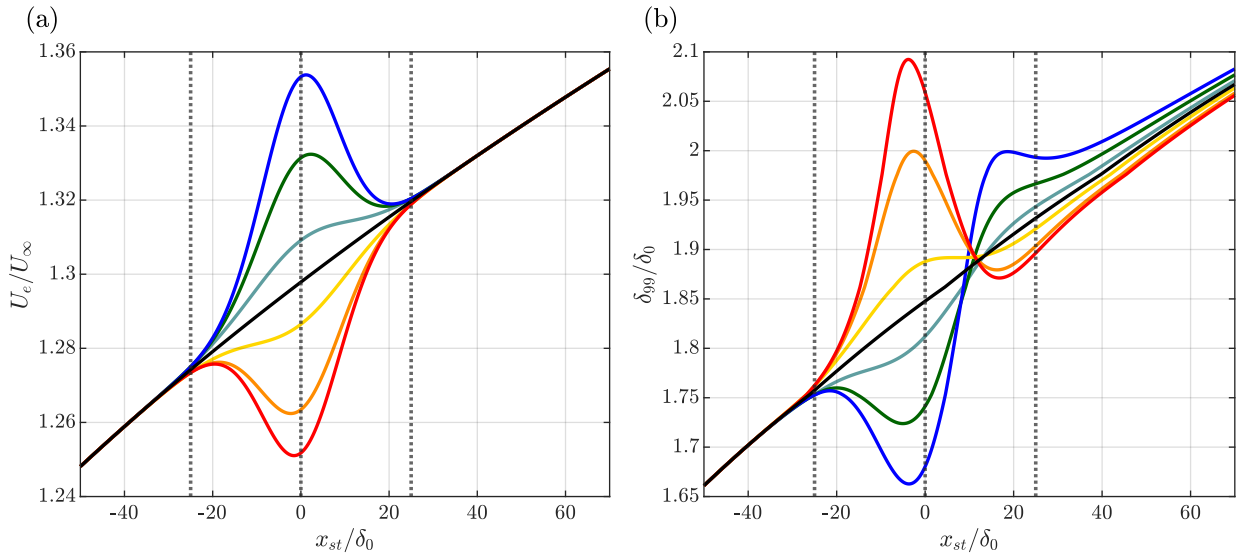

Figure C.2: Chordwise evolution of (a) External Velocity and (b) Boundary layer thickness in $50\delta_0$ cases; $-2.0p_f$ (red), $-1.5p_f$ (orange), $-0.5p_f$ (yellow), $0.5p_f$ (cyan), $1.5p_f$ (dark green), $2.5p_f$ (blue), and clean case (black); black dotted lines at $x_{st}/\delta_0 = -w/2,\ 0,$ and $w/2$ show region of ΔP imposition in deformed cases.

C.2. Wall-tangential Base Flow

The chordwise evolution of U_B and W_B at two different wall-normal heights ($y/\delta_0 = 0.5$ and $y/\delta_0 = 1$) in $30\delta_0$ cases are considered in Figure C.3 and Figure C.4 respectively.

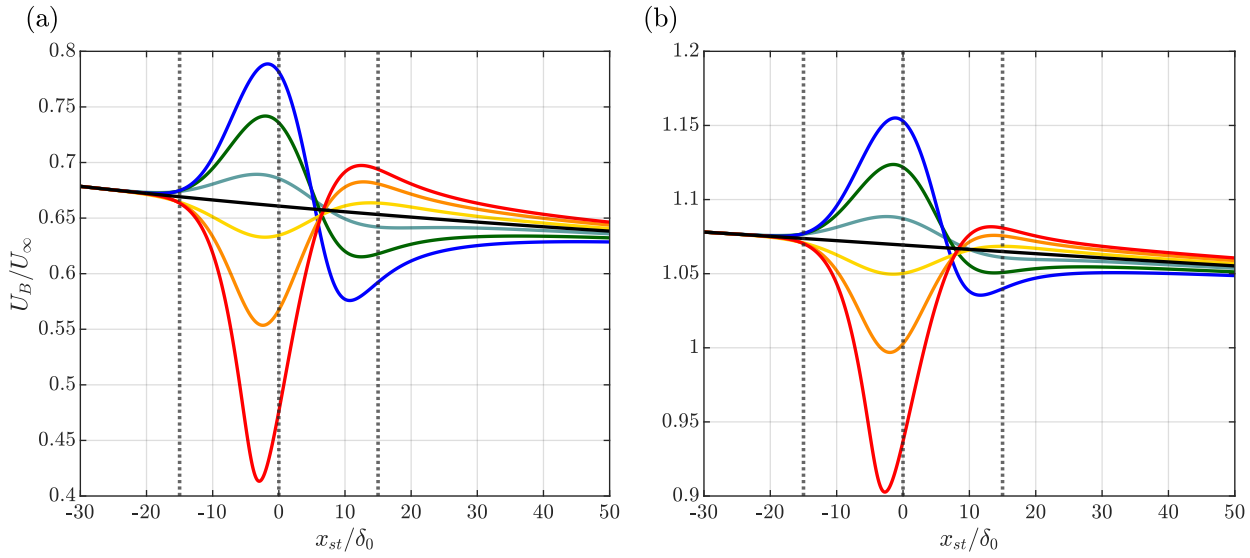

Figure C.3: Chordwise evolution of chordwise velocity in $30\delta_0$ cases at $y/\delta_0 =$ (a) 0.5 and (b) 1.0; $-2.5p_f$ (red), $-1.5p_f$ (orange), $-0.5p_f$ (yellow), $0.5p_f$ (cyan), $1.5p_f$ (dark green), $2.5p_f$ (blue), and clean case (black); black dotted lines at $x_{st}/\delta_0 = -w/2,\ 0,$ and $w/2$ show region of ΔP imposition in deformed cases.

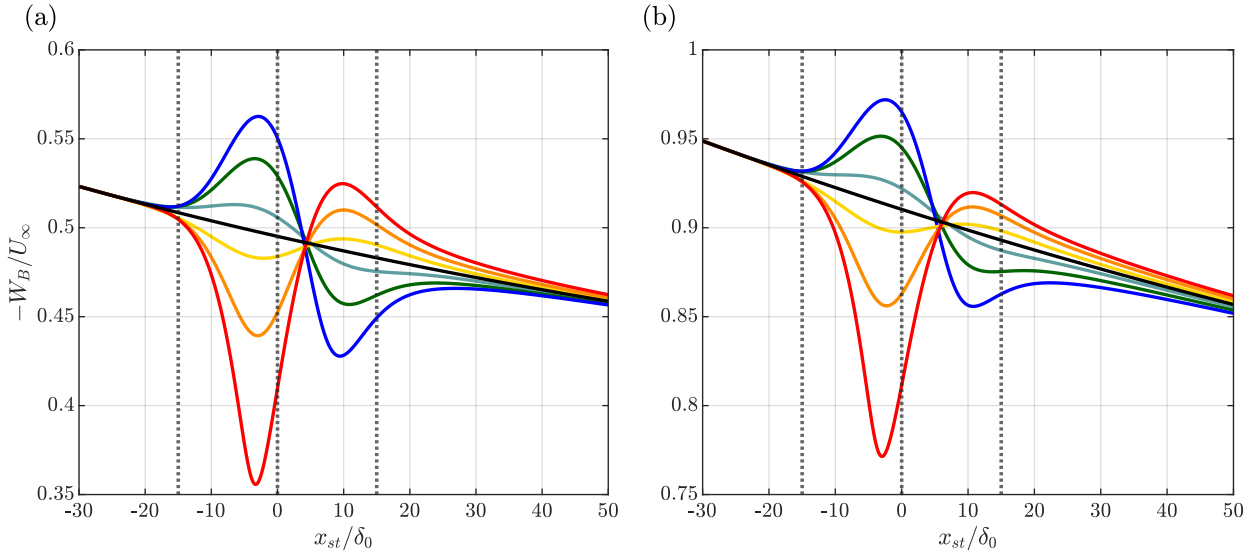

Figure C.4: Chordwise evolution of spanwise velocity in $30\delta_0$ cases at $y/\delta_0 =$ (a) 0.5 and (b) 1.0; $-2.5p_f$ (red), $-1.5p_f$ (orange), $-0.5p_f$ (yellow), $0.5p_f$ (cyan), $1.5p_f$ (dark green), $2.5p_f$ (blue), and clean case (black); black dotted lines at $x_{st}/\delta_0 = -w/2,\ 0,$ and $w/2$ show region of ΔP imposition in deformed cases.

C.3. Wall-normal Velocity and Chordwise Derivative of Wall-tangential Base Flow

The chordwise evolution of U_{B_x}, V_B, and W_{B_x} at a particular wall-normal height ($y/\delta_0 = 0.75$) in $30\delta_0$ cases are considered in Figure C.5 (a), (b), and (c) respectively. Only one height is considered as the trends of U_{B_x}, V_B, and W_B remain consistently similar to those shown in Figure C.5 within the boundary layer.

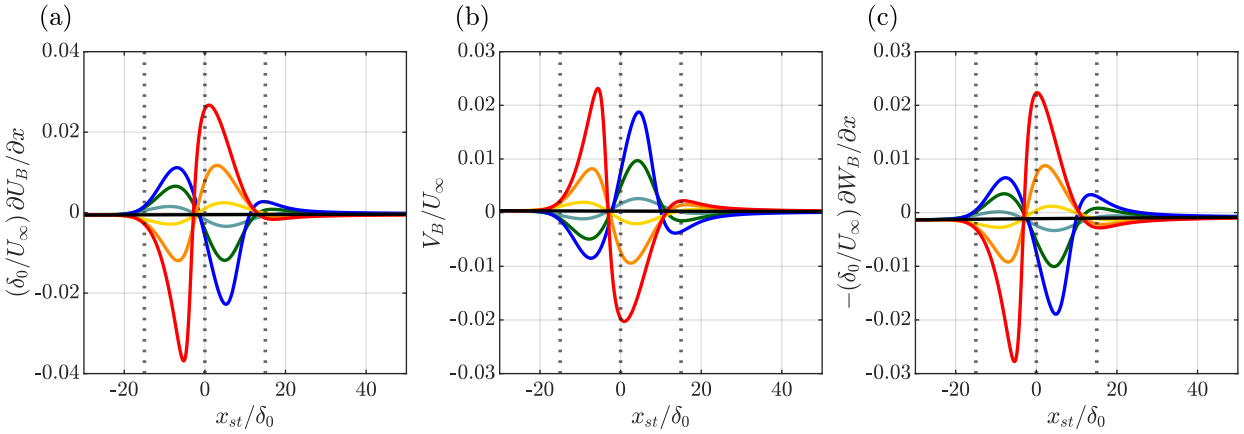

Figure C.5: Chordwise evolution of (a) U_{B_x}, (b) V_B, and (c) $-W_{B_x}$ in $30\delta_0$ cases at $y/\delta_0 = 0.75$; $-2.5p_f$ (red), $-1.5p_f$ (orange), $-0.5p_f$ (yellow), $0.5p_f$ (cyan), $1.5p_f$ (dark green), $2.5p_f$ (blue), and clean case (black); black dotted lines at $x_{st}/\delta_0 = -w/2,\ 0,$ and $w/2$ show region of ΔP imposition in deformed cases.

C.4. Base Flow Shear Profiles

The wall-normal variation of shear of U_B and W_B are shown in Figure C.6 and Figure C.7 for $30\delta_0$ cases at four different positions, two in the first half of deformation and two in the second half of deformation.

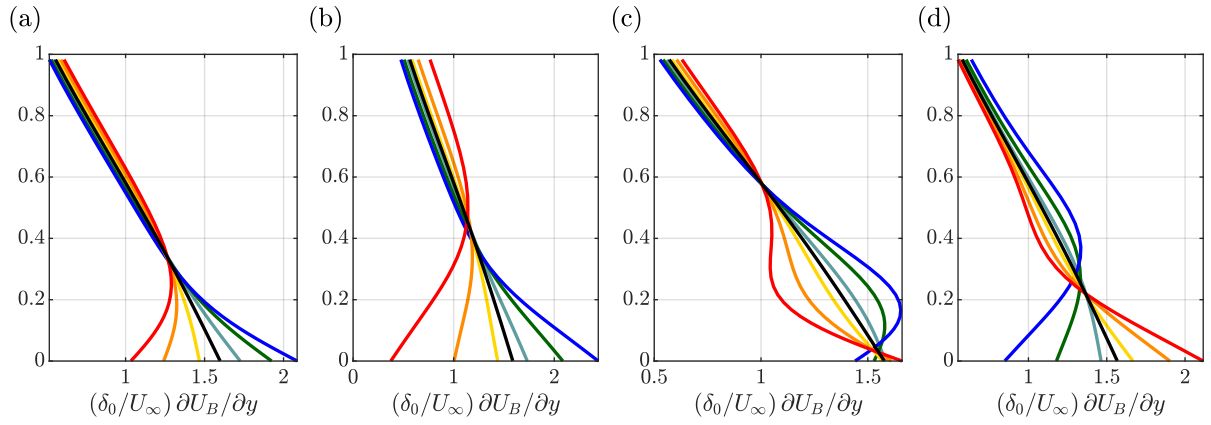

Figure C.6: Wall-normal variation of chordwise velocity shear in $30\delta_0$ cases at x_{st}/δ_0 = (a) -0.3w, (b) -0.1w, (c) 0.1w, and (d) 0.3w; $-2.5p_f$ (red), $-1.5p_f$ (orange), $-0.5p_f$ (yellow), $0.5p_f$ (cyan), $1.5p_f$ (dark green), $2.5p_f$ (blue), and clean case (black).

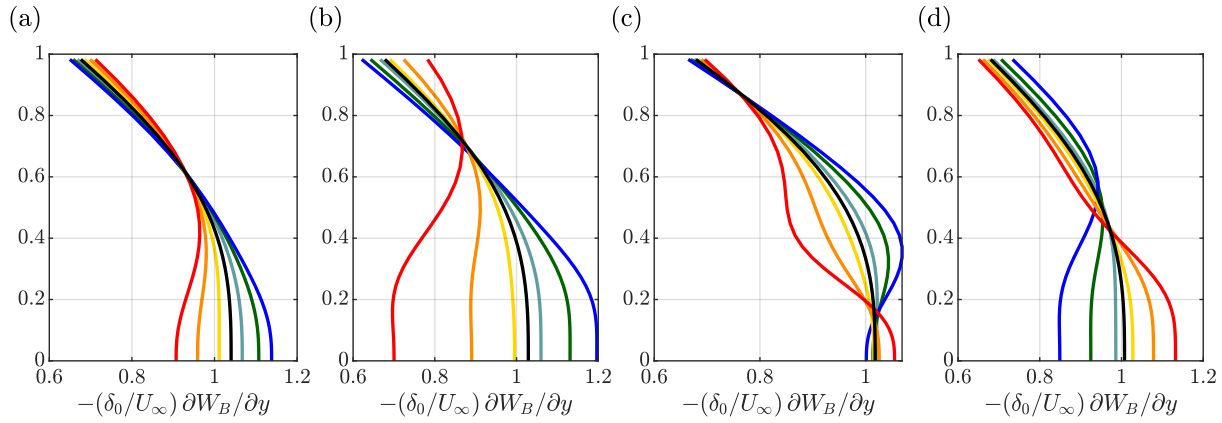

Figure C.7: Wall-normal variation of chordwise velocity shear in $30\delta_0$ cases at x_{st}/δ_0 = (a) -0.3w, (b) -0.1w, (c) 0.1w, and (d) 0.3w; $-2.5p_f$ (red), $-1.5p_f$ (orange), $-0.5p_f$ (yellow), $0.5p_f$ (cyan), $1.5p_f$ (dark green), $2.5p_f$ (blue), and clean case (black).

C.5. Crossflow Velocity Variation

The chordwise evolution of crossflow velocity at two different wall-normal heights ($y/\delta_0 = 0.05$ and $y/\delta_0 = 0.25$) in $30\delta_0$ cases is considered in Figure C.8.

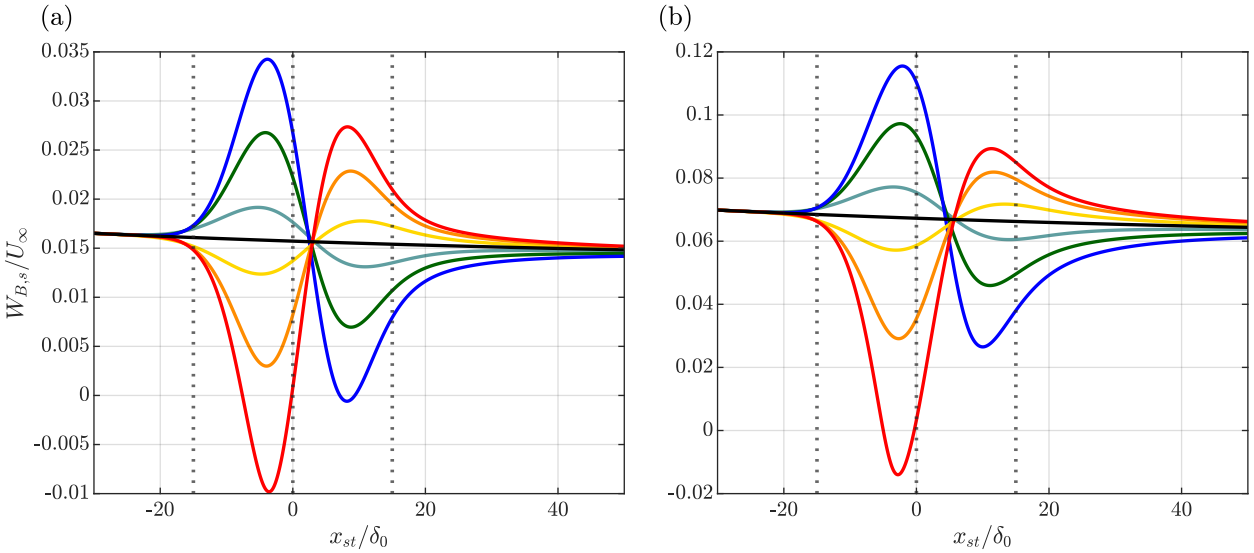

Figure C.8: Chordwise evolution of crossflow velocity in $30\delta_0$ cases at y/δ_0 = (a) 0.05 and (b) 0.25; $-2.5p_f$ (red), $-1.5p_f$ (orange), $-0.5p_f$ (yellow), $0.5p_f$ (cyan), $1.5p_f$ (dark green), $2.5p_f$ (blue), and clean case (black); black dotted lines at $x_{st}/\delta_0 = -w/2,\ 0,$ and $w/2$ show region of ΔP imposition in deformed cases.

D

Perturbation Properties of Two-Way cases

D.1. Evolution of Normalized Amplitude Function

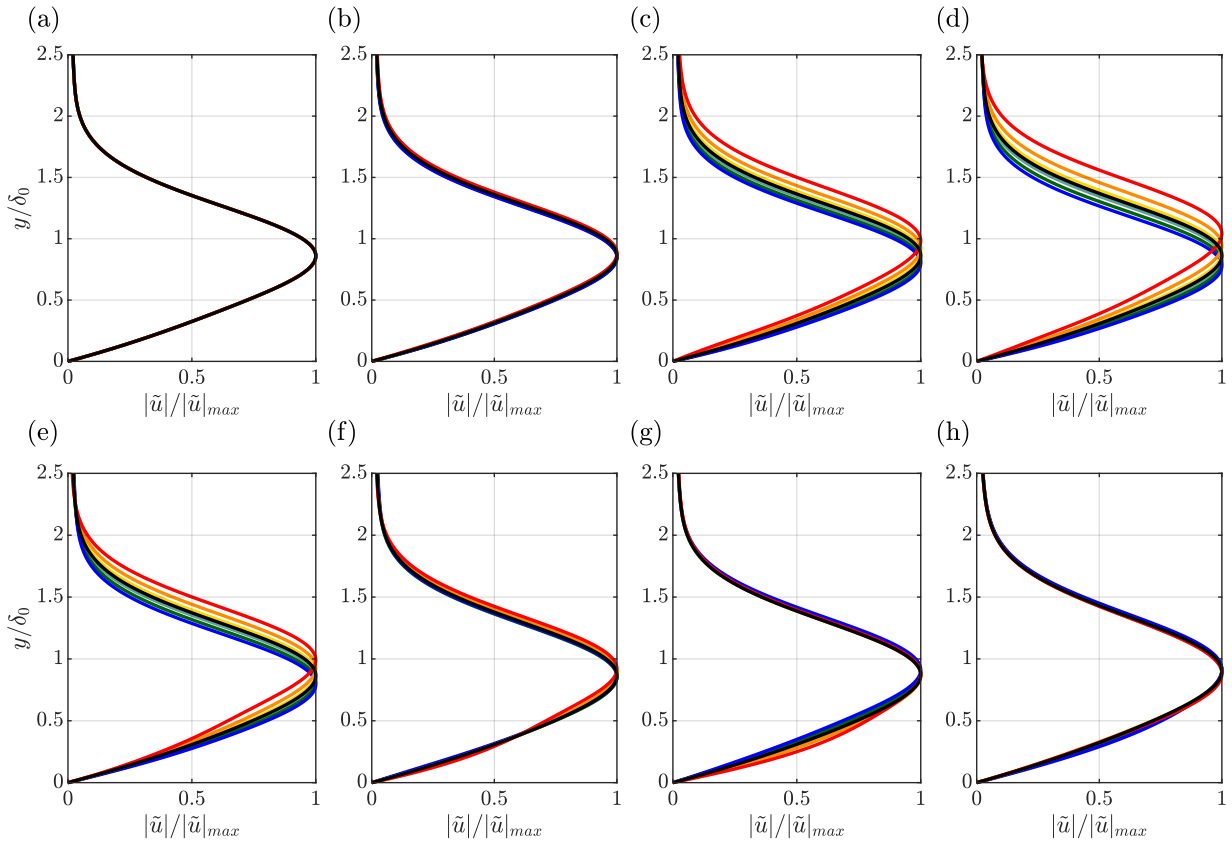

Figure D.1: Wall-normal variation of normalized amplitude function of u' in clean case (black), $0.5p_f$ $30w$ case (cyan), $1.5p_f$ $30w$ case (dark green), $2.5p_f$ $30w$ case (blue), $-0.5p_f$ $30w$ case (yellow), $-1.5p_f$ $30w$ case (orange), and $-2.5p_f$ $30w$ (red) at x_{st}/δ_0 = (a) $-0.75w$, (b) $-0.4w$, (c) $-0.2w$, (d) $-0.05w$, (e) $0.05w$, (f) $0.2w$, (g) $0.4w$, and (h) $0.75w$.

The wall-normal variation of normalized amplitude function of perturbation, wherein the perturbation amplitude function is normalized by the maximum value of $\tilde{u}$ is shown for $30\delta_0$ cases for u' in Figure D.1, v' in Figure D.2, w' in Figure D.3 at various locations.

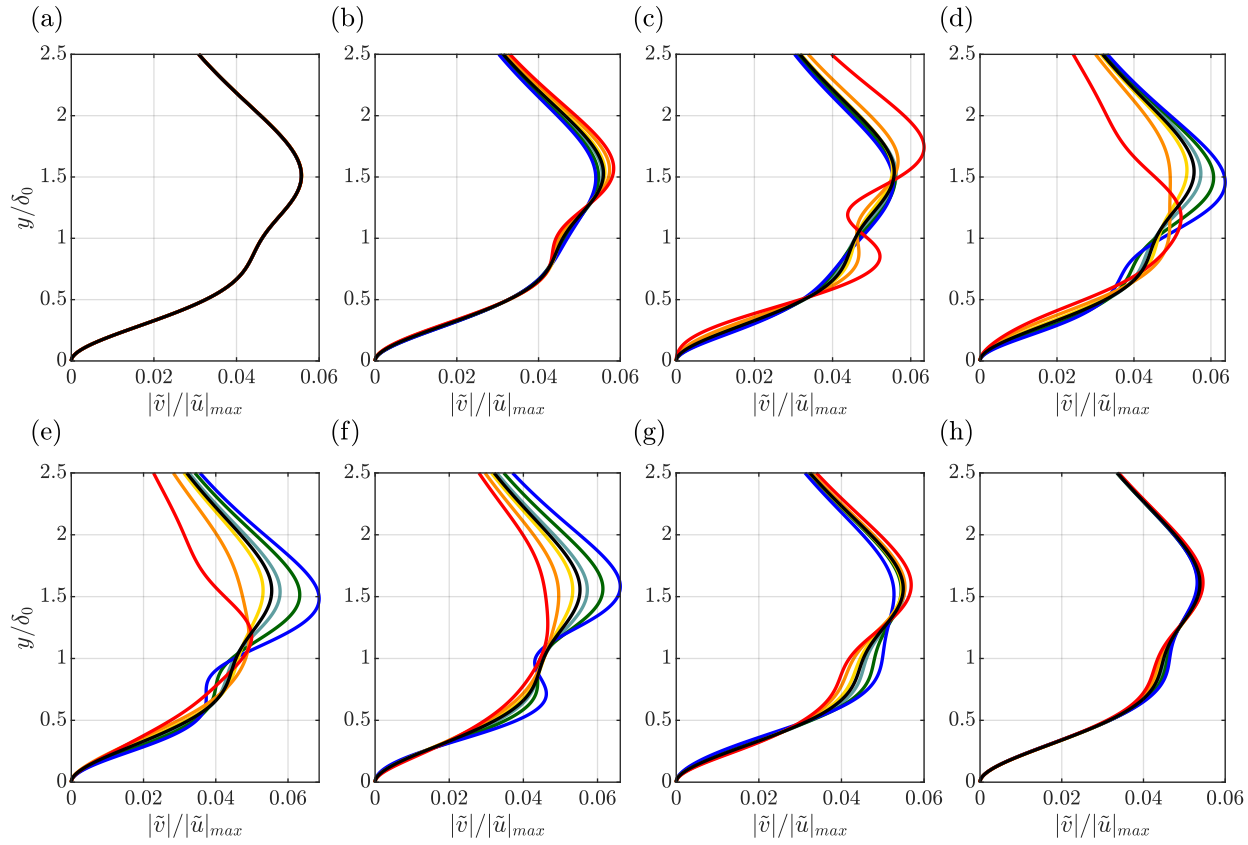

Figure D.2: Wall-normal variation of normalized amplitude function of v' in clean case (black), $0.5p_f$ $30w$ case (cyan), $1.5p_f$ $30w$ case (dark green), $2.5p_f$ $30w$ case (blue), $-0.5p_f$ $30w$ case (yellow), $-1.5p_f$ $30w$ case (orange), and $-2.5p_f$ $30w$ (red) at $x_{st}/\delta_0 =$ (a) $-0.75w$, (b) $-0.4w$, (c) $-0.2w$, (d) $-0.05w$, (e) $0.05w$, (f) $0.2w$, (g) $0.4w$, and (h) $0.75w$.

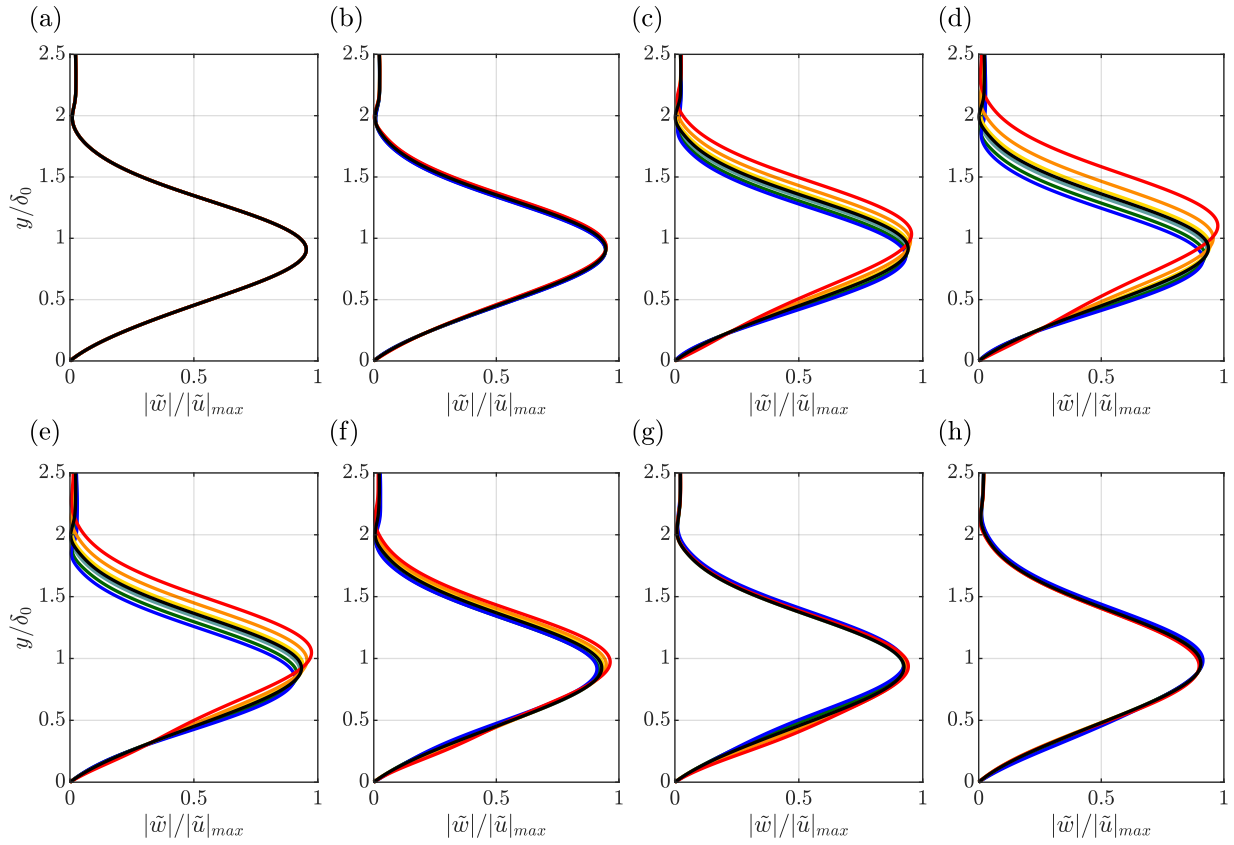

Figure D.3: Wall-normal variation of normalized amplitude function of w' in clean case (black), $0.5p_f$ $30w$ case (cyan), $1.5p_f$ $30w$ case (dark green), $2.5p_f$ $30w$ case (blue), $-0.5p_f$ $30w$ case (yellow), $-1.5p_f$ $30w$ case (orange), and $-2.5p_f$ $30w$ (red) at $x_{st}/\delta_0 =$ (a) $-0.75w$, (b) $-0.4w$, (c) $-0.2w$, (d) $-0.05w$, (e) $0.05w$, (f) $0.2w$, (g) $0.4w$, and (h) $0.75w$.

D.2. Amplitude and Growth Rate Evolution

The amplitude and growth rate evolution in $10\delta_0$ and $50\delta_0$ cases considered in the thesis are shown in Figure D.4 and Figure D.5 respectively, where their behaviour is consistent with the behaviour seen in the $30\delta_0$ cases for both positive and negative p_f cases.

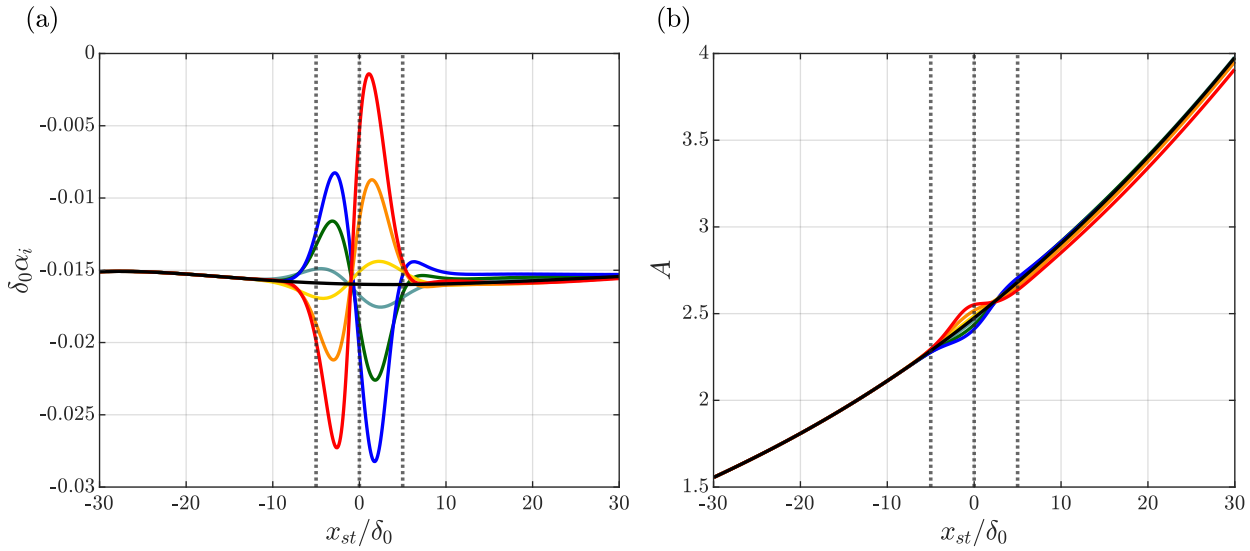

Figure D.4: Chordwise evolution of (a) growth rate and (b) Amplitude in $10\delta_0$ cases; $-2.5p_f$ (red), $-1.5p_f$ (orange), $-0.5p_f$ (yellow), $0.5p_f$ (cyan), $1.5p_f$ (dark green), $2.5p_f$ (blue), and clean case (black); black dotted lines at $x_{st}/\delta_0 = -w/2,\ 0,$ and $w/2$ show the region of ΔP imposition in deformed cases.

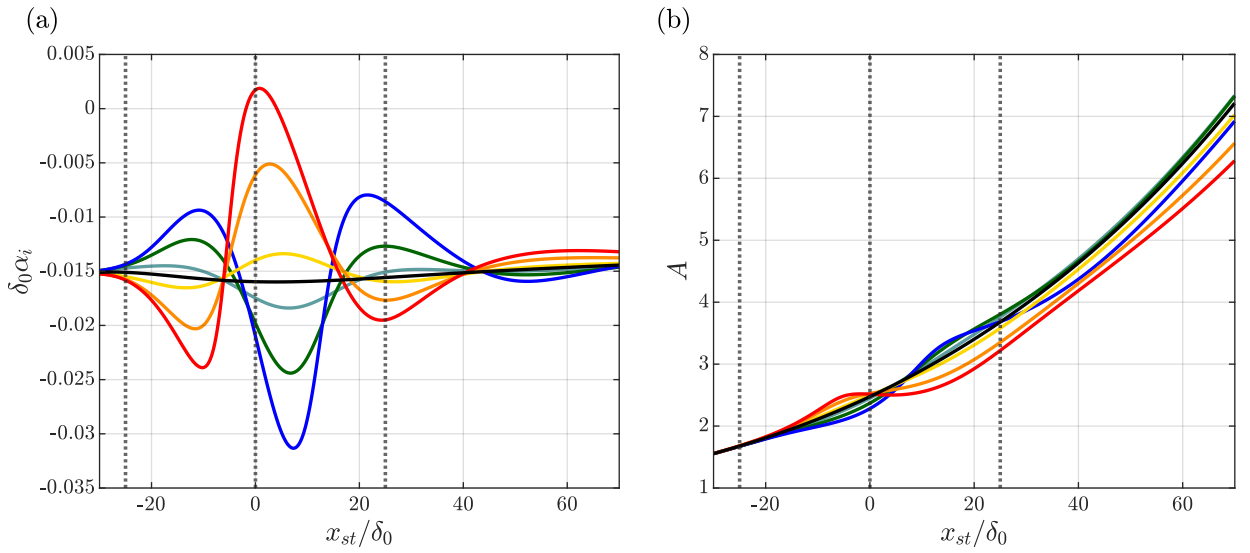

Figure D.5: Chordwise evolution of (a) growth rate and (b) Amplitude in $50\delta_0$ cases; $-2.0p_f$ (red), $-1.5p_f$ (orange), $-0.5p_f$ (yellow), $0.5p_f$ (cyan), $1.5p_f$ (dark green), $2.5p_f$ (blue), and clean case (black); black dotted lines at $x_{st}/\delta_0 = -w/2,\ 0,$ and $w/2$ show the region of ΔP imposition in deformed cases.

D.3. Production Term Trends

D.3.1. Cosine of Phase Difference

The trends of $\cos(\phi_1 - \phi_3)$, $\cos(\phi_1 - \phi_2)$, and $-\cos(\phi_3 - \phi_2)$ are shown for $30\delta_0$ cases in Figure D.6, Figure D.7, and Figure D.8 respectively. To further show the local increase and decrease of $\cos(\phi_1 - \phi_2)$ in favourable and adverse ΔP regions respectively, its evolution is plotted at two different wall-normal heights in Figure D.9.

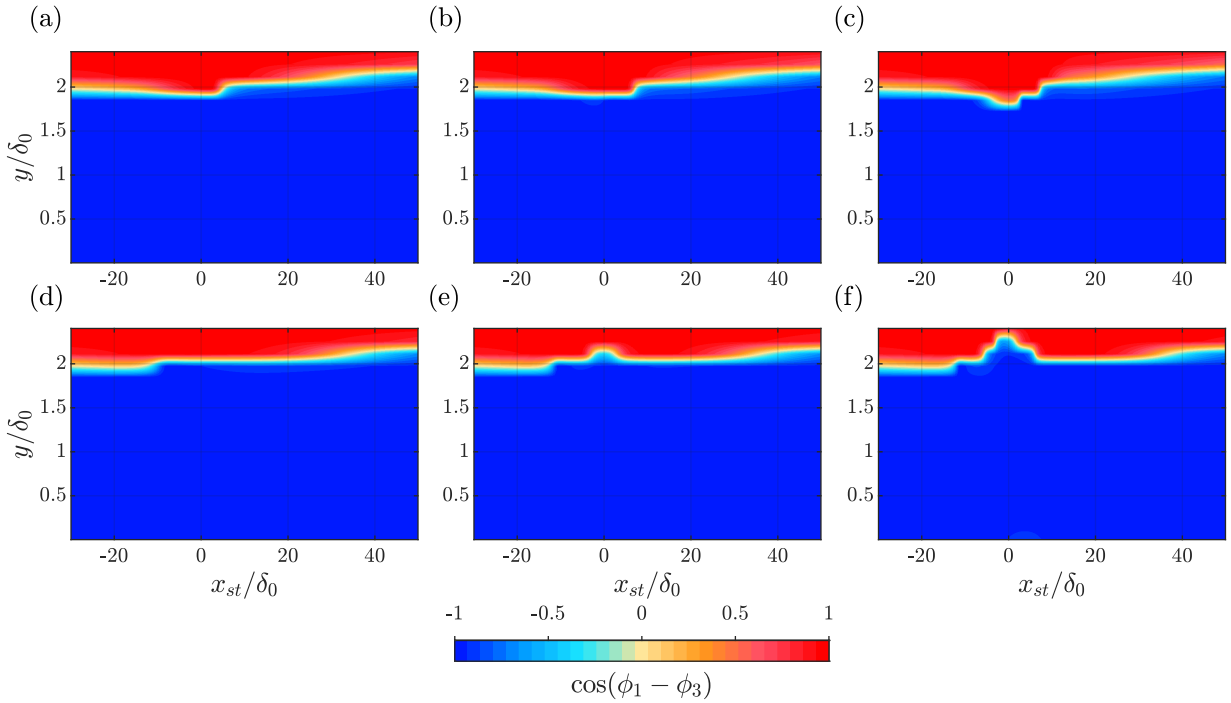

Figure D.6: Contours of $\cos(\phi_1 - \phi_3)$ in (a) $0.5p_f$ $30w$ case, (b) $1.5p_f$ $30w$ case, (c) $2.5p_f$ $30w$ case, (d) $-0.5p_f$ $30w$ case, (e) $-1.5p_f$ $30w$ case, and (f) $-2.5p_f$ $30w$ case; black dotted lines at $x_{st}/\delta_0 = -w/2,\ 0,$ and $w/2$ show the region of ΔP imposition in deformed cases.

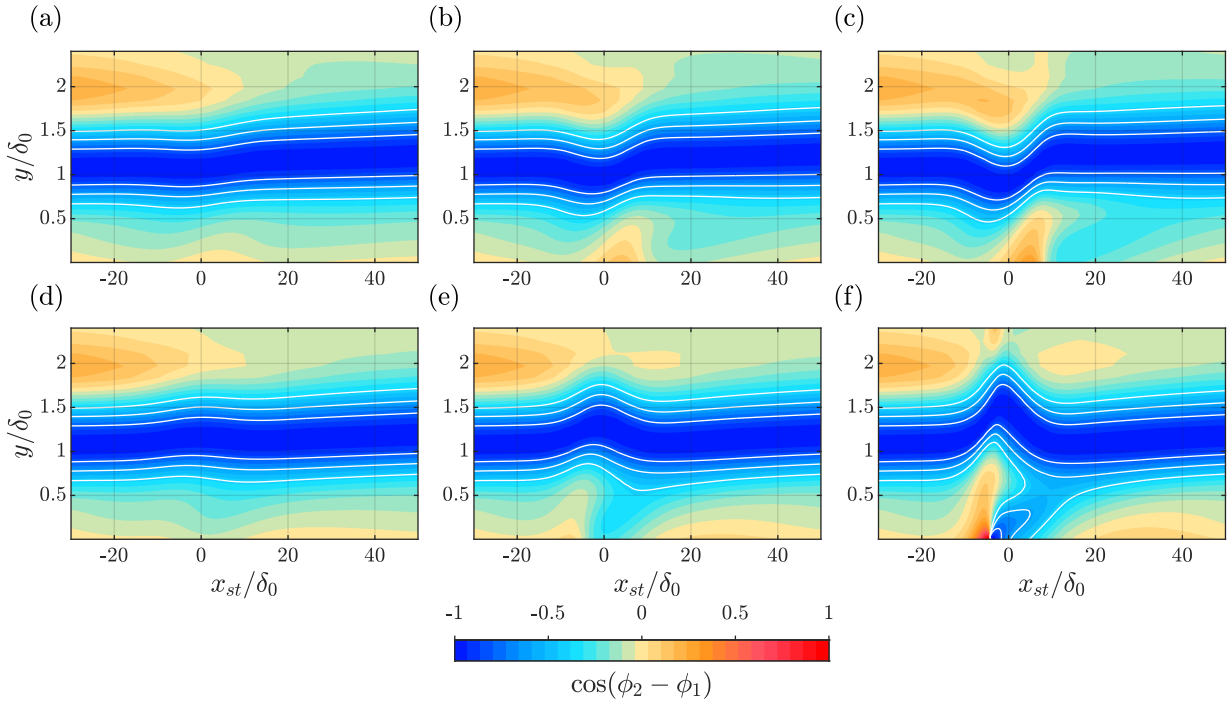

Figure D.7: Contours of $\cos(\phi_2 - \phi_1)$ in (a) $0.5p_f$ $30w$ case, (b) $1.5p_f$ $30w$ case, (c) $2.5p_f$ $30w$ case, (d) $-0.5p_f$ $30w$ case, (e) $-1.5p_f$ $30w$ case, and (f) $-2.5p_f$ $30w$ case; white solid lines show constant cosine contour lines in the range -1 to -0.4; black dotted lines at $x_{st}/\delta_0 = -w/2,\ 0,$ and $w/2$ show the region of ΔP imposition in deformed cases.

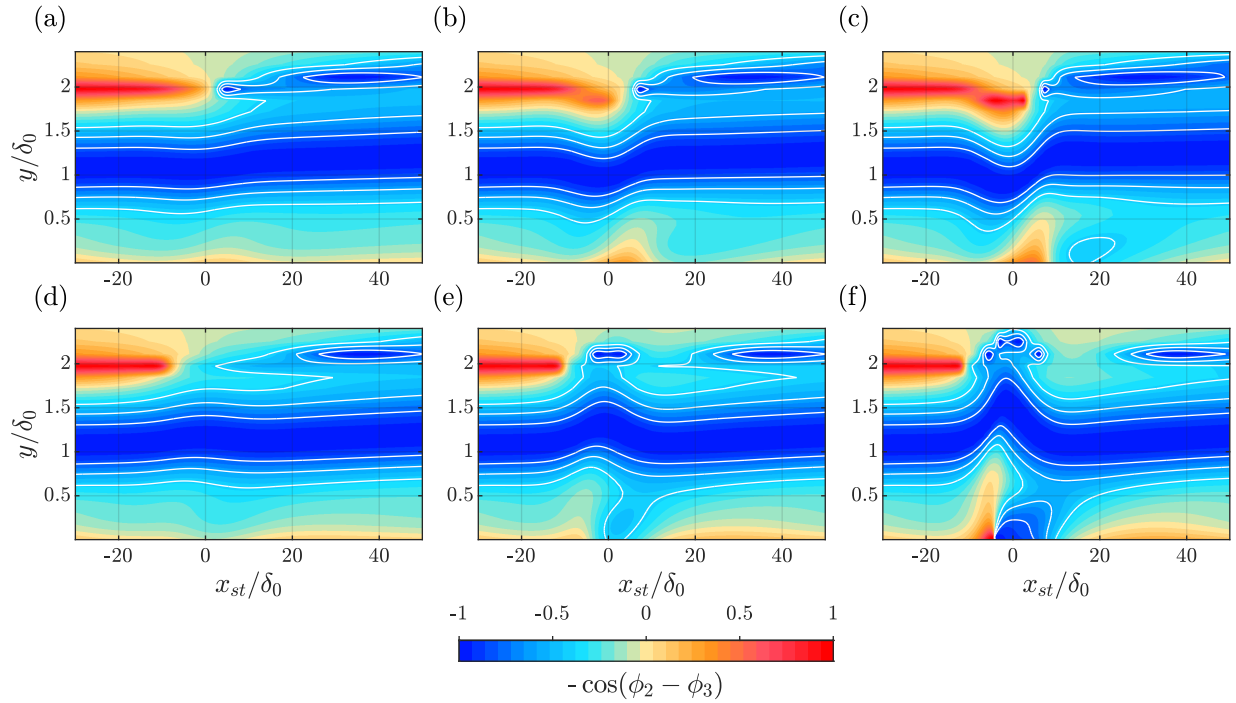

Figure D.8: Contours of -cos($\phi_2 - \phi_3$) in (a) $0.5p_f$ $30w$ case, (b) $1.5p_f$ $30w$ case, (c) $2.5p_f$ $30w$ case, (d) $-0.5p_f$ $30w$ case, (e) $-1.5p_f$ $30w$ case, and (f) $-2.5p_f$ $30w$ case; white solid lines show constant cosine contour lines in the range -1 to -0.4; black dotted lines at $x_{st}/\delta_0 = -w/2,\ 0,$ and $w/2$ show the region of ΔP imposition in deformed cases.

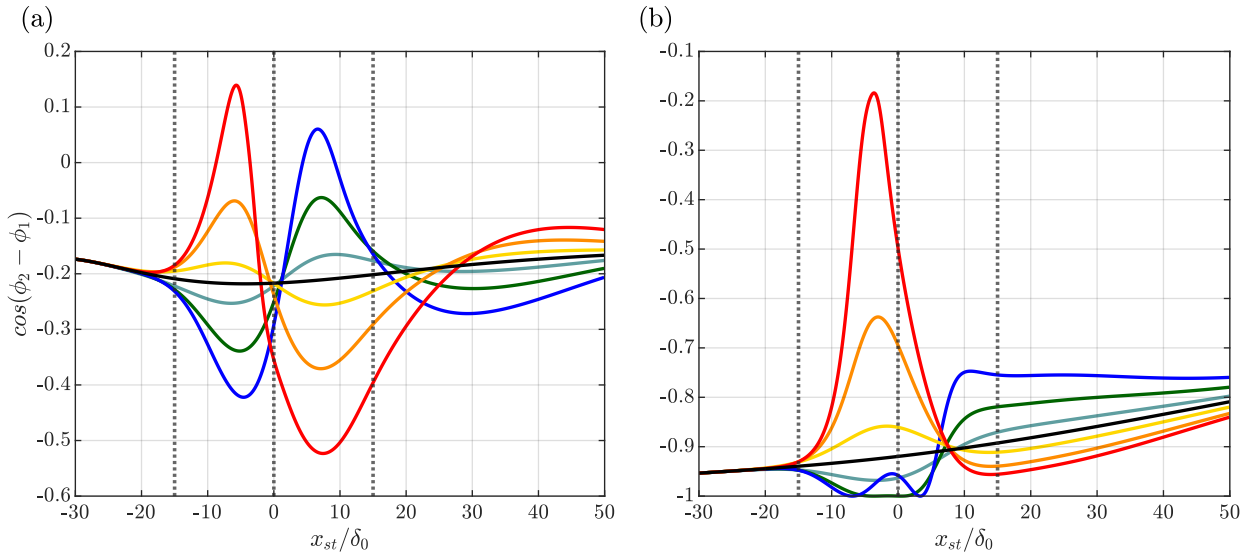

Figure D.9: Chordwise evolution of cos($\phi_2 - \phi_1$) in $30\delta_0$ cases at $y/\delta_0 =$ (a) 0.5 and (b) 1.0; $-2.5p_f$ (red), $-1.5p_f$ (orange), $-0.5p_f$ (yellow), $0.5p_f$ (cyan), $1.5p_f$ (dark green), $2.5p_f$ (blue), and clean case (black); black dotted lines at $x_{st}/\delta_0 = -w/2,\ 0,$ and $w/2$ show the region of ΔP imposition in deformed cases.

D.3.2. $\mathcal{P}_{x_d}$ and $\mathcal{P}_{y_d}$ Trends

The chordwise variation of $\mathcal{P}_{x_d}$, $\mathcal{P}_{y_d}$, and $\mathcal{P}$ at two different wall-normal heights for $30\delta_0$ cases are shown in Figure D.10. Enhanced $\mathcal{P}$ with respect to clean case is observed in regions of positive $\mathcal{P}_{x_d}$ or flow deceleration and vice versa.

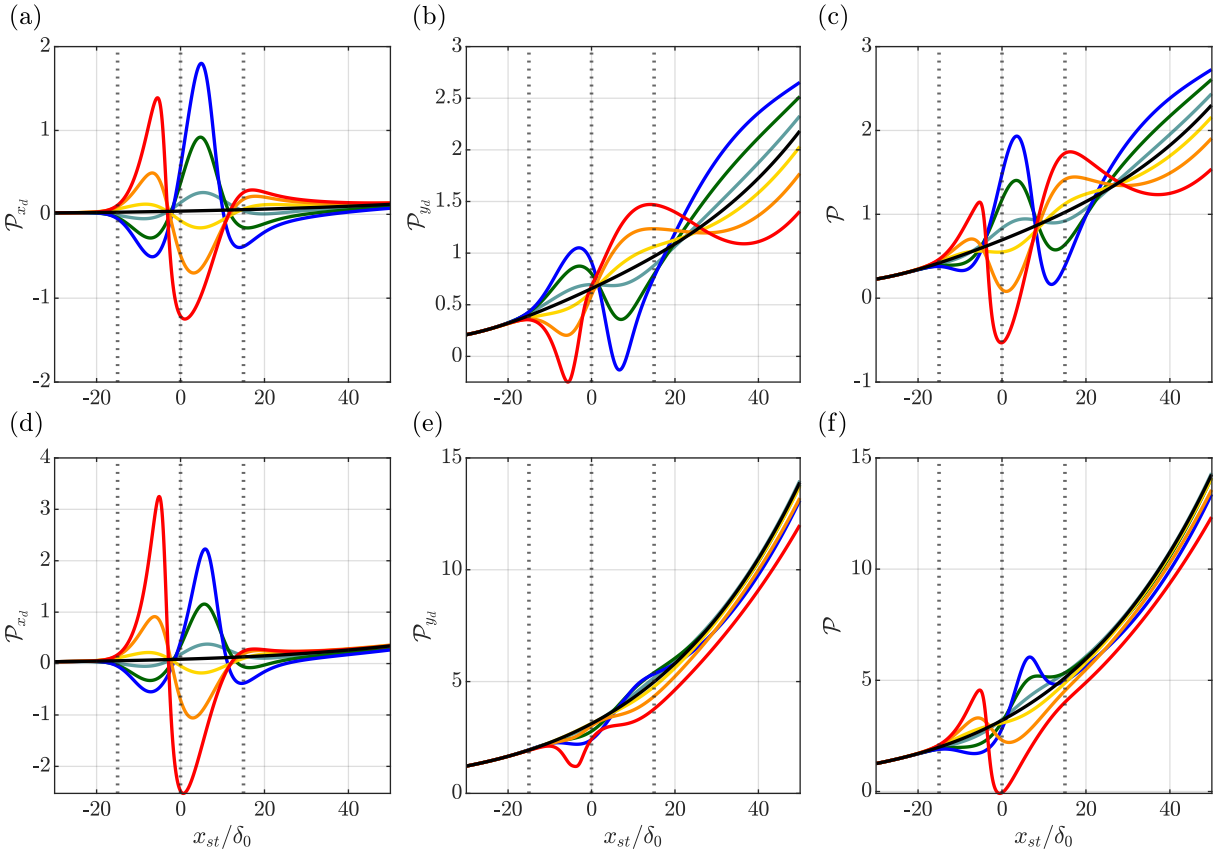

Figure D.10: Evolution of $\mathcal{P}_{x_d}$ (a,d), $\mathcal{P}_{y_d}$ (b,e), $\mathcal{P}$ (c,f) in clean case (black), $0.5p_f$ $30w$ case (cyan), $1.5p_f$ $30w$ case (dark green), $2.5p_f$ $30w$ case (blue), $-0.5p_f$ $30w$ case (yellow), $-1.5p_f$ $30w$ case (orange), and $-2.5p_f$ $30w$ (red) at $y/\delta_0 = 0.5$ (top) and $y/\delta_0 = 1$ (bottom); black dash-dotted lines at $x_{st}/\delta_0 = -w/2,\ 0,$ and $w/2$ show the region of ΔP imposition in deformed cases.

D.4. Lift-up Effect

The contours of $\cos(\phi_{1,t} - \phi_1)$ and $\sin(\phi_{1,t} - \phi_1)$ are shown for $30\delta_0$ in Figure D.12 and Figure D.11 to show that they take values close to 1 and 0 respectively, proving that $\phi_{1,t}$ and ϕ_1 take values close to each other.

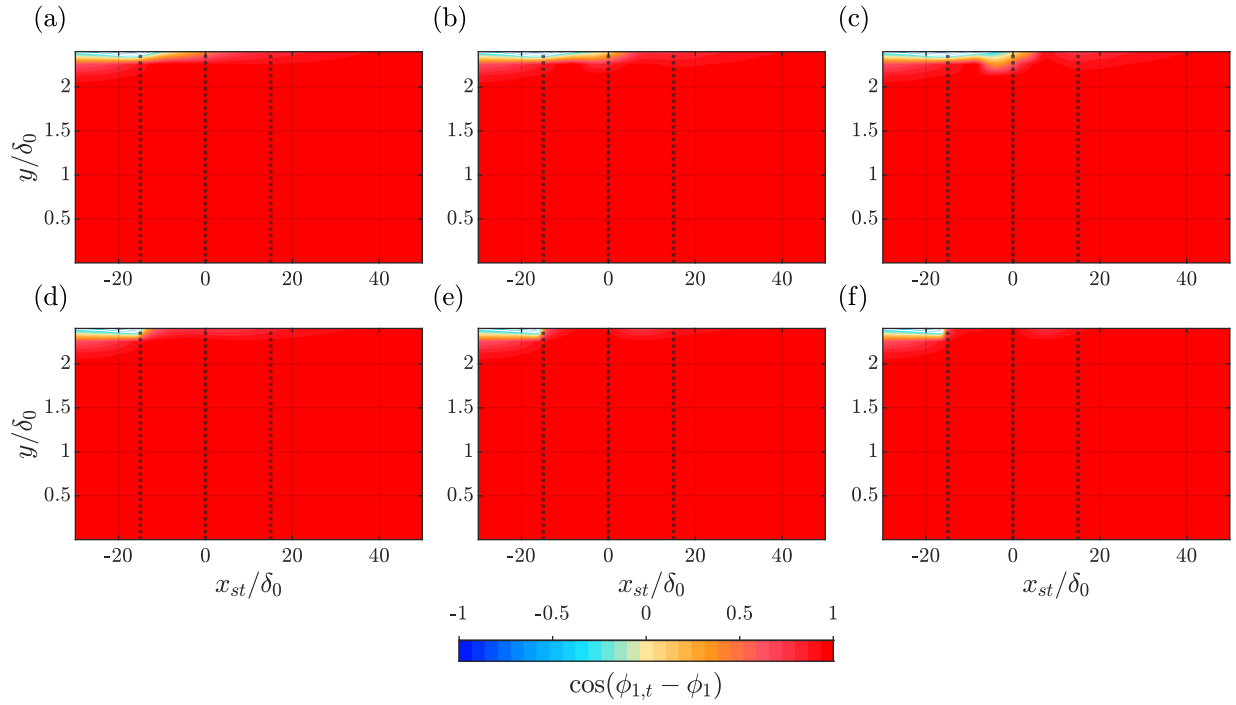

Figure D.11: Contours of $\cos(\phi_{1,t} - \phi_1)$ in (a) $0.5p_f$ $30w$ case, (b) $1.5p_f$ $30w$ case, (c) $2.5p_f$ $30w$ case, (d) $-0.5p_f$ $30w$ case, (e) $-1.5p_f$ $30w$ case, and (f) $-2.5p_f$ $30w$ case; black dotted lines at $x_{st}/\delta_0 = -w/2,\ 0,$ and $w/2$ show the region of ΔP imposition in deformed cases.

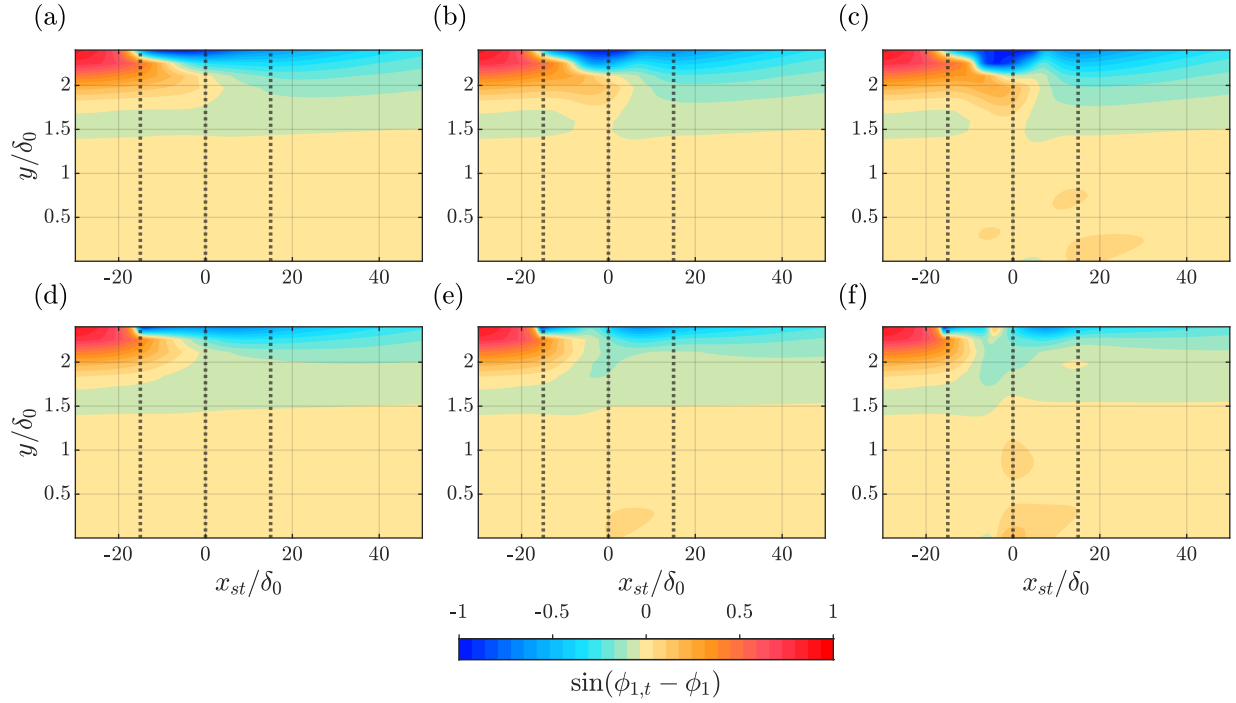

Figure D.12: Contours of $\sin(\phi_{1,t} - \phi_1)$ in (a) $0.5p_f$ $30w$ case, (b) $1.5p_f$ $30w$ case, (c) $2.5p_f$ $30w$ case, (d) $-0.5p_f$ $30w$ case, (e) $-1.5p_f$ $30w$ case, and (f) $-2.5p_f$ $30w$ case; black dotted lines at $x_{st}/\delta_0 = -w/2,\ 0,$ and $w/2$ show the region of ΔP imposition in deformed cases.

The chordwise evolution of $\cos(\phi_1 - \phi_2)$ and $\cos(\phi_{1,t} - \phi_{2,n})$ in $30\delta_0$ cases are compared in Figure D.13 at $y/\delta_0 = 0.5$ to show that V_B consistently causes $\cos(\phi_1 - \phi_2)$ to deviate from $\cos(\phi_{1,t} - \phi_{2,n})$ in case the underlying base flow is synthetically deformed.

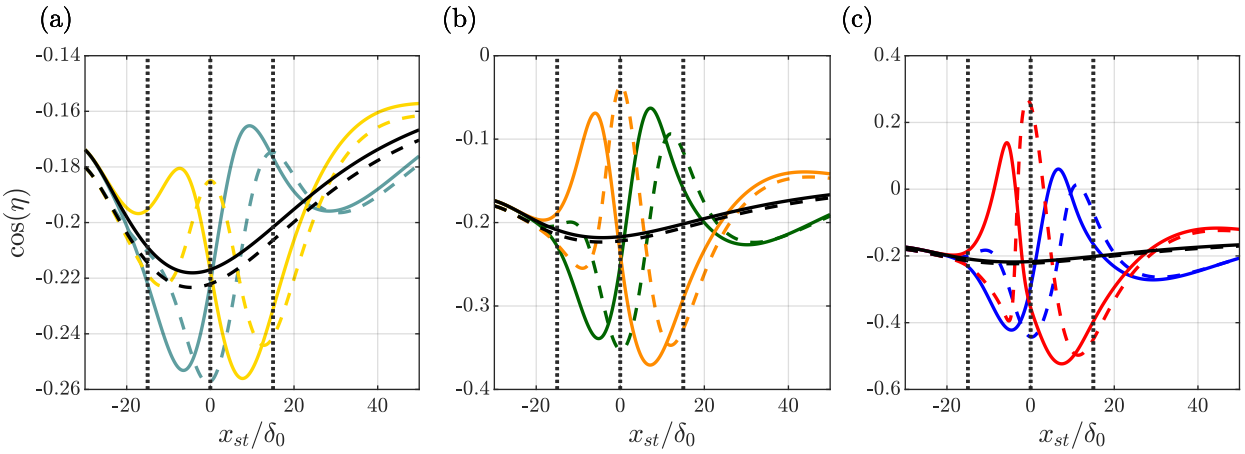

Figure D.13: Chordwise evolution of cos(η) where $\eta = \phi_2 - \phi_1$ (solid) and $\phi_{2,n} - \phi_{1,t}$ (dashed) in $30\delta_0$ cases; $-2.0p_f$ (red), $-1.5p_f$ (orange), $-0.5p_f$ (yellow), $0.5p_f$ (cyan), $1.5p_f$ (dark green), $2.5p_f$ (blue), and clean case (black); low p_f cases shown in (a), medium p_f cases shown in (b), and high p_f cases shown in (c); black dotted lines at $x_{st}/\delta_0 = -w/2,\ 0,$ and $w/2$ show the region of ΔP imposition in deformed cases.

D.5. Orr Mechanism

The wall-normal variation of $-\phi_1$ is compared at three different chordwise locations in $30\delta_0$ cases in Figure D.14.

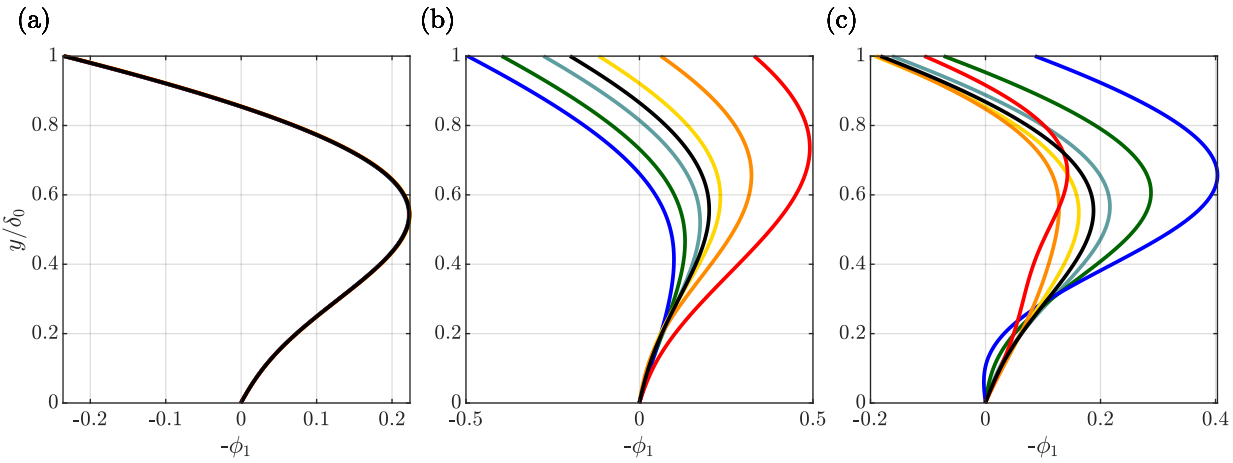

Figure D.14: Wall-normal variation of $-\phi_1$ in clean case (black), $0.5p_f$ $30w$ case (cyan), $1.5p_f$ $30w$ case (dark green), $2.5p_f$ $30w$ case (blue), $-0.5p_f$ $30w$ case (yellow), $-1.5p_f$ $30w$ case (orange), and $-2.5p_f$ $30w$ case (red) at $x_{st}/\delta_0 =$ (a) $-0.75w$, (b) $-0.2w$, and (c) $0.4w$.

Contours of ϕ_d are shown for $30\delta_0$ cases in Figure D.15, where it appears that the influence of Orr mechanism drastically decreases with decrease of p_f.

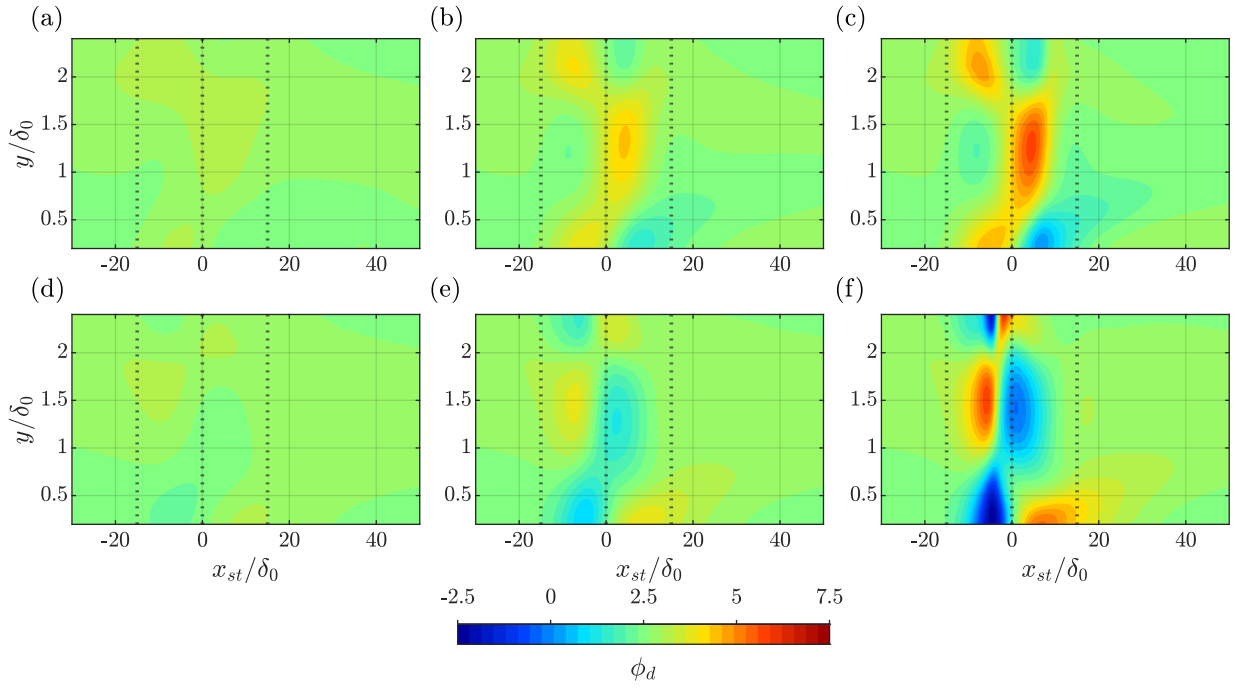

Figure D.15: Contours of ϕ_d in (a) $0.5p_f$ $30w$ case, (b) $1.5p_f$ $30w$ case, (c) $2.5p_f$ $30w$ case, (d) $-0.5p_f$ $30w$ case, (e) $-1.5p_f$ $30w$ case, and (f) $-2.5p_f$ $30w$ case; black dotted lines at $x_{st}/\delta_0 = -w/2,\ 0,$ and $w/2$ show the region of ΔP imposition in deformed cases.

E

Perturbation Properties of Three-way cases

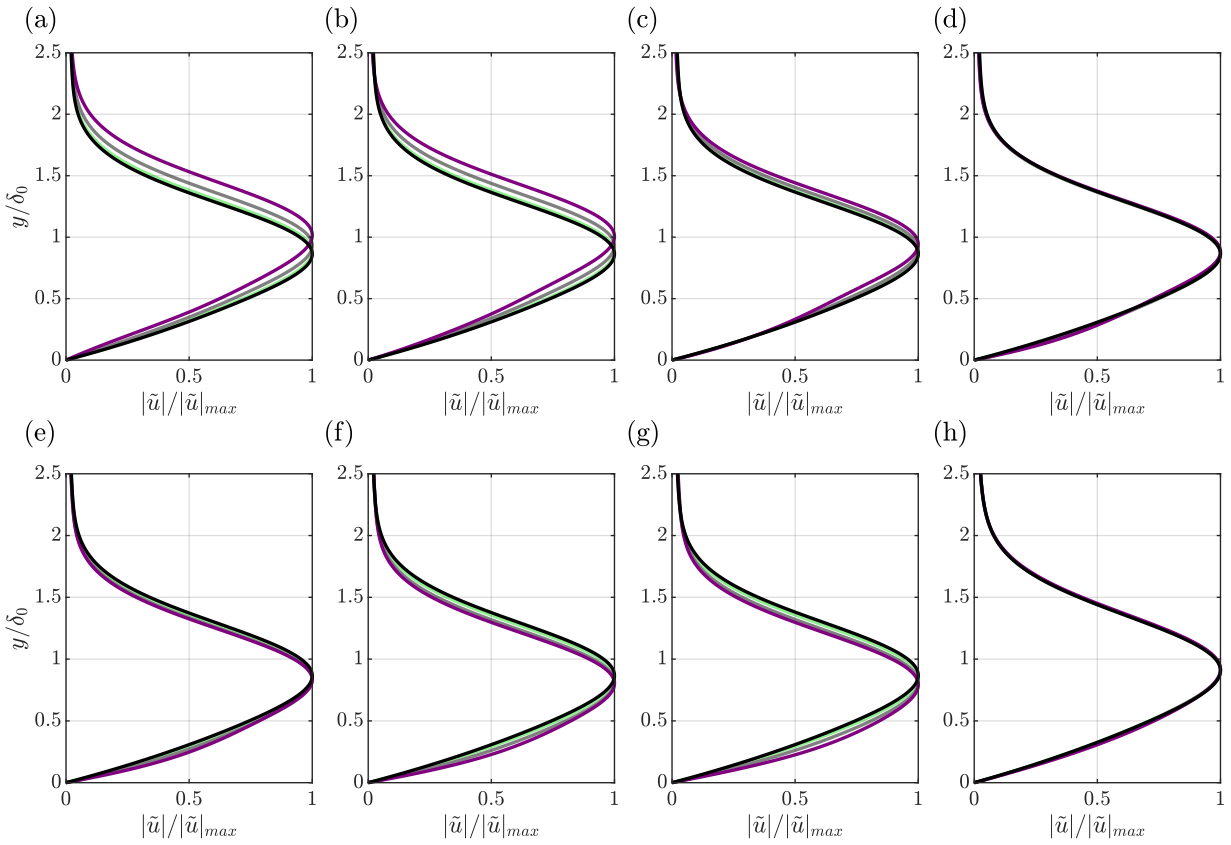

Figure E.1: Wall-normal variation of normalized amplitude function of u' in three-way cases; $0.5p_f$ (light green), $1.5p_f$ (grey), $2.5p_f$ (purple), and clean case (black) at x_{st}/δ_0 = (a) $-0.4w$, (b) $-0.25w$, (c) $-0.15w$, (d) $-0.05w$, (e) $0.05w$, (f) $0.15w$, (g) $0.25w$, and (h) $0.4w$.

The wall-normal variation of normalized amplitude function of u', wherein the perturbation amplitude function is normalized by the maximum value of $\tilde{u}$ is shown for $30\delta_0$ cases in Figure E.1. No secondary peaks emerge. Amplitude evolution trends in synthetic three-way and step cases are shown in Figure E.2 (b) and Figure E.3 respectively. In both cases, amplitude growth with respect to the clean case is enhanced in the first region of wall-tangential base flow deceleration used for comparison i.e. most of the first adverse ΔP region of synthetic three-way cases and the adverse pressure gradient region before $x_{st}/\delta_0 = -4$ in FFS cases.

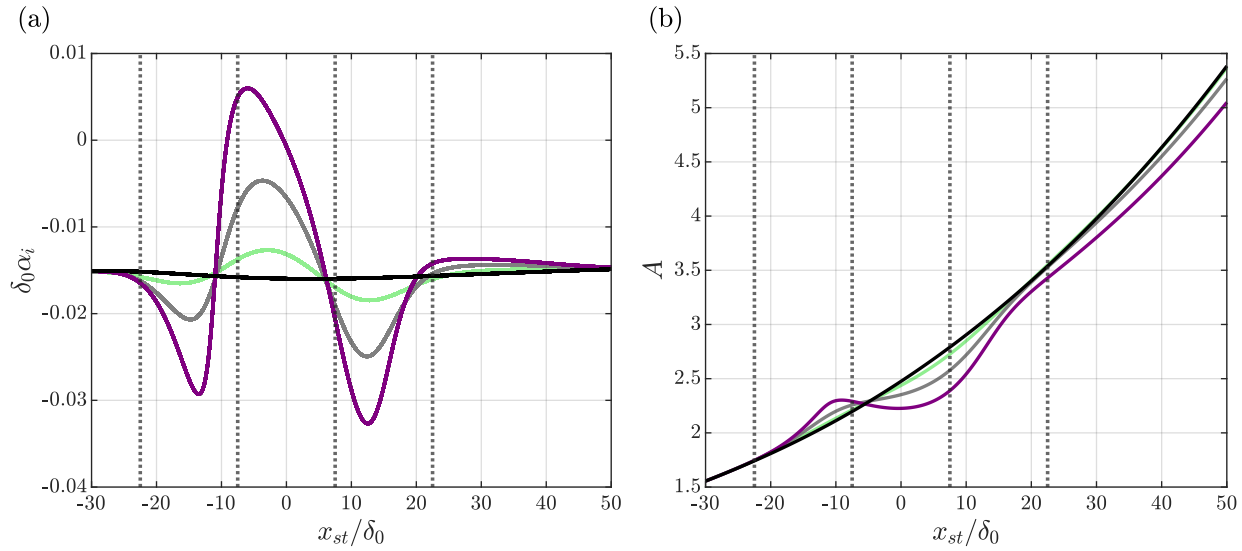

Figure E.2: Chordwise evolution of (a) growth rate and (b) Amplitude in three-way cases; $0.5p_f$ (light green), $1.5p_f$ (grey), $2.5p_f$ (purple), and clean case (black); black dotted lines at $x_{st}/\delta_0 = -3w/4,\ -w/4,\ w/4,$ and $3w/4$ show the region of ΔP imposition in deformed cases.

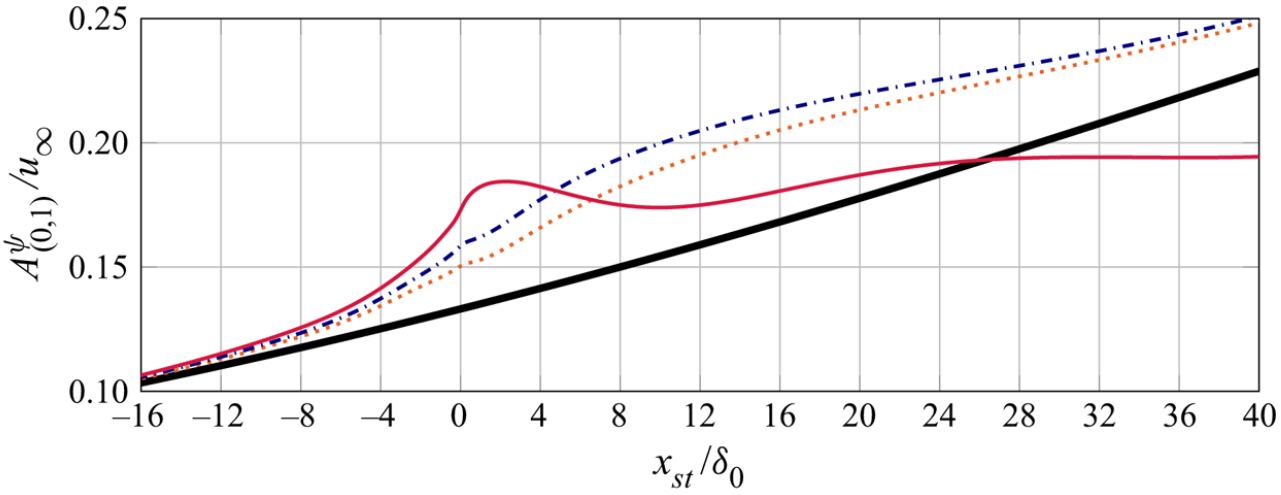

Figure E.3: Chordwise amplitude evolution based on the value of total fundamental perturbation vector norm (denoted as ψ) at primary peak (*top*) in the smooth case (thick solid black), step case I (dotted orange), step case II (dashed-dotted blue), and step case III (thin solid red); reproduced from Casacuberta, Hickel, Westerbeek, and Kotsonis (2022).

The chordwise variation of $\mathcal{P}_{x_d}$, $\mathcal{P}_{y_d}$, and $\mathcal{P}$ at two different wall-normal heights for three-way cases are shown in Figure E.4. Enhanced $\mathcal{P}$ with respect to clean case is observed in regions of positive $\mathcal{P}_{x_d}$ or flow deceleration and vice versa.

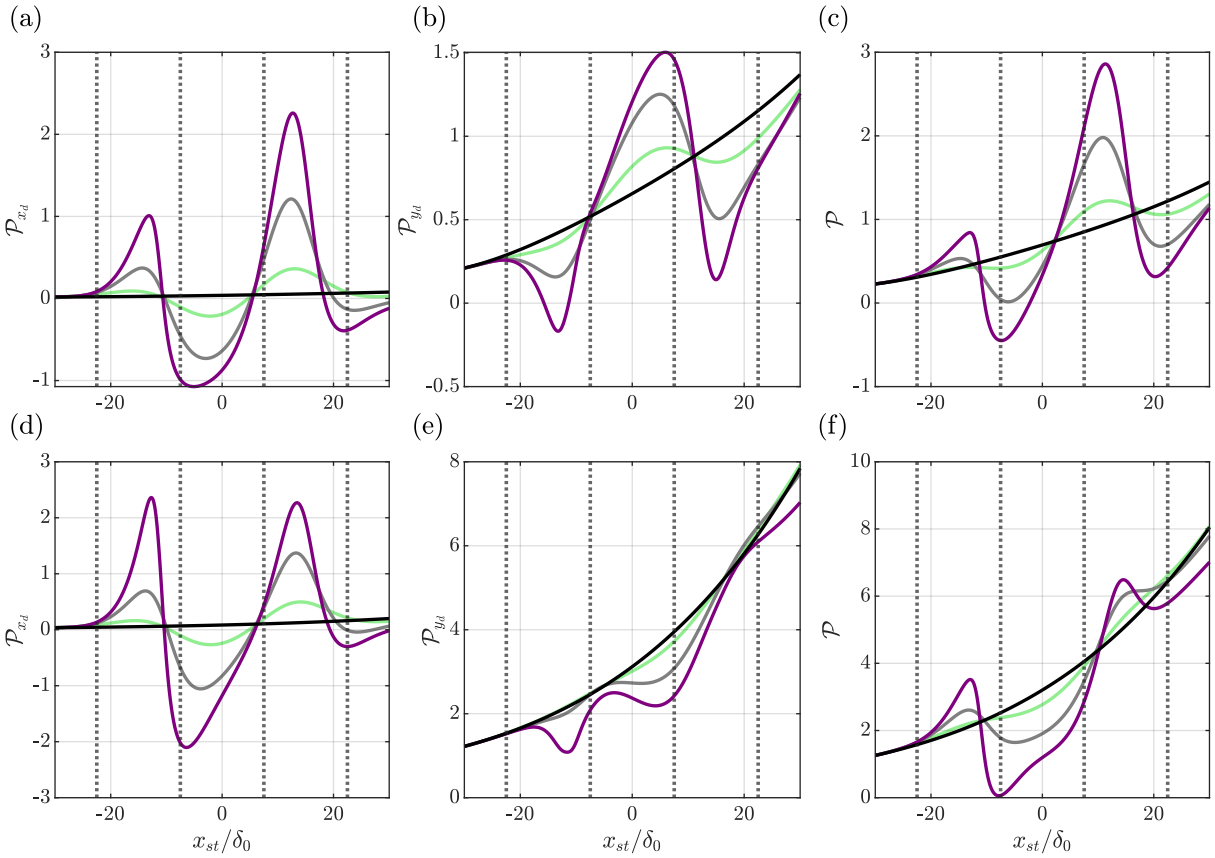

Figure E.4: Evolution of $\mathcal{P}_{x_d}$ (a,d), $\mathcal{P}_{y_d}$ (b,e), $\mathcal{P}$ (c,f) in three-way cases; $0.5p_f$ (light green), $1.5p_f$ (grey), $2.5p_f$ (purple), and clean case (black); black dotted lines at $x_{st}/\delta_0 = -3w/4,\ -w/4,\ w/4,$ and $3w/4$ show the region of ΔP imposition in deformed cases.